# Development of Biologically Active Metal Complexes: Synthesis, Spectroscopy and Biological Evaluation of Ruthenium-based Benzimidazolium Complexes Against Cancer

A Master's Dissertation

by

**Humbelani Ramulumo**


University of Cape Town

Department of Chemistry

February 2022

Supervisor: Dr. Siyabonga Ngubane

Co-supervisor: Dr. Prinessa Chellan

## Acknowledgement

I would like to extend my deepest thanks to the UCT department of Chemistry and my supervisors Dr Siyabonga Ngubane and Co-Supervisor Dr. Prinessa Chellan for assistance, support, guidance as well as constructive criticism throughout the course of my project. I would also like to acknowledge and appreciate the University of Cape Town for offering me the resources and space to carry out my research. I also offer a special thanks the University of Stellenbosch for running ESI-MS and elemental analysis experiments as well as offering me space to carry out experiments through a collaborative action. I would also like to acknowledge Professor Sharon Prince of the UCT Faculty of Health Sciences faculty for collaborating with us and offering resources to conduct biological studies. I offer a special thanks to my colleagues and friends in the Chemistry department and the Ngubane Research Group support and guidance. Special thanks to Dr. Shepherd Siangwata for being a kind, encouraging and patient mentor, Mr Thato Medupe, and Mr Sinethemba Mkhize for their supportive friendship and assistance in interpretation and discussion of my results. I would also like to thank all my sponsors; the National Research Foundation, Ada and Bertie Levenstein Bursary and the University Research Committee for funding. Lastly, I would like to appreciate my family for their support, believing in me and motivation throughout the entire journey.

## Declaration

I declare that "**Development of Biologically Active Metal Complexes: Synthesis, Spectroscopy and Biological Evaluation of Ruthenium-based Benzimidazolium Complexes Against Cancer**" is my own work and to my knowledge, has not been submitted to examination for the award of any degree. All the sources of information used to collect and analyse data are acknowledged, cited, and completely referenced at the end of each chapter.

Signed by candidate

Humbelani Ramulumo

29/03/2022

## Abstract

The study focused on the synthesis and characterisation of ionic imidazopyridine tetracarboxylato diruthenium complexes bearing different counterions like $NO_3$, $PF_6$ and $BF_4$. The biological activity of the synthesized complexes was evaluated against MCF-7 breast cancer cells as well as the non-tumorigenic MCF-12A epithelial cell lines. The complexes were fully characterized using a variety of analytical techniques such as spectroscopy ($^1$H, UV-Vis and FTIR) and cyclic voltammetry. Mass spectrometry was used to identify the masses of the products of interests to confirm the successful formation of new species.

The stability of the solvents in DMSO at room temperature conditions was evaluated for a period of 72 h, and the complexes showed sufficient stability. All the synthesized complexes displayed significantly good anticancer activity against the MCF-7 breast cancer cell line. The complexes displayed good solubility in solvents like DMSO and biological media relative to the diruthenium tetraacetate chloride precursor complex as well as the ligands. The resulting complexes displayed superior anticancer activity in comparison to the free uncoordinated ligands and this was comparable to that of the anticancer drug Cisplatin. The complexes bearing ligands with ferrocene displayed the best anticancer activity with $IC_{50}$ values in the µM range and comparable to those of cisplatin. The complex **C7** containing 2-ferrocenyl-1H-Imidazo(4,5-c)pyridine (**L3**) had the greatest anticancer activity ($IC_{50}$ value of 66.47 µM) towards the MCF-7 breast cancer cell line while complex **C5** containing the phenyl substituted ligand showed the lowest anticancer activity with an $IC_{50}$ value of 79.58 µM. The selectivity indices (S.I.) of the complexes **C5**, **C7** and **C13** were also determined from the $IC_{50}$ values of the MCF-12A and the MCF-7 breast cancer cell. Complex **C5** was highly cytotoxic to the non-tumorigenic cell line at all tested concentrations and reduced cell viability of MCF-12A cell line by more than 90% at the maximum tested concentration. Complexes **C7** and **C13** displayed moderate cytotoxicity towards the healthy cell lines relative to cisplatin. The selectivity studies indicated that one of the compounds bearing a phenyl substituted ligand was toxic to the normal healthy cell line.

## List of Abbreviations

| Abbreviation | Term |
|---|---|
| FTIR | Fourier Transform Infrared Spectroscopy |
| UV-Vis Spectroscopy | Ultraviolet-Visible Spectroscopy |
| FTIR | Fourier Transform Infrared Spectroscopy |
| GSH | Glutathione |
| DNA | deoxyribonucleic acid |
| ROS | Reactive Oxygen Species |
| 2,3-DAP | 2,3-Diaminopyridine |
| 3,4-DAP | 3,4-Diaminopyridine |
| FCA | Ferrocene carboxaldehyde |
| OAc | Acetate |
| TFA | Trifluoroacetic acid |
| DMSO | Dimethyl Sulfoxide |
| TLC | Thin Layer Chromatography |
| CV | Cyclic Voltammetry |
| NMR | Nuclear Magnetic Resonance |
| COSY | Homonuclear Correlation Spectroscopy |
| HSQC | Heteronuclear Single Quantum Coherence |
| Dept NMR | Decoupled NMR |
| ESI-TOF | Electrospray Ionisation Time of Flight |
| HRMS | High Resolution Mass Spectrometry |
| LCMS | Liquid Chromatography Mass Spectrometry |
| EA | Elemental Analysis |

# Chapter 1: Introduction

## 1.1 Background on cancer therapy

Cancer is a disease that occurs when there is rapid growth of tumour cells due to uncontrolled cell division and this happens when the tumour suppressor genes responsible for controlling cell differentiation become ineffective. Cancer cells can be localised in one affected tissue to form benign tumour and can be carried in the blood stream from one affected tissue to other unaffected areas of the body to form malignant tumour. Malignant cells can grow to form more lumps or tumours through a process called metastases and are difficult to treat. Cancer is responsible for a large proportion of disease-related death cases reported world-wide and it is the second leading cause of death in the world.[1] The WHO estimated 20 million global new cases in 2020 with approximately 10 million deaths as shown in **Figure 1.1**.[2] Breast cancer was the most prevalent form of cancer in females whereas in males, prostate cancer was the most frequently diagnosed.

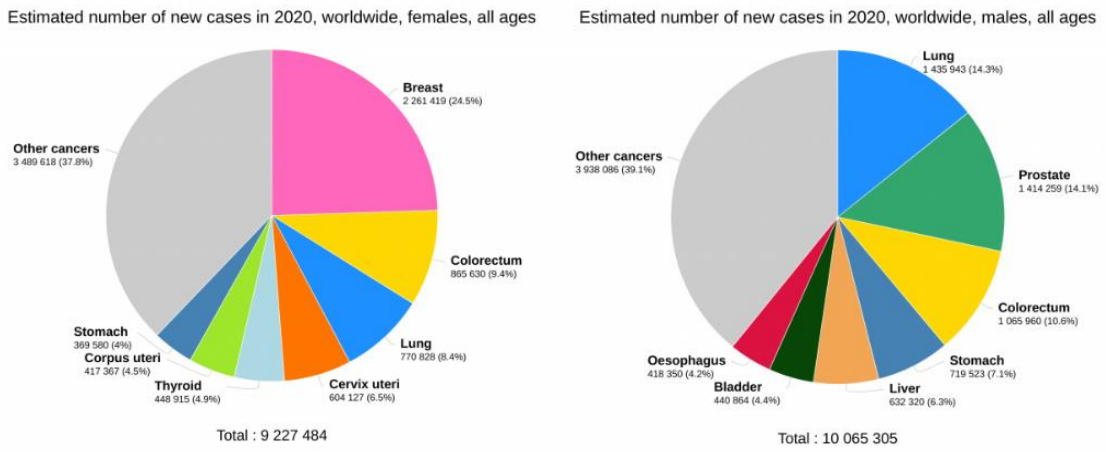


**Figure 1.1.** Cancer estimates and distribution between males and females as presented by the International agency for cancer research.[3]

Various carcinogens such as tobacco smoke and exposure to UV-rays can play a role in cancer progression. Many possible types of cancers have been identified such as lymphoma, sarcoma, and neuroblastoma where the tumors can be localised in different parts of the body as shown in **Figure 1.2**. Following the serendipitous discovery of cisplatin and other platinum (pt)-based derivatives, metallodrugs containing metals such as platinum (Pt), ruthenium (Ru), copper (Cu) and Zinc (Zn) have been of great interest to researchers.[4,5,6-8] This is due to metals having unique and tuneable properties such as redox activity, variable coordination and reactivity with diverse organic substrates, which allows them to display a wide range of biological activities.

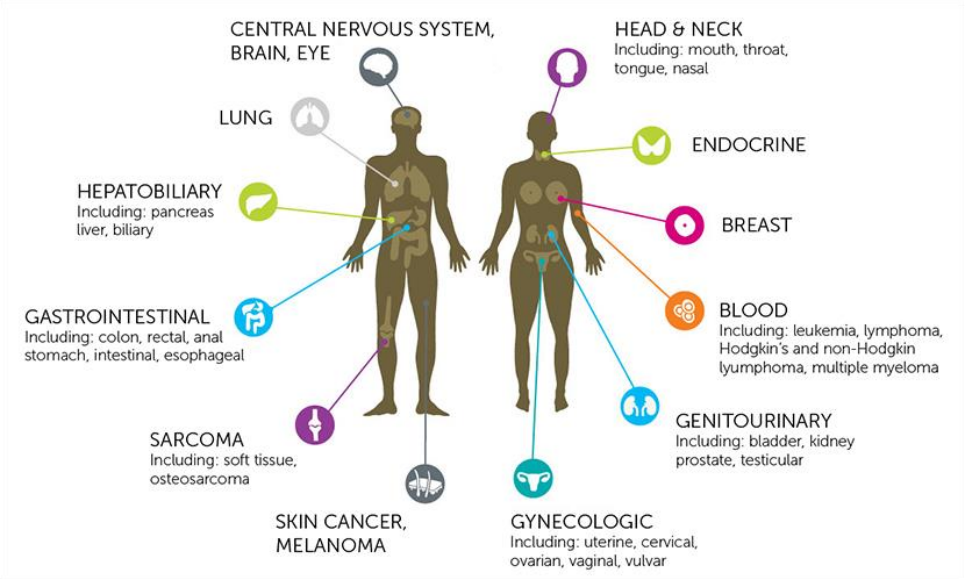


**Figure 1.2.** Distribution of the common cancer types in male compared to female.[9]

## 1.2 Metallodrugs in anticancer therapy

Metal centres can form chemical bonds with donor atoms of varying electronegativity to form complexes with varying stabilities, as explained by the HSAB principle.[8] Cisplatin (cis-diammine-dichloroplatinum (II)) (*abbreviated* CDDP) is a Pt (II)-based drug given as a first line drug in anticancer therapy. It's discovery follows the study on the effect of an electric current on the bacteria *Escherichia coli* by Rosenberg and VanCamp,[5] which has since paved way for further studies on other second generation Pt (II) drugs such as carboplatin and oxaliplatin which have similar mode of action.[10] The mechanism of action of cisplatin involves binding to N-7 guanine on DNA and crosslinking the DNA strands as shown in **Figure 1.3**. After intravenous administration of the drug and cellular uptake, chloride exchange with water results in the formation of positively charged aqua species which can irreversibly bind to DNA. Platinum-based anticancer drug complexes are the leading drug candidates and contribute to approximately 50% of chemotherapeutic drugs administered worldwide.[11]

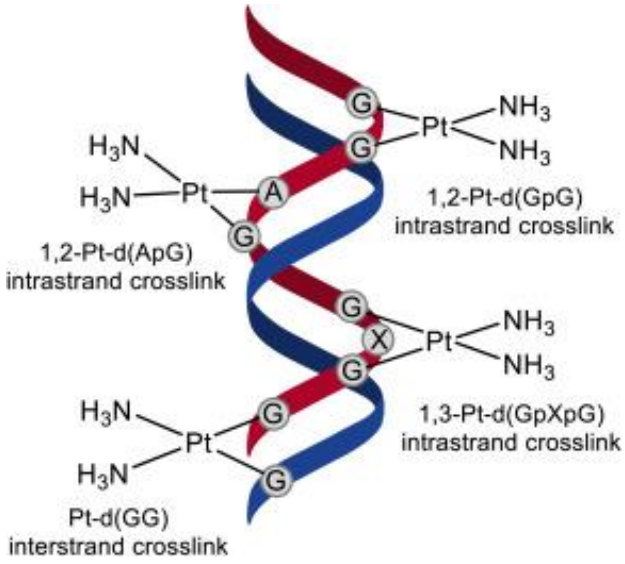


**Figure 1.3.** Illustration of the intra-strand DNA adducts and crosslinks resulting from cisplatin binding to DNA nucleotides. [12]

Several drawbacks such as limited selectivity against cancer cells, ineffectiveness against certain cancer cells and various side effects such as toxicity limit the applicability of many Pt-based metallodrugs and their success in clinical trials. Other drawbacks associated with cisplatin and its derivatives include chemoresistance, neurotoxicity and nephrotoxicity.[13] As a result, second generation Pt (IV) prodrugs which mainly exhibit octahedral geometry have been developed to try and combat the cytotoxic side effects of Pt (II)-based drugs and to reduce resistance.[14] Structures of some of these complexes are displayed in **Figure 1.4**. These derivates have made their way through clinical trials, however still display cross-resistance with Cisplatin, and also fail to address the major challenges associated with the administration of Cisplatin.[15]

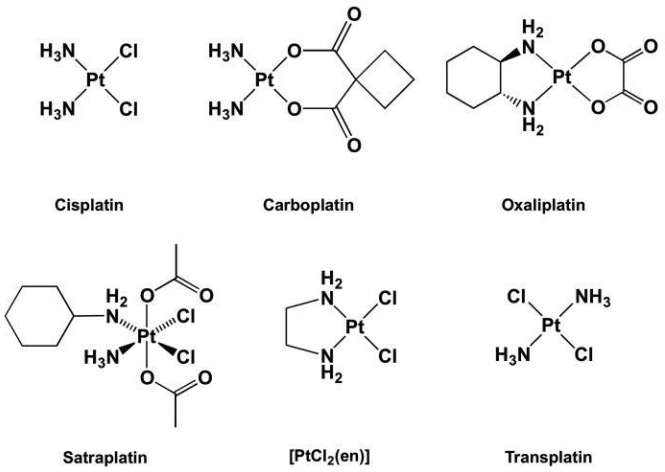


**Figure 1.4.** Structures of the second and third generation platinum-based anticancer drugs.[16]

Ruthenium-based complexes possess unique properties compared to Pt-based complexes, such as better selectivity to cancer cells, allowing them to act as potential alternative drug candidates with unique mechanism of action.[17] Ruthenium is on the second row of transition metals, is less oxyphilic and slightly acidic which allows it to display properties applicable in anticancer diagnostics.[18] Ru can bind to DNA through covalent or non-covalent interactions such as electrostatic and stacking interactions and It can also bind to proteins such as glutathione (GSH), albumin and mitochondrial proteins which affects the normal functioning of the cells.[18] Ruthenium also has the ability to mimic iron binding to transferrin receptors, affecting its rate of uptake into cells.[10] The activation of Ru(III) by its reduction to Ru (II) in cells by interacting with biological reducing agents such as glutathione means the complexes can be administered in their less active form.

Ru complexes have been extensively studied and although many of them show low levels of cytotoxicity and high selectivity, no Ru anticancer drugs have been commercialised for therapeutic use.[20] Their mechanism of action is not clearly understood, however is proposed to be mainly *via* apoptosis involving altering the permeability of the cell membrane. Other Ru complexes have been shown to accumulate in organelles such as mitochondria or ribosomes, affecting affect cell functioning.[21] Examples of Ru complexes that have progressed to clinical trials and currently under chemotherapy development are shown in **Figure 1.5**. Imidazolium (NAMI-A) acts by disrupting the cell cycle, Indazolium (KP1019) affects mitochondrial pathways while NKP-1339 is a salt form of KP1019 designed to improve on the solubility of KP1019. Other complexes of ruthenium such as arene-Ru Schiff base (RAS) complexes have also displayed low $IC_{50}$ values in the μM range and inhibited various cancers.[22]

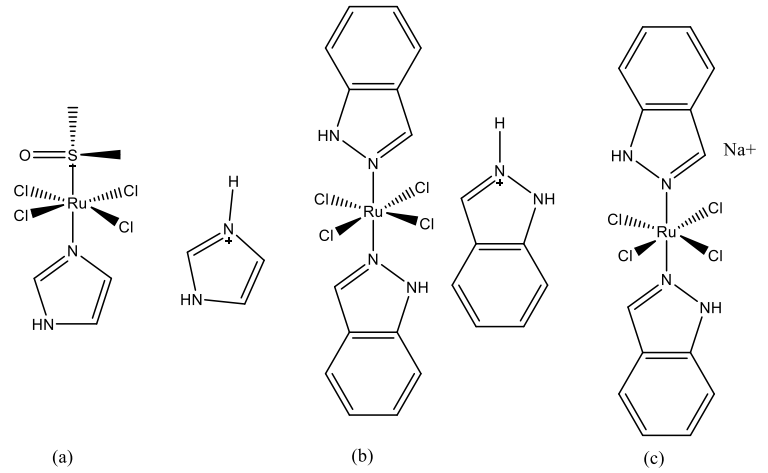


**Figure 1.5.** Structures of Ru-based metallodrugs in clinical trials for cancer therapy (a) NAMI-A, (b) KP-1019 and (c) NKP1339.[17]

### 1.3 Ruthenium-bimetallic complexes

Many studies of the effect of Ru complexes on anticancer activity have focused on monoruthenium complexes due to their unique and tuneable chemical properties.[23] Bimetallic structures consisting of diruthenium centres bridged by N, N or O, O bridging ligands are highly stable structures with a $D_4h$ symmetry. The synthesis of diruthenium tetraacetate chloride was first reported by Wilkinson in 1966.[24] The complex was later reported to exist in the solid state as a polymeric complex bridged by chloride ligands in a zigzag fashion.[25] The complexes are generally insoluble in aqueous solution, but the addition of suitable ligands can render the complexes more soluble. For binuclear diruthenium complexes, divalent ($Ru_2^{4+}$) and mixed-valent ($Ru_2^{5+}$) states exist.

Mixed valent paddlewheel complexes of the form $M_2(OAc)_4(L)_2$ where M = Ru and L = $H_2O$, THF, or Cl have been described,[26] where the synthesis procedures mostly involve $[M_2(OAc)_4Cl]$ as the precursor complex, and the metals have oxidation states of II or III.[27] The oxidation state of the metal produces a paramagnetic complex with an unpaired electron (as in $Ru_2^{2+}$ and $Ru_2^{5+}$), and the resulting nuclear magnetic resonance (NMR) spectrum yields broader and highly shifted resonance peaks. **Figure 1.6** shows the general structure of a paddlewheel complex consisting of two Ru metal centres with four μ-bridged ligand groups, where both metal centres are equivalent and the total oxidation state is a sum of the individual oxidation states.[28] The addition and linkage of ligands to the metal centres at the axial position to form an extended polymeric chain with better solubility has been reported.[29]

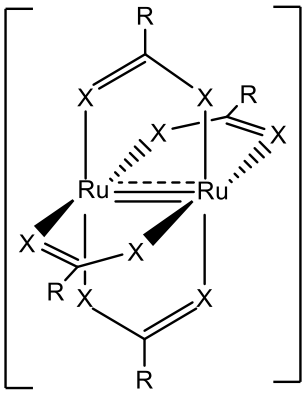


X= N, O, etc.

R= H, Me, OMe, etc.

**Figure 1.6**. General structure of a Ru-based paddlewheel complex.

The magnetic, catalytic, electronic and mesomorphic properties of paddlewheel structures have previously been studied.[30] Silva and co-workers presented the synthesis of diruthenium tetraacetate complexes bridged by non-steroidal anti-inflammatory drugs such as ibuprofen and naproxen. This equatorial displacement of the acetate groups with the ligands increased the efficacy of the ligands relative to the free uncoordinated ligands.[31] The synthesis of a diruthenium acetate complex bearing the isomers of indolylglyoxylyl dipeptide ligands has also been reported by Barressi et al.[32] This study found that complexation improved the efficacy of the ligands and the resulting complex $[Ru_2(EB776)_4Cl]$ displayed a low $IC_{50}$ value against glioblastoma cell lines while its isomer $[Ru_2(EB106)_4Cl]$ was completely inactive.

### 1.4 Coordination of ligands to metal centres

Various ligands such as phenanthroline, benzimidazoles and bipyridines have been studied for their anticancer properties and potential to improve on the anticancer activity of metal complexes containing Platinum Group Metals (PGMs).[33, 34] The donor numbers and geometry of the ligands affects the intracellular binding characteristics to the metal, which creates a unique electronic environment around the metal centre. These ligands can coordinate as bidentate *O, O* donors in the case of carboxylates or *N, N* chelates in the case of nitrogen donors such as benzamidines or formamidine groups. Ligands can also coordinate in monodentate fashion using single donor atoms. The coordination of the ligands to the metal centres affects the reactivity, oxidation state of the metal, lipophilicity of the complexes and can also activate an inactive complex. Inactive ligands such as hydrazine have been found to exhibit activity after complexation to metal centres.[35]

## 1.5 Benzimidazole ligands

The benzimidazole ligand (**Figure 1.7**) is a useful pharmacophore that forms a major framework in many impactful cancer agents that have been studied[36] and it forms part of wide variety of natural products such as vitamin B12.[37] The solubility of benzimidazoles in alcohol is higher than in water and the solubility decreases with an increase in alcohol chain length. The introduction of various polar and non-polar groups around the ring also affects the solubility.[38] The activity of many benzimidazole derivatives has been found to be comparable to that of known antimalarial drugs such as quinines.[39] The reactivity of the imidazole ring allows the ligand to act as an acid through donation of a proton or to accept a proton using the lone pair on the nitrogen atom which is also involved in metal coordination.

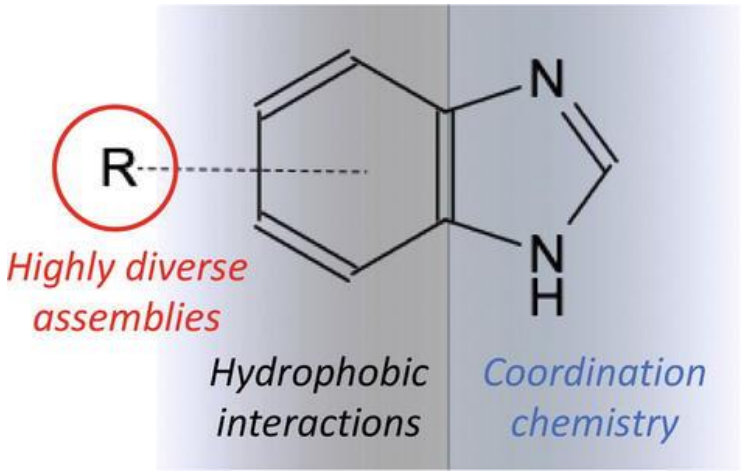


**Figure 1.7.** Structure of a benzimidazole framework, showing the functionalities of the pharmacophore.

The synthesis of benzimidazoles involves a cyclic condensation reaction between a diaminobenzene ring and the carbonyl functional group of an aldehyde or carboxylic acid. The reactions to synthesise the scaffolds are performed under strongly acidic conditions or in the presence of milder acidifying reagents.[40]

## 1.6 Imidazopyridine ligands

These are an interesting class of benzimidazole heterocyclic structures containing a pyridine ring fused to the 4,5-position of an imidazole group. The structures possess a broad variety of physiological properties such as antiviral, antibacterial, anti-inflammatory and they are an important scaffold in some marketed drugs.[41] Aromatic *N*-heterocyclic structures such as imidazole are present in important biologically active compounds as well as in many natural products like biotin, histidine and the hormone histamine.[42] Imidazopyridine groups form components of nucleic acid purine bases which are an essential building blocks of DNA.

The position of the nitrogen atom in the pyridine ring, together with the aromatic system influence the properties of the imidazopyridine structures.[43] The nitrogen atom on the pyridine ring interacts with nitrogen of the imidazole group and this can improve the binding affinity of the ligands to metal cations.[44,45] The scaffold can influence the interaction of target compounds with biological molecules as well as the Absorption, Distribution, Metabolism and Excretion (ADME) parameters of its resulting derivatives.[41] Azaindoles are structurally analogous to imidazopyridine ligands and only lack one nitrogen on the imidazole ring. Azaindole derivatives displaying cytotoxicity against human carcinoma cell lines were reported by Pavel and coworkers.[46] Although insufficient biological data on whether the utilisation of different indole isomers affects cytotoxicity, the results showed that complexation with 4-azaindole isomer produced complexes which were less effective than its 7-azaindole analogue. This result showed that the position of the nitrogen atom on the pyridine ring affects the anticancer activity.

The structures displayed in **Figure 1.8** are some common pharmacologically active compounds containing the imidazopyridine moiety. Zolpidem and the other examples of imidazopyridine ligands have been shown to act in the central nervous system by inhibiting neurotransmitters.[47] In another study the cytotoxic effect of an imidazopyridine derivative on cervical cancer was presented, and the derivative was found to exhibit anticancer activity through mitochondrial-mediated and apoptotic pathways.[48] Bukowski et al., also synthesised a series of thiosemicarbazones fused with the imidazo[4,5-b]pyridine ring and these showed promising anti-mycobacterial activity.[49] Some derivatives of imidazopyridine have been found to display antiproliferative activity by acting as inhibitors of Phosphoinositide 3-Kinase Signaling.[50] Saeedi and coworkers reported on the synthesis and anticancer evaluation of Imidazopyridine derivatives linked to carbamate moieties, which showed that imidazopyridine ligands are potent inhibitors of α-glucosidase enzyme.[51]

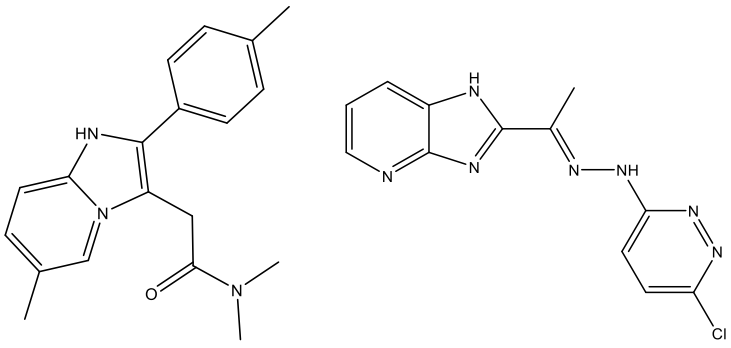


**Figure 1.8.** The structure of zolpidem (left) and a thiosemicarbazones fused derivative of imidazo[4,5-b]pyridine (right).

Derivatives of Imidazopyridine that contain aromatic aldehydes and pyridine groups are effective inhibitors of tumour growth and display antiproliferative activity against breast and prostate cancers. Muniyan et al., reported on the antiproliferative activity of novel imidazopyridine derivatives containing modified phenyl and amine groups.[52] The compounds inhibited cell proliferation and invitro tumorigenicity in castration resistant prostate cancer cells. The structures of some imidazopyridine derivatives displaying antitumour properties are shown in **Figure 1.9**. The imidazopyridine derivative termed CHEQ-2 reported by Song et al., inhibited the growth of liver tumour and the proliferation of various cancers in humans.[53] Baveetsias et al., presented a study on various ligands containing imidazopyridine moieties which are potent inhibitors of the Aurora kinase proteins, the latter playing a key role in cancer initiation and progression.[54] Other derivatives of imidazopyridine that have been studied supressed the growth of breast cancer cells during the G1-phase of the cell cycle,[55] while others inhibited the migration of cancer cells and decreased metastasis progression. It has been speculated that the biological activity of imidazopyridine ligands may be related to their structural similarity to the natural purine bases.

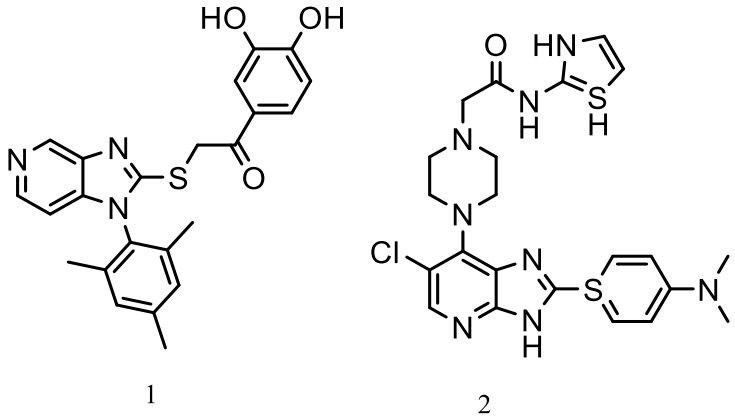


**Figure 1.9.** Examples of imidazopyridine derivatives which are potential tumour inhibitors; CHRQ-2 (1) and an aura kinase inhibitor (2).

### 1.7 Axially coordinated diruthenium paddlewheel complexes

The synthesis of diruthenium tetraacetate complexes coordinated by ligands on the axial and equatorial sides have been reported, but the studies on the anticancer application of the complexes and their mechanism of action are limited. Hitoshi and co-workers presented on the successful synthesis of the first crystal structure of a diruthenium tetra-fluoroacetate complex which was axially bridged by phenazine ligands.[56] The axial interaction of the structures with purine bases such as adenine and guanine was later presented by Gangopadhyay.[57] This work showed that binding to guanine was possible when the acetate

groups on ruthenium acetate were substituted with acetamides, to minimise the degree of repulsion between the acetates and the carbonyl group of the guanine ring.

The synthesis of polymeric complexes of multinuclear Ru, Mo and Rh tetraacetate, containing *trans*-1,2-Bis(N-methylimidazol-2-yl)ethylene ligand was reported by Nico and coworkes.[29] The trans-bie ligand linked the metal centre of one complex to the metal of the next complex, resulting in the formation of an extended one dimensional chain. It was also observed that the complexes crystallised in a 1:1 ligand: complex ratio even when excess of the ligand was used during the synthesis. Manowong et al., presented on the synthesis and characterisation of complex bis-[PcRu(CO)][$Ru_2(ap)_4(C{\equiv}CC_5H_4N)_2$], in which a ruthenium complex is linked to two ruthenium (II) phthalocyanines ligands shown in **Figure 1.10**.[58] The complex was stable and there was weak interactions between the central complex and axially bridging subunits.

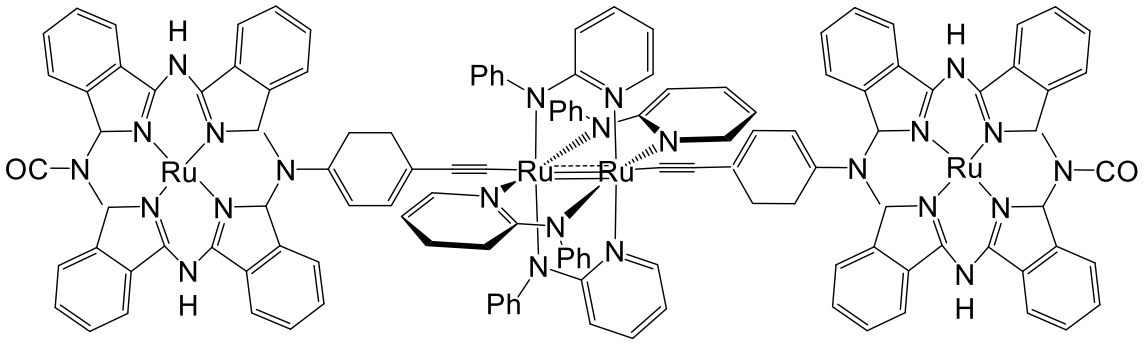


**Figure 1.10.** Structure of a diruthenium complex linked to two ruthenium (II) phthalocyanines ligands.[58]

Another study on the axial coordination of N-donor ligands such as imidazole, caffeine and azaindole to diruthenium acetate was presented by Brendan and co-workers.[59] The ligands coordinated as di-adduct structures to the metal centres using non-protonated basic nitrogen groups. The lantern structure of the diruthenium paddlewheel was retained in the complex. Perhaps a more insightful study on the mechanism of the reactions and kinetics of reactivity between diruthenium tetraacetate and biologically relevant reducing agents was presented by Santos and co-workers.[60] The work studied the interaction of ascorbic acid and glutathione (**Figure 1.11**) with a ruthenium acetate complex, which opened avenue to understanding the interaction of biologically reducing agents with the complexes. A study on the thermodynamics of axial substitution of chlorides with the amino acids such as glycine or histidine on diruthenium tetraacetate complexes showed the formation stable complexes in solution.[61] Other non-nitrogen based ligands such as phosphene have also been axially coordinated to

diruthenium complexes, such as the mixed-valent phosphene diadduct complexes of diruthenium acetate synthesised and structurally characterised by Aquino and coworkers.[62]

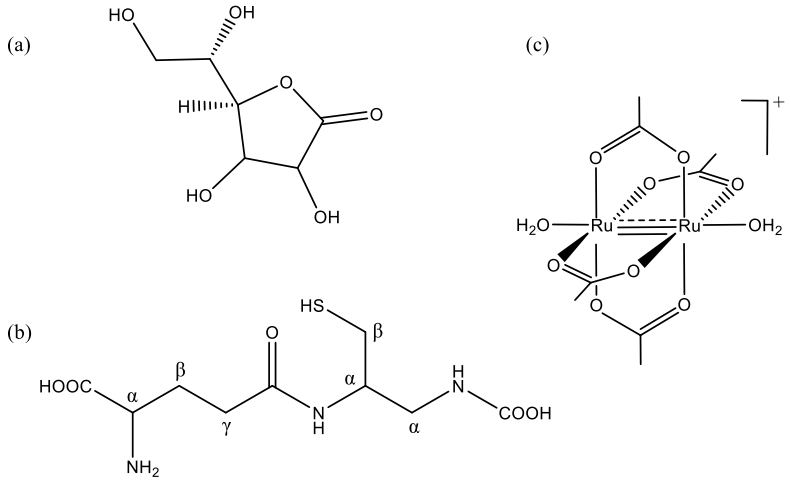


**Figure 1.11**. The structures of ascorbic acid (a), glutathione (b) and the mixed valent diaqua-$Ru_2$ species (c).

### 1.8 Ferrocene pharmacophore in anticancer studies

Ferrocene has previously been reacted with various compounds to generate novel hybrid complexes with antitumour and antimalarial properties. The presence of the ferrocene pharmacophore in ligands is known to assist in the generation of Reactive Oxygen Species (ROS) such as $O_2^{\cdot}$, $OH^{\cdot}$ and $H_2O_2$ which can target the DNA and cell membrane of cells.[63] ROS are known to be generated from the oxidised form of $Fe^{3+}$ which has an unpaired electron in one of its orbitals ($t_{2g}$), and this produces a highly stable free radical species which has the ability to induce oxidative DNA damage.[64] Some metallodrug complexes containing ferrocene which have been used for malaria purposes are shown in **Figure 1.12**.

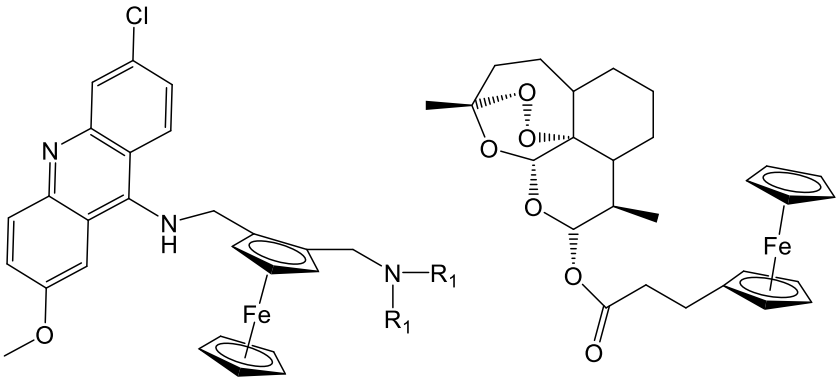


**Figure 1.12.** Antimalarial drugs such as mepacrine and artemisinin which are some of the approved ligands known for fighting malarial parasites.[65]

The emergence of chemoresistance to drugs has fuelled the development of new ideas for the synthesis of metal-based drugs from bioactive compounds to build newer drug candidates that may be potential anticancer drugs.

## 1.9 Research Rationale

Previous studies on the anticancer activity of ruthenium complexes have focused on monoruthenium complexes due to their unique and tuneable chemical properties.[23] Diruthenium complexes have displayed the potential to attack tumour cells by cleaving DNA, and are an interesting class of potential antineoplastic agents which haven't been widely investigated for their anticancer and antimalarial properties.[66] The mechanism of action of diruthenium complexes and how they interact with DNA is still not clearly understood, and majority of studies on diruthenium tetraacetate complexes have focused on obtaining structural, kinetics and reactivity information. Very few studies have been presented on the interaction and binding of biologically relevant ligands to the axial sites of diruthenium tetraacetate complexes, and understanding this interaction is essential to predict the behaviour and interaction of such complexes with nucleotides of DNA. This project has the potential to shed light to the understanding of the mechanism of action of novel diruthenium complexes, which are potential drugs.

Imidazopyridine ligands are an interesting class of bioactive ligands that display interesting activity against neurodegenerative conditions, are tumour inhibitors and structural analogues of nucleic acids. The project aims to evaluate biological activity against MCF-7 breast cancer cells given the incorporation of Ru (with beneficial properties relative to platinum), biologically active ligands (benzimidazole and ferrocene) and the cationic nature to effect solubility. The introduction of ferrocene groups to the second position of imidazopyridine ligands has the potential to introduce beneficial properties such as the generation of reactive oxygen species which are capable of damaging cancer cells. Attaching a phenyl group to the ligands can offer the ability to intercalate between DNA bases. The introduction of a propyl chain has the potential to affect the lipophilicity of the ligands and acts as an excipient that can assist the passing of ligands through the cell membrane.[67] It has been shown previously that the propyl groups have the potential to affect activity through steric and electronic influence.[68,69] The direct synthesis and characterisation of DNA nucleotides is cumbersome; hence the selection of structurally analogous ligands allows for an alternative means of studying the binding of ligands and ruthenium complexes to DNA. Ionic forms of complexes are generally known to be more soluble than their neutral counterparts, thus the introduction of counterions like $NO_3^-$, $PF_6^-$ and $BF_4^-$ can help improve the activity of the complexes through affecting solubility and ability to form ion pairs with the ligands.[70-72]

### 1.10 Aims and specific objectives

- The aims of the research project were to synthesise bimetallic complexes of tetrakis(acetato)chloridodiruthenium(II,III) herein referred to as diruthenium tetraacetate chloride as shown in **Scheme 1.1**. The complexes will be converted to ionic form using different counterions and will be coordinated to derivatives of imidazopyridine ligands substituted on the second position by aryl, ferrocenyl, and propyl groups. The position of the nitrogen atom on the pyridine of the ligands will be varied by selecting different diamino pyridine starting reagents as shown in **Scheme 1.2**. The complexes will be evaluated for activity and selectivity against breast cancer cell lines, focusing on the immortalised MCF-7 breast cancer cells and the non-tumorigenic MCF-12A cell lines.

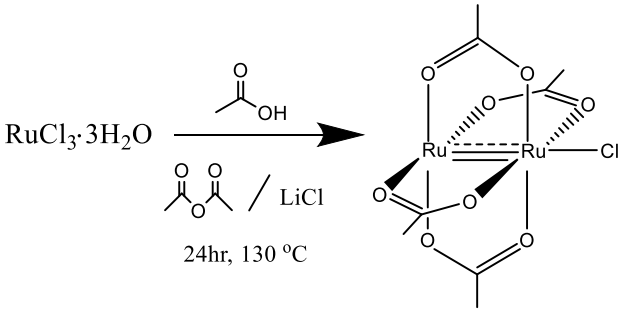


**Scheme 1.1.** Synthesis of diruthenium tetraacetate chloride complex.

- The objectives of the project were to synthesise and fully characterise a series of imidazopyridine ligands containing three different substituents on the second position of the imidazopyridine ligand. To vary the position of the nitrogen atom on the pyridine ring of the ligand by selecting the diamine 2,3-DAP and 3,4-DAP as starting reagents.

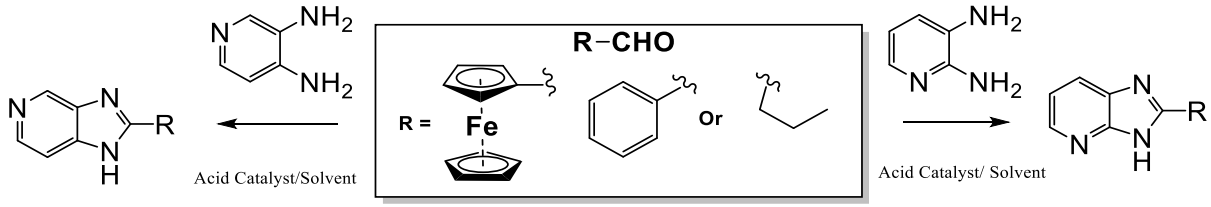


**Scheme 1.2.** Synthesis of imidazopyridine ligands from diaminopyridines and various aldehydes.

- Using known and modified synthetic procedures, to achieve the successful synthesis of a series of ionic bimetallic diruthenium tetraacetate complexes bearing imidazopyridine ligands on the axial site, with the pyridine nitrogen on either position 4 or 7 of the ring as shown in **Scheme 1.3**.

- Different imidazopyridine derivatives will be coordinated into vacant positions on the axial position of diruthenium tetraacetate complexes to arrive at mixed ligand complexes.

- The synthesised complexes will be analysed by using a variety of analytical techniques such as Fourier Transform Infrared spectroscopy (FTIR) to evaluate the presence or absence of functional groups in the complexes, UV-Vis spectroscopy will be used to determine the presence of transitions between the ligand and the metal centres (n $\rightarrow \pi$ or $\pi \rightarrow \pi^*$), NMR spectroscopy to determine the purity and confirm the successful synthesis of the of the ligands or complexes, and Cyclic Voltammetry for electrochemical properties. Mass spectrometry, Liquid Chromatography Mass Spectrometry (LCMS) and elemental analysis will be used to ascertain the successful synthesis of ligands and complexes as well as the purity. In the case of ligands containing the ferrocene metal centres, only NMR spectrometry and elemental analysis will be used to confirm synthesis since no LCMS can be run on metal-based ligands. Care was taken to limit the use of elemental analysis on complexes containing $PF_6^-$ and $BF_4^-$ counterions due to potential formation of a fluoride ion which can damage the instrument.

- To determine the position of coordination of the imidazopyridine ligands in the resulting complexes (whether the coordination is through axial or equatorial position) using mass spectrometry, elemental analysis, or X-ray crystallography.

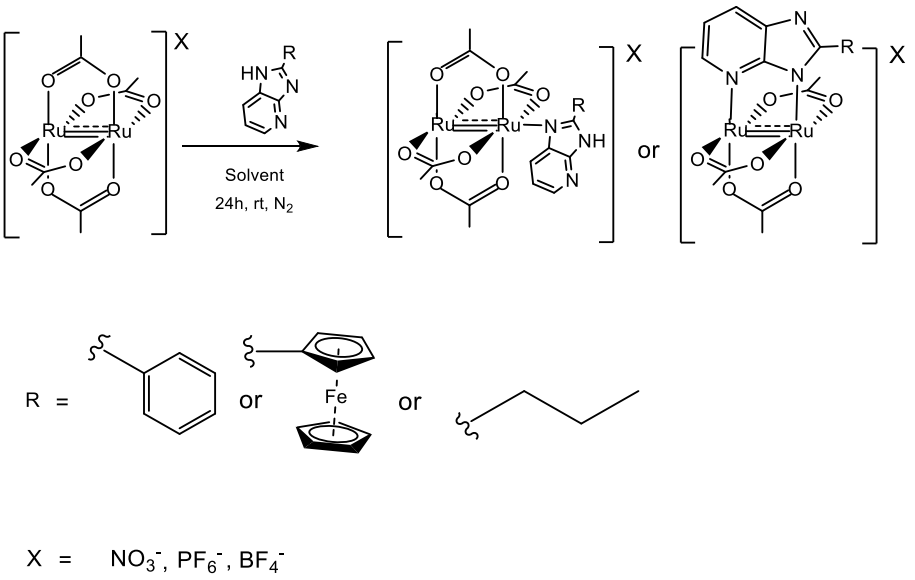


**Scheme 1.3.** Reaction of diruthenium tetraacetate complex with an excess amount of imidazopyridine ligands containing nitrogen on either position 4 or 7 of the pyridine ring. Two possible structures can be formed due to possible axial or equatorial substitution as shown.

- To vary the position of the pyridine nitrogen of the imidazopyridine ligand to position 5 or 6 in the ligand coordinated to the complex. The structure of the desired complex is shown in **Scheme 1.4** and this shows ligand coordination on the axial position of the ring, where the ligand is likely to coordinate on the equatorial position.

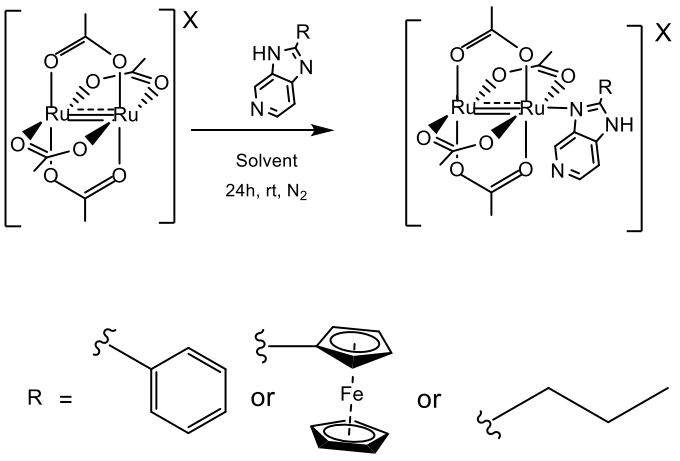


**Scheme 1.4.** Structure of diruthenium tetraacetate complexes bridged by imidazopyridine ligands where the pyridine nitrogen is at position 5 or 6 of the ligand.

- To evaluate the biological activities of the ligands and their corresponding complexes using MTT assays and obtain cytotoxicity values ($IC_{50}$) against MCF-7 breast cancer cells. The biological activity of the complexes will be determined in cancerous cells and compared with the non-cancerous MCF-12A cells.

## 1.11 References


1. Hassanpour, S. H.; Dehghani, M., Review of cancer from perspective of molecular. *J. Cancer Res.* **2017,** *4* (4), 127-129.
2. Sung, H.; Ferlay, J.; Siegel, R.; Laversanne, M.; Soerjomataram, I.; Jemal, A.; Bray, F., Global Cancer Statistics 2020: GLOBOCAN Estimates of Incidence and Mortality Worldwide for 36 Cancers in 185 Countries. *Cancer J. Clin* **2021,** *71*. 209-249
3. UICC, G. C. C. GLOBOCAN 2020: New Global Cancer Data. https://www.uicc.org/news/globocan-2020-new-global-cancer-data.
4. Biot, C.; Castro, W.; Botté, C.; Navarro, M., The therapeutic potential of metal-based antimalarial agents: Implications for the mechanism of action. *Dalton transactions (Cambridge, England : 2003)* **2012,** *41*, 6335-6349.
5. Mjos, K. D.; Orvig, C., Metallodrugs in Medicinal Inorganic Chemistry. *Chem. Rev.* **2014,** *114* (8), 4540-4563.
6. Komeda, S.; Casini, A., Next-Generation Anticancer Metallodrugs. *Curr Top Med Chem.* **2012,** *12*, 219-35.
7. Valletta, E., Metal complexes in cancer therapy In *Poster*, Cittadella, Ed. 2013.
8. Abid, M.; Shamsi, F.; Azam, A., Ruthenium Complexes: An Emerging Ground to the Development of Metallopharmaceuticals for Cancer Therapy. *Mini-Rev Med. Chem.* **2016,** *15*, 1-15.
9. Husabio. What is cancer?. Available at: https://www.cusabio.com/cancer.html. (Accessed 24 July 2022)
10 Lazarevic, T.; Rilak, A.; Bugarcic, Z. D., Platinum, palladium, gold and ruthenium complexes as anticancer agents: Current clinical uses, cytotoxicity studies and future perspectives. *Eur J Med Chem* **2017,** *142*, 8-31.
11. Zaki, M.; Arjmand, F.; Tabassum, S., Current and future potential of metallo drugs: Revisiting DNA-binding of metal containing molecules and their diverse mechanism of action. *Inorganica Chimica Acta* **2016,** *444*, 1-22.
12. Avendaño, C.; Menéndez, J. C., Chapter 5 - DNA Alkylating Agents. In *Medicinal Chemistry of Anticancer Drugs (Second Edition)*, Avendaño, C.; Menéndez, J. C., Eds. Elsevier: Boston, 2015; pp 197-241.
13. Ghosh, S., Cisplatin: The first metal based anticancer drug. *Bioorg. Chem.* **2019,** *88*, 102925.
14. Wang, Z.; Deng, Z.; Zhu, G., Emerging platinum(iv) prodrugs to combat cisplatin resistance: from isolated cancer cells to tumor microenvironment. *Dalton Trans.* **2019,** *48* (8), 2536-2544.
15. Kilpin, K.; Dyson, P., ChemInform Abstract: Enzyme Inhibition by Metal Complexes: Concepts, Strategies and Applications. *Chem. Sci.* **2013,** *4*, 1410-1419.

16. Hall, M. D.; Telma, K. A.; Chang, K. E.; Lee, T. D.; Madigan, J. P.; Lloyd, J. R.; Goldlust, I. S.; Hoeschele, J. D.; Gottesman, M. M., Say no to DMSO: dimethylsulfoxide inactivates cisplatin, carboplatin, and other platinum complexes. *Cancer Res.* **2014,** *74* (14), 3913-3922.
17. Lee, S. Y.; Kim, C. Y.; Nam, T. G., Ruthenium Complexes as Anticancer Agents: A Brief History and Perspectives. *Drug. Des. Devel Ther.* **2020,** *14*, 5375-5392.
18. Macedo, T.; Colina-Vegas, L.; PaixÃO, M.; Navarro, M.; Barreto, B.; Oliveira, P.; Macambira, S.; Machado, M.; Prudêncio, M.; D'Alessandro, S.; Basilico, N.; Moreira, D.; Batista, A.; Soares, M., Chloroquine-containing organoruthenium complexes are fast-acting multistage antimalarial agents. *Parasitol. Res.* **2016,** 1543-1556.
19. Garbutcheon-Singh, K.; Myers, S.; Harper, B.; Ng, N.; Dong, Q.; Xie, C.; Aldrich-Wright, J., The effects of 56MESS on mitochondrial and cytoskeletal proteins and the cell cycle in MDCK cells. *Metallomics.* **2013,** 1061-1067.
20. Page, S., Ruthenium compounds as anticancer agents. *J. Chem. Educ* **2012,** *49*, 26-29.
21. Li, X.; Gorle, A.; Ainsworth, T.; Heimann, K.; Woodward, C.; Collins, J.; Keene, F., RNA and DNA binding of inert oligonuclear ruthenium(II) complexes in live eukaryotic cells. *Dalton Trans.* **2014,** 3594-3603.
22. Chow, M. J.; Licona, C.; Yuan Qiang Wong, D.; Pastorin, G.; Gaiddon, C.; Ang, W. H., Discovery and Investigation of Anticancer Ruthenium–Arene Schiff-Base Complexes via Water-Promoted Combinatorial Three-Component Assembly. *J. Med. Chem.* **2014,** *57* (14), 6043-6059.
23. Pal, A.; Hanan, G., Stereoselective formation of a meso-diruthenium(II,II) complex and tuning the properties of its monoruthenium analogues. *Dalton Trans.* **2014,** *43*.
24. Stephenson, T. A.; Wilkinson, G., New ruthenium carboxylate complexes. *J. inorg. nucl. chem.* **1966,** *28* (10), 2285-2291.
25. Drysdale, K. D.; Beck, E. J.; Stanley Cameron, T.; Robertson, K. N.; A.S. Aquino, M., Crystal structures and physico-chemical properties of a series of $[Ru_2(O_2CCH_3)_4L_2](PF_6)$ adducts (L = $H_2O$, DMF, DMSO). *Inorg. Chim. Acta.* **1997,** *256* (2), 243-252.
26. Nico Fritsch, a. F., vorgelegt von. One Dimensional Coordination Polymers Based on Bridging N,N Donor Ligands. Erlangen-Nuremberg, 2014.
27. Stephenson, T. A.; Wilkinson, G., New ruthenium carboxylate complexes. *Inorg. Nucl. Chem.* **1966,** *28* (10), 2285-2291.
28. Norman, J. G.; Renzoni, G. E.; Case, D. A., Electronic structure of Ru2(O2CR)4+ and Rh2(O2CR)4+ complexes. *J. AM. CHEM. SOC.* **1979,** *101* (18), 5256-5267.
29. Fritsch, N.; Wick, C. R.; Waidmann, T.; Dral, P. O.; Tucher, J.; Heinemann, F. W.; Shubina, T. E.; Clark, T.; Burzlaff, N., Multiply Bonded Metal(II) Acetate (Rhodium,

Ruthenium, and Molybdenum) Complexes with the trans-1,2-Bis(N-methylimidazol-2-yl)ethylene Ligand. *Inorg. Chem.* **2014,** *53* (23), 12305-12314.

30. Aquino, M., Recent developments in the synthesis and properties of diruthenium tetracarboxylates. *Coord. Chem. Rev.* **2004,** *248*, 1025-1045.
31. Ribeiro, G.; Benadiba, M.; Colquhoun, A.; Silva, D., Diruthenium(II, III) complexes of ibuprofen, aspirin, naproxen and indomethacin non-steroidal anti-inflammatory drugs: Synthesis, characterization and their effects on tumor-cell proliferation. *Polyhedron* **2008,** *27*, 1131-1137.
32. Barresi, E.; Tolbatov, I.; Marzo, T.; Zappelli, E.; Marrone, A.; Re, N.; Pratesi, A.; Martini, C.; Taliani, S.; Da Settimo, F.; La Mendola, D., Two mixed valence diruthenium(ii,iii) isomeric complexes show different anticancer properties. *Dalton Trans.* **2021,** *50* (27), 9643-9647.
33. Al Matarneh, C. M.; Mangalagiu, II; Shova, S.; Danac, R., Synthesis, structure, antimycobacterial and anticancer evaluation of new pyrrolo-phenanthroline derivatives. *J. Enzyme Inhib. Med. Chem.* **2016,** *31* (3), 470-80.
34. Adeniyi, A.; Ajibade, P., The Anticancer Activities of Some Nitrogen Donor Ligands Containing bis-Pyrazole, Bipyridine, and Phenanthroline Moiety Using Docking Methods. *Bioinorg. Chem. Appl.* **2018,** *2018*, 1-12.
35. El-Tabl, A.; Aly, F.; Shakdofa, M.; Shakdofa, A., Synthesis, characterization, and biological activity of metal complexes of azohydrazone ligand. *J. Coord. Chem.* **2010,** *63*, 700-712.
36. Purushottamachar, P.; Ramalingam, S.; Njar, V., Development of Benzimidazole Compounds for Cancer Therapy. IntechOpen: 2019.
37. Shah, K.; Chhabra, S.; Shrivastava, S.; Mishra, P., Benzimidazole: A promising pharmacophore. *J. Med. Chem.* **2013,** 1335-1353.
38. O'Shea, D. Synthesis, Characterisation and Biological Activity of Novel Carboxylate Complexes Incorporating Phenanthroline and Benzimidazole Ligands Technological University Dublin, Dublin 2004.
39. Skinner-Adams, T. S.; Davis, T. M.; Manning, L. S.; Johnston, W. A., The efficacy of benzimidazole drugs against Plasmodium falciparum in vitro. *Trans R Soc Trop Med Hyg* **1997,** *91* (5), 580-4.
40. Alaqeel, S. I., Synthetic approaches to benzimidazoles from o-phenylenediamine: A literature review. *J. Saudi Chem. Soc.* **2017,** *21* (2), 229-237.
41. Vanda, D.; Zajdel, P.; Soural, M., Imidazopyridine-based selective and multifunctional ligands of biological targets associated with psychiatric and neurodegenerative diseases. *Eur. J. Med. Chem.* **2019,** *181*, 111569.

42. Bellet, V.; Lichon, L.; Arama, D.; Gallud, A.; Lisowski, V.; Maillard, L.; Garcia, M.; Martinez, J.; Masurier, N., Imidazopyridine-fused [1,3]-diazepinones part 2: Structure-activity relationships and antiproliferative activity against melanoma cells. *Eur. J. Med. Chem.* **2016,** *125*.
43. Leboho, T. C. Novel Syntheses of 5- and 7-Azaindole Derivatives. University of the Witwatersrand
Johannesburg, 2013.
44. Zapata, F.; Caballero, A.; Espinosa, A.; Tárraga, A.; Molina, P., Imidazole-Annelated Ferrocene Derivatives as Highly Selective and Sensitive Multichannel Chemical Probes for Pb(II) Cations. *Inorg. Chem.* **2009,** *74* (13), 4787-4796.
45. Wang, S.; Huang, X.; Ge, Z.; Wang, X.; Li, R., Metal-free C-3 alkylation of imidazopyridines with xanthates and convenient access to alpidem and zolpidem. *RSC Adv.* **2016,** *6* (68), 63532-63535.
46. Štarha, P.; Trávníček, Z., Azaindoles: Suitable ligands of cytotoxic transition metal complexes. *J. Inorg. Biochem.* **2019,** *197*, 110695.
47. Suma, V.; Sreenivasulu, R.; Venkata Basaveswara Rao, M.; Subramanyam, M.; Ahsan, M.; Alluri, R.; Rao, K., Design, synthesis, and biological evaluation of chalcone-linked thiazole-imidazopyridine derivatives as anticancer agents. *J. Med. Chem.* **2020,** *29*, 1643–1654.
48. Wang, J.; Wu, H.; Song, G.; Yang, D.; Huang, J.; Yao, X.; Qin, H.; Chen, Z.; Xu, Z.; Xu, C., A Novel Imidazopyridine Derivative Exerts Anticancer Activity by Inducing Mitochondrial Pathway-Mediated Apoptosis. *Biomed Res Int.* **2020,** *2020*, 4929053.
49. Bukowski, L.; Zwolska, Z.; Augustynowicz-Kopec, E., Synthesis and antituberculotic activity of some new imidazo[4,5-b]pyridine derivatives. *J. Heterocycl. Chem.* **2006,** *42* (10), 1358-1365.
50. Kim, O.; Jeong, Y.; Lee, H.; Hong, S.-S.; Hong, S., Design and Synthesis of Imidazopyridine Analogues as Inhibitors of Phosphoinositide 3-Kinase Signaling and Angiogenesis. *Journal of J. Med. Chem.* **2011,** *54* (7), 2455-2466.
51. Saeedi, M.; Raeisi-Nafchi, M.; Sobhani, S.; Mirfazli, S. S.; Zardkanlou, M.; Mojtabavi, S.; Faramarzi, M.; Akbarzadeh, T., Synthesis of 4-alkylaminoimidazo[1,2-a]pyridines linked to carbamate moiety as potent α-glucosidase inhibitors. *Mol. Divers.* **2020**.
52. Muniyan, S.; Chou, Y.-W.; Ingersoll, M. A.; Devine, A.; Morris, M.; Odero-Marah, V. A.; Khan, S. A.; Chaney, W. G.; Bu, X. R.; Lin, M.-F., Antiproliferative activity of novel imidazopyridine derivatives on castration-resistant human prostate cancer cells. *Cancer Lett.* **2014,** *353* (1), 59-67.

53. Song, Y. n.; Lin, X.; Kang, D.; Li, X.; Zhan, P.; Liu, X.; Zhang, Q., Discovery and characterization of novel imidazopyridine derivative CHEQ-2 as a potent CDC25 inhibitor and promising anticancer drug candidate. *Eur. J. Med. Chem.* **2014,** *82*, 293-307.
54. Bavetsias, V.; Sun, C.; Bouloc, N.; Reynisson, J.; Workman, P.; Linardopoulos, S.; McDonald, E., Hit generation and exploration: imidazo[4,5-b]pyridine derivatives as inhibitors of Aurora kinases. *Bioorg. Med. Chem. Lett.* **2007,** *17* (23), 6567-6571.
55. He, L.-J.; Yang, D.-L.; Chen, H.-Y.; Huang, J.-H.; Zhang, Y.-J.; Qin, H.-X.; Wang, J.-L.; Tang, D.-Y.; Chen, Z.-Z., A Novel Imidazopyridine Derivative Exhibits Anticancer Activity in Breast Cancer by Inhibiting Wnt/β-catenin Signaling. *OncoTargets and ther.* **2020,** *13*, 10111-10121.
56. Miyasaka, H.; Clérac, R.; Campos-Fernández, C. S.; Dunbar, K. R., The first crystal structure of a one-dimensional chain of linked RuII✓RuII units. *J. Chem. Soc, Dalton Trans.* **2001,** (6), 858-861.
57. Gangopadhyay, S.; Gangopadhyay, P. K., Adenine and adenosine derivatives of tetraacetatodiruthenium (II,III) cation. *J. Inorg. Biochem.* **1997,** *66* (3), 175-178.
58. Manowong, M.; van caemelbecke, E.; Rodríguez-morgade, M.; Bear, J.; Kadish, K.; Torres, T., Synthesis and characterization of bis-[PcRu(CO)][$Ru_2(ap)_4$(C equivalent to $CC_5H_4N)_2$]. *J. Porphyr. Phthalocyanines* **2014,** *18*.
59. Bland, B. R. A.; Gilfoy, H. J.; Vamvounis, G.; Robertson, K. N.; Cameron, T. S.; Aquino, M. A. S., Hydrogen bonding in diruthenium(II,III) tetraacetate complexes with biologically relevant axial ligands. *Inorganica. Chimica. Acta.* **2005,** *358* (13), 3927-3936.
60. Santos, R. L. S. R.; van Eldik, R.; de Oliveira Silva, D., Kinetic and mechanistic studies on reactions of diruthenium(ii,iii) with biologically relevant reducing agents. *Dalton Trans.* **2013,** *42* (48), 16796-16805.
61. Santos, R. L. S. R.; van Eldik, R.; de Oliveira Silva, D., Thermodynamics of Axial Substitution and Kinetics of Reactions with Amino Acids for the Paddlewheel Complex Tetrakis(acetato)chloridodiruthenium(II,III). *Inorg. Chem.* **2012,** *51* (12), 6615-6625.
62. Briand, G. G.; Cooke, M. W.; Cameron, T. S.; Farrell, H. M.; Burchell, T. J.; Aquino, M. A. S., An Axial Phosphine Diadduct of Diruthenium(II,III) Tetraacetate. *Inorg. Chem.* **2001,** *40* (14), 3267-3268.
63. Ramirez-Vick, J.; Acevedo, C.; Melendez, E.; Singh, S., Cytotoxicity and Reactive Oxygen Species Generated by Ferrocenium and Ferrocene on MCF7 and MCF10A Cell Lines. *Journal of J. Cancer Sci.* **2012,** *4*, 271-275.
64. Tabbì, G.; Cassino, C.; Cavigiolio, G.; Colangelo, D.; Ghiglia, A.; Viano, I.; Osella, D., Water stability and cytotoxic activity relationship of a series of ferrocenium derivatives.

ESR insights on the radical production during the degradation process. *J. Med. Chem.* **2002,** *45* (26), 5786-96.

65 Biot, C.; Castro, W.; Botte, C. Y.; and Navarro, M., The therapeutic potential of metal-based antimalarial agents: Implications for the mechanism of action. *Dalt. Trans.* 2012, 41, 6335-6349

66. Osterloh, W. R.; Galindo, G.; Yates, M. J.; Van Caemelbecke, E.; Kadish, K. M., Synthesis, Structural and Physicochemical Properties of Water-Soluble Mixed-Ligand Diruthenium Complexes Containing Anilinopyridinate Bridging Ligands. *Inorg. Chem.* **2020,** *59* (1), 584-594.
67. Nemes, D.; Kovács, R.; Nagy, F.; Mező, M.; Poczok, N.; Ujhelyi, Z.; Pető, Á.; Fehér, P.; Fenyvesi, F.; Váradi, J.; Vecsernyés, M.; Bácskay, I., Interaction between Different Pharmaceutical Excipients in Liquid Dosage Forms-Assessment of Cytotoxicity and Antimicrobial Activity. *Mol. (Basel, Switzerland)* **2018,** *23* (7), 1827.
68. Fatima, T.; Haque, R.; Rizal, M.; Ahmad, A.; Asif, M.; Ahamed, M. B. K.; Abdul Majid, A. M. S., Effect of lipophilicity of wingtip groups on the anticancer potential of mono N-heterocyclic carbene silver(I) complexes: Synthesis, crystal structures and in vitro anticancer study. *Appl. Organomet. Chem.* **2017,** *31*.3735-3749
69. Atif, M.; Bhatti, H. N.; Haque, R. A.; Iqbal, M. A.; Ahamed Khadeer, M. B.; Majid, A., Synthesis, Structure, and Anticancer Activity of Symmetrical and Non-symmetrical Silver(I)-N-Heterocyclic Carbene Complexes. *Appl. Biochem. Biotechnol.* **2020,** *191* (3), 1171-1189.
70. Haghdoost, M.; Golbaghi, G.; Guard, J.; Sielanczyk, S.; Patten, K.; Castonguay, A., Synthesis, characterization and biological evaluation of cationic organoruthenium( ii ) fluorene complexes: influence of the nature of the counteranion. *Dalton Trans.* **2019,** *48*. 13396-13405
71. Golbaghi, G.; Haghdoost, M. M.; Yancu, D.; López de los Santos, Y.; Doucet, N.; Patten, S. A.; Sanderson, J. T.; Castonguay, A., Organoruthenium(II) Complexes Bearing an Aromatase Inhibitor: Synthesis, Characterization, in Vitro Biological Activity and in Vivo Toxicity in Zebrafish Embryos. *Organometallics* **2019,** *38* (3), 702-711.
72. Zhang, H.; Guo, L.; Tian, Z.; Tian, M.; Zhang, S.; Xu, Z.; Gong, P.; Zheng, X.; Zhao, J.; Liu, Z., Significant effects of counteranions on the anticancer activity of iridium(iii) complexes. *Chem. commun.* **2018,** *54* (35), 4421-4424.

# Chapter 2: Results and discussion

## 2.1 General synthesis of imidazopyridine ligands

Reaction of *o*-phenylenediamine with carboxylic acids and aldehydes are well known for producing benzimidazoles, through the Phillips Ladenburg and the Weidenhagen reactions.[1,2] The method requires the presence of a water or alcohol solution and often requires the use of high temperatures with poor resulting yields. The reactions have been shown to be possible using aromatic aldehydes or carboxylic acids and the easily available *o*-phenylenediamine following similar mechanisms of action.[3,4] Strongly oxidising conditions increase the electrophilicity of the carbonyl carbon of an aldehyde or carbonyl which allows the reactions to occur more efficiently.[5] Using solvent free methods such as microwave or ultrasonication decreases the possibility of side reactions occurring, which would otherwise result in the formation of catalysts requiring further purification.[6] Traditional procedures are also limited by the use of expensive reagents and catalysts which are often difficult to synthesize. The synthesis of a benzimidazole ligand using *o*-phenylenediamine and formic acid has been reported by Wegner and Millet.[7] Another mechanism for the synthesis of a benzimidazole involving the use of triethyl orthoformate as a reagent has been presented.[8] The procedure shows the carbon atom of the triethyl orthoformate providing the right electrophilicity and oxidation state for the cyclisation process to occur.

For the synthesis of imidazopyridine class of ligands, diaminopyridines are used to substitute *o*-phenylenediamines as starting reagents. The diaminopyridines are structural analogues of diaminobenzenes and their reaction with aldehydes results in the formation of a deactivated $\pi$-system of ligands.[9] The classical synthetic approach employed for synthesising imidazopyridine ligands in this project involved the use of harsh acidic reaction conditions and Lewis acids. The reaction conditions were varied to obtain better reaction yields due to the electron-deficient nature of the pyridine ring which decreases the reactivity of the ring. Pyridine is a deactivating ring due to the presence of an $sp^2$ hybridised nitrogen atom which is electronegative, therefore the nucleophilicity of the ring is decreased relative to a benzene ring. The nitrogen atom increases the polarity of the molecule relative to benzene and decreases the $\pi$-electron density since the lone pair on the nitrogen atom is located on an orbital perpendicular to the ring. A comparison of the $\pi$-system of benzene and pyridine is shown in **Figure 2.1**.

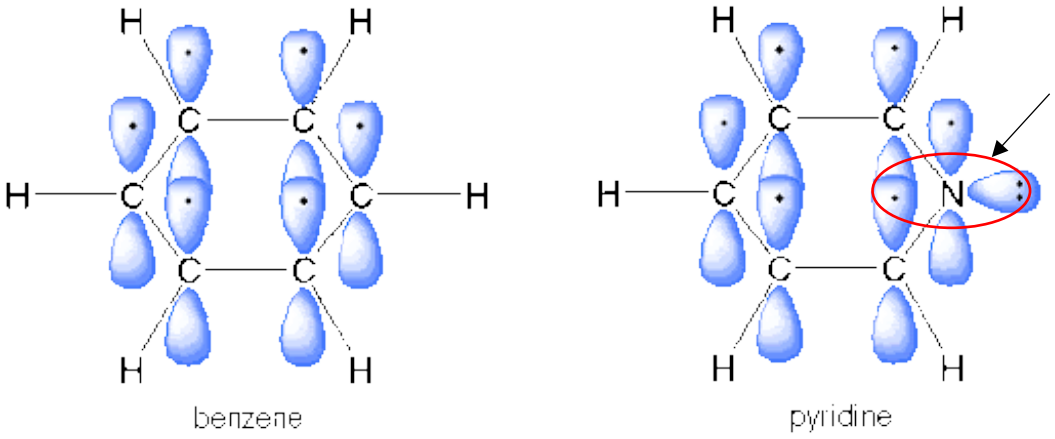


**Figure 2.1.** Comparison of the π-electron system of benzene and pyridine.

The procedure followed for the synthesis involved reacting either 2,3 diaminopyridine (2,3-DAP) or 3,4-diaminopyridine (3,4-DAP) to vary the position of the nitrogen atom around the pyridine ring. The diamines were reacted with selected aldehydes through a one pot cyclic condensation reaction, to afford the desired 2-substituted imidazopyridine ligands. The reaction of the diaminopyridine starting materials with different aldehydes follows the same mechanism of reaction to that followed using diaminobenzene rings as shown in **Scheme 2.1**. In the first step of the reaction, there is a nucleophilic addition of the amine functional group to the electrophilic carbonyl atom, and this requires the presence of an acid to increase the electrophilicity of the carbonyl carbon. In diaminopyridine, the two amino groups possess different reactivity due to the presence of the basic nitrogen group at the ortho/ para position of an amino group in the pyridine ring. 2,3-DAP has been proposed to possess better reactivity than 3,4-DAP due to the position of the basic nitrogen on the pyridine which cooperates with the nitrogen of the imidazole ring through an aligned orbital, increasing the nucleophilicity.[10] The nucleophilic addition step is followed by the formation of a Schiff base intermediate via an iminium ion formation and elimination of a water molecule. Thus, the presence of a drying agent like magnesium sulphate promotes the cyclisation step. An intramolecular nucleophilic attack of the free amine to the carbon of the Schiff base occurs to afford the cyclised dihydrobenzimidazole. Dihydrobenzimidazole then reacts with oxygen in an open-air atmosphere to produce the oxidised benzimidazole via a single electron transfer (SET) mechanism.

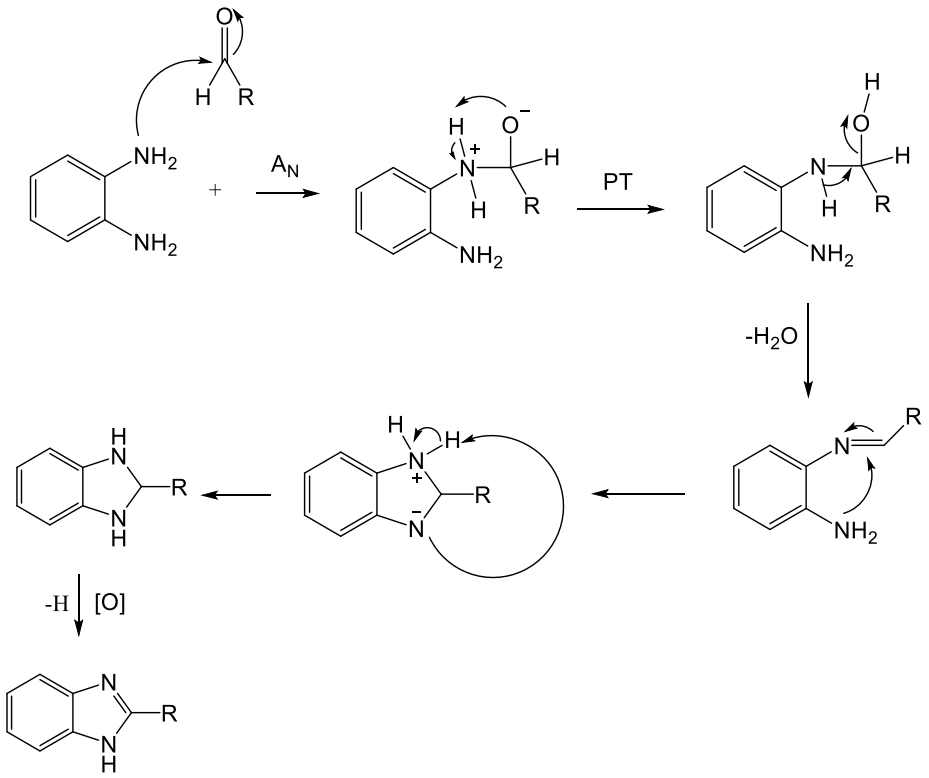


**Scheme 2.1.** General mechanism for the formation of a benzimidazole ligand through a cyclic condensation reaction.

### 2.1.1 Synthesis of 2-aryl-1H-Imidazo(4,5-b)pyridine (L1)

This section reports on the synthesis of 2-substituted Imidazopyridine ligands prepared by modifying the literature procedures reported by Zapata et al.[11] The synthesis of 2-aryl-H-Imidazo(4,5b)pyridine (**L1**) was carried out using the procedure shown in **Scheme 2.2**. Benzaldehyde was reacted with 2,3-DAP in selected solvents and acids to afford the desired products, where the successful synthesis of the desired ligand was possible in ethanol and the presence trifluoroacetic acid (TFA) catalyst. Two tautomers of the product (**L1a** and **L1b**) with slightly different polarities were isolated and separated by using silica column chromatography. The products elute as a single spot using Thin Layer Chromatography (TLC) when eluted with 50–60% ethyl acetate/ hexane. Increasing the polarity to 100% ethyl acetate separates two bands with close polarities (Rf values 0.71 and 0.64). **L1a** was the less polar product and was obtained as an orange-brown solid which was partially soluble in polar organic solvents like ethyl acetate and methanol while **L1b** was obtained as a green-white solid which was soluble in DMSO and insoluble in ethyl acetate or methanol. Computational studies using DFT showed **L1a** to be the most stable isomer[12] with low polarity and dipole moment while **L1b** was the more polar product. The two isomers are interchangeable though proton transfer in polar aprotic solvent such as methanol.

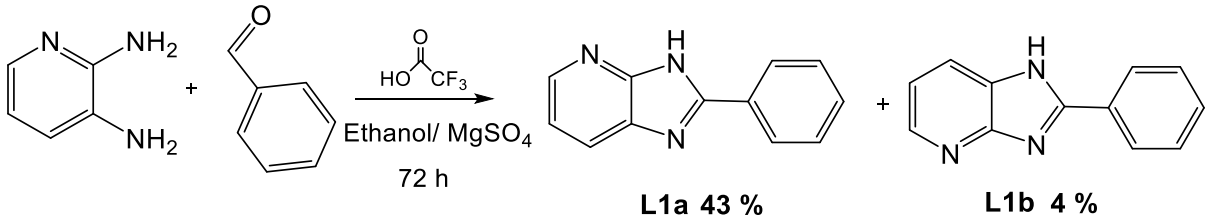


**Scheme 2.2.** Synthetic procedure for the synthesis of 2-aryl-1H-Imidazo(4,5b)pyridine(**L1a** and **L1b**).

Unsymmetrical substitution on the amino groups of 2,3-DAP with benzaldehyde produces two possible tautomers of imidazopyridine ligands. These two isomers are due to tautomerisation of the proton on the imidazole ring and have been distinguished using two-dimensional NMR techniques such as HSQC.[13] In the case of benzimidazoles without an extra nitrogen on the pyridine ring, the isomers are indistinguishable by NMR techniques since they resonate at a frequency greater than the NMR time scale. Two separate and slightly broad imine signals are often detected around 12 ppm using $^{1}$H NMR due to the presence of the tautomers in solution. The purity of both tautomers was greater than 96%, with the LCMS spectra for both attached in **Figure S1** of the appendix.

### 2.1.2 Characterisation of 2-aryl-1H-Imidazo(4,5-b)pyridine (L1)

#### *2.1.2.1 $^{1}$H NMR spectroscopy*

The proton $^{1}$H NMR spectrum of **L1a** is shown in **Figure 2.2**, and this is indistinguishable from the $^{1}$H NMR spectrum of its tautomeric form **L1b** shown in **Figure S2** of the appendix. This is because of slow chemical exchange resulting in chemical shift difference that is not enough to resolve in the $^{1}$H NMR spectrum. The $^{13}$C NMR spectra were also similar between the tautomers and only small shifts were obser*v*ed in the position of the quaternary carbons due to greater sensitivity to chemical environment as compared to $^{1}$H NMR. The spectrum of **L1a** shows signals with a total integration of 8 protons in the aromatic region which is equivalent to the number of protons labelled *a – f* in the ligand. The amine (N-H) protons were not observed on the spectra in methanol and DMSO and this was attributed to the protons exchanging with solvent under the conditions.

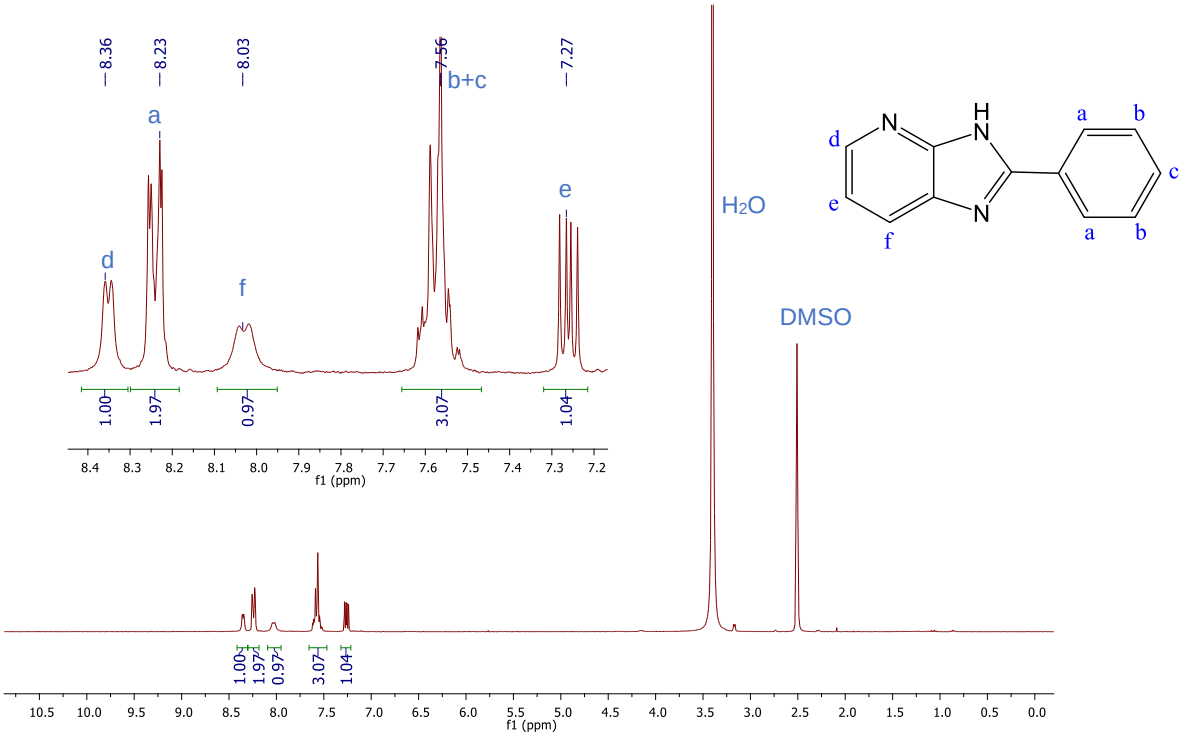


**Figure 2.2.** $^{1}$H NMR spectrum of 2-aryl-1H-Imidazo(4,5-b)pyridine ligand (**L1**) obtained in DMSO-$d_6$.

### *2.1.2.2 Infrared spectroscopy*

The infrared spectra of both **L1a** and **L1b** shows the absence of the diamine groups of 2,3-DAP starting material, confirming that they have reacted to form the cyclic imidazole ring (**Figure 2.3**). Absence of the carbonyl absorption band of benzaldehyde and presence of the ν(C=N) band of the ligand confirms the formation of a new product. The amine ν(N–H) band of the imidazole ring occurs at 3049 cm$^{-1}$ in the spectra of both **L1a** and **L1b**. Slight differences in the position of the imine ν(C=N) band were observed in the expanded spectra of both **L1a** and **L1b**. The imine band of the imidazole ring is observed at 1544 cm$^{-1}$ in **L1a**, whilst it is shifted to a lower wavenumber of 1537 cm$^{-1}$ in **L1b**, which can be attributed to increased conjugation through the imine double bonds of the pyridine and imidazole when they are adjacent to each other. The imine ν(C=N) band of the pyridine ring occurs at 1460 cm$^{-1}$ in both **L1a** and **L1b**.

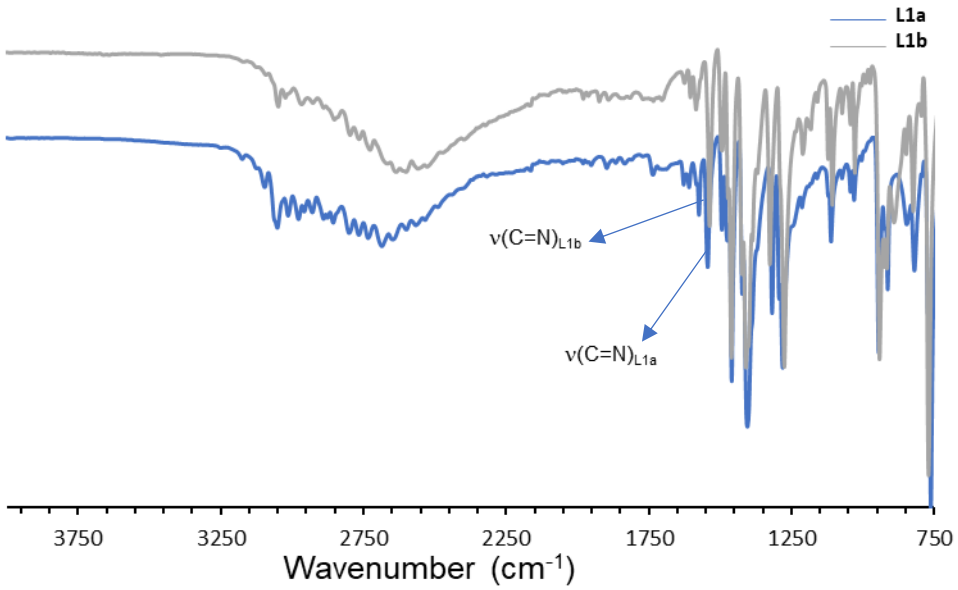


**Figure 2.3** Stacked IR spectra of the ligands **L1a** and **L1b**.

### *2.1.2.3 UV-Vis spectroscopy*

The stacked UV-Vis spectra of both ligands occur in **Figure 2.4** and this shows the presence of bands in the UV region between 200 and 300 nm. The band at 310 nm is assigned to $\pi \rightarrow \pi^*$ or $n \rightarrow \pi^*$ transitions of the ligand and is observed in both ligand **L1a** and **L1b**. A hypsochromic blue shift is also observed in the absorbance band centred at $\lambda_{max}$ 211 nm in **L1b** relative to **L1a** and this also displays an increase in intensity.

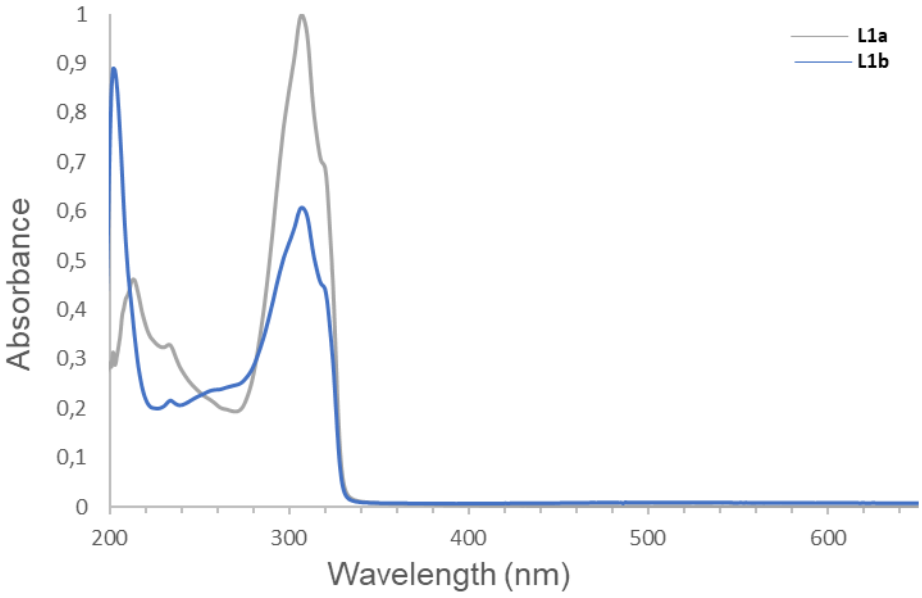


**Figure 2.4.** UV-Vis spectrum (obtained in methanol; 1 x $10^{-4}$ M) of the ligand **L1a** and its tautomeric form **L1b**.

### 2.1.3 Synthesis of 2-Aryl-1H-Imidazo(4,5-c)pyridine ligand (L2)

An attempt to synthesise the ligand 2-Aryl-1H-Imidazo(4,5-c)pyridine (**L2**) was performed by following the procedure used for the synthesis of **L1** as shown in **Scheme 2.3**. After 72 h under the reaction conditions, TLC showed the formation of multiple spots of different polarity and some of the spots corresponded to the starting materials. Purification of the products using ethyl acetate/ water extraction and separation of the products using column chromatography showed that an intermediate Schiff base product (which is unstable on the silica) was isolated and no desired imidazopyridine product had been formed in the reaction. The intermediate was isolated as a green solid and forms when the intermediate mono amine fails to fully cyclise into the desired imidazopyridine ligand.[14,15]

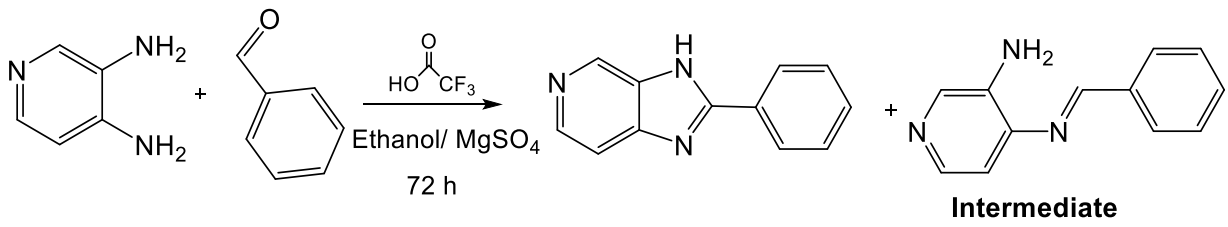


**Scheme 2.3.** Procedure for the formation of the Schiff base intermediate obtained from reaction between benzaldehyde and 3,4-DAP.

Formation of the Schiff base was detected using the IR spectrum shown in **Figure 2.5** which shows two amine bands between 3000 – 4000 $cm^{-1}$, indicating the presence of unreacted amine groups.

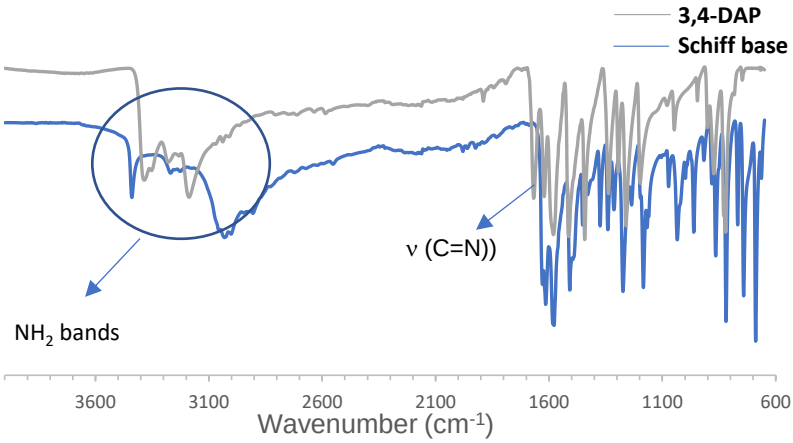


**Figure 2.5.** Stacked Infrared spectra of the starting material (3,4-DAP) and the Schiff base intermediate product.

The $^{1}$H NMR spectrum of the Schiff base shows a total integration of 9 protons labelled *a* – *f*, indicating the presence of an extra proton when compared to the proton count expected on the product **L2**. This extra proton is the imine proton labelled *a* in **Figure 2.6** and is observed as a sharp singlet at 7.97 ppm. The amine $NH_2$ protons of the Schiff base are not observed on the spectrum due to proton exchange with the solvent.

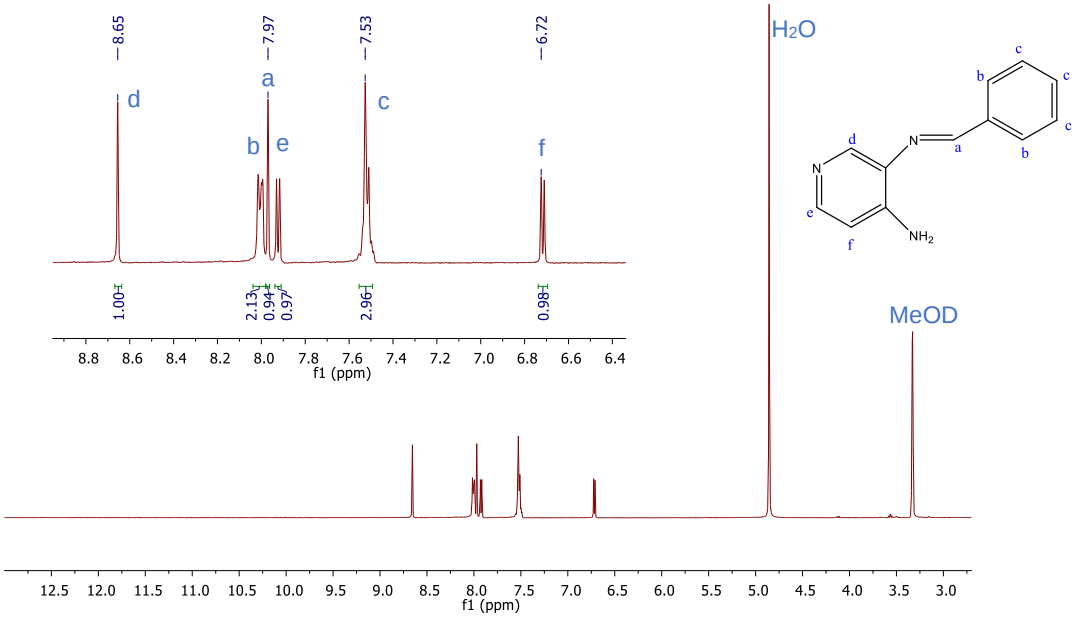


**Figure 2.6.** $^{1}$H NMR Spectrum (obtained in MeOD) of the Schiff base product.

The reaction to synthesise the desired 2-Aryl-1H-Imidazo(4,5-c)pyridine (**L2**) product was repeated following the conditions shown in **Scheme 2.4**, employing the use of nitrobenzene solvent which is a stronger oxidising agent than ethanol. The product **L2** was isolated by using silica column chromatography and obtained as a polar green-white solid by vacuum filtration. The product was obtained at a low yield, which was attributed to the incomplete conversion of the starting materials to the desired products over 48 hours of running the experiments, and this was also indicated by TLC. This showed that the formation of the imidazopyridine ligand from the reagents did not proceed readily under the oxidising conditions. The electronic effects of the pyridine ring discussed earlier were thought to contribute to the incompletion of the reactions. A spot of low polarity was also observed on the TLC and the fraction corresponding to the spot was isolated using silica column chromatography. This by-product was isolated as traces of a yellow-white microcrystalline solid product (3% yield) by vacuum filtration.

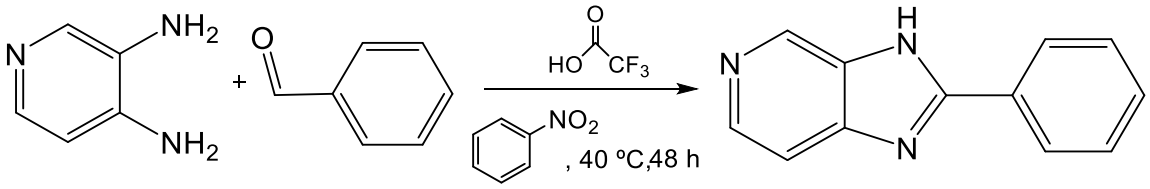


**Scheme 2.4.** Procedure for the synthesis of 2-aryl-1H-Imidazo(4,5-c)pyridine (**L2**).

### 2.1.4 Characterisation of Aryl-1H-Imidazo(4,5-c)pyridine ligand (L2)

#### *2.1.4.1 $^{1}$H NMR spectroscopy*

The $^{1}$H NMR spectrum of **L2** (**Figure 2.7**) shows the presence of aromatic proton signals in the region between 7.50 – 9.00 ppm. These signals integrate for a total of 8 protons, corresponding to the protons on the pyridine and phenyl rings of the ligand. The protons on the phenyl ring occur as multiplets at 8.16 and 7.60 ppm due to coupling between the signals labelled *a* – *c*. The most de-shielded sharp singlet at 8.91 ppm corresponds to proton assigned *d* on the pyridine ring which is adjacent to the nitrogen of the pyridine and nitrogen on the imidazole ring. The most shielded proton assigned *f* on the pyridine ring occurs as a doublet at 7.69 ppm.

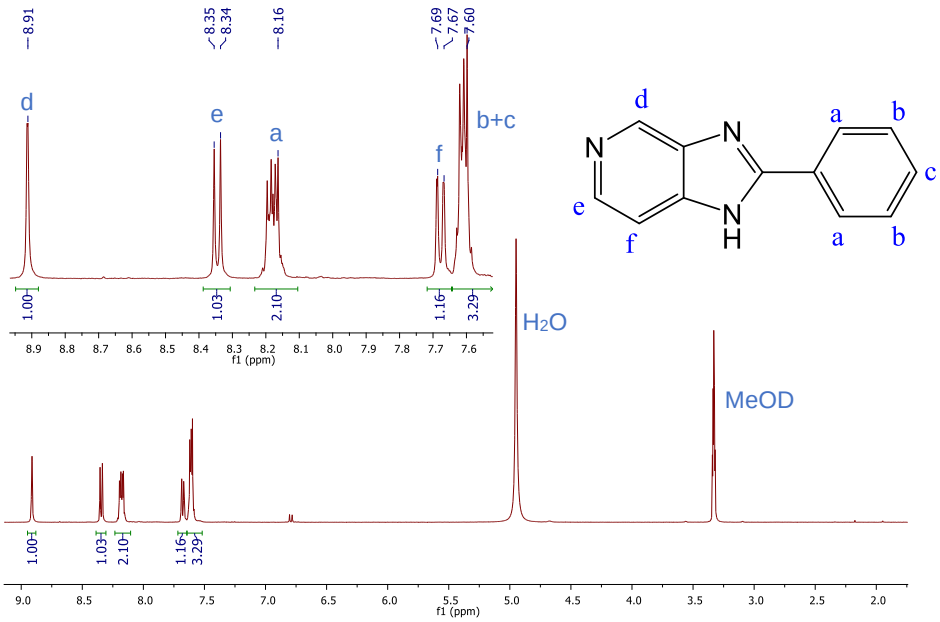


**Figure 2.7.** $^{1}$H NMR spectrum of 2-aryl-1H-Imidazo(4,5-c)pyridine (**L2**) obtained in MeOD.

The by-product isolated from the reaction was analysed using $^{1}$H NMR spectroscopy as shown in **Figure 2.8**. The proton NMR spectrum shows the presence of signals in the aromatic region, with a total integration of 14 protons. Signals between 7.50 and 8.15 ppm integrated for a total

of ten protons and these were assigned to the signals on the phenyl rings of the ligand labelled *e* – *i* on the proposed structure.

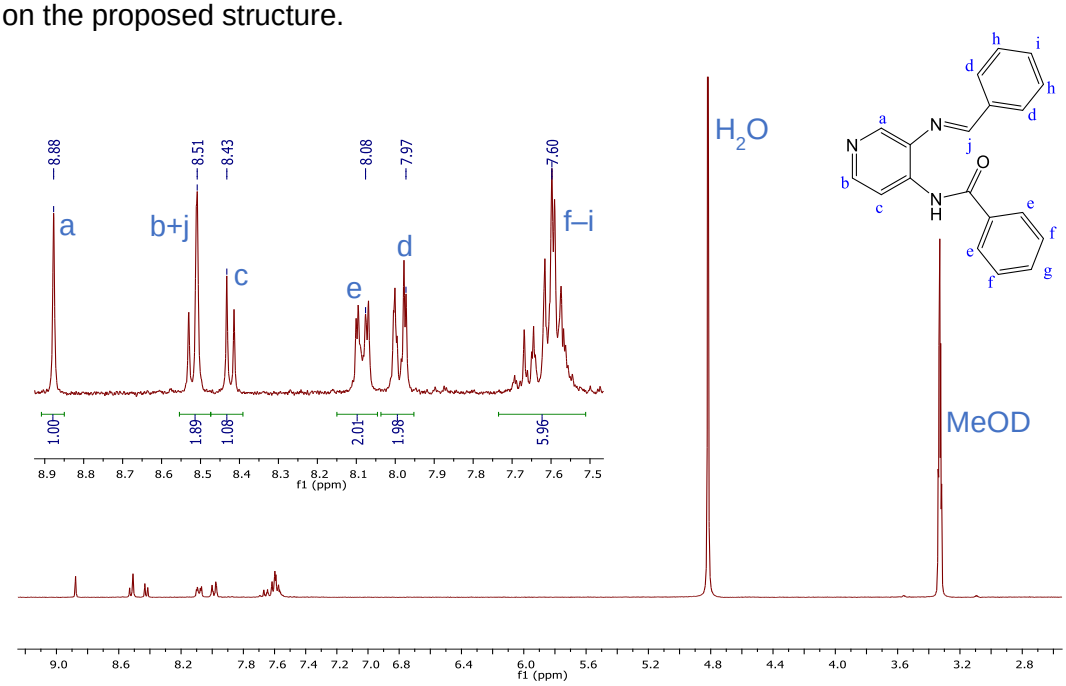


**Figure 2.8.** $^{1}$H NMR spectrum of the by-product isolated from reaction to form **L2**.

This by-product was also analysed using LCMS, and was 99.5% pure with a molecular ion peak corresponding to a mass of 302 g/mol. The LCMS spectra of the by-product and the ligand **L2** occur in **Figure S3** of the appendix. The proposed structure and mechanism of formation of the product is shown in **Scheme 2.5**. A Schiff base and an amide formation reaction were proposed to have occurred between the amine groups of the diamino pyridine ring, benzaldehyde and the TFA catalyst. One possible explanation was that during the reaction, some benzaldehyde undergoes trifluoro methylation through the addition of a $CF_3$ carbanion from TFA at the carbonyl carbon, to form Trifluoro-1-phenylethanone. This can then undergo a nucleophilic addition reaction with the free amine group of 3,4-DAP, followed by proton transfer and elimination of trifluoromethane.

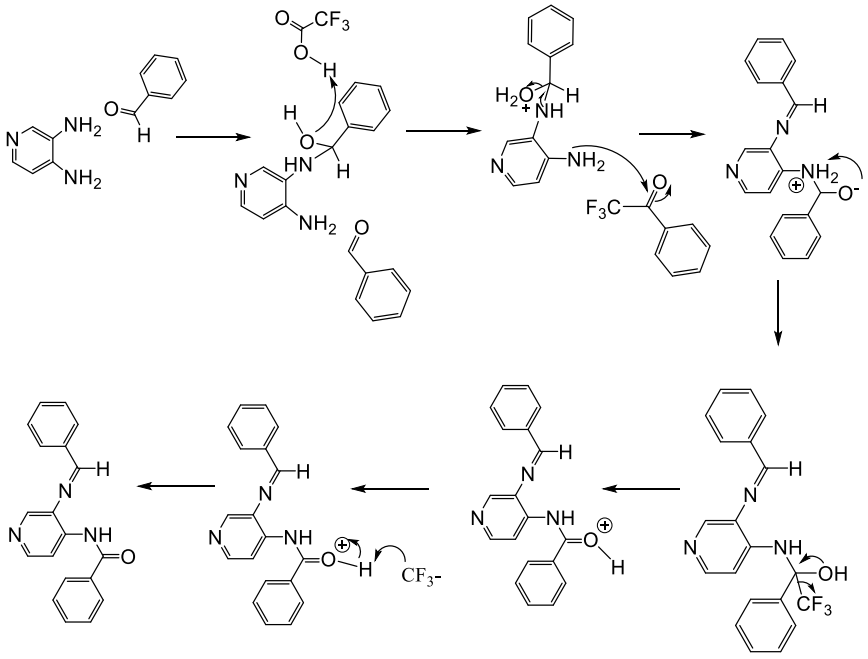

**Scheme 2.5.** Proposed mechanism of formation of the by-product from the reaction.

$^{13}$C NMR, COSY and HSQC were used to confirm the assignments of the NMR signals. The $^{13}$C DEPT NMR spectrum of the by-product attached in **Figure S4** revealed the presence 14 carbons in the aromatic region which is equivalent to the number of non-quaternary carbons present in the structure. The COSY NMR spectrum is shown in **Figure 2.9**. No coupling was observed between signals labelled *a* – *c* with any of the other signals on the phenyl rings, confirming that signals *a* – *c* are located on the pyridine ring of the ligand. Similarly, no coupling is observed between the signals labelled *d* and *e*, confirming that they are on different phenyl rings. Coupling is observed individually between the signals *d* or *e* with the signals labelled *f* – *l* on the phenyl rings.

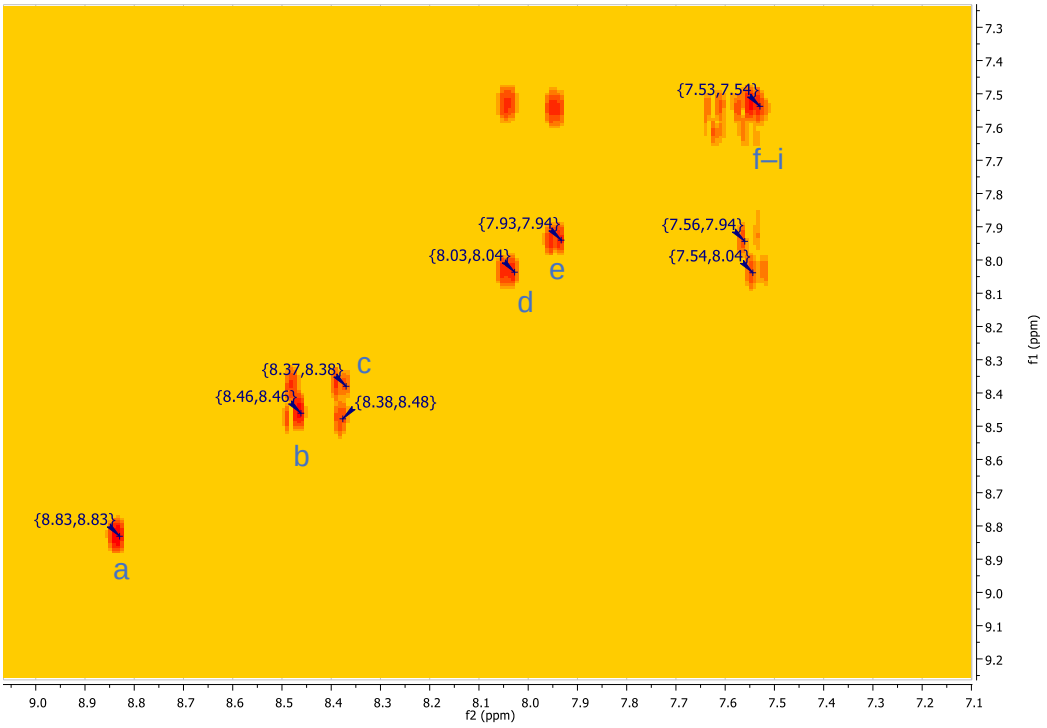


**Figure 2.9.** COSY NMR spectrum of the by-product obtained from the reaction between benzaldehyde and 3,4-DAP.

### *2.1.4.2 Infrared spectroscopy*

The infrared spectrum of the isolated product is shown in **Figure 2.10**. The spectrum shows the absence of the amine groups of 3,4-DAP starting material in the product. A single band is observed at 3347 $cm^{-1}$ which is assigned to an amine N-H stretch of the Schiff base, and this is not observed in the starting materials. The bands at 1661, 1625 and 1574 $cm^{-1}$ were assigned to the $\nu$(C=O) of the carbonyl band, amide $\nu$(C=N) stretches of the pyridine and the Schiff base, respectively.

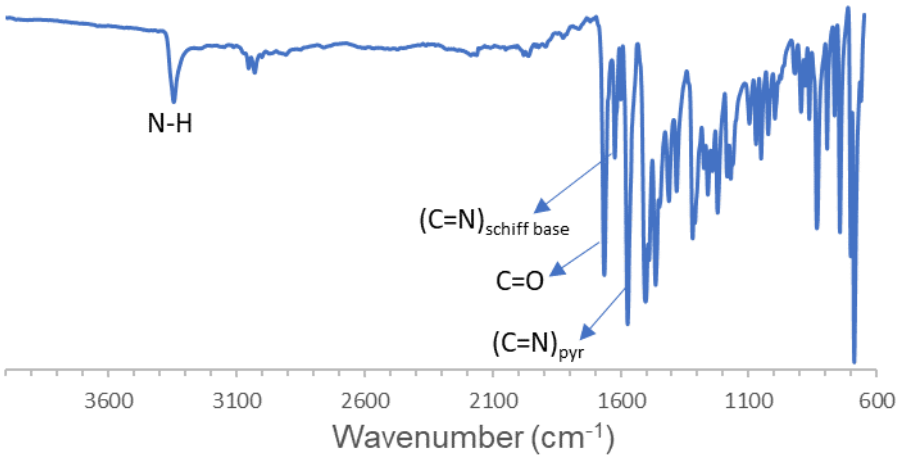


**Figure 2.10.** Infrared spectrum of the Schiff base isolated from the reaction between benzaldehyde and 3,4-DAP.

### *2.1.4.3 UV-Vis spectroscopy*

The UV-Vis spectrum of the ligand **L3** was obtained in methanol and the spectrum obtained is attached in **Figure 2.11**. Three absorbance bands occur between 200 and 300 nm in the UV middle region with the $\lambda_{max}$ of the absorbance bands centred at 207, 239 and 295 nm. The latter can be assigned to the $\pi$ to $\pi^*$ / n to $\pi^*$ transitions of the ligand. The by-product isolated from the reaction also shows an absorbance band with $\lambda_{max}$ centred at 268 nm. This absorbance band can also be assigned to the $\pi$ to $\pi^*$ / n to $\pi^*$ transitions of the product due to the presence of the pyridine aromatic ring in the ligand.[2] A shoulder band also occurs in the UV-Vis spectrum of the by-product at 332 nm.

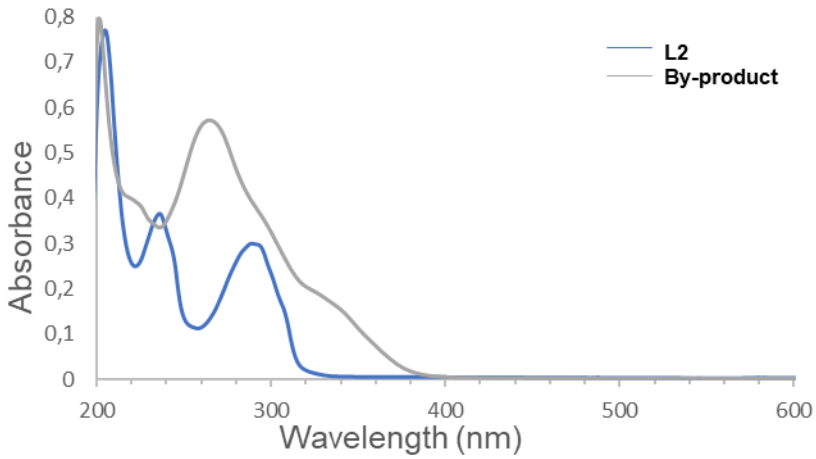


**Figure 2.11.** UV-Vis spectrum (obtained in methanol) of the ligand **L2** and the by-product isolated from the reaction.

A summary of the yields obtained using the different reaction conditions to synthesise **L2** is shown in **Table 2. 1**. The table also shows the temperature the reactions were conducted in, since the boiling points of the acids employed were varied. Although the yields of benzimidazoles would be expected to be higher at high temperatures due to faster reaction kinetics, volatile acids like TFA with low boiling points tend to evaporate from the warm solution. Weaker acids like acetic acid and *p*-toluenesulphonic acid have high boiling points, and high temperatures could be employed during the reaction, however the degree of protonation on the carbonyl oxygen of the aldehyde would be less. The low yields obtained for the product were also due to loss of the product during the work-up and purification steps.

**Table 2. 1**. Summary of the products of the reaction between 3,4-DAP with benzaldehyde in the presence of different acid catalysts.

| Solvent | Temperature (°C) | Acid | Product | Yield (%) |
|---|---|---|---|---|
| Toluene | 80 | p-toluene sulphonic acid | **L2** | 10 |
| Water/Ethanol | 40 | TFA | Schiff base | - |
| Nitrobenzene | 40 | TFA | **L2** | 41 |

### 2.1.5 Synthesis of 2-ferrocenyl-1H-Imidazo(4,5-b)pyridine (L3)

Attempts to synthesise 2-ferrocenyl-1H-imidazo(4,5-b)pyridine (**L3**) was performed as shown in **Scheme 2.6**. The use of weak oxidising solvents like toluene in the presence of acetic acid or *p*-toluenesulphonic acid resulted in the formation Schiff base products with the IR and $^{1}$H NMR spectra shown in **Figure S5** and **Figure S6** of the appendix, respectively. Due to the presence of some water in DMSO the Schiff base gets hydrolysed and peaks corresponding to the starting material are also observed in the spectrum. No desired product was formed under weakly acidic conditions at elevated temperature (80 °C), after 72 h of stirring. The reaction in the presence of DMF and sodium metabisulphite as a Lewis acid resulted in slightly improved yields.

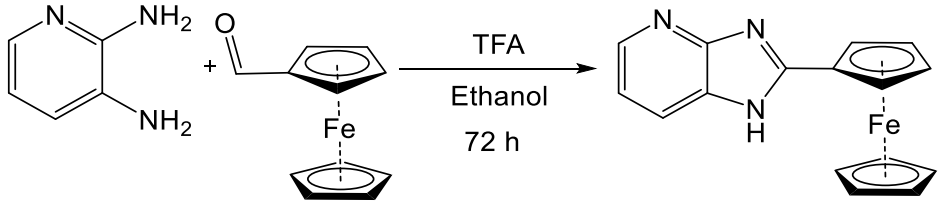


**L3**

**Scheme 2.6.** Procedure for the synthesis of 2-ferrocenyl-1H-Imidazo(4,5-b)pyridine (**L3**).

### 2.1.6 Characterisation of 2-ferrocenyl-1H-Imidazo(4,5-b)pyridine(L3)

#### *2.1.6.1 $^{1}$H NMR spectroscopy*

The use of chloroform as a solvent and acetic acid catalyst or ethanol/ water in the presence of trifluoroacetic acid resulted in the formation of ligands **L3a** and **L3b** with slightly different polarities on the TLC. The formation of bis-substituted N-methylferrocenyl-2-ferrocenyl-1H-imidazo(4,5-b)pyridine product was also observed on the TLC but the spot was faint and the product isolated using column chromatography obtained could not be successfully purified due to low yield. Therefore, only the two products **L3a** and **L3b** were successfully isolated and characterised using $^{1}$H NMR, $^{13}$C NMR spectroscopy and infrared spectroscopy. The proton NMR spectrum of the less polar product **L3a** is shown in **Figure 2.12**. The spectrum shows the presence of signals in the aromatic region with a total integration of three protons, corresponding to the protons on the pyridine ring of the ligand. The signals observed between 4.10 and 5.25 ppm integrate for a total of 9 protons, corresponding to the number of protons on the ferrocenyl ring. The synthesis of the ligands was also confirmed using 2D COSY and HSQC NMR experiments, with the COSY spectrum shown in **Figure S7** of the appendix.

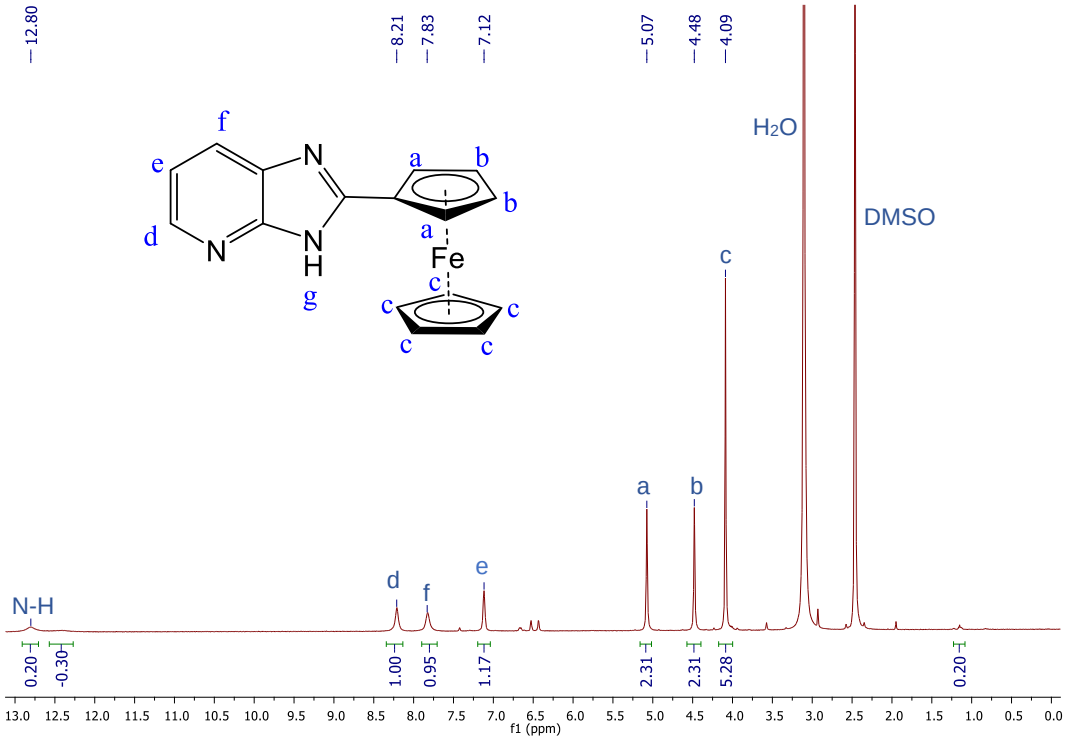


**Figure 2.12**. $^{1}$H NMR spectrum (in DMSO-$d_6$, 300MHz) of 2-ferrocenyl-1H-Imidazo(4,5-b)pyridine (**L3a**).

The $^{1}$H NMR spectrum of the more polar product **L3b** obtained using DMSO is shown in **Figure 2.13**. The spectrum shows the presence of signals between 4.10 and 5.25 ppm (*a*, *b*, and *c*), corresponding to protons on the ferrocenyl ring. The signals at 5.11 and 4.53 ppm correspond to protons on the cyclopentadiene ring attached to the imidazopyridine moiety. The peak at 4.12 ppm corresponds to protons on the unsubstituted cyclopentadiene ring. The integration on this peak shows only four protons due to the removal of one proton on the cyclopentadiene ring to form a ferrocenyl carbanion. The presence of the two amine protons is observed downfield at 12.98 and 15.56 ppm. These peaks correspond to the protons on the imine nitrogen of the imidazole ring and two signals are observed due to rotation around the single bond to form two tautomers in solution. The integration of the peak at 13.10 is close to one, showing that this was the proton abstracted from the cyclopentadiene ring. The electron rich free nitrogen of the imidazole ring is thought to be removing an $H^{+}$ cation from the ferrocenyl ring to leave the carbanion ring. Proton transfer is known to occur on imidazopyridines and purine rings. This proton transfer is known to occur via a self-catalysis or solvent-based mechanism.[16] The spectrum also shows signals between 7.0 and 8.3 ppm (*d*, *f* and *e*), and the total integration on these protons is three, corresponding to the protons on the pyridine ring of the ligand. The signals labelled *d* and *f* appear as broad signals and are not clearly resolved when the compound is analysed at 300 Mhz. Upon increasing the

resolution to 600 MHz, the signals *d* and *f* are more resolved as shown by the $^{1}$H NMR spectrum. From the spectrum, it is also easy to see that there is more than one species of the ligand present in solution due to the presence of free rotation resulting in proton transfer between the lone pair on the imidazole nitrogen and the unsubstituted cyclopentadiene ring of ferrocene. However, the proton transfer can only be confirmed by using single crystal X-ray diffraction techniques.

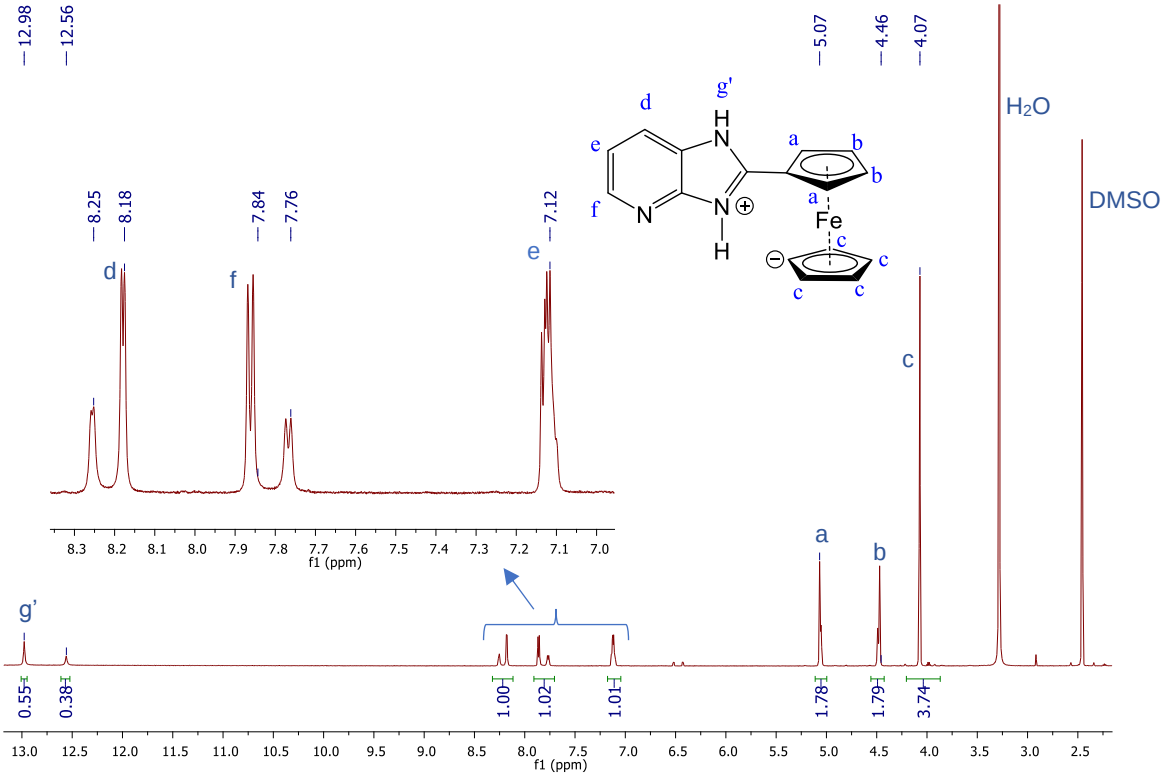


**Figure 2.13**. $^{1}$H NMR spectrum (in DMSO-$d_6$, 600 MHz) of 2-ferrocenyl-1H-Imidazo(4,5-b)pyridine (**L3b)**.

The product **L3b** was also reacted with a concentrated solution of hydrochloric acid in water, to protonate all the nitrogen atoms of the molecule as well as to protonate the cyclopentadiene ring. A slight excess of $AgPF_6$ was added to the solution to precipitate the solution and the resulting AgCl precipitate was removed by filtering under gravity. The resulting product was isolated as a yellow-pink solid and its $^{1}$H NMR spectrum showed broad signals in the aromatic and ferrocenyl regions. $^{1}$H NMR spectroscopy was repeated with the addition of a few drops of TFA, which resulted in the formation of a highly soluble pink solution and the proton NMR spectrum obtained is shown in **Figure 2.14**.

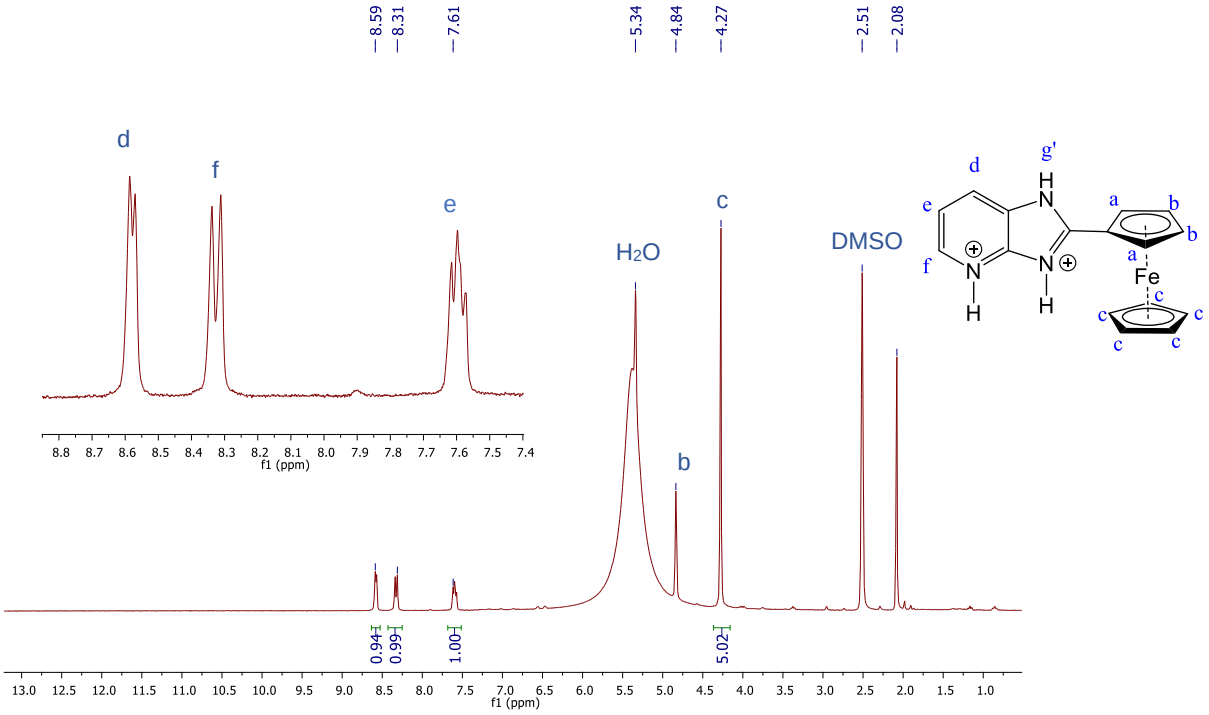


**Figure 2.14.** $^{1}$H NMR spectrum of the product obtained from the addition of TFA to **L3b**.

In addition to the proton transfer observed in product **L3b**, different conformations of the ligand were also possible due to possible free rotation around the single bond between the imidazole and ferrocenyl ring as observed previously for **L1**. This leads to four possible tautomers resulting from a change in the position of the nitrogen atom of the pyridine ring. The structures of the conformations are shown in **Figure 2.15**. These tautomers between imidazopyridine ligands have been described by Barraclough et al.[13] and are successfully distinguished by using a combination of 1D and $^{1}$H -$^{13}$C chemical shifts.[17] Purine bases like adenine have also been found to exist as mixtures of the tautomeric forms in polar solvents.[16,18] The tautomeric forms resulting in proton transfer from the imidazole ring to one of the nitrogen on the pyridines have not yet been reported.

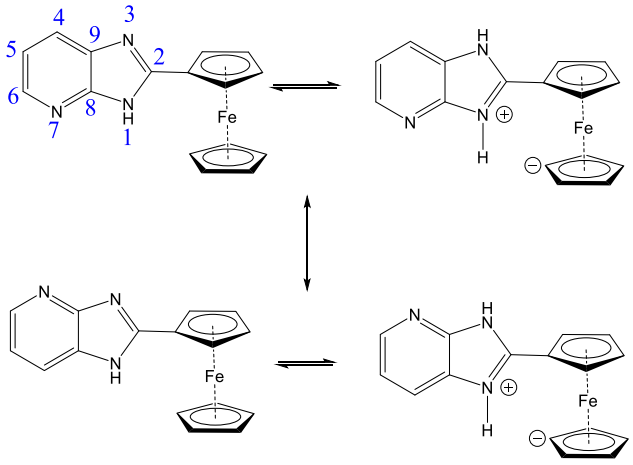

**Figure 2.15.** Tautomeric conformations possible for 2-ferrocenyl-1H-Imidazo(4,5-b)pyridine ligand (**L3**).

### *2.1.6.2 Infrared spectroscopy*

Infrared spectroscopy was used to compare the changes in the stretching frequencies of the functional groups on ligands **L3a** and **L3b.** The infrared spectrum of each ligand is shown in **Figure S8** of the appendix. The amine groups of the 2,3-DAP starting material were not observed around 3330 and 3176 $cm^{-1}$ in the products, showing that they had reacted to form the imidazole ring. The spectra of the two products show similarities in the position of the absorbance bands, with the imine $\nu$(C=N) bands appearing in the region around 1625 – 1563 $cm^{-1}$. The two ligands show differences in the intensity of the absorbance bands resulting from change in the conformation of the ligand.

### *2.1.6.3 UV-Vis spectroscopy*

The UV-Vis spectra of the two conformations of ligand **L3** obtained in methanol is attached in **Figure 2.16**. Both conformations show the presence of a band at 314 nm which is assigned to the $\pi$ to $\pi^*$ / n to $\pi^*$ transitions of the ligand and these display different intensities. The ligands also show an absorbance band centred around 454 nm corresponding to the ligand to metal $\pi$ to $\pi^*$ transitions of the ferrocenyl ring. A slight change in the position of the high energy absorbance bands centred around 200 – 250 nm is observed between the tautomers.

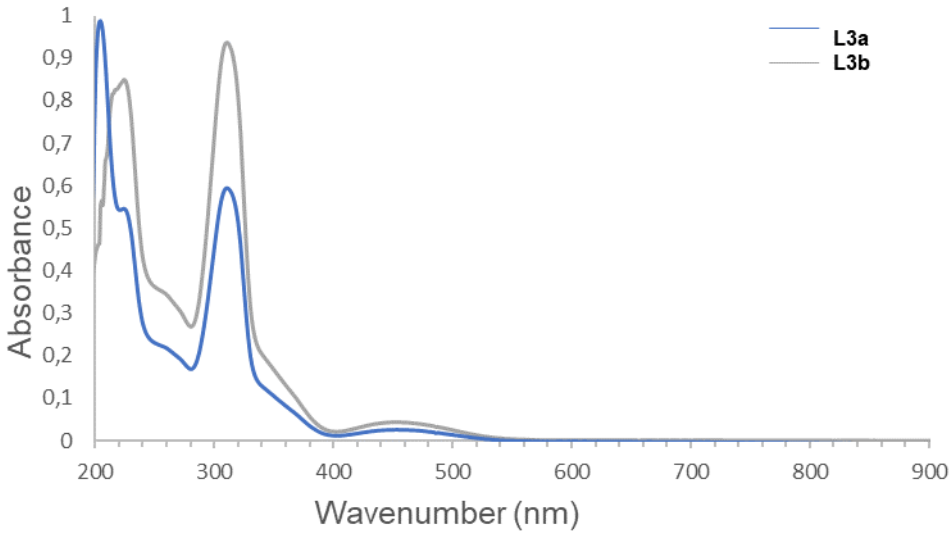


**Figure 2.16.** UV-is spectrum of **L3a** and **L3b** obtained in methanol.

### *2.1.6.4 Electrochemistry*

The electrochemical process of the ligand **L3** was compared with that of the unsubstituted ferrocene standard. Cyclic voltammetry was performed using 1 x $10^{-4}$ M of the ligand in a solution containing 0.10 M TBACl as the supporting electrolyte solution. The cyclic voltammograms obtained are shown in **Figure 2.17**. The ferrocene standard shows a reversible oxidation peak with oxidation potential at 0.39 V, and this is shifted towards the anode in the ligand **L3**. This anodic shift implied a decreased electron density on the ferrocenyl ring upon substitution on ferrocene with the imidazopyridine moiety, making it difficult to oxidise the metal centre. The imidazopyridine ligand is deactivating and removes electron density from the metal. There was no difference between the oxidation peak and oxidation potential of the tautomers **L3a** and **L3b**.

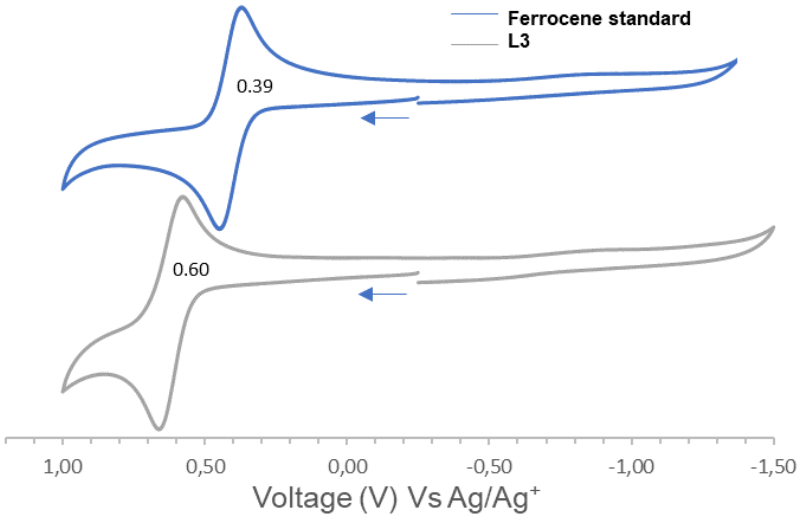


**Figure 2.17.** Cyclic voltammograms comparing the electrochemical processes of the ligand **L3** and ferrocene**,** obtained in a methanol solution containing 0.10 M TBACl at a scan rate of 100 mV/s.

### 2.1.7 Synthesis and characterisation of 2-ferrocenyl-1H-Imidazo(4,5-c)pyridine (L4)

The synthesis of 2-ferrocenyl-1H-Imidazo(4,5-b)pyridine (**L4**) was performed using the same procedure followed for the synthesis of **L3** as shown in **Scheme 2. 7**. Refluxing an equimolar amount of ferrocene carboxaldehyde (FCA) and 3,4-DAP in toluene and acetic acid produced a mixture of two products with different polarities. An incomplete conversion of the starting materials to the desired products was observed after 72 hours. Silica column chromatography was used to separate the two products from the unreacted material. The less polar product was isolated as traces of a violet-coloured oil which was obtained at a low yield. The product has similar polarity to the starting material FCA, and co-elution occurred when using silica gel chromatography to isolate the products.

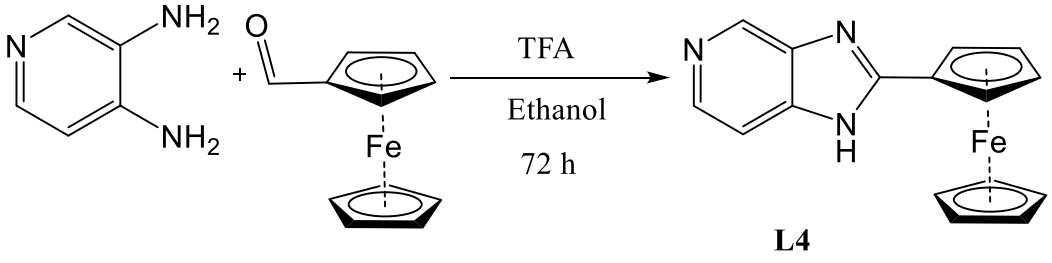


**Scheme 2. 7.** Procedure for the synthesis of 2-ferrocenyl-1H-Imidazo(4,5-c)pyridine (**L4**).

Attempt to remove the FCA by doing an ethyl acetate/ water extraction in the presence of sodium bisulphite was not successful. As a result the $^{1}$H NMR spectrum of the less polar

product in DMSO shows the presence of a bis-substituted N-methylferrocenyl-2-ferrocenyl-1H-Imidazo(4,5-c)pyridine product (**Figure S9** of the appendix) with a small amount of unreacted FCA. Since only traces of the product was isolated, the less polar product could not be successfully purified.

The more polar product was confirmed to be the desired 2-ferrocenyl-1H-Imidazo(4,5-b)pyridine(**L4**) and the $^{1}$H NMR spectrum obtained is shown in **Figure 2.18**. **L4** was the major product and was obtained at a relatively low yield of 34% and was isolated as a brown solid. The highest yield was obtained using nitrobenzene as an oxidising solvent and trifluoroacetic acid as the acid catalyst.

### *2.1.7.1 $^{1}$H NMR spectroscopy*

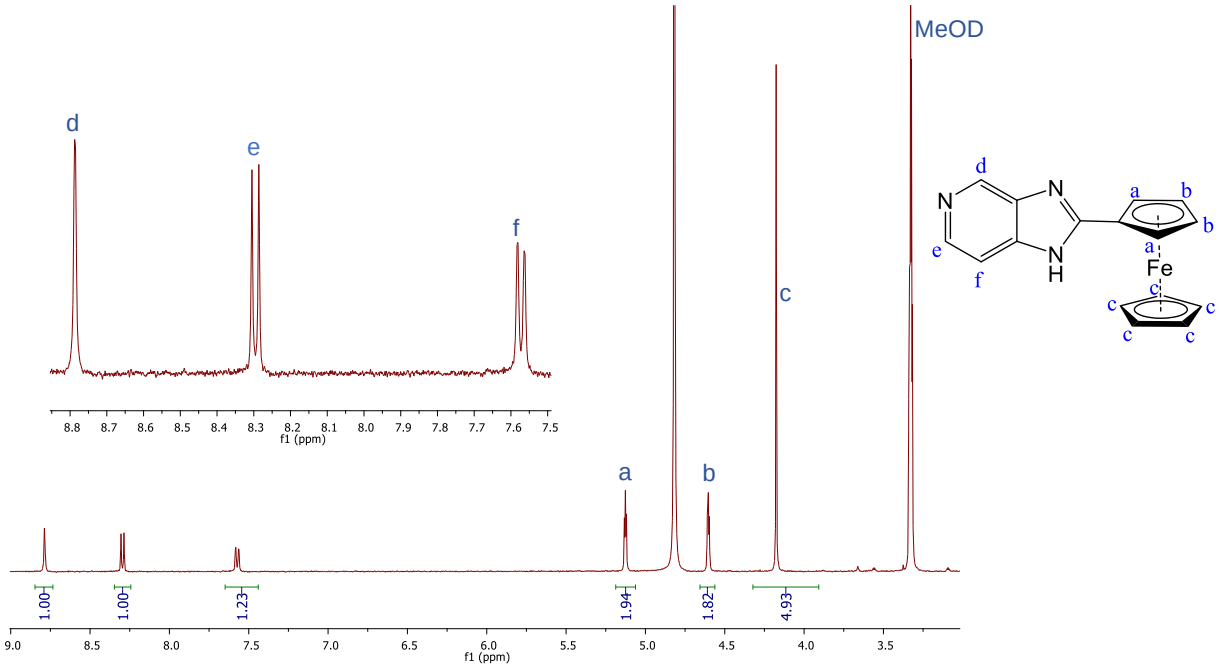


**Figure 2.18.** $^{1}$H NMR spectrum (in MeOD) of 2-ferrocenyl-1H-Imidazo(4,5-c)pyridine (**L4**).

### *2.1.7.2 UV-Vis spectroscopy*

The UV-Vis spectrum of the ligand **L4** was obtained in methanol and the spectrum obtained is attached in **Figure 2.19**. The spectrum shows the presence of an absorbance band with $\lambda_{max}$ centred at 300 nm which can be assigned to the $\pi$ to $\pi^*$ or n to $\pi^*$ transitions of the ligand. This band is slightly shifted to a lower wavelength or higher energy with respect to that observed in the ligand **L3**, showing that it is greatly affected by changing the position of the nitrogen on the pyridine ring of the ligands. The ligands also show a smaller absorbance band centred around 454 nm corresponding to the ligand to metal transition of the ferrocenyl ring.

This absorbance band was observed around the same region as that of the ligand **L3**, indicating that changing the position of the nitrogen from 4/7 in the ligand **L3** to position 5/6 in the pyridine ring of the ligand **L4** has little effect on the ligand to metal π to π transition.

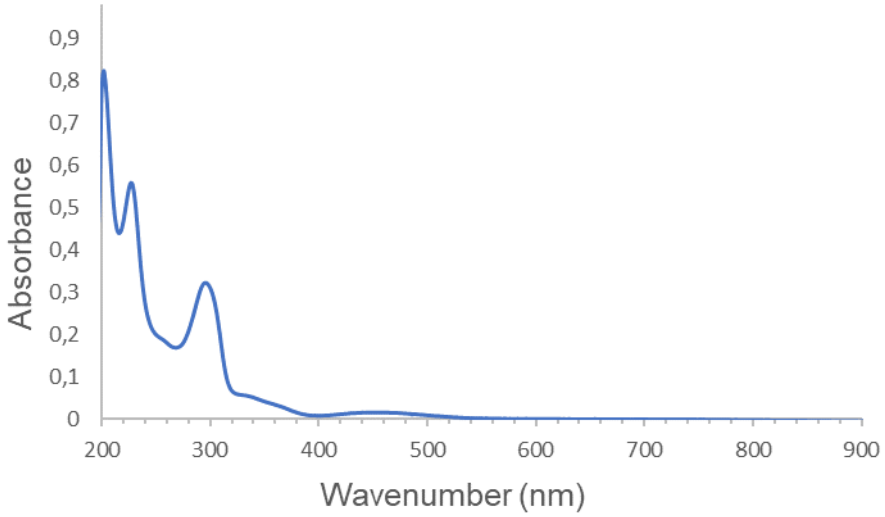


**Figure 2.19.** UV-is spectrum of **L4** obtained in methanol.

### *2.1.7.3 Infrared spectroscopy*

The infrared spectrum of the ligand occurs in **Figure S10** of the appendix and these confirmed the successful synthesis of the desired ligand **L4**. Absence of the amine groups of 3,4-DAP is observed between 3000 – 3500 $cm^{-1}$ which confirmed their successful reaction with the aldehyde to form the imidazole ring. The imine bands of the imidazole and pyridine ring occur at 1558 and 1569 $cm^{-1}$, respectively. These bands are slightly shifted to a lower wavenumber with respect to those of the ligand **L3**.

### *2.1.7.4 Electrochemistry*

The electrochemical process of the ligand **L4** was obtained in a solution containing TBACl as a supporting electrolyte and compared with that of the unsubstituted ferrocene standard. The cyclic voltammogram obtained is shown in **Figure 2.20**. The ferrocene standard shows a reversible oxidation peak with potential at 0.39 V, which is shifted towards the anodic region in the ligand **L4**. This peak is observed around the same region as that of **L3** in the solution with an oxidation potential of 0.60 V. This shows that changing the position of the nitrogen of the pyridine ring on the ligand does not affect the electron density of the metal in the ferrocenyl ring and does not change the electronic properties of the ligand.

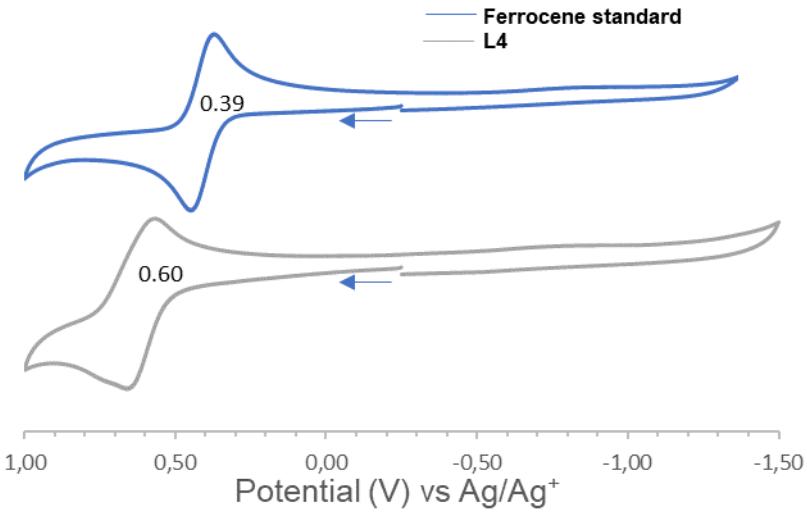


**Figure 2.20.** Stacked cyclic voltammograms comparing the electrochemical processes of the ligand **L4** and the ferrocene standard**,** obtained in a methanol solution containing 0.10 M TBACl, at a scan rate of 100 mV/s.

### 2.1.8 Synthesis of 2-Propyl-1H-Imidazo(4,5-b)pyridine (L5)

The ligand **L5** was synthesised by reacting equimolar amounts of 2,3 DAP and butyraldehyde, following the procedures used in the synthesis of ligand **L1** to **L4**. The reaction was repeated several times due to poor yields being obtained and difficulty in separating the product from the Schiff base intermediates being formed. A yellow-brown coloured oil was isolated at a moderate yield and was characterised using UV-Vis spectroscopy FTIR and NMR spectroscopy.

### 2.1.9 Characterisation of 2-propyl-1H-Imidazo(4,5-b)pyridine (L5)

#### *2.1.9.1 $^{1}$H NMR spectroscopy*

The proton NMR spectrum of the product obtained in DMSO is shown in **Figure 2.21**. The spectrum shows evidence of successful synthesis of the desired ligand **5** which is shown by the presence of three signals in the aromatic region having a total integration of three protons. The presence of the propyl chain is shown by the peaks at 2.80, 1.81 and 0.94 ppm which integrate for 7 protons. The extra peak at 1.15 was attributed to the ethyl acetate trapped in the product. The protons of the pyridine ring occur between 7.00 and 8.45 ppm in the aromatic region and have a total integration of 3. The signals *a* and *b* are further split into smaller peaks due to the presence of the less stable tautomeric form of the ligand resulting from changing the position of the nitrogen atom on the pyridine. It was not possible to separate the tautomers using chromatography since only one spot was detected. The signals labelled *g* and *g'* downfield at 12.82 and 12.48 ppm correspond to the amine signal of the imidazole ring where

tautomerisation of the hydrogen atom occurs to result in two separate signals, as observed previously for the ligand **L3**.

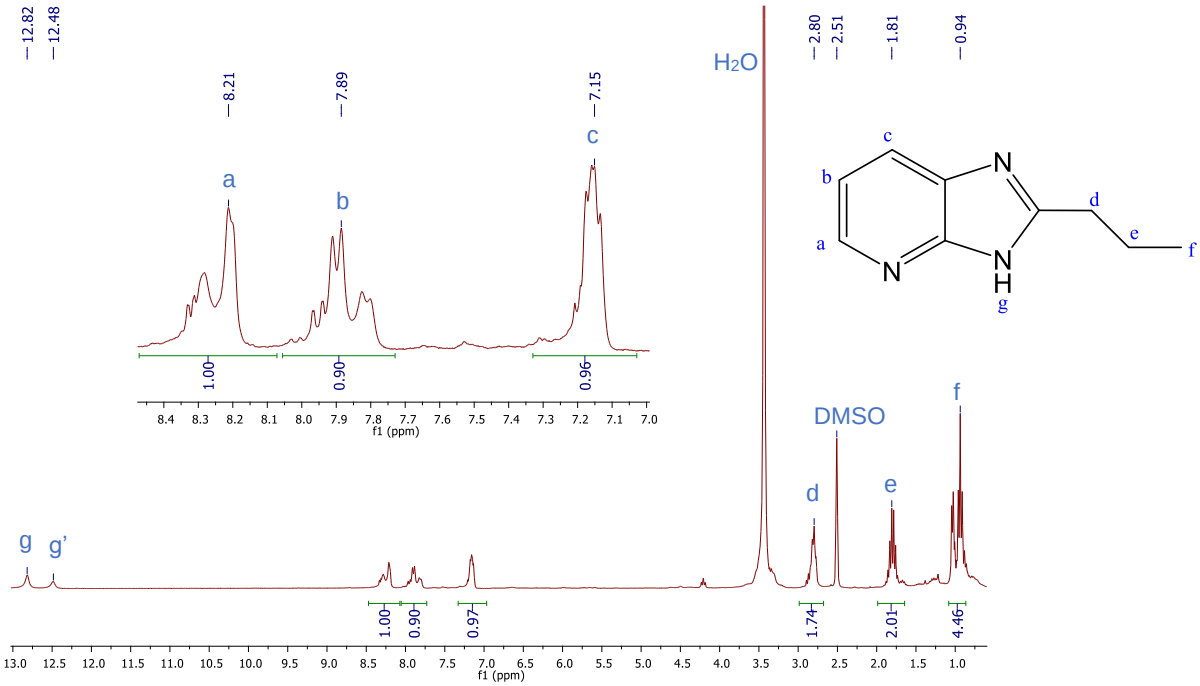


**Figure 2.21.** $^{1}$H NMR spectrum (in DMSO)-$d_6$ of 2-propyl-1H-Imidazo(4,5-b)pyridine (**L5**).

### *2.1.9.2 Infrared spectroscopy*

The infrared spectrum of the ligand shows the presence of strong C-H bands between 2850 – 2900 $cm^{-1}$ which are absent in the spectrum of 2,3-DAP. The stacked infrared spectrum of the ligand and the starting material is shown in **Figure 2.22**. FTIR confirmed the cyclisation of the butyraldehyde chain with the diaminopyridine to form the imidazole ring of the desired ligand. A new imine $\nu$(C=N) stretching band is observed and centred at 1609 $cm^{-1}$ and this is assigned to the imine band of the imidazole ring. These bands occur at a slightly higher frequency relative to those observed for the ligands **L1** – **L4** and this can be attributed to the poor donation of electron density into the imine double bond by the propyl chain, relative to the phenyl or ferrocenyl moieties. The poor donation of electrons results in a shorter imine double bond in comparison to that observed for the phenly and ferrocenyl substitituded ligands. The successful reaction of the diamine groups of 2,3-DAP is confirmed by the absence of the amine $NH_2$ stretching bands in the product.

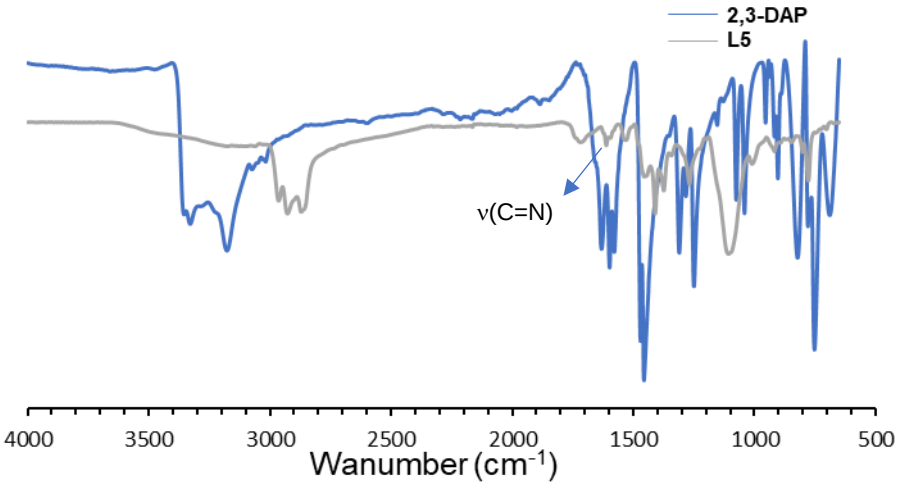


**Figure 2.22.** FTIR spectrum of the ligand 2-propyl-1H-Imidazo(4,5-b)pyridine (**L5**) overlapped with the spectrum of 2,3-DAP.

### *2.1.9.3 UV-Vis spectroscopy*

The UV-Vis absorbance spectrum of the ligand is shown in **Figure 2.23** and this shows the presence of an absorbance band with $\lambda_{max}$ centred at 287 nm. This band is split into a smaller band centred at ca. 252 nm which was not considered because of the possibility of solvent effects in this region. The band in the UV region is assigned to the $\pi$ to $\pi^*$ transitions of the ligand as previously observed for **L1** – **L4**. Another band was also observed as a shoulder in the near UV-region between 320 and 395 nm.

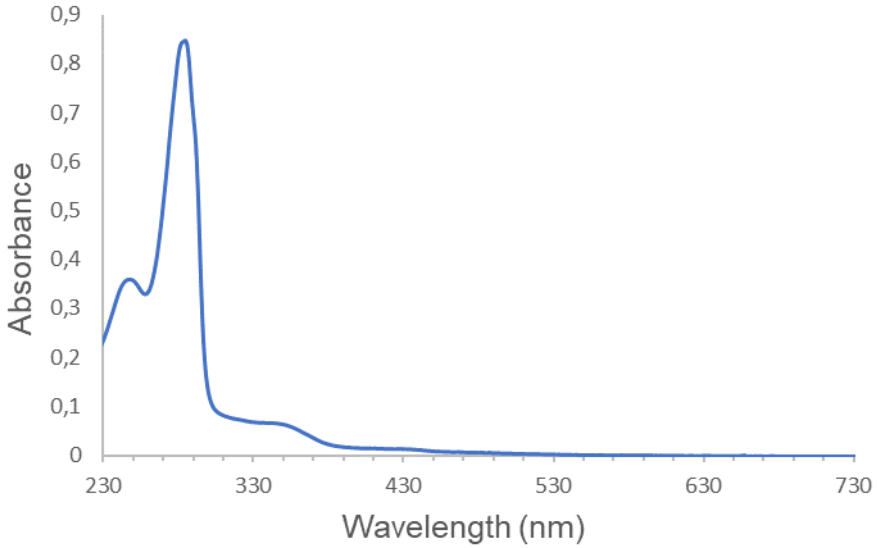


**Figure 2.23.** UV-Vis spectrum of the ligand **L5** (obtained in methanol).

### 2.1.10 Summary

The synthesis of imidazopyridine ligands substituted with phenyl, ferrocenyl and propyl moieties has been successfully carried out under different conditions. The ligands were obtained at relatively low yields and further strategies need to be employed to optimise the reactions with the intention of improving the reaction yields. The ligands were successfully characterised by using an array of analytical techniques such as $^{1}H$ and $^{13}C$ NMR, UV-Vis, Infrared spectroscopy as well as LCMS where applicable. The assignments of the ligands were also confirmed by using 2D NMR spectroscopy such as COSY and HSQC. A comparison of the position of the imine $\nu$(C=N) bands of the ligands observed was performed by using FTIR spectroscopy as shown in **Table 2.2**. Changes observed in the position of these bands upon coordination of the ligands to the diruthenium tetraacetate complexes are described in the next section.

**Table 2.2.** Summary of the properties of imidazopyridine ligands synthesised and successfully characterised.

| Ligand | Appearance | Imidazole Imine position $\nu$(C=N) [$cm^{-1}$] | Pyridine imine position $\nu$(C=N) [$cm^{-1}$] |
|---|---|---|---|
| **L1** | Green-white solid | 1537 | 1459 |
| **L2** | Orange-brown solid | 1625 | 1462 |
| **L3** | Reddish-brown solid | 1560 | 1560 |
| **L4** | Reddish/orange-brown | 1565 | 1430 |
| **L5** | Orange Oil | 1711 | 1612 |

## 2.2 General synthesis of diruthenium tetraacetate complexes

### 2.2.1 Synthesis of diruthenium tetraacetate chloride

Diruthenium tetraacetate chloride precursor complex $Ru_2(OAc)_4Cl$ (**C1**) was synthesised by modification of the literature procedures reported by Stephenson and Wilkinson.[19,20] In the solid state, the complex is known to exist as a polymeric framework where the axial positions are occupied by chloride ligands. Occupation of the axial sites by the solvent molecules is known to occur in solution, which disrupts the polymeric structure. The synthesis procedure involved refluxing hydrated ruthenium trichloride at high temperatures in the presence of acetic anhydride and acetic acid, under exposure to an oxygen atmosphere. The procedure followed is shown in **Scheme 2.8**. The product was isolated as a light brown solid in sufficiently high yields of 65 – 70% and was soluble in polar organic solvents and water. The lithium chloride in the reaction improved the hydroelectric constant of the solution and ensured coordination of the chloride to the axial site of the paddlewheel structure. It has previously been shown that if the reaction is performed in an excess amount of anhydrous lithium chloride, the yield of the product is increased and that comparable yields can be obtained under oxygen and nitrogen conditions.[19]

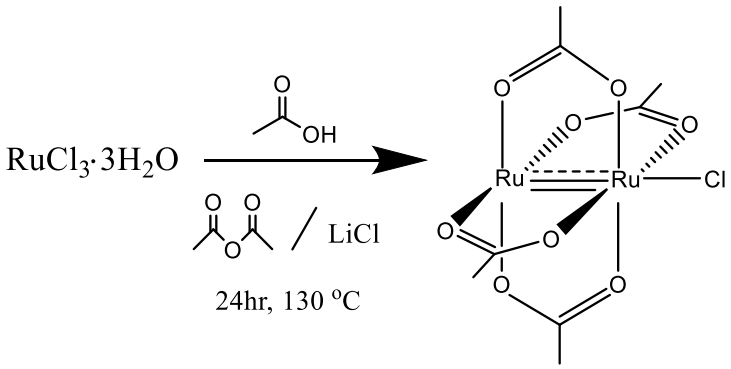


**Scheme 2.8** Synthesis of diruthenium tetraacetate chloride precursor complex, $Ru_2(OAc)_4Cl$ (**C1**)**.** Successful synthesis of the complex was confirmed by using infrared spectroscopy, UV-Vis spectroscopy and mass spectrometry.

### 2.2.2 Characterisation of diruthenium tetraacetate chloride by FTIR, UV-Vis spectroscopy and mass spectrometry

The infrared absorption spectra of diruthenium tetraacetate chloride (**C1)** is shown in **Figure 2.24**. Analysis of the complex revealed the presence of absorption bands at 1433 and 1396 $cm^{-1}$ which are assigned to the antisymmetric and symmetric stretching vibrations of the acetate groups, respectively. These stretching vibrations confirmed the successful synthesis of symmetric paddlewheel complexes. $\nu$(C-H) absorption bands corresponding to the acetate groups are observed at 2931 $cm^{-1}$. The $\nu$(Ru-Ru) stretch occurs in the fingerprint region around

1048 $cm^{-1}$ while the $\nu$(C-$CH_3$) bending occurs at 688 $cm^{-1}$. The complex was also analysed using UV-Vis spectroscopy in methanol and the maximum absorbance of the complex was in the region previously observed in literature.[21] The absorbance band occurred in the visible region with $\lambda_{max}$ centred at 431 nm, and is assigned to the ligand to metal $\pi(Ru_2) \rightarrow \pi^*$(RuO, $Ru_2$) transition. In DMSO, no spectrum could be obtained since the complex was highly insoluble with visible precipitation.

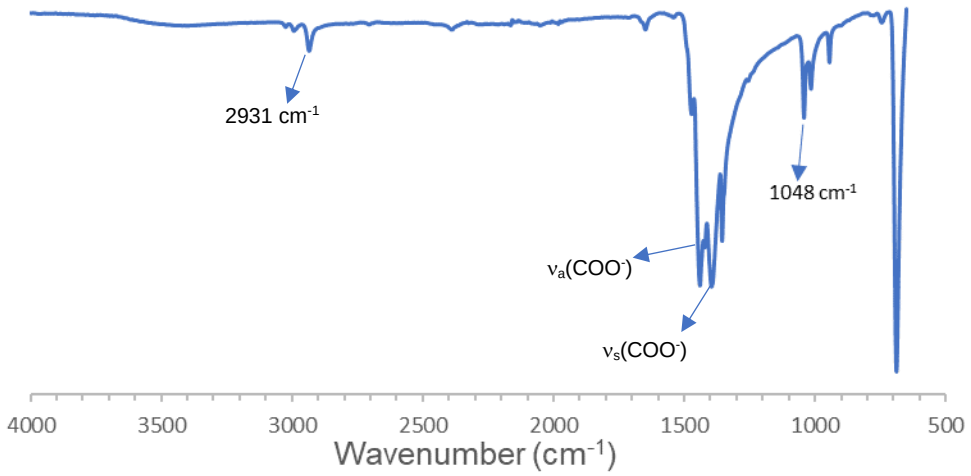


**Figure 2.24**. FTIR spectrum of the precursor complex **C1**.

Mass spectrometry was used to confirm the successful synthesis of the precursor complex and the mass spectrum obtained is shown in **Figure 2.25**. The spectrum shows the presence of a molecular ion peak at m/z of 438.86 which corresponds $[M\text{-}Cl]^+$. The two peaks with m/z between 450 and 470 were assigned to the solvated forms of the complex where the acetonitrile coordinates axially to the ruthenium atoms. Peak at m/z 920 is attributed to the oligomeric form of the complex where the ruthenium atom of one complex is linked to the ruthenium of another complex to form an extended chain.

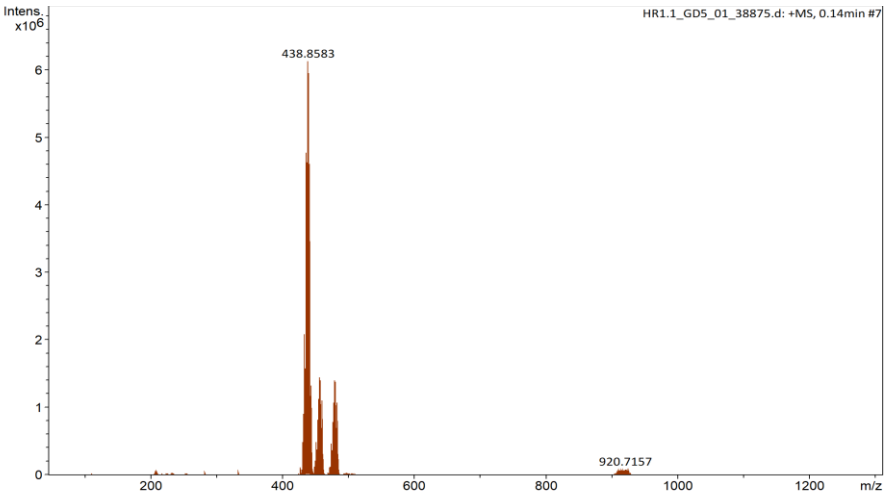


**Figure 2.25** Mass spectrum of the precursor complex $Ru_2(II,III)(OAc)_4Cl$ (**C1**).

### 2.2.3 Ion exchange reactions using different counterions

Ion exchange reactions were performed on the complex **C1** to synthesise more soluble ionic complexes. It has previously been shown that the presence of a counterion in a complex can promote anion directed self-assembly which can be used for developing supramolecular structures.[22] Studies involving metathesis reactions of chloride with $BF_4^-$ and $NO_3^-$ counterions on mononuclear and binuclear complexes of ruthenium were presented by Xu and coworkers.[23] Observations using single crystal X-ray diffraction showed a decrease in the Ru-Ru bond distance upon chloride substitution, which was consistent with the presence of a triple bond order of 2.5. The anions were incorporated into the coordination sphere of the ruthenium centre and weakly coordinated to the metal centres as axially coordinated ligands. In non-coordinating solvents, oligomerisation of the paddlewheel units occurs, and each unit is held to its neighbour via intermolecular forces between the metal and the oxygen atoms of the acetate groups.[24,25] The potential of the complexes bearing the counterions to self-assemble and form polymers has enabled the development of the complexes into synthons which have application in linear and polymer development.[26] The synthesis of the cationic ruthenium species $[Ru_2(OAc)_4(H_2O)_2]PF_6$ using $NH_4PF_6$ in an equimolar amount of $AgSO_4$ has previously been reported by Drysdale et. al.[27] This complex was air and light stable over long periods of time when analysed using electronic absorption spectroscopy.

### 2.2.4 Synthesis and characterisation of the ionic precursor complexes $[Ru_2(OAc)_4]X$ (where X= $NO_3^-$, $PF_6^-$ and $BF_4^-$)

The cationic mixed valent complexes (**C2** – **C4**) were synthesised by following literature procedures involving direct metathesis reactions.[28,29] The first step in the synthesis involved disrupting the intramolecular forces of diruthenium tetraacetate chloride by dissolving the

precursor complex in a small amount of dry methanol. This was followed by the addition of one molar equivalent of a silver salt to the solution to remove the axially coordinated and labile chloride ligand. This created vacant positions on the axial site of the precursor complex, which increased the potential for coordination to ligands. The reaction procedure followed is shown in **Scheme 2.9**. The driving force towards the successful formation of the cationic complex was the formation of a white silver chloride precipitate which could be removed by using filtration techniques. The complex **C2** was synthesised through the reaction of an equimolar amount of complex **C1** and $AgNO_3$. The formation of silver chloride precipitate was observed within 10 to 15 minutes of reaction onset; however, the reaction was allowed to occur for 24 h to ensure the complete counterion exchange of the chloride ligand. Complex **C2** was obtained as a reddish-brown solid at high yields (70 – 90%), and was soluble in polar organic solvents like methanol, water, DMSO and partially soluble in non-polar solvents like petroleum ether.

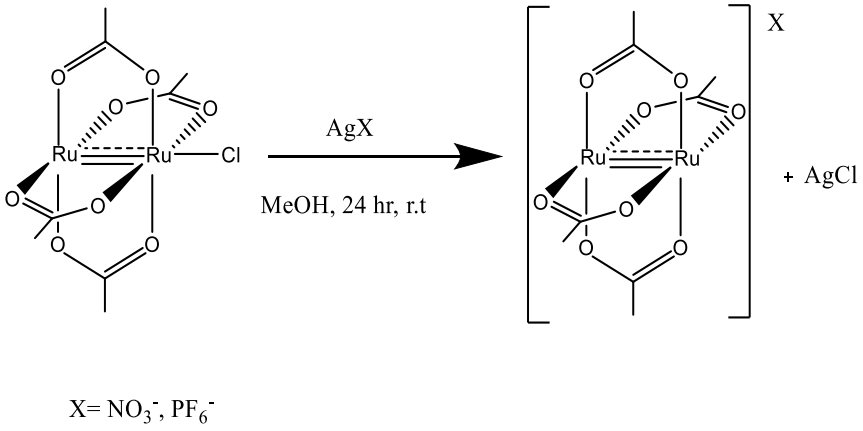


**Scheme 2.9.** Synthesis of the $[Ru_2(OAc)_4]X$ ionic species.

The precursor complex **C3** was also synthesised following the same procedure used for the synthesis of **C2**, by the reaction of equimolar amounts of complex **C1** with $AgPF_6$ salt. The reaction occurred readily, with similar observations to those seen in the synthesis of complex **C2**. The product was obtained as a light-brown solid at an almost crude yield of 93%, and was soluble in polar organic solvents like methanol, THF, water and insoluble in ether.

Attempts to synthesise $[Ru_2(OAc)_4(THF)_2]BF_4$(**C4)** following the same procedure used for complex **C2** and **C3** (in methanol) was not successful and the formation of silver chloride, which is indicative of chloride substitution, was not observed after 24 hours of the reaction. A dark-black solid product was obtained which likely included by products of decomposition. The reaction was repeated, and the complex successfully synthesised when stirring an equimolar amount of complex **C1** with $AgBF_4$ in dry THF, under a nitrogen atmosphere in the dark (**Scheme 2.10**). The product was obtained as a brown solid in a moderate yield of 43%. A lack

of reactivity of the $BF_4^-$ counterion with the ruthenium acetate complex was thought to be accountable for the low yields obtained in comparison to the yields of **C2** and **C3**. The product's partial solubility in non-polar solvents also reduced the amount of product that precipitated from the solution.

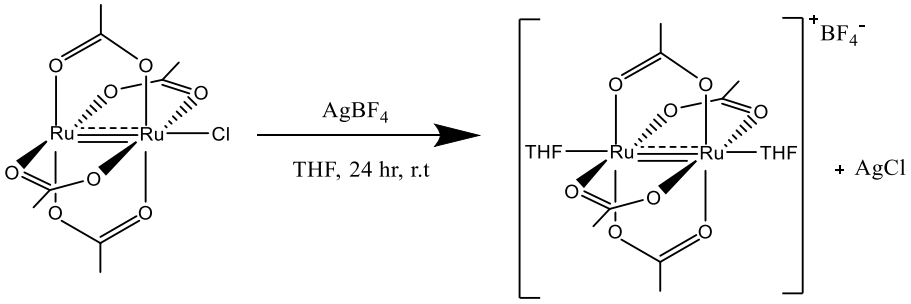


**Scheme 2.10.** Procedure for the synthesis of complex **C4**.

The complexes obtained were analysed using a variety of analytical techniques such as Infrared spectroscopy (IR), UV-Vis spectroscopy, Mass spectrometry, cyclic voltammetry and elemental analysis. The changes in the electronic spectra of the complexes with respect to those of the precursor complex **C1** were compared.

### *2.2.4.1 Infrared spectroscopy*

Since the complexes were suspected to be mixed valent Ru (II), (III), the paramagnetic nature of ruthenium in the 5+ oxidation state made it difficult to use NMR spectroscopy techniques to characterise the complexes. Infrared spectroscopy was used to analyse the synthesised complexes, using attenuated total reflectance. The presence of a counter ion was observed in the isolated products as shown by the stacked spectra of complex **C1** and **C2** in **Figure 2.26**, suggesting successful displacement of the chloride ligand. Complex **C2** displays similar absorption bands to **C1**, which are characteristic of the acetate symmetric and antisymmetric $\nu(OCO^-)$ stretches around 1432 – 1395 $cm^{-1}$. The stretching frequency of the bands does not appear to be shifted upon removal of the chloride ligand. The stretching frequency of the nitrate counterion $\nu_{sym}(NO_3^-)$ is observed as a very strong signal around 1266 $cm^{-1}$ in the product. The spectrum shows the absence of a broad signal between 3000 to 3500 $cm^{-1}$, indicating the absence of methanol or water in the complex. This showed that although methanol is a coordinating solvent, it was not coordinated to the complex and there was vacant space available for axial coordination of the neutral N–donor ligands to the metal centre.

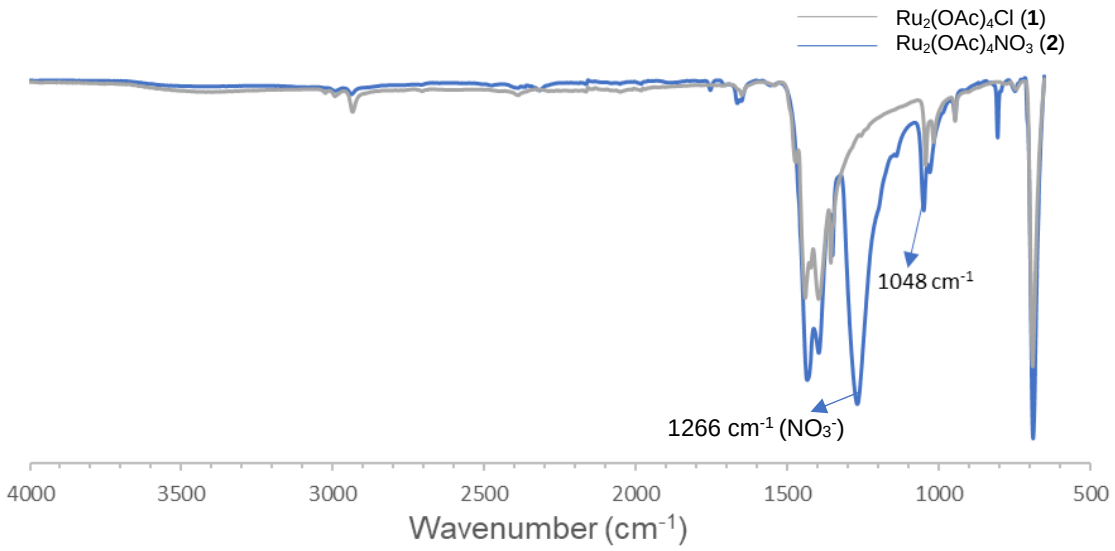


**Figure 2.26.** Stacked Infrared spectra of the precursor complexes **C1** and **C2**.

Comparing complexes **C1** and **C3**, a slight shift in the position of the C-H stretching bands of **C3** to a lower wavenumber relative to **C1** is observed (**Figure 2.27**). The presence of a $PF_6^-$ counterion is shown by the strong band at 830 $cm^{-1}$ assigned to $\nu_{sym}(PF_6^-)$, which confirms the successful synthesis of an ionic complex. The $\nu$(Ru-Ru) band at 1042 $cm^{-1}$ is shifted to a lower wavenumber of 1020 $cm^{-1}$ in **C3**. Strong absorption bands corresponding to the asymmetric and symmetric $\nu(OCO^-)$ stretching occur at 1439 and 1400 $cm^{-1}$, respectively. The spectrum also shows no significant coordination of solvents like water or methanol in the product. The overlaid infrared spectrum of complexes **C1** and **C4** occurs in **Figure S11** of the appendix. Similar results were also obtained for complex **C4** $[Ru_2(OAc)_4(THF)_2]BF_4$), which also shows additional absorption bands at 3557 and 3373 $cm^{-1}$ assigned to the unsymmetrical and symmetrical methylene (C-H) stretches of THF coordinated to the complex, respectively. Evidence of coordinated THF is also shown by the presence of the ether (C-O) band at 1101 $cm^{-1}$.

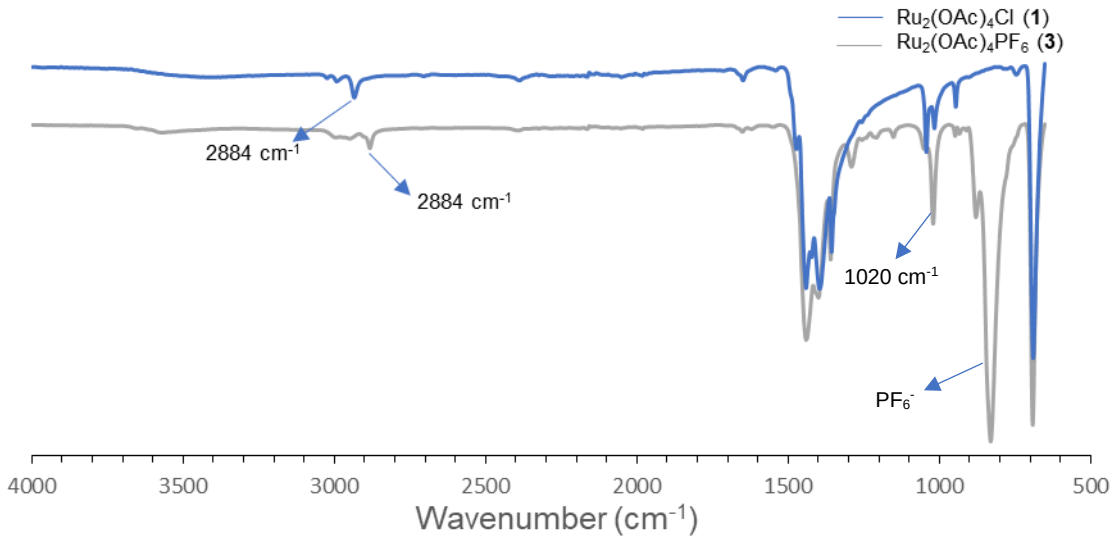


**Figure 2.27.** Stacked infrared spectra of precursor complexes **C1** and **C3**.

### *2.2.4.2 UV-Vis spectroscopy*

The electronic absorption spectra of **C1, C2** and **C3** show absorbance bands in the UV region with $\lambda_{max}$ centred around 200 − 300 nm and in the visible region (approx. 430 nm) which corresponds to what is previously reported in literature.[29] The UV-Vis spectra of **C1** – **C3** is shown in **Figure 2.28** while that of **C4** occurs in **Figure S12** of the appendix. The UV band centred at ~ 200 − 300 nm has been proposed to possess Ligand to Metal Charge Transfer properties ($\sigma \rightarrow \sigma^*$ transition) and changes in the spectral properties observed around this region was not considered due to possible solvent interference. The characteristic absorption band with $\lambda_{max}$ of 431 nm is assigned to the ligand to metal $\pi$ (RuO, $Ru_2$) → $\pi^*(Ru_2)$ transitions as previously discussed. The UV-Vis spectra were obtained in methanol, which is a coordinating polar solvent. It has been reported that in non- coordinating solvents, the $\pi$ (RuO, $Ru_2$) → $\pi^*(Ru_2)$ transition band is usually observed at a higher wavelength.[28] The transition observed in this region has been shown to have little dependence on the axial ligand and varying the axial chloride ligand was found to have little influence on the position of the band, hence the band is observed around the same $\lambda_{max}$ region for complexes **C1** – **C4**. Another absorbance band was observed for **C2** in the NIR (900–1200 nm) and this was assigned to the $\delta(Ru_2) \rightarrow \delta^*(Ru_2)$ transition but could also be assigned to a Laporte forbidden band.[30]

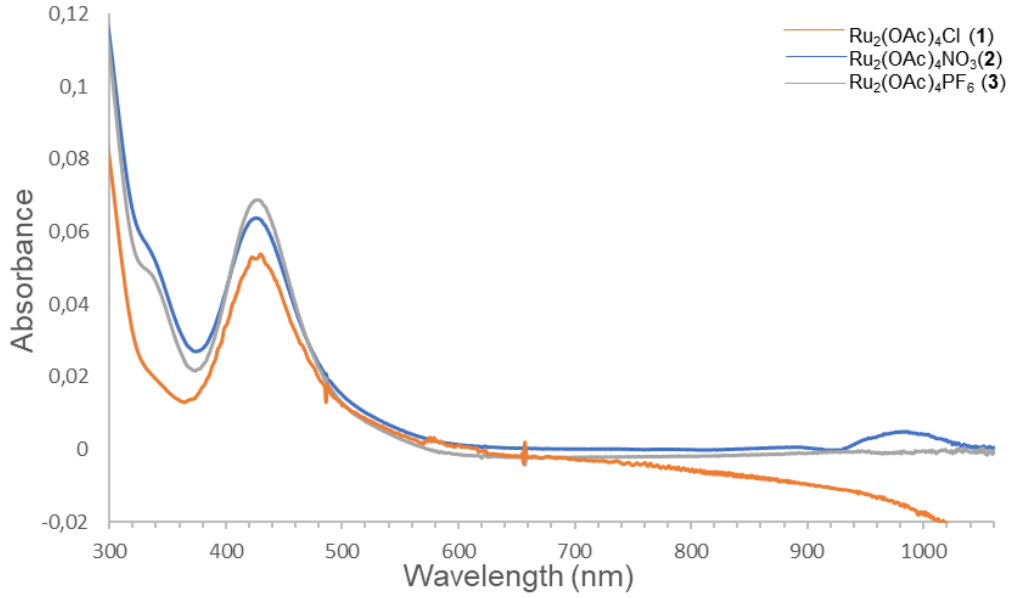


**Figure 2.28.** Overlayed UV-Vis spectra of the precursor complexes **C1**, **C2** and **C3** obtained in methanol.

### *2.2.4.3 Electrochemistry*

Diruthenium acetate complexes possess a rich redox chemistry and display reversible and non-reversible redox electrochemical properties. Studying the redox behaviour of the complexes may help understand as well as predict the behaviour of the complexes during biological studies in the presence of reducing agents. The electronic states of the compounds have been studied to understand the reduction and oxidation properties observed. The higher oxidation state processes ($Ru_2^{5+/6+}$ and $Ru_2^{6+/7+}$) are observed for stronger *N*, *N* or *O*, *O* donor ligands that can stabilise the metal centre in the oxidised form.[31] A single $Ru_2^{5+/4+}$ reduction process is usually observed within the solvent's potential window for diruthenium acetate complexes, owing to the poor electron donating ability of the methyl groups.[32] The interaction of the axial ligand and metal centre is affected by orbital alignment and symmetry arrangement between the metal centre and ligand. Orbital mixing occurs between the orbitals of the metal centre and the oxygen of the acetate groups,[33] The energy separation between the different orbitals is dependent on the oxidation state of the metal as well as the nature of the axial ligand. The CV results obtained for the complexes **C2** – **C5** were compared to a standard ferrocene ($Fc/Fc^+$) oxidation. The reversible oxidation process of ferrocene in different solutions of supporting electrolytes is shown in **Figure 2.29**.

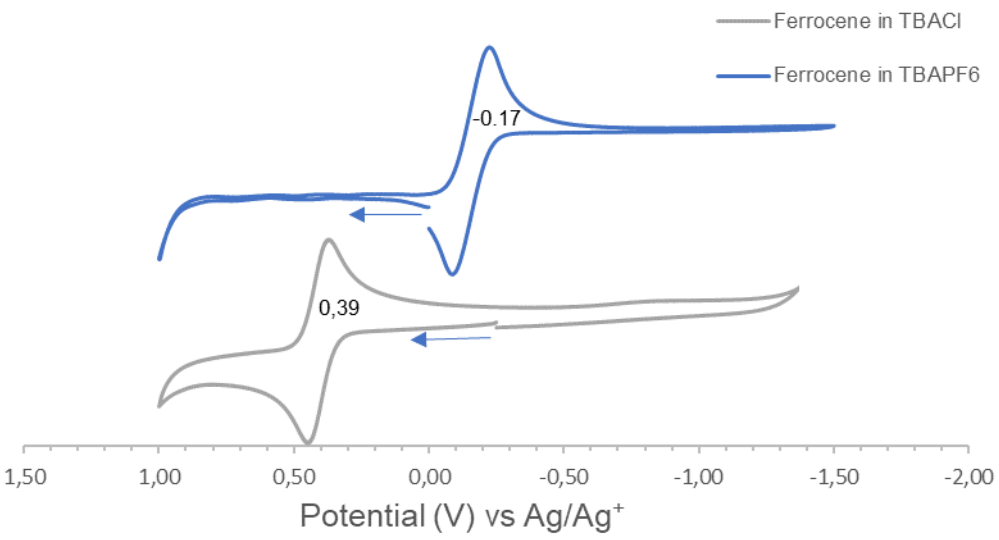


**Figure 2.29.** Cyclic voltammograms of ferrocene in methanol solution containing 0.1M electrolyte solutions (TBACl vs. $TBAPF_6$).

Attempt to analyse the complex $[Ru_2(OAc)_4]Cl$ (**C1**) using cyclic voltammetry was done in different solvents and due to poor solubility of the complex and visible precipitation, no electrochemical processes could be observed in acetonitrile, DMSO, THF and DMF. In methanol, a single reversible reduction process was observed in different supporting electrolyte solutions, and the value of this reduction potential was in agreement with what is reported in literature.[34,35] The half wave potentials were compared to a ferrocene standard in the respective electrolyte solutions.

The position of the $Ru^{5+/4+}$ reduction process of **C1** in a methanol solution containing 0.10 M of the electrolyte solutions $TBANO_3$ and $TBAPF_6$ occurred at a more negative potential in comparison to that of the same complex in TBACl as shown in **Figure 2.30**. This is because the presence of TBACl ensures coordination of the chloride ligand to the complex, whereas the presence of $TBANO_3$ or $TBAPF_6$ favours dissociation of the chloride ligand due to a counterion exchange of the chloride ligand with the $NO_3^-$ or $PF_6^-$ anion. The increased electron density on the metal makes it harder to reduce the metal centre and shifts the reduction potential towards the cathodic region.

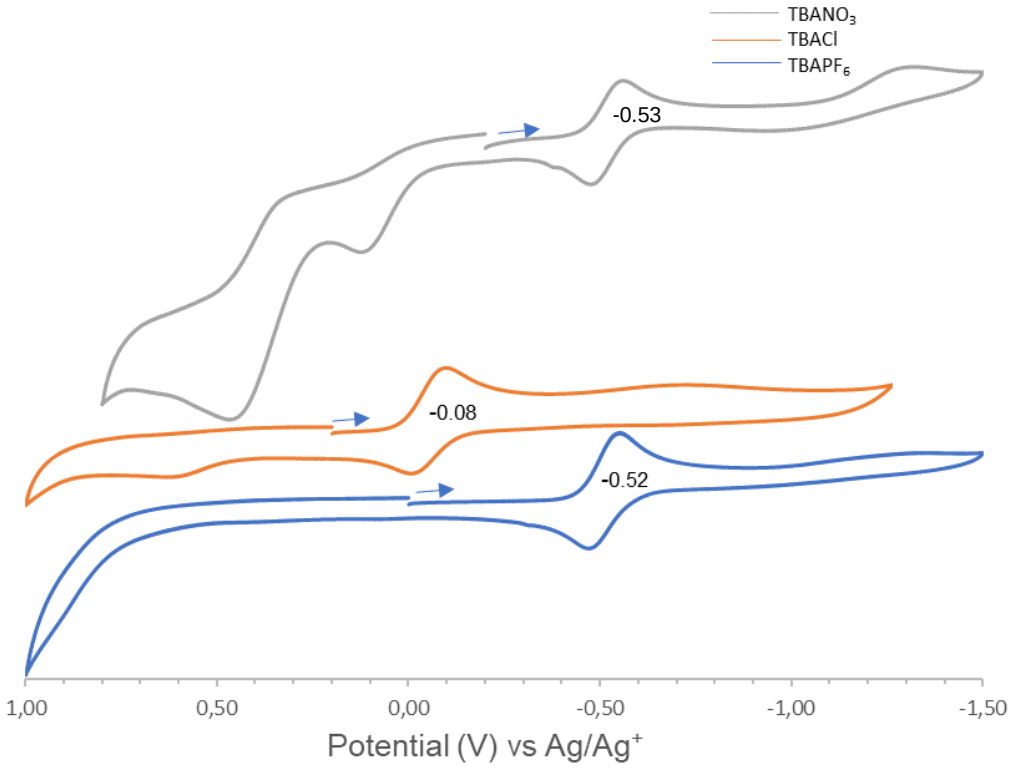


**Figure 2.30.** Cyclic voltammograms of the complex **C1**, obtained in a methanol solution containing 0.10 M of the electrolyte solutions $TBANO_3$, TBACl and $TBAPF_6$. The scan rate is 100 mV/s.

Successful synthesis of the precursor complex **C2** and **C4** was confirmed by using elemental analysis which showed the formation of the desired precursor complex, while mass spectrometry was used to confirm the synthesis of **C3** and **C4**. The mass spectra of the complexes occur in **Figure S13** of the appendix. A molecular ion base peak with 100% abundance at m/z of 438.84 is assigned to [M-X], where X represents a counterion, while the peaks at m/z 479 and 516 correspond to the solvated species of the complex.

## 2.3 General synthesis of diruthenium acetate complexes axially coordinated by ligands

Mixed valent complexes of diruthenium tetraacetate with Ru (II,III) bridged by adenine and adenosine ligands have been successfully synthesised and characterised by Gangopadbyay.[10] Although the complexes were paramagnetic, they were partly analysed using $^1$H NMR spectroscopy which revealed that the complex bearing adenine was a polymeric form where the diruthenium metal centres were bridged by adenine via the N-9 and N-3 atom. However, structural elucidation of the complexes was not possible since no single crystal data could be obtained. The derivative bearing adenine was a distinct di-adduct, in which the

adenosine ligand coordinates to the metal centre through N-7. The first crystal structure of a one-dimensional polymer of ruthenium acetate bridged by phenazine ligands on the axial position of ruthenium was later reported by Hitoshi and co-workers.[36] The structure exhibited weak antiferromagnetic coupling between the two ruthenium units, with an appreciable zero-field splitting in the ground state of the complex. Brendan and co-workers reported the successful synthesis of the mixed valent $[Ru_2(OAc)_4L_2]PF_6$ complexes, with L being the ligands imidazole, 7-azaindole and caffeine axially coordinated to the diruthenium metal centres.[9] Vamvounis and co-workers reported on the ligand substitution reaction which displaces the $H_2O$ molecules in the complex $[Ru_2(OAc)_4(H_2O)_2]PF_6$, which was carried out in 2-propanol using excess of the quinuclidine ligand under argon. It was observed that under air-free conditions the precipitate that formed could remain stirring indefinitely without any apparent change and that the exposure of the reaction solutions to air led to product decomposition and low yields.[37]

A recent and interesting study on the axial coordination of diruthenium tetraacetate was presented by Rodrigo and co-workers, who studied the kinetic reactions upon the coordination of the amino acids glycine, cysteine and histidine, etc. to the axial position of ruthenium acetate complexes.[28] A reversible binding process occurred between the amino acids and the ruthenium centres, through the deprotonated nitrogen or the carbonyl oxygen of the amino acids. Using deconvoluted UV-Vis spectroscopy, it was shown that an incomplete and reversible reaction occurs between the ruthenium species and the amino acids, which is then followed by a slow decomposition process due to disruption of the paddlewheel complex. The decomposition process results from the displacement of an acetate group by a ligand to form monomeric complexes. The schematic of this reaction is shown in **Scheme 2.11**.

$$\left[Ru_2(CH_3COO)_4(H_2O)_2\right]^{+} + H_3NCH_2COO^{-} \underset{K_{-1}}{\overset{K_1}{\rightleftharpoons}} \left[Ru_2(CH_3COO)_4(H_2O)_2(H_3NCH_2COO)\right] + H_3O^{+}$$

$$\left[Ru_2(CH_3COO)_4(H_2O)_2(H_3NCH_2COO)\right] \longrightarrow \text{decomposition products}$$

**Scheme 2.11.** Mechanistic view of the reaction that occurs between diruthenium tetraacetate with the amino acid glycine, cysteine, and histidine.

For our synthesis of the desired complexes containing imidazopyridine ligands attached to the diruthenium tetraacetate precursor complexes, the literature procedures reported by Gangopadhyay et al.[10] and Brendan et. al.[9] were modified. The synthesis of imidazopyridine-based ligands containing aryl, alkyl and ferrocenyl groups attached to the 2-position of the imidazole ring was described previously. The ligands shown in **Figure 2.31** were successfully

synthesised and characterised using spectroscopic and spectrometry techniques. This section describes the coordination of the synthesised imidazopyridine ligands to the axial position of the precursor diruthenium tetraacetate ionic species.

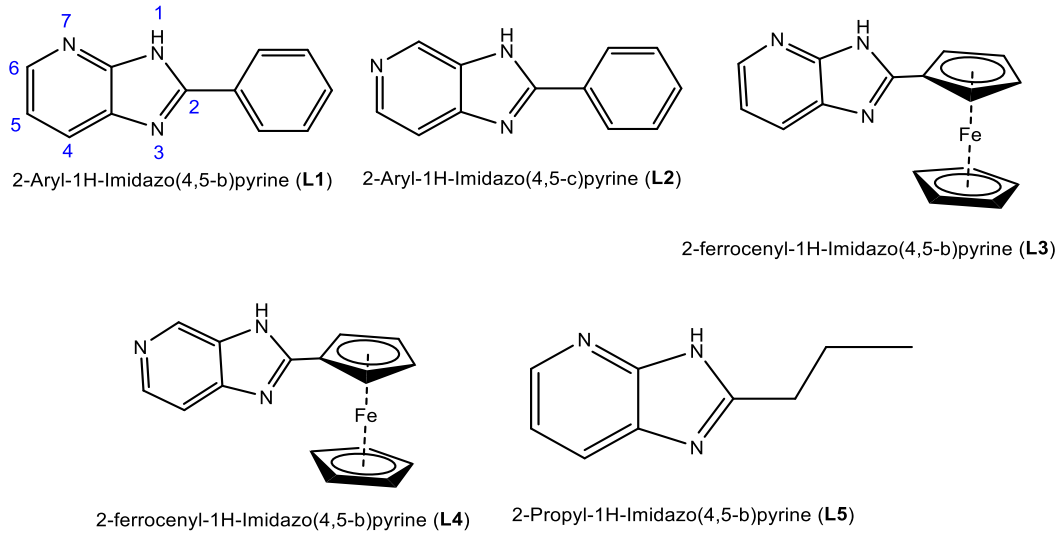


**Figure 2.31.** The structures of the imidazopyridine derivatives successfully synthesised and characterised. A change in position of the nitrogen atom on the pyridine ring of the ligands creates the regiomers **L1** and **L2** as well as **L3** and **L4**. The more stable tautomer of **L1** with pyridine nitrogen on position seven ( vs. position 4) of the ring was used for the complexation reactions.

Complexation to the ruthenium metal centre could occur through the lone pairs on the basic nitrogen atoms of the imidazole and pyridine rings. It was also assumed that coordination of the ligands to the diruthenium centres would preferably occur via the nitrogen atom of the imidazole ring since this nitrogen is more basic than the pyridine nitrogen. The amine proton of the imidazole ring could also be abstracted, followed by interaction of the resultant anionic nitrogen atom with the ruthenium metals. In the absence of a suitable base, the possibility of this deprotonation occurring would be less. Two possible interactions between the imidazopyridine ligands and the diruthenium core were thus possible. In the case where the pyridyl nitrogen is at position 6 (**L1** and **L3**) only coordination via the axial site of the ruthenium core is possible. On the other hand, if the pyridyl nitrogen is at position 7 (**L2** and **L4**), bidentate coordination is possible such that the equatorial bridging acetate is displaced by the ligand in the presence of a base.

Due to the aforementioned bidentate nature of the less stable tautomers of **L1**, **L3** and **L5** the equatorial substitution would only occur over prolonged stirring of the reaction materials and

at elevated temperatures. To our knowledge this is the first report of diruthenium tetraacetate bearing Imidazopyridine ligands either on the axial or equatorial sites, thus the products expected from the substitution reactions represented novel class of compounds. Complexation reactions with imidazopyridine ligands containing pyridine nitrogen on position 4 or 7 were proposed to occur as shown in **Scheme 2.12**. Two species could potentially be formed under the conditions, depending on the type of coordination and number of ligands that coordinate to the metal centre. The first species is a monomeric complex consisting of two imidazopyridine ligands coordinated axially to the metal centre by the nitrogen of the imidazole ring. The second type of complex could result from the ligand equatorially bridging the different diruthenium paddlewheel units.

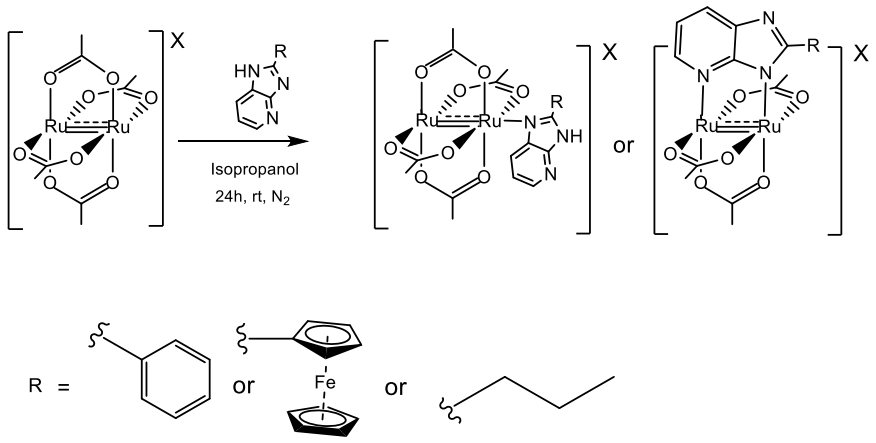


**Scheme 2.12.** Synthetic procedure for the coordination of diruthenium tetraacetate complexes containing imidazopyridine ligands with nitrogen atoms on position 4 or 7.

The imidazopyridine ligands with nitrogen atoms on position 5 or 6 did not have the right geometry to displace both acetate groups on the equatorial positions and only the axially coordinated complexes were thought to be possible in this case (**Scheme 2.13**). The reactions were performed in methanol or isopropanol, and the choice of solvent depended on the solubility of both the ligands and the precursor complexes. In most cases the ligand and the precursor complex were dissolved separately in isopropanol and then the ligand solution was transferred dropwise to the stirring precursor complex solution. In cases where the ligand showed full solubility in the solvent, both reagents were mixed-together in the reaction vessel.

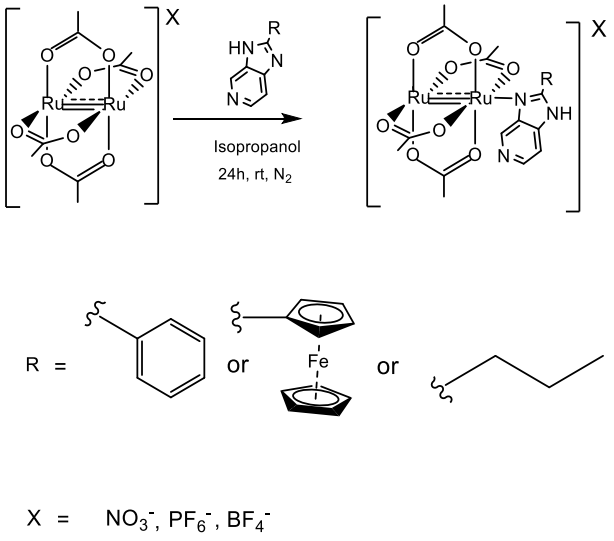


**Scheme 2.13.** Synthetic procedure for the coordination of diruthenium tetraacetate. complexes containing imidazopyridine ligands with pyridine nitrogen atom on position 5 or 6.

Purification methods involved co-precipitation and recrystallization techniques where possible, using DCM, hexane, and ethanol. Synthesised complexes exhibited distinctive bands corresponding to acetate stretches $\nu(OCO^-)$ and imine $\nu(C=N)$ vibrations when analysed using infrared spectroscopy. A general trend indicating the successful coordination of the ligand to the metal centre was the shift in stretching frequency of the imine $\nu(C=N)$ band of either the imidazole or pyridine ring of the ligand to a lower wavenumber which is attributed to back bonding effect as illustrated in **Figure 2.32**. This shift results from the donation of a lone pair of electrons from the ligand to an empty $\sigma^*$ orbital of the ruthenium metal, with the metal simultaneously donating electron density from a filled d orbital to an empty $\pi^*$ orbital of the ligand. This effect weakens the imine $\nu(C=N)$ bond and shifts the vibration of the bond to a lower wavenumber. Comparison of these bands with those of the starting material provided preliminary evidence of complexation of the ligands to the metal centres. The presence of the symmetric and antisymmetric acetate bands in the complexes confirmed the retainment of the lantern tetraacetate paddlewheel structure in the complex and the $D_{4h}$ symmetry of the complex.

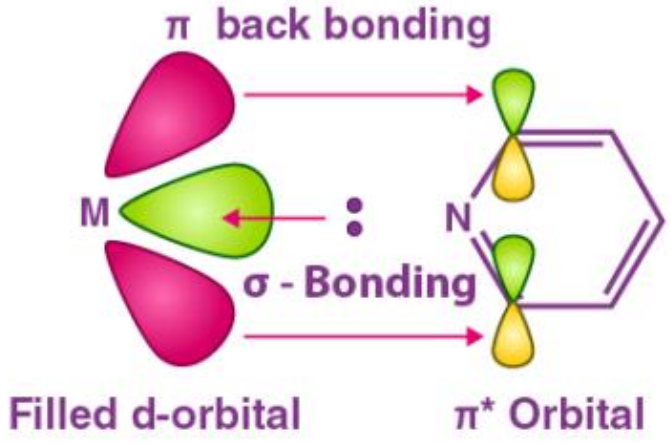


**Figure 2.32**. Illustration of back bonding effect between the filled d-orbitals of a metal and the empty π* orbitals of a ligand.

The complexes were analysed using a variety of analytical techniques such as Infrared spectroscopy, UV-Vis spectroscopy Cyclic Voltammetry, mass spectrometry and elemental analysis.

## 2.4 Synthesis and characterisation of imidazopyridine diruthenium tetraacetate complexes with $NO_3^-$ counterions $[Ru_2(OAc)_4]L]NO_3$ (C5 – C8)

Attempt to synthesise the complexes **C5** – **C8** was performed by stirring the precursor complex **C2** with excess of the ligands **L1** – **L4** at an elevated temperature (60 °C) for 24 h in isopropanol, under a nitrogen atmosphere. Thin layer chromatography served as a useful technique to monitor the progress of the reaction. The spot corresponding to the ligand was observed to decrease in intensity over time, while that of the precursor complex **C2** remained at the baseline, and this showed evidence of complexation of the ligand. The products were isolated as dark-brown powder-like microcrystals by co-precipitation techniques involving layering the concentrated reaction mixtures with THF or DCM and petroleum ether/ hexane (v/v; 1:9) and filtered under vacuum. For the product obtained in methanol (**P1**), infrared spectroscopy showed the presence of a broad band in the region 3631 – 3000 $cm^{-1}$ due to the coordination of methanol (**Figure 2.33**). This band was difficult to remove even after intensive drying of the product.

Infrared spectroscopy also revealed a new absorbance band at 1637 $cm^{-1}$ which was absent in the starting material and is assigned to a displaced carbonyl group of the acetate. This band occurs at a different region from the ν(C=O) bands of the acetate groups, and this showed

evidence of possible substitution of a bridging acetate. For the products (**P2** – **P3**) obtained in isopropanol, a new band appeared around 1850 $cm^{-1}$ which could be assigned to a carbonyl group. Analysis of all these products using cyclic voltammetry in a methanol solution containing 0.10 M of suitable supporting electrolyte solutions did not show any electrochemical process, including the expected $Ru_2^{5+/4+}$ reduction process. This indicated that there was possibly disruption in the paddlewheel structure which was also supported by the absence of the symmetric and antisymmetric stretches of the acetate groups on the IR spectra between 1400 – 1600 $cm^{-1}$.

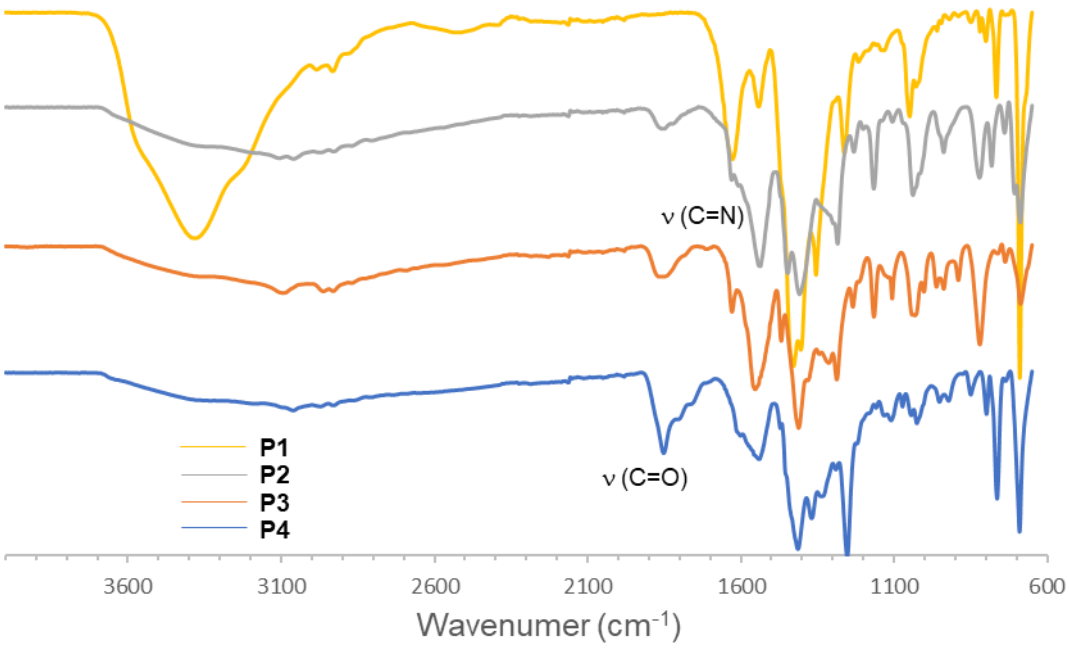


**Figure 2.33.** Infrared spectra of the products (**P1** – **P4**) obtained by stirring the precursor complex **C2** with excess of the ligands **L1** – **L4** at 60 °C overnight.

The reactions were repeated, by reacting excess of the ligands **L1** – **L4** and the precursor complex **C2** at room temperature, in isopropanol. Complex **C5** was obtained from reacting an excess of the ligand **L1** with the precursor complex **C2** as shown in **Figure 2.14**. The precursor complex, $[Ru_2(OAc)_4]Cl$ (**C1**) was also reacted with excess of the same ligand **L1** in the presence of silver nitrate using a direct metathesis displacement reaction. Using this route, the formation of silver chloride precipitate occurred but took longer when compared to isolating the ionic complex **C2** first.

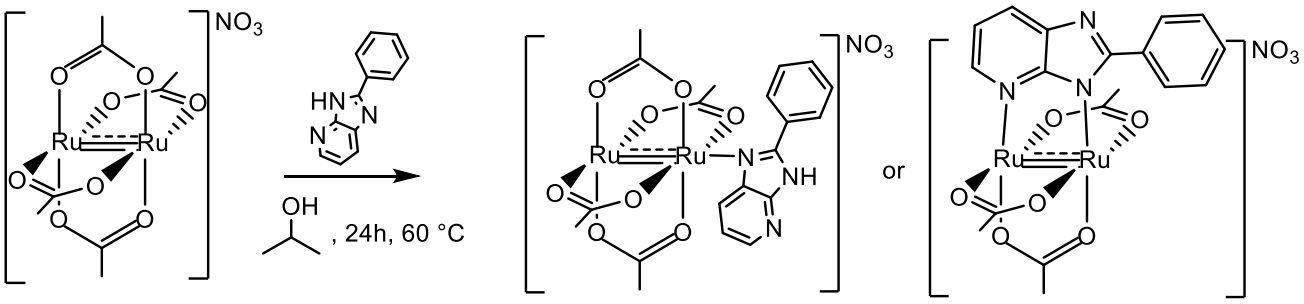


**Scheme 2.14.** The synthesis procedure and possible structures of complex **C5** using the precursor complex **C2** and excess of the ligand **L1**.

The complexes **C6** – **C8** were also synthesised following the same procedure, by stirring the precursor complex **C2** with an excess amount of ligand **L2** – **L4** for 24 hours at room temperature. Successful formation of new products was monitored by using TLC. The products were isolated as powder-like microcrystals at relatively moderate yields (43 – 85%) and were found to be soluble in polar organic solvents like methanol or DMSO, partially soluble in water and poorly soluble in non-polar solvents. The complexes were analysed using a variety of analytical techniques such as infrared spectroscopy, UV-Vis spectroscopy, mass spectrometry and cyclic voltammetry. The resulting complexes are paramagnetic due to the unpaired electrons and the delta and pi antibonding orbitals being degenerate $\sigma^2\pi^4\delta^2(\delta^*\pi^*)^3$, hence could not be characterised using $^1$H NMR spectroscopy. The number of unpaired electrons and the magnetic susceptibilities of the complexes were determined using the Evan's method.[38]

### 2.4.1 *Infrared spectroscopy*

Infrared spectroscopy was used as a preliminary technique for the detecting successful complexation of the ligand to form a new product. Analysis of the complex **C5** using Infrared spectroscopy revealed the presence of distinct bands at 1606 and 1542 cm$^{-1}$ which were assigned to the imine $\nu$(C=N) bands of the ligand as shown in **Figure 2.34**. The position of these bands was not significantly shifted from those of the free, unbound ligand. The imine $\nu$(C=N) stretching band of the pyridine ring at 1545 cm$^{-1}$ was shifted to a lower wavenumber in the complex indicating that it was also involved in coordinating to the ruthenium metal centre. The nitrate stretching is observed as a broad band around 1270 cm$^{-1}$. The bands on the complex appeared broader in comparison to those on the free ligand, which indicated that there was increased hydrogen bonding occurring in the complex.

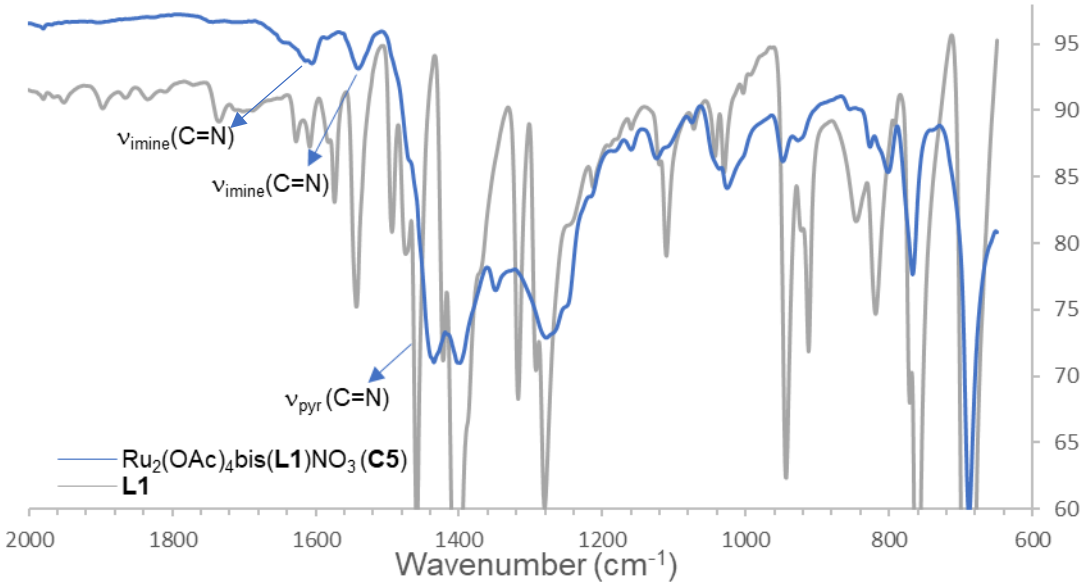


**Figure 2.34.** Expanded Infrared spectrum of complex **C5**, overlaid with the spectrum of the ligand **L1**.

Similar FTIR observations occur for **C6** containing 2-aryl-1H-imidazo(4,5-c)pyridine (**L2**) where the nitrogen atom on the pyridine ring of the ligand is at position 5 or 6 of the ligand. The infrared spectrum of **C6** occurs in **Figure S14** of the appendix and this shows a greater extent of decrease in the position of the imidazole imine stretching band relative to the free ligand, which is attributed to the back bonding effect. The infrared spectrum of the complex **C7** shown in **Figure 2.35** also shows significant shifting to lower wavenumber of the imine $\nu$(C=N) stretches in the region 1562 – 1530 $cm^{-1}$. The presence of the antisymmetric and symmetric stretches assigned to the $\nu(OCO^-)$ groups is observed around 1415 – 1400 $cm^{-1}$ in all the complexes. The presence of the $NO_3^-$ counterion was also observed in the spectra of all the complexes **C5** – **C8** around 1280 $cm^{-1}$, which confirmed the successful synthesis of the complexes in their ionic form. The IR of **C8** did not show a significant difference as compared to that of the ligand **L4** (**Figure S15**). In general, the appearance of the bands in the fingerprint region for **C5** – **C8** were significantly different from those of the precursor complexes and the free ligand, with the appearance of new bands for the product, providing evidence of formation of a new product.

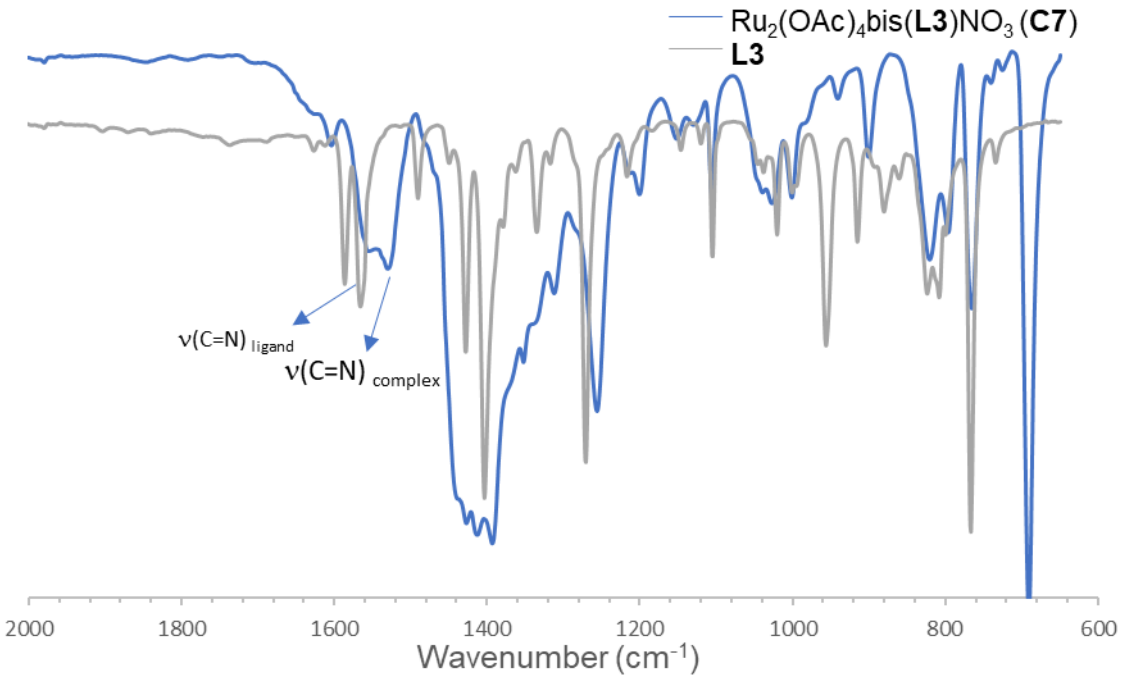


**Figure 2.35.** Expanded infrared spectrum of complex **C7** overlaid with the spectrum of the ligand **L3**.

### 2.4.2 *UV-Vis spectroscopy*

UV-Vis spectroscopy was used to compare the electronic absorption transitions observed on the precursor complexes, the free ligand and those on the resulting complexes **C5** – **C8**. The change in UV absorbance upon complexation of the ligand was brought about by the π to π or π to π* interactions with the ruthenium centres. Confirmation on whether these transitions are allowed based on symmetry of the metal and ligand orbitals can be confirmed by using Huckel molecular orbital theory.[24] UV-Vis data was obtained using 1 x $10^{-4}$ M of complex solution in methanol, however dilutions were performed for absorbance values to agree with the beer lambert's law, and λ values ranged from 200 to 1200 nm. Representative stacked UV-Vis spectra of **C5** and **C7** containing the phenyl substituted ligand **L1** and ferrocenyl substituted ligand **L3**, respectively are shown in **Figure 2.36**. The stacked UV-Vis spectra of the complexes **C6** and **C8** are shown in **Figure S16** of the appendix. Similar trends were observed in the absorbance spectra, characterised by the appearance of a shoulder band around 431 nm which is assigned to the π(RuO, $Ru_2$) → π*$Ru_2$ transition band of the complex, as previously reported for diruthenium tetraacetate complexes. This band is overlapped with the π → π* transition band of the ferrocenyl ring for complexes **C7** and **C8** containing the ferrocenyl ligands. A ligand centred band which can be assigned to π → π* or n → π* transitions is observed in the UV region around 290 – 300 nm. The ligand centred bands result from the

ligands donating an electron density to the LUMO of the metal centre, stabilising the π* HOMO of the ruthenium metal centres which lowers the energy of the π to π* transition and increases the ligand character of the π* orbital of the metal.[24] UV-Vis spectroscopy provided evidence of ligands **L1** and **L3** as stronger donor ligands when compared to **L2** and **L4** due to the ligand centred band positioned at slightly lower wavelength in the spectra. For **C7** and **C8**, a new absorption band appeared as a shoulder around 385 nm which can be assigned to allowed metal d – d transitions.[39]

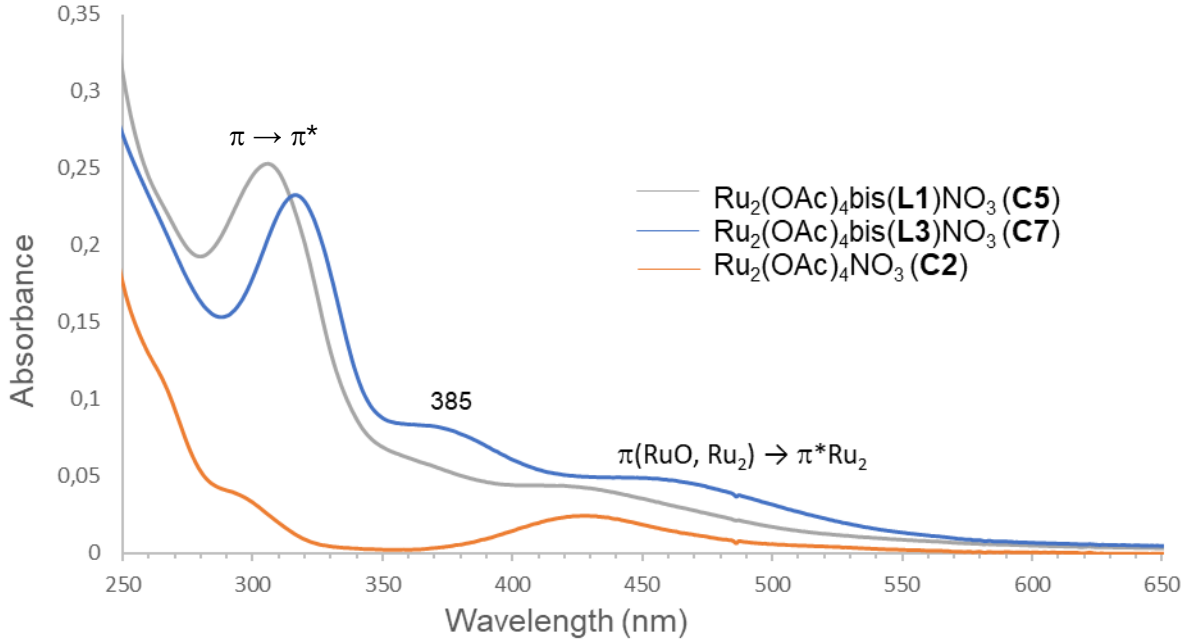


**Figure 2.36.** Overlaid UV-Vis spectra of complex **C2**, **C5** and **C7** (obtained in methanol).

### 2.4.3 *Electrochemistry*

Electrochemical experiments for complexes **C5** – **C8** containing $NO_3^-$ counterions were performed in methanol solutions containing either 0.10 M of TBACl or $TBANO_3$ as supporting electrolytes. The values of the $E_{1/2}$ wave potentials were in the range of previously reported diruthenium acetate complexes.[20,25] Complex **C1** had a reduction potential of -0.08 V in TBACl as shown in **Figure 2.30** previously, which is shifted in the anodic direction by 40 mV in the complex **C2** to a reduction potential of 0.32 V (**Figure 2.37**). This indicates that it is easier to reduce the ruthenium cores in the cationic complex **C2** relative to **C1**, due to a decreased electron density on the ruthenium cores upon introduction of the $NO_3^-$ counterion. The reduction potential of complex **C2** is slightly shifted by 10 mV in the anodic region to a reduction potential of 0.31 mV in **C5** upon the coordination of the ligand **L1**, which shows that the ligand is slightly deactivating.

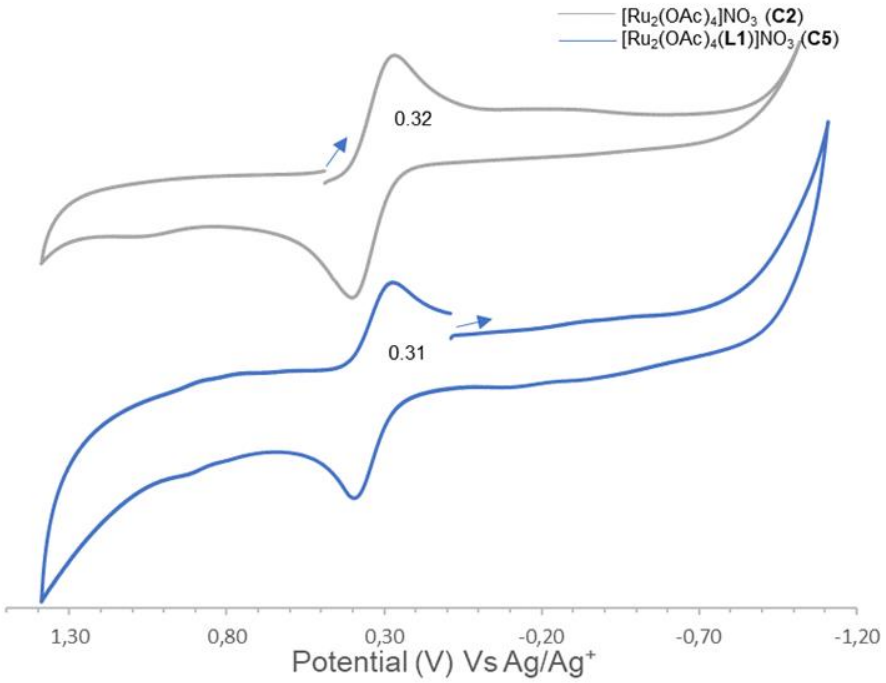


**Figure 2.37.** Cyclic voltammograms showing the electrochemical processes of the complexes **C2** and **C5** obtained in a methanol solution containing 0.10 M TBACl at a scan rate of 100 mV/s.

In addition to the $Ru_2^{5+/4+}$ reduction process observed in complexes **C5** – **C8**, a reversible oxidation peak is observed in **C7** and **C8** due to the presence of ferrocene in the coordinated ligands. The cyclic voltammogram of **C7** obtained in TBACl is shown in **Figure 2.38** while the voltammogram of the same complex obtained in $TBANO_3$ is shown in **Figure S17** of the appendix. The potentials occur in the same region in both TBACl and $TBANO_3$, which is indicative of the fact that there is no counterion exchange of the complex $NO_3^-$ anion with that of the chloride from the TBACl supporting electrolyte. The oxidation couple of ferrocene in both **C7** and **C8** is not significantly shifted, relative to that of the free uncoordinated ligands. This shows that there is little effect on the electron density of the ferrocenyl-based ligands upon coordination to the diruthenium metal centres. The ferrocenyl oxidation peak shows a two-electron transfer process with the oxidation peak twice the size of the $Ru_2^{5+/4+}$ reduction process. This indicates the presence of two ferrocenyl-based ligands coordinated to the metal centres. The two-electron transfer process observed indicates that there is coupling between the two ferrocenyl centres, and this is contrary to what has been observed by Darryl et al.,[40] whereby upon equatorial substitution of the acetate groups with ferrocenyl moieties in diruthenium acetate, two separate and clearly resolved $Fc/Fc^+$ oxidations occurred. This indicates that there is a weaker redox coupling between the equatorially positioned ferrocenyl moieties relative to the axially coordinated ones. **C2** has a reduction potential of 0.31 V, which

is slightly shifted towards the anodic region by 30 mV in the complex **C7**, indicating a decreased electron density on the ruthenium metal upon coordination of the ferrocenyl ligand **L3**. This shows that the ligand **L3** greatly deactivates the complex **C7**, relative to the phenyl ligands **L1** and **L2** in complexes **C5** and **C6**, respectively. A similar observation to **C7** is seen for complex **C8** containing the ferrocenyl ligand **L4**, which is shown in **Figure S18** of the appendix.

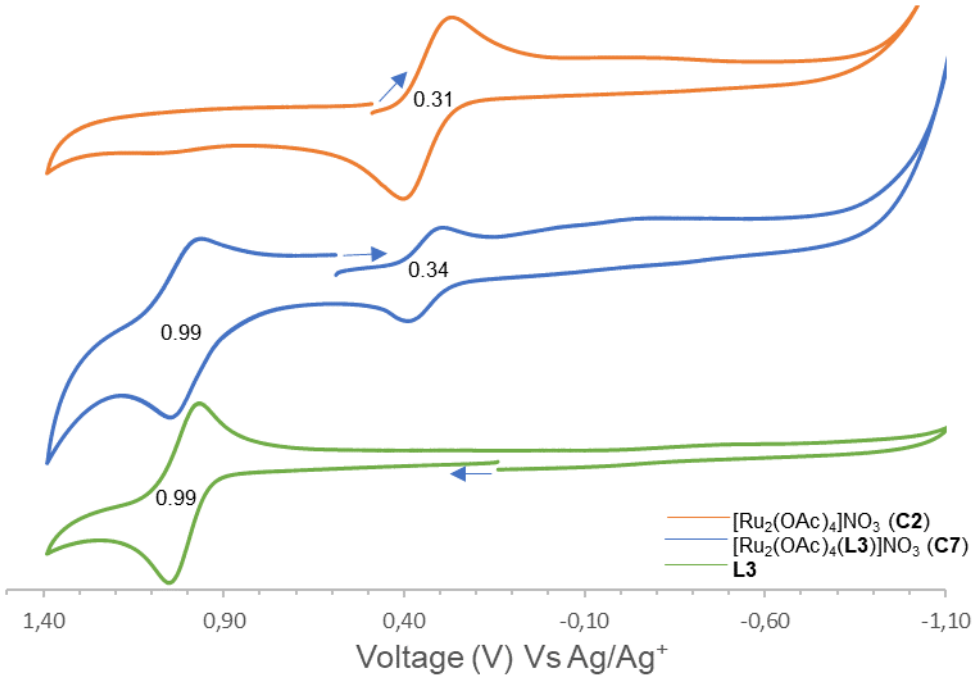


**Figure 2.38.** Cyclic voltammograms showing the electrochemical processes of the complexes $[Ru_2(OAc)_4]NO_3$, $[Ru_2(OAc)_4(\mathbf{L3})]NO_3$ and the Ligand **L3,** obtained in a methanol solution containing 0.10 M TBACl. The scan rate is 100 mV/s.

## 2.5 Synthesis and characterisation of imidazopyridine diruthenium tetraacetate complexes with $PF_6^-$ counterions $[Ru_2(OAc)_4L]PF_6$ (C9 – C12)

The complexes **C9** – **C12** were synthesised following the same procedure followed for the synthesis of **C5** – **C8**. The procedure for the synthesis of **C9** is shown in **Figure 2.15** as a representative, which shows the reaction of an excess of the ligand **L1** with the precursor complex **C3** containing a $PF_6^-$ counterion. The complexes were isolated as brown powder-like microcrystals at good yields (75 – 83%) using the same purification techniques followed for complexes **C5** – **C8** and were successfully characterised using the same analytical techniques.

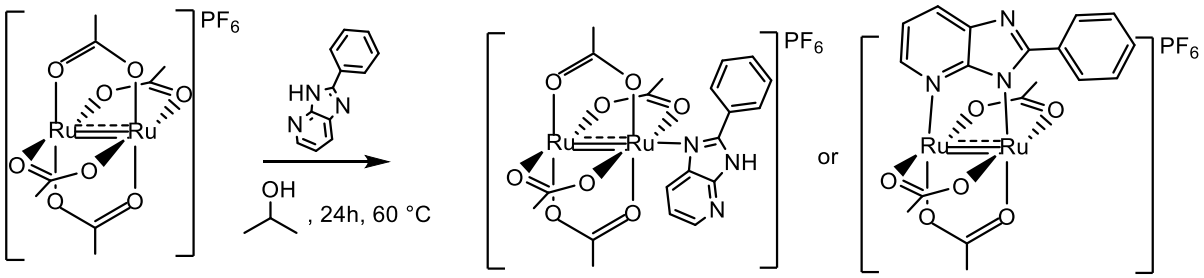


**Scheme 2. 15.** The synthesis procedure and possible structures of complex **C9** using the precursor complex **C3** and excess of the ligand **L1**.

### 2.5.1 *Infrared spectroscopy*

The Infrared spectrum of complex **C9** containing the ligand **L1** and a $PF_6^-$ counterion shows two sharp distinctive bands assigned to the $\nu(COO^-)$ stretching vibrations, as seen in **Figure 2.39**. These bands were observed on the same spectral range as those of the precursor complexes **C1** and **C3**. The presence of the asymmetric and symmetric $\nu(COO^-)$ bands confirmed the retainment of the acetate groups in the product, indicating a $D_4h$ symmetry retention upon ligand complexation. The similarity in the values of the stretching frequency of the symmetric and antisymmetric bands has been attributed to the high symmetry of the resulting acetate bridged complexes.[20] The imine $\nu(C=N)$ band of the imidazole ring of the ligand occurs at the same spectral range as that of **C5** (1540 $cm^{-1}$) and shifting in the stretching frequency of the pyridine imine $\nu(C=N)$ band (1604 $cm^{-1}$) in the complex occurs. The presence of a $PF_6^-$ counterion in the complex is shown by presence of the imine $\nu(PF_6^-)$ stretch around 841 $cm^{-1}$.

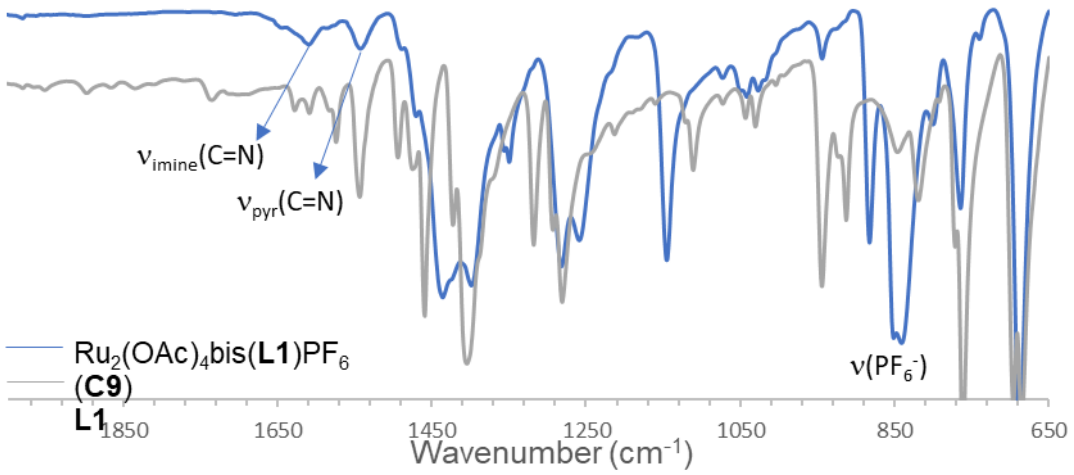


**Figure 2.39.** An expanded view of the infrared spectrum of complex **C9**, overlaid with the spectrum of **L1**.

The stacked infrared spectra of the complexes **C10** – **C12** of the complexes occur in **Figure S19** of the appendix. The imine ν(C=N) bands of the imidazole ring occur in the range 1630 – 1550 $cm^{-1}$ in the complexes and displays a slight shifting to lower stretching frequency due to back bonding effect. The presence of a $PF_6^-$ counterion is detected in the complexes around 840 $cm^{-1}$ which shows the successful formation of complexes in an ionic form.

### 2.5.2 *UV-Vis spectroscopy*

The UV-Vis spectrum of **C9** and **C10** is shown in **Figure 2.40**, and this shows absorbance bands corresponding to the ligand centred π → π* transition with $\lambda_{max}$ centred at 310 nm. The band assigned to π(RuO, $Ru_2$) → π*$Ru_2$ transition occurs as a smaller shoulder between 418 – 431 nm as previously observed for the $NO_3^-$ bearing complexes. For **C10**, a new absorbance band occurs as a shoulder between 335 and 400 nm and this was not observed in the starting material which provided further evidence of complexation of the ligand to the metal centre. Similar results were observed for the complex **C11** and **C12** containing the ferrocenyl substituted ligands **L4** and **L3** as shown in **Figure S20** of the appendix. The shoulder band assigned to the ligand to metal π(RuO, $Ru_2$) → π*$Ru_2$ transition in the region 419 – 477 nm is overlapped with the ferrocenyl ligand to metal π → π* transition band of the ligands **L3** and **L4**. Changing the counterion from $NO_3^-$ to $PF_6^-$ did not appear to have a significant effect on the shape of the absorbance bands in the spectra, while changing from coordinated **L1** to **L2** resulted in a slight shift to a lower wavelength in the ligand centred transition band in the UV region, and this effect was also observed in the free uncoordinated ligands.

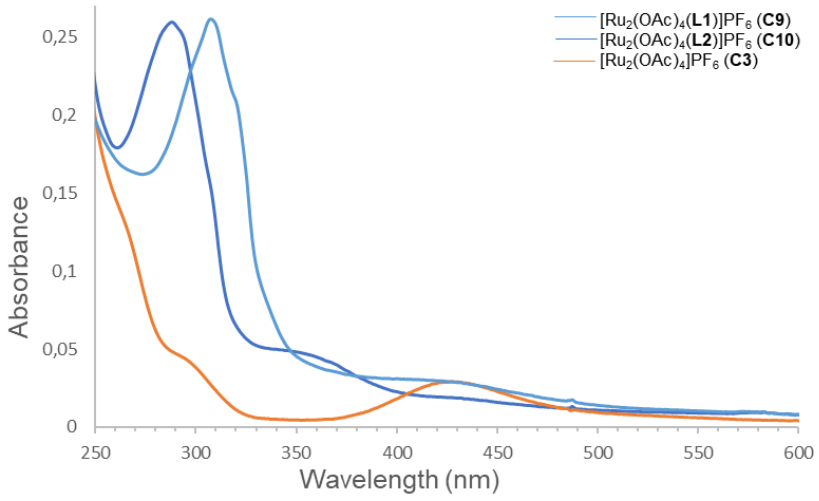


**Figure 2.40.** Overlaid UV-Vis spectra (in methanol) of the complexes **C9**, **C10** and the precursor complex **C3**.

### 2.5.3 *Electrochemistry*

A comparison of the electrochemical processes of the complexes **C9** – **C12** with those of the precursor complex **C3** was performed using cyclic voltammetry, in a solution containing 0.10 M $TBAPF_6$ as the supporting electrolyte. The $Ru_2^{5+/4+}$ reduction potentials of **C9** – **C12** follow the same trend as **C1** in the $TBAPF_6$ supporting electrolyte and were observed at more negative potentials relative to the reduction potentials in $TBANO_3$ shown in **Figure 2.30** previously. This shows that a $PF_6^-$ counterion increases the electron density on the ruthenium centres relative to the $NO_3^-$ counterion. The cyclic voltammogram of **C9** is shown in **Figure 2.41**. The $Ru_2^{5+/4+}$ reduction potential is anodically shifted by 60 mV from a potential of -0.76 V in **C3** to a potential of -0.70 V in the complex **C9**. This shift implies that there is a decreased electron density on the ruthenium centres upon coordination of the ligand **L1**, relative to the precursor complex **C3**, making it easier to reduce the metal centre. Complex **C10** containing the ligand **L2** displays a reversible reduction potential which is not significantly different from that of **C3** upon coordination of the ligand **L2,** and this is shown in **Figure S21** of the appendix.

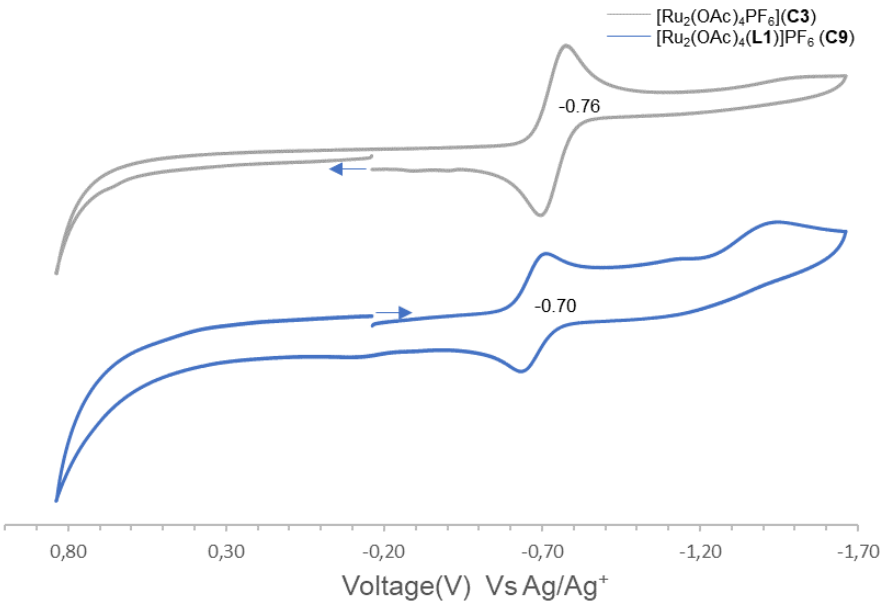


**Figure 2.41.** Cyclic voltammograms of the complexes $[Ru_2(OAc)_4]PF_6$ and $[Ru_2(OAc)_4$ (**L1**)$]PF_6$, obtained in a methanol solution containing 0.10 M $TBAPF_6$ at a scan rate of 100 mV/s.

Complex **C3** shows a $Ru_2^{5+/4+}$ reduction process of -0.76 V, which is slightly shifted in the anodic region by 10 mV to a potential of -0.75 V in the complex **C11**, as shown in **Figure 2.42**. This shift is slightly cathodic, relative to that observed for the complex **C7** bearing an $NO_3^-$ counterion, and this is attributed to the $PF_6^-$ counterion making it slightly difficult to reduce the

metal centre. A shift in the reduction process upon coordination of **L3** shows that the presence of the ligand significantly affects the electronic properties of the ruthenium cores, and further provides further evidence of ligand coordination. The ferrocene ($Fc/Fc^+$) oxidation potential of the phenyl complex **C11** indicates a single electron transfer process as shown by the similar ratios of the reduction and oxidation peaks, which is contrary to what has been observed for **C7** and **C8** which showed two electron transfer processes. This is indicative of the presence of one ligand **L3** in the complex **C11**. The oxidation potential of **L3** displays a cathodic shift of 60 mV to a new potential of -0.11 V in the complex **C11**, which shows that there is an increased electron density on **L3** upon complexation to form **C11**. The cyclic voltammogram of **C12** is shown in **Figure S22** of the appendix this shows a reversible two-electron transfer ($Fc/Fc^+$ oxidation process) and a $Ru_2^{5+/4+}$ reduction process which is shifted by 20 mV towards the anode in the complex.

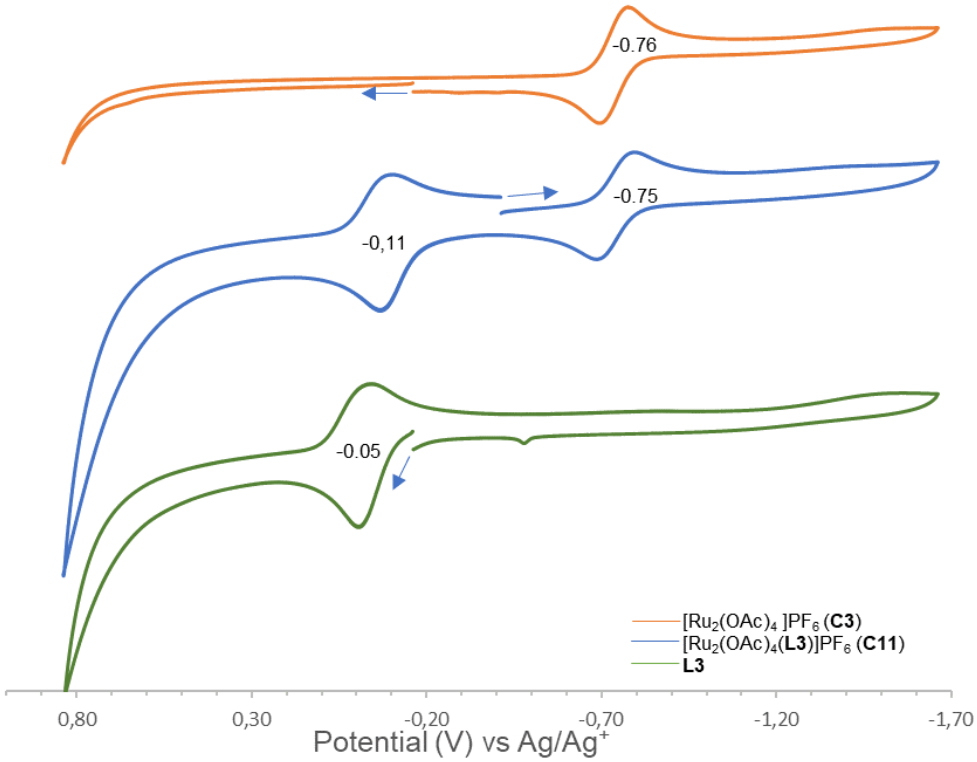


**Figure 2.42.** Stacked cyclic voltammograms of the complexes $[Ru_2(OAc)_4]PF_6$ (**C3**), $[Ru_2(OAc)_4$**L3**$]PF_6$(**C11**) and the ligand **L3**. Voltammograms obtained in a methanol solution containing 0.10 M $TBAPF_6$ at a scan rate of 100 mV/s.

The cyclic voltammograms of ligands **L3** and **L4** show that under the same solvent and electrolyte conditions the oxidation potential of **L3** is slightly shifted by 0.10 V in the anodic direction, showing that it was more difficult to oxidise **L3** than **L4**. The shape of the oxidation

peak of **L4** is also clearly well reversible, whereas the anodic potential of **L3** exhibits a slight cathodic shift which altered the shape of the duck shape curve.

## 2.6 Synthesis and characterisation of imidazopyridine diruthenium tetraacetate complexes with $BF_4$ counterions (C13)

A complex containing a $BF_4^-$ counterion (**C13**) was also synthesised and compared with those bearing $NO_3^-$ and $PF_6^-$ counterions. The reaction between an excess amount of the ligand **L3** with the precursor complex $[Ru_2(OAc)_4(THF)_2]BF_4$ (**C4**) was performed at room temperature to synthesise the complex **C13**, which was isolated as a brown solid and fully characterised using the same analytical techniques used for **C5** – **C12**. The complex **C13** displays similar absorption properties to those of **C5** – **C12** using FTIR as shown in **Figure 2.43**. The presence of the $BF_4^-$ counterion is confirmed by the strong absorbance bands between 1100 – 1000 $cm^{-1}$. Displacement of the coordinated THF of the precursor complex **C4** is shown by the absence of the ν(C-O) and ν(C-H) bands of the THF solvent around 3000 $cm^{-1}$.

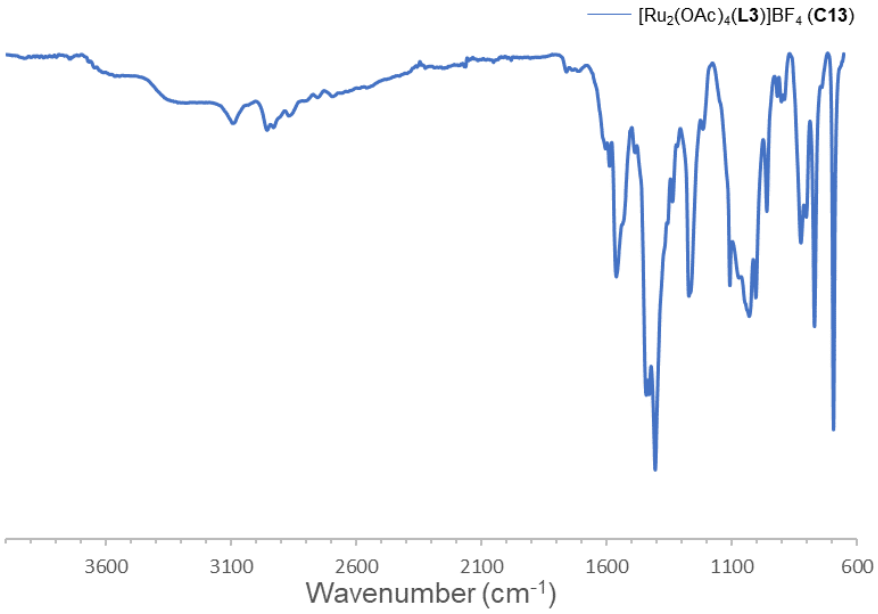


**Figure 2.43.** Infrared spectrum of the $BF_4^-$ complex **C13**.

The complex was analysed using cyclic voltammetry in a solution containing 0.10 M of $TBABF_4$ as a supporting electrolyte and displays a reversible reduction ($Ru_2^{5+/4+}$) process that is not significantly shifted from that of the precursor complex **C4**. This is shown by the spectrum attached in **Figure S23** of the appendix. Complex **C13** also displays a reversible oxidation peak that is shifted towards the cathode by 70 mV relative to the potential of -0.20 V observed for the ligand **L3**.

The difference in the stretching frequency values (Δexp) of the acetate bands ν(OCO$^-$) was compared between the complexes **C5** – **C13** and this is summarised in **Table 2.3**. The difference in the values remained constant from **C5** to **C13** which shows evidence of retainment in the symmetry of the complexes upon ligand coordination to the ruthenium bimetalic centres.

**Table 2.3** Comparison of the symmetric and asymmetric stretching bands of acetate groups for the complexes **C5** – **C13**.

| Complex | Chemical formula | $\nu_{asym}$(OCO$^-$) [cm$^{-1}$] | $\nu_{sym}$(OCO$^-$) [cm$^{-1}$] | Δexp [cm$^{-1}$] |
|---|---|---|---|---|
| **C5** | $[Ru_2(OAc)_4(\mathbf{L1})]NO_3$ | 1436 | 1400 | 36 |
| **C6** | $[Ru_2(OAc)_4(\mathbf{L1})]PF_6$ | 1436 | 1394 | 42 |
| **C7** | $[Ru_2(OAc)_4(\mathbf{L2})]NO_3$ | 1449 | 1402 | 39 |
| **C8** | $[Ru_2(OAc)_4(\mathbf{L2})]PF_6$ | 1433 | 1395 | 38 |
| **C9** | $[Ru_2(OAc)_4(\mathbf{L3})]NO_3$ | 1428 | 1393 | 35 |
| **C10** | $[Ru_2(OAc)_4(\mathbf{L3})]PF_6$ | 1436 | 1396 | 40 |
| **C11** | $[Ru_2(OAc)_4(\mathbf{L4})]NO_3$ | 1440 | 1403 | 37 |
| **C12** | $[Ru_2(OAc)_4(\mathbf{L4})]PF_6$ | 1440 | 1405 | 35 |
| **C13** | $[Ru_2(OAC)_4(\mathbf{L4})]BF_4$ | 1439 | 1404 | 35 |

A summary of the UV-vis data for the complexes obtained in methanol is shown in **Table 2.4**. The table compares the different spectral properties observed between the synthesised complexes and the absorbance properties of the free ligands. In general, the position of the ligand centred band in the UV region of the spectrum was only slightly shifted by a small amount in comparison to the coordinated ligand. Band II was observed as a shoulder in some complexes bearing the ferrocenyl or phenyl substituted ligand, and this could not be assigned based on only the experimental studies conducted so far.

**Table 2.4.** Summary of the position of the absorbance bands for the synthesised complexes **C13** – **C14**. Band II and III occurred as shoulders that are greatly reduced or completely absent in some complexes.

| | $\lambda_{max}$, nm (ε x $10^{-3}$, $M^{-1}$ $cm^{-1}$) | | | |
|---|---|---|---|---|
| **Complex** | **Band I (Ligand)** | **Band I (complex)** | **Band II (Shoulder)** | **Band III (Shoulder)** |
| **C5** | 310 | 310 | - | 433 |
| **C6** | 310 | 310 | - | 423 |
| **C7** | 280 | 307 | 385 | 426 |
| **C8** | 280 | 320 | 351 | 424 |
| **C9** | 311 | 320 | - | 440 |
| **C10** | 311 | 316 | 374 | - |
| **C11** | 297 | 301 | 362 | 455 |
| **C12** | 297 | 315 | 366 | 440 |
| **C13** | 314 | 311 | 426 | 431 |

Cyclic voltammetry allowed for comparison of the electrochemical properties of the complexes in different solutions. **Table 2.5** compares the half wave potentials as well as the cathodic and anodic peak currents for the reduction process of the isolated complexes **C5** – **C13**. The ratio of the cathodic and anodic current peaks ($I_{pc}/I_{pa}$) of unity was calculated and found to be closer to unity in all the complexes, which confirmed the reversibility of the reduction peaks. A comparison of the cathodic and anodic potentials for complexes is also presented in the table. The slight anodic shift observed in the $Ru_2^{5+/4+}$ reduction was accounted for by $\pi$-back bonding between the ligand and the diruthenium metal core as previously described for diruthenium acetate complexes. This effect of back bonding can either result in an increase or decrease in the stabilization of the $Ru_2^{4+}$ oxidation state of the complexes.

**Table 2.5.** Summary of the electrochemical potentials ($Ru_2^{5+/4+}$) for complexes **C5** – **C13** in methanol

| Metal Complex | | Potential (V) vs. $Ag/Ag^+$ | | | $I_{pc}/I_{pa}$ |
|---|---|---|---|---|---|
| | | $E_{Pc}$ | $E_{Pa}$ | $E_{1/2}$ | |
| **C5** | $[Ru_2(OAc)_4(\mathbf{L1})]NO_3$ | 0.23 | 0.41 | 0.32 | 0.92 |
| **C7** | $[Ru_2(OAc)_4(\mathbf{L3})_2]NO_3$ | 0.28 | 0.38 | 0.34 | 1.45 |
| **C8** | $[Ru_2(OAc)_4(\mathbf{L4})_2]NO_3$ | 0.22 | 0.40 | 0.31 | 1.26 |
| **C9** | $[Ru_2(OAc)_4(\mathbf{L1})]PF_6$ | -0.75 | -0.65 | -0,70 | 1.05 |
| **C10** | $[Ru_2(OAc)_4(\mathbf{L2})]PF_6$ | -0.81 | -0.70 | -0.76 | 1.04 |
| **C11** | $[Ru_2(OAc)_4(\mathbf{L3})]PF_6$ | -0.80 | -0.72 | -0.78 | 1.15 |
| **C12** | $[Ru_2(OAc)_4(\mathbf{L4})_2]PF_6$ | -0.82 | -0.72 | -0.77 | 1.01 |
| **C13** | $[Ru_2(OAc)_4(\mathbf{L3})]BF_4$ | -0.80 | -0.69 | -0.77 | 1.42 |

## 2.7 $^1$H NMR spectroscopy

Due to the paramagnetic nature of the synthesised complexes **C1** – **C13**, the Evan's method for calculating the number of unpaired electrons was used to characterise the complexes and determine if they retain their paramagnetic electronic configuration upon ligand complexation. The magnetic susceptibility measurements of the precursor complexes **C2** – **C4** was calculated at room temperature in solution and compared with that of the imidazopyridine diruthenium tetraacetate complexes **C5**, **C7**, and **C10**. A comparison of the shifts observed between the deuterated solvent signals was performed in the presence and absence of the paramagnetic sample (**C5**) and the overlaid spectra is shown in **Figure 2.44**. The $^1$H NMR spectrum of the precursor complex **C2** is shown in **Figure S24** the appendix while that of the complex **C7** occurs in **Figure S25** of the appendix. It was observed that the signals of the reference sample were shielded from the magnetic field by the paramagnetic compound and shifted to a higher field.

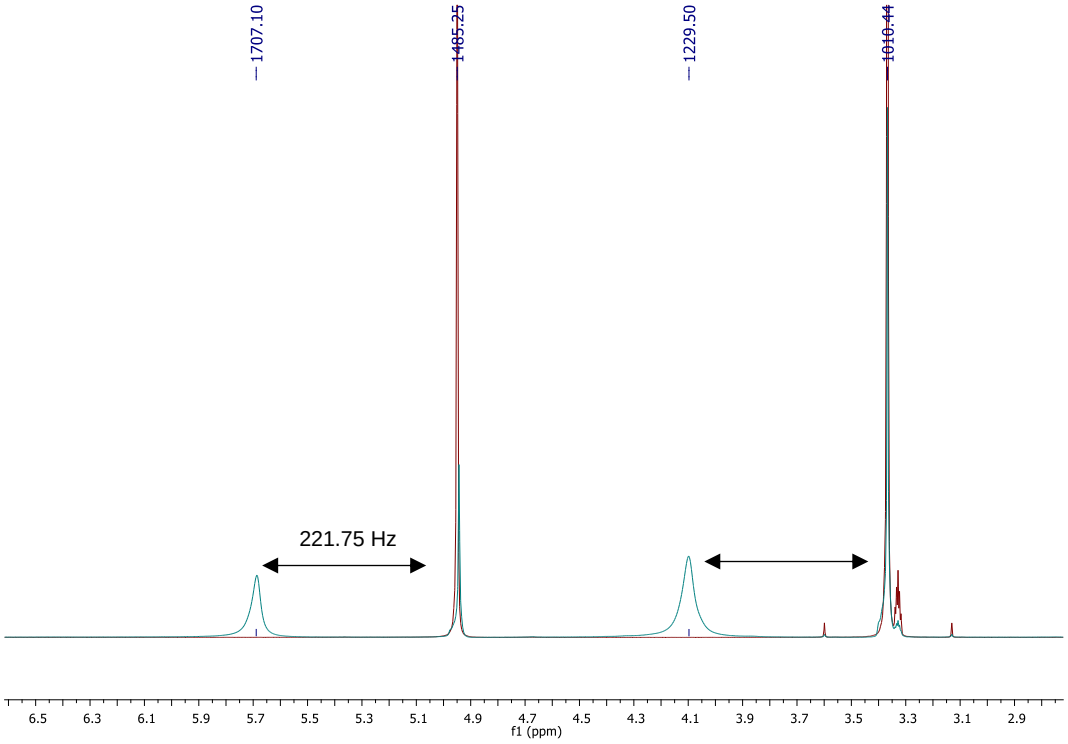


**Figure 2.44.** Evan's method: Determination of unpaired electrons. Stacked $^{1}$H NMR spectra of a 50:1 MeOD: MeOH mixture (red) and in the paramagnetic complex **5** (cyan blue).

Results showed that the change in counterions $NO_3^-$, $PF_6^-$ and $BF_4^-$ had little effect on the shift of the solvent due to the paramagnetic solvent. The measurements gave magnetic moment values ranging from 3.36 – 4.20 BM which indicated the presence of three unpaired electrons in the ground state with a spin moment S = 3/2. This evidence obtained provided a vital interpretation that the complexes are three electron paramagnetic and exhibit low-spin paramagnetism as previously reported for mixed valent diruthenium complexes with $Ru_2$ (II, III).[39] This indicated that there was no change in the electron configuration of the ground state $\sigma^2\pi^4\delta^2(\delta^*\pi^*)^3$ in the complex and there was little effect of ligand coordination on the population of the $\delta^*$ and $\pi^*$ orbitals of the metal centre.[41]

## 2.8 Mass spectrometry

The complexes **C5** – **C13** were analysed by high resolution ESI mass spectrometry (HRMS) in the positive ion mode to detect and identify the masses of the products of interest. Mass spectra provided vital evidence on elucidating the structures of the complexes and the spectra of the complexes showed similar fragmentation patterns. Mass spectra showed the presence of peaks corresponding to complexes coordinated by one ligand for the complexes with $PF_6^-$ counterions (**C9, C10** and **C11**) while evidence for bis-ligated complexes was observed for the

remaining complexes. The isotopic signatures indicating the bis-substituted complexes $[M]^+$ for the phenyl and ferrocenyl substituted ligands occurred at m/z = 830.0210 – 830.0237 and 1044.9613 – 1047.9559, respectively. This evidence for a bis-ligated complex supported the observations on the cyclic voltammograms for the complexes with ferrocenyl ligands **C7** and **C8** where the voltammograms showed a two-electron transfer process on the ferrocene rings, indicating the presence of two ligands coordinating to the metal centres. Mass spectroscopy showed fragmentation of the complexes with the presence of a peak $[M\text{-}\mathbf{L}]^+$ appearing at m/z = 634.94 – 634.95 and m/z = 741.12 – 742.91 for the complexes with phenyl and ferrocenyl substituted ligands, respectively. A representative mass spectrum of complex **C8** showing the peak at 1045.9595 corresponding to a bis-coordinated complex is shown in **Figure 2. 45**, where two ligands coordinate axially to the ruthenium centres. Mass spectra of the other complexes are attached in **Figure S26** –**Figure S33** of the appendix. The experimental values are consistent with the calculated isotopic distributions as summarised for the $[M\text{-}\mathbf{L}]^+$ peak shown in **Table 2.6**.

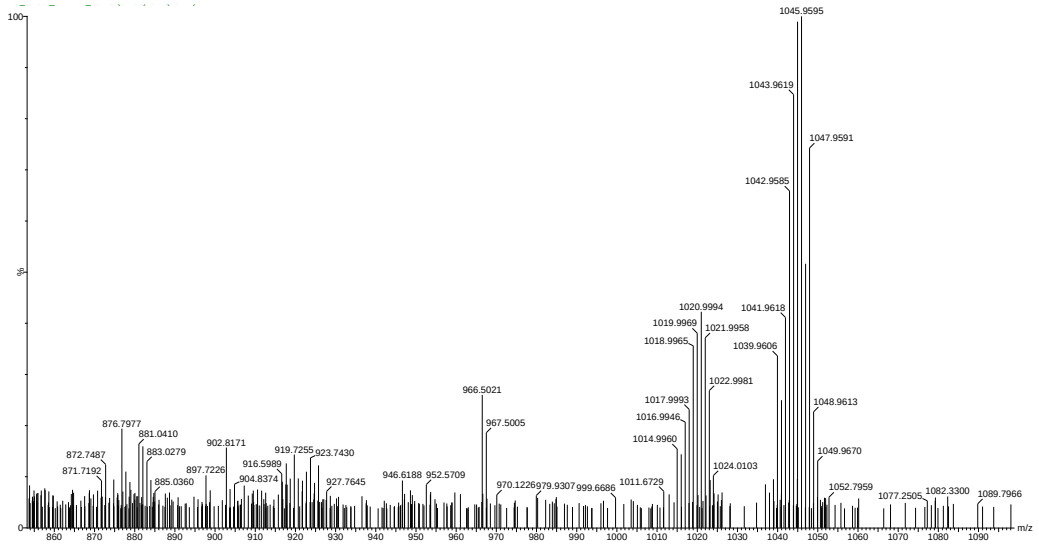


**Figure 2. 45.** Representative mass spectrum of complex **C8**, showing the $[M]^+$ fragmentation peak.

The base peak with 100% abundance at m/z 438.86 is assigned to $[M\text{-}2\mathbf{L}]^+$ corresponding to the diruthenium tetraacetate complex with fragmentation of the coordinated ligands. A peak at m/z of 516.17 was observed in the precursor complexes **C2**, **C3** and **C4** as well as the resulting complexes **C5** – **C13** and was due to solvent coordination.

**Table 2.6.** Comparison of the observed and calculated ESI-TOF masses of the synthesised complexes.

| Complex | Calculated mass $[M-L]^+$ | Observed mass $[M-L]^+$ | Observed mass $[L]^+$ |
|---|---|---|---|
| **C5** | 634.14 | 634.9459 | - |
| **C6** | 634.14 | 634.9454 | - |
| **C7** | 743.18 | 742.9104 | 304.0540 |
| **C8** | 743.18 | 741.1271 | 304.0537 |
| **C9** | 634.14 | 634.9434 | - |
| **C10** | 634.14 | 633.9440 | 196.0871 |
| **C11** | 744.05 | 742.9097 | 304.0539 |
| **C12** | 744.05 | 741.9117 | - |
| **C13** | 744.05 | 741.9091 | - |

## 2.9 Elemental analysis and Structure elucidation

Elemental analysis was used to confirm the successful synthesis of the desired complexes and compare with the mass spectrometry and cyclic voltammetry results. For the complexes with $NO_3^-$ counterions (**C6** to **C8**) elemental analysis showed evidence for the formation of 1:2 bis-ligated complexes and for the $PF_6^-$ derivative complexes (**C9** to **C11**), evidence for mono-ligated complexes was observed. These results agreed with the mass spectroscopy result and the electron transfer processes observed on the cyclic voltammograms of these complexes. Results agreed with the expected percentage of hydrogen and nitrogen for all the complexes (error approx. 1%). However, the percentage of carbon was found to be slightly higher or lower in some complexes, with a % carbon error of approx. 3% and this was attributed to the ability of the complexes to polymerize using the extra free nitrogen on the pyridine ring as previously observed for diruthenium complexes bridged by nitrogen-based ligands.[43] The ability of the complexes to exist as polymers can prevent the complete combustion of carbon during elemental analysis, thus causing the deviation in the observed amount of carbon. There was also possible reversible binding of the imidazole nitrogen atom on the ruthenium atom as previously observed by Rodrigo and co-workers upon coordination of amino acids to diruthenium centres,[28] which can also contribute to the observed deviation in the amount of carbon in the sample.

The formation of mono or bis-ligated complexes was rationalised in terms of the general trend in the coordination ability of counterions to the ruthenium metal centres, which is in the order

$NO_3^-$ > $PF_6^-$ > $BF_4^-$.[43] While the $NO_3^-$ counterion is more coordinating, the negative charge on the $NO_3^-$ is localised between the NO bonds and stabilised through resonance effect which decreases the charge available for the ruthenium metal centres, limits the iron pairing with the metal cation and makes the counterion more labile than the $PF_6^-$ and $BF_4^-$ counterions. Thus, in the presence of the $NO_3^-$ counterion, it can be inferred that more vacant space is available on the axial position of the metal centres which favours the accommodation of two coordinating ligands, such that bis-ligated complexes are formed. In the presence of the $PF_6^-$ and $BF_4^-$ counterions, the lack of resonance stabilisation of the negative charge and the bigger size of the counterions relative to the $NO_3^-$ counterion result in more interaction of the $PF_6^-$ and $BF_4^-$ counterions with the metal centres and the coordinating ligands, and this allows for the accommodation of one ligand. Presence of bis-ligated complexes and mono-ligated complexes for $NO_3^-$, $PF_6^-$ and $BF_4^-$ counterions was previously confirmed by the $Fc/Fc^+$ couples on the cyclic voltammograms of the complexes and this agrees with mass spectrometry and elemental analysis results.

### 2.10 Evaluation of complex stability by UV-Vis spectroscopy

The stability of the complexes **C5** – **C13** was evaluated at 24 h intervals in DMSO over a period of 72 h at room temperature. The complexes display stable absorbance bands in the UV region which are assigned to the ligand-centred $\pi \rightarrow \pi^*$ transitions as previously observed in methanol. All the complexes remained stable in solution with no new significant absorbance bands detected, however absorbance fluctuations occurred in some complexes which was attributed to a slight change in concentration due to interaction with the DMSO solvent. A representative UV-Vis spectrum of the complex **C5** is shown in **Figure 2. 45**, while the spectra obtained for the other complexes is shown in **Figure S34** –**Figure S40** of the appendix. The complexes **C5** and **C6** display an absorbance band in the visible region at ca. 452 and 444 nm, respectively. This band remained constant over the period of analysis and was assigned to the ligand to metal $\pi \rightarrow \pi^*$ transition. For complexes **C7** – **C13**, the $\pi \rightarrow \pi^*$ transition band exhibited fluctuations overtime which was likely due to dissociation of the ligand as well as microscopic precipitation of the compounds.

The results obtained in the study provided sufficient evidence that the complexes may not be undergoing significant solvation and were quite stable. Additionally, some of the complexes such as **C5**, **C7** and **C10** may precipitate at the microscopic level even though this is not visibly observed, resulting in the absorbance fluctuations observed in the solvent.

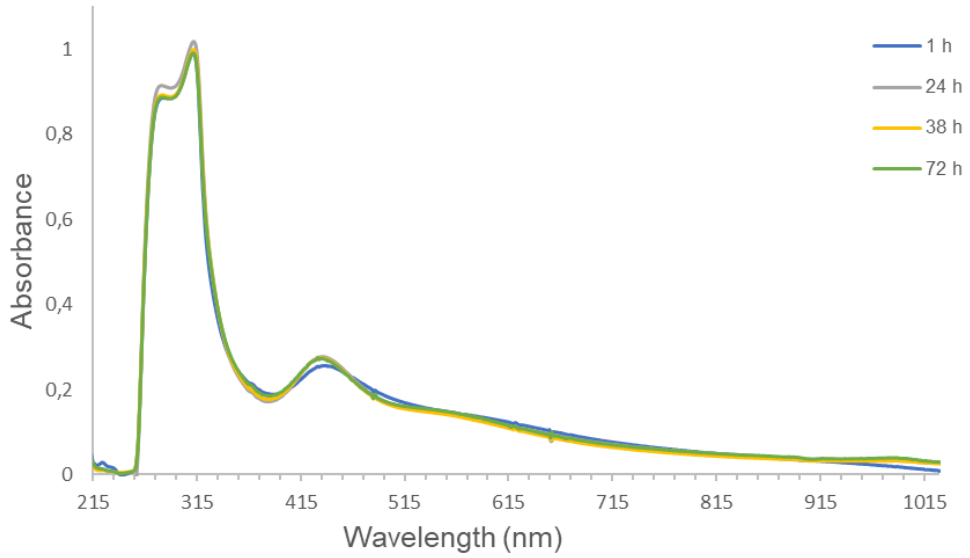


**Figure 2.46.** UV-Vis spectrum of $[Ru_2(OAc)_4(\mathbf{L1})]NO_3$(**C5**) obtained in DMSO, at different time periods.

The same observation on stability is seen for the complexes **C5** – **C13** regardless of the counterions coordinated to the complexes or the type of substituent present on the imidazopyridine ligands. No changes were observed for the higher energy absorbance bands centred in the UV region between 250 and 300 nm and no significant new absorbance bands were observed for the complexes, providing evidence of good complex stability in the DMSO solvent.

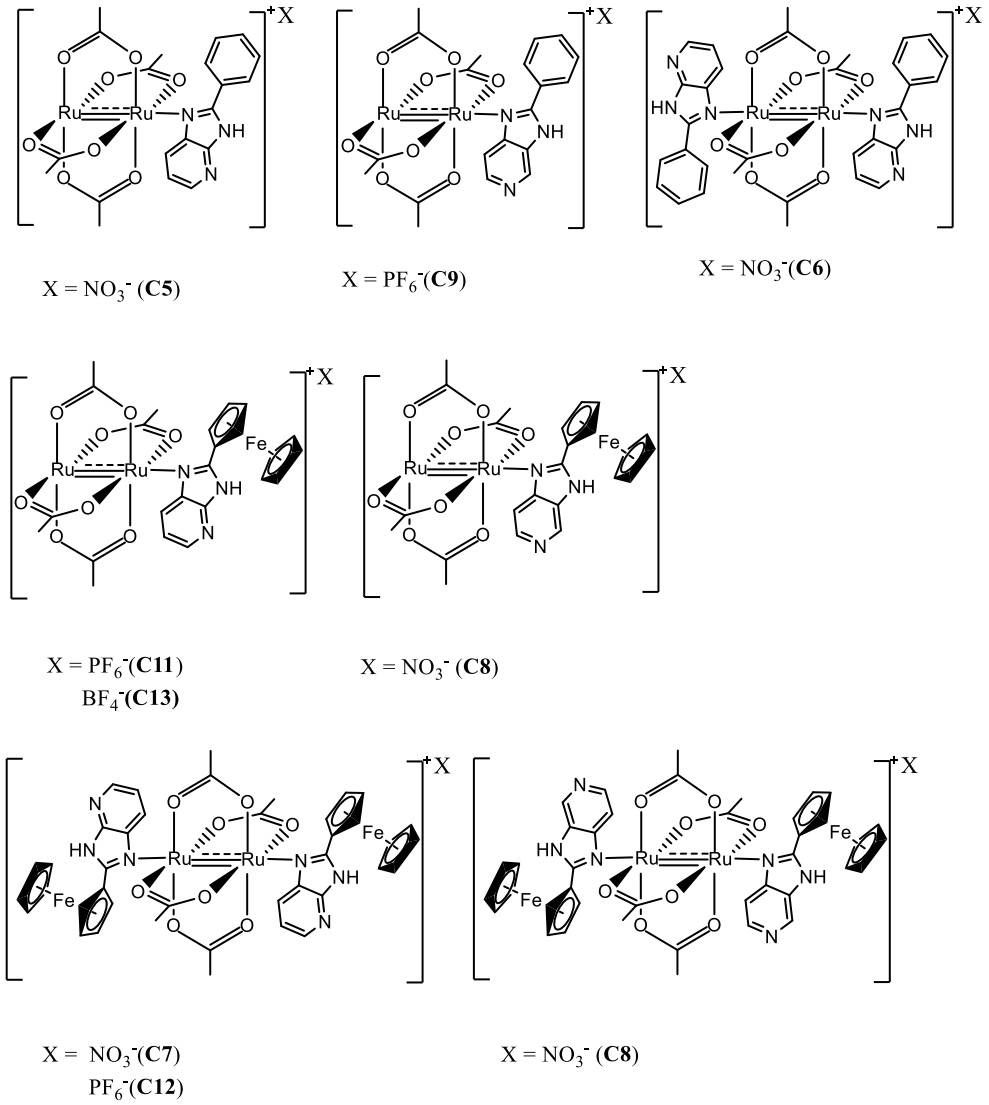


**Figure 2. 47.** Proposed structures of imidazopyridine diruthenium acetate complexes (**C5** - **C13**) synthesised

### 2.11 Summary and conclusions

Imidazopyridine ligands substituted with phenyl, ferrocenyl and propyl moieties (**L1** – **L5**) have been successfully synthesised and characterised by using an array of analytical techniques such as $^{1}H$ and $^{13}C$ NMR, UV-Vis, Infrared spectroscopy, cyclic voltammetry as well as LCMS. Assignments of the ligands were also confirmed by using 2D NMR spectroscopy such as COSY and HSQC.

Ligands **L1** – **L4** were successfully complexed to the precursor diruthenium acetate complexes (**C1** – **C4**) to synthesise complexes of diruthenium tetraacetate (**C5** – **C13**) which were isolated at sufficiently good yields (65 – 83%). The ligands can coordinate to ruthenium metals axially in mono-ligated or bis-ligated fashion, depending on the type of counterions present on the complex. The successful synthesis of the complexes was confirmed using suitable analytical

techniques such as FTIR and UV-Vis spectroscopy, mass spectrometry, cyclic voltammetry, and elemental analysis. CV shows the presence of a single $Ru^{5+/4+}$ reduction process, and an $Fe/Fe^{+}$ oxidation for complexes with ferrocene ligands, which is shifted from that of the free ligand. The complexes displayed good stability in DMSO when evaluated over a period of 72h at room temperature. No suitable single crystals of the novel complexes could be obtained to ascertain the nature, number of ligands and mode of ligand coordination to the metal centres, however the analytical techniques employed support the formation of the desired complexes.

## 2.12 References


1. Mamedov, V., Recent Advances in the Synthesis of Benzimidazol(on)es via Rearrangements of Quinoxalin(on)es. *RSC Adv.* **2016,** 42132-42172.
2. O'Shea, D. Synthesis, Characterisation and Biological Activity of Novel Carboxylate Complexes Incorporating Phenanthroline and Benzimidazole Ligands Technological University Dublin, Dublin 2004.
3. Poor Heravi, M. R., Boric Acid Catalyzed Convenient Synthesis of Benzimidazoles in Aqueous Media. *J. Chem.* **2013,** *2013*.
4. Herrera Cano, N.; Uranga, J. G.; Nardi, M.; Procopio, A.; Wunderlin, D. A.; Santiago, A. N., Selective and eco-friendly procedures for the synthesis of benzimidazole derivatives. The role of the Er(OTf)(3) catalyst in the reaction selectivity. *Beilstein J. Org. Chem.* **2016,** *12*, 2410-2419.
5. Kantharaju, K., Synthesis and Pharmacological Profile of Benzimidazoles. In *Chemistry and Applications of Benzimidazole and its Derivatives*, IntechOpen: 2019.
6. Bashir, D., Ultrasound promoted expeditious, catalyst free and solvent free approach for the synthesis of N,N'-diarylsubstituted formamidines at room temperature. *Tetrahedron Lett.* **2013**.
7. Wegner E. C., M. W. H., Benzimidazole. *Org. Syn. Coll.* **1939,** *2* (501), 19.
8. Grieco, G.; Blacque, O.; Berke, H., A facile synthetic route to benzimidazolium salts bearing bulky aromatic N-substituents. *Beilstein J. Org. Chem.* **2015,** *11*, 1656-1666.
9. Bland, B. R. A.; Gilfoy, H. J.; Vamvounis, G.; Robertson, K. N.; Cameron, T. S.; Aquino, M. A. S., Hydrogen bonding in diruthenium(II,III) tetraacetate complexes with biologically relevant axial ligands. *Inorganica. Chimica. Acta.* **2005,** *358* (13), 3927-3936.
10. Gangopadhyay, S.; Gangopadhyay, P. K., Adenine and adenosine derivatives of tetraacetatodiruthenium (II,III) cation. *J. Inorg. Biochem.* **1997,** *66* (3), 175-178.
11. Zapata, F.; Caballero, A.; Espinosa, A.; Tárraga, A.; Molina, P., Imidazole-Annelated Ferrocene Derivatives as Highly Selective and Sensitive Multichannel Chemical Probes for Pb(II) Cations. *Inorg. Chem.* **2009,** *74* (13), 4787-4796.
12. Heidarnezhad, Z.; Vahedpour, M.; Razavizadeh, A., A theoretical DFT study on the stability of imidazopyridine and its derivatives considering the solvent effects and NBO analysis. *Izvestiya po Khimiya Bulgarska Akademiya na Naukite* **2015,** *47*.
13. Barraclough, P. L., J.C .; Nobbs, M.S .; Williams, J.M., 13C NMR Studies of Tautomerism in Imidazo [ 4,5=c]pyridines. *Magn. Reson. Chem.* **1989,** *27*, 992-994.
14. Püsküllü, M.; Karaaslan, C.; Bakar Ates, F.; Goker, H., Synthesis and potent cytotoxicity of some novel imidazopyridine derivatives against MCF-7 human breast adenocarcinoma cell line. *J. Heterocycl. Chem.* **2015,** *51*. 723–733

15. Elderfield, R. C.; Meyer, V. B., The Reaction of o-Phenylenediamines with Carbonyl Compounds. III. Benzophenones and Dibenzyl Ketones1. *J. Am. Chem. Soc.* **1954,** *76* (7), 1883-1887.
16. Chou, P.-T.; Wu, G.-R.; Wei, C.-Y.; Cheng, C.-C.; Chang, C.-P.; Hung, F.-T., Photoinduced Double Proton Tautomerism in 4-Azabenzimidazole. *J. Phys. Chem. B* **1999,** *103* (45), 10042-10052.
17. Barraclough, P.; Firmin, D.; Iyer, R.; King, W. R.; Lindon, J. C.; Nobbs, M. S.; Smith, S.; Wharton, C. J.; Williams, J. M., Protonation equilibria of cardiotonic polyaza heterocycles. *J. Chem. Soc., Perkin Trans.* **1988,** (10), 1839-1846.
18. Raczyńska, E. D.; Gal, J.-F.; Maria, P.-C.; Kamińska, B.; Igielska, M.; Kurpiewski, J.; Juras, W., Purine tautomeric preferences and bond-length alternation in relation with protonation-deprotonation and alkali metal cationization. *J. Mol. Model.* **2020,** *26* (5), 93.
19. Mitchell, R. W.; Spencer, A.; Wilkinson, G., Carboxylato-triphenylphosphine complexes of ruthenium, cationic triphenylphosphine complexes derived from them, and their behaviour as homogeneous hydrogenation catalysts for alkenes. *J. Chem. Soc. Dalton Trans.* **1973,** (8), 846-854.
20. Stephenson, T. A.; Wilkinson, G., New ruthenium carboxylate complexes. *J. inorg. nucl. chem.* **1966,** *28* (10), 2285-2291.
21. Aquino, M., Recent developments in the synthesis and properties of diruthenium tetracarboxylates. *Coord. Chem. Rev.* **2004,** *248*, 1025-1045.
22. Ogasawara, M.; Macgregor, S. A.; Streib, W. E.; Folting, K.; Eisenstein, O.; Caulton, K. G., Characterization and Reactivity of an Unprecedented Unsaturated Zero-Valent Ruthenium Species: Isolable, Yet Highly Reactive. *Journal of the J. Am. Chem. Soc.* **1996,** *118* (42), 10189-10199.
23. Xu, G.-L.; Jablonski, C. G.; Ren, T., Ru2(DMBA)4(BF4)2 and Ru2(DMBA)4(NO3)2: the first examples of diruthenium compounds containing BF4− and NO3− as ligands. *Inorganica Chim. Acta.* **2003,** *343*, 387-390.
24. Chisholm, M.; Christou, G.; Folting, K.; Huffman, J.; James, C.; Samuels, J.; Wesemann, J.; Woodruff, W., Solution studies of Ru-2(O(2)CR)(4)(n)+ complexes (n=0, 1; O(2)CR=octanoate, crotonate, dimethylacrylate, benzoate, p-toluate) and solid-state structures of Ru-$_2$($O_2$C-p-tolyl)$_4$($THF)_2$, [Ru-$_2$($O_2$C-p-tolyl)$_4$($THF)_2$]$^+$[$BF_4$]$^-$, and Ru-2(O2C-p-tolyl)$_4$($CH_3CN)_2$: Investigations of the axial ligation of the Ru-2 core. *Inorg. Chem.* **1996,** *35*.
25. Aquino, M., Diruthenium and Diosmium Tetracarboxylates: Synthesis, Physical Properties and Applications. *Coord. Chem. Rev.* **1998,** *170*, 141-202.

26. Leininger, S.; Olenyuk, B.; Stang, P., Self-Assembly of Discrete Cyclic Nanostructures Mediated by Transition Metals. *Chem. Rev.* **2000,** *100*, 853-908.
27. Drysdale, K. D.; Beck, E. J.; Stanley Cameron, T.; Robertson, K. N.; A.S. Aquino, M., Crystal structures and physico-chemical properties of a series of [Ru2(O2CCH3)4L2](PF6) adducts (L = H2O, DMF, DMSO). *Inorg. Chim. Acta.* **1997,** *256* (2), 243-252.
28. Santos, R. L. S. R.; van Eldik, R.; de Oliveira Silva, D., Thermodynamics of Axial Substitution and Kinetics of Reactions with Amino Acids for the Paddlewheel Complex Tetrakis(acetato)chloridodiruthenium(II,III). *Inorg. Chem.* **2012,** *51* (12), 6615-6625.
29. Castro, M. A.; Roitberg, A. E.; Cukiernik, F. D., Theoretical and Experimental Studies of Diruthenium Tetracarboxylates Structure, Spectroscopy, and Electrochemistry. *J. Org. Chem.* **2008,** *47* (11), 4682-4690.
30. Santos, R. L. S. R.; van Eldik, R.; de Oliveira Silva, D., Kinetic and mechanistic studies on reactions of diruthenium(ii,iii) with biologically relevant reducing agents. *Dalton Trans.* **2013,** *42* (48), 16796-16805.
31. Malinski, T.; Chang, D.; Feldmann, F. N.; Bear, J. L.; Kadish, K. M., Electrochemical studies of a novel ruthenium(II, III) dimer, trifluoroacetamidatoruthenium chloride (Ru2(HNOCCF3)4Cl). *Inorg. Chem.* **1983,** *22* (22), 3225-3233.
32. Van Caemelbecke, E.; Phan, T.; Osterloh, W. R.; Kadish, K. M., Electrochemistry of metal-metal bonded diruthenium complexes. *Coord. Chem. Rev.* **2021,** *434*, 213706.
33. Multiple Bonds Between Metal Atoms. F. Albert Cotton, C. A. M., Richard A. Walton, Ed. 2005.
34. Osterloh, W. R.; Galindo, G.; Yates, M. J.; Van Caemelbecke, E.; Kadish, K. M., Synthesis, Structural and Physicochemical Properties of Water-Soluble Mixed-Ligand Diruthenium Complexes Containing Anilinopyridinate Bridging Ligands. *Inorg. Chem.* **2020,** *59* (1), 584-594.
35. Seddon, E. A., Seddon, K.R, *The Chemistry of Ruthenium, Volume 19*. 1984; Vol. R. J. H. Clark.
36. Miyasaka, H.; Clérac, R.; Campos-Fernández, C. S.; Dunbar, K. R., The first crystal structure of a one-dimensional chain of linked RuII-RuII units. *J. Chem. Soc, Dalton Trans.* **2001,** (6), 858-861.
37. Vamvounis, G.; Caplan, J.; Cameron, T. S.; Robertson, K.; Aquino, M., Synthesis, structure and electrochemistry of nitrogen base adducts of tetraacetatodiruthenium(II,III): Dependence of redox potential and Ru-Ru bond length on axial ligand donor strength. *Inorganica Chim. Acta* **2000,** *304*, 87-98.

38. Evans, D. F., 400. The determination of the paramagnetic susceptibility of substances in solution by nuclear magnetic resonance. *Journal of the Chemical Society (Resumed)* **1959,** (0), 2003-2005.
39. Vasantha Kumar, B. C.; Manjunatha, K. B.; Ramakrishna, D., Ruthenium-Benzimidazole complex: Structural, optical and solvent-free catalytic studies. *Adv. Chem. Eng.* **2020,** *2*, 100010.
40. Boyd, D.; Crutchley, R.; Fanwick, P.; Ren, T., Fc-Fc Electronic Interaction through Equatorial Pathways of a Diruthenium Core. *Inorg. chem.* **2010,** *49*, 1322-4.
41. Chisholm, M. H.; Christou, G.; Folting, K.; Huffman, J. C.; James, C. A.; Samuels, J. A.; Wesemann, J. L.; Woodruff, W. H., Solution Studies of Ru2(O2CR)4n+ Complexes (n = 0, 1; O2CR = Octanoate, Crotonate, Dimethylacrylate, Benzoate, p-Toluate) and Solid-State Structures of Ru2(O2C-p-tolyl)4(THF)2, [Ru2(O2C-p-tolyl)4(THF)2]+[BF4]-, and Ru2(O2C-p-tolyl)4(CH3CN)2: Investigations of the Axial Ligation of the Ru2 Core. *Inorg. Chem.* **1996,** *35* (12), 3643-3658.
42. Fritsch, N.; Wick, C. R.; Waidmann, T.; Dral, P. O.; Tucher, J.; Heinemann, F. W.; Shubina, T. E.; Clark, T.; Burzlaff, N., Multiply Bonded Metal(II) Acetate (Rhodium, Ruthenium, and Molybdenum) Complexes with the trans-1,2-Bis(N-methylimidazol-2-yl)ethylene Ligand. *Inorg. Chem.* **2014,** *53* (23), 12305-12314.
43. Jung, O.-S.; Kim, Y.; Lee, Y.-A.; Park, K.-M.; Lee, S. S., Subtle role of polyatomic anions in molecular construction: Structures and properties of AgX bearing 2,4′-thiobis(pyridine) (X- = $NO_3^-$, $BF_4^-$, $ClO_4^-$, $PF_6^-$, $CF_3CO_2^-$, and $CF_3SO_3^-$). *Inorg. chem.* **2003,** *42*, 844-850.

# Chapter 3: Biological evaluation of imidazopyridine ligands and diruthenium tetraacetate complexes

## 3.1 Diruthenium complexes and imidazopyridine ligands in anticancer studies

Breast cancer exhibits poor prognosis and high relapse rates following chemotherapy interventions, thus it is important to develop anticancer agents which have the ability to inhibit breast cancer and on one hand, to be able to minimize the side-effects.[1] Diruthenium acetate complexes have demonstrated the ability to attack tumour cells and have the potential to be developed into anticancer agents.[2] These multinuclear complexes have also displayed the ability to interact with DNA, cleave the DNA and reduce cytotoxicity relative to the platinum derivatives.[3,4] Their limited solubility in water and organic solvents like DMSO limit the biological studies of the complexes and various strategies have been employed to try improving their solubility in aqueous media. The potential of diruthenium complexes to access a variety of redox active states plays a role in influencing the interaction with biologically reducing agents in the cells.

The anticancer activity of the precursor complex $Ru_2(OAc)_4Cl$ has not been evaluated in DMSO solvent due to the poorly soluble nature of the complex and precipitation in aqueous solution. However, derivatives of the complexes have since been developed that improved the anticancer activity through synergistic means. Studies by Silva and co-workers presented the synthesis of complexes bearing the non-steroidal anti-inflammatory drugs such as ibuprofen and naproxen on the equatorial position of diruthenium tetraacetate.[3,5] The results showed that coordination of the ligands to the mixed valent structures led to a synergistic effect that slightly lowered the cell viability against the C6 rat glioblastoma cell lines both *in vivo* and *in vitro*. Cell viability of the naproxen free ligand was 82.7% and this was decreased by 10.6% to a cell viability of 72.1% in the complex $[Ru_2(npx)_4(H_2O)_2]PF_6$ after 24h, which was only minor improvement in anticancer activity. Uncoordinated ibuprofen showed cell viability of 94.2%, and upon complexation to form $Ru_2(ibp)_4Cl$ the cell viability was decreased by 16.8 to a viability of 77.4%. This study showed only a slight improvement in the anticancer activity which was not significantly changed from that of the ligand, indicating further need for exploration of other ligands such as benzimidazoles that can bridge or coordinate to diruthenium tetraacetate and improve the activity. Barressi et al.[2], recently reported on the synthesis of diruthenium acetate complexes bearing isomers of indolylglyoxylyl dipeptide ligands. Equatorial coordination of one isomer to the diruthenium complex improved the efficacy against glioblastoma cell lines relative to the free uncoordinated ligands, with an $IC_{50}$ value in the μM range (1.58 ± 0.14 μM).[2] Coordination using the other isomer of the same ligand resulted in a complex that was

completely inactive. Studies on the physiological properties of water soluble diruthenium acetate complexes bridged by anilinopyridinate ligands has also been reported by Osterloh and co-workers, and further work involving anticancer activity of these complexes by our group showed an increased activity against MCF-7 breast cancer cells.[6,7]

Imidazopyridine derivatives have been reported to display cytotoxicity against breast cancer cells through the inhibition of β-catenin signalling pathways.[8] The ligands can inhibit proliferation of breast cancer cells through cell cycle arrest and by inducing apoptosis.[9] Diruthenium tetraacetate chloride complex displays poor solubility, which limits its applicability in biological studies, hence the complexation of imidazopyridine ligands to the complex allows for the incorporation of interesting properties of the ligand which can be conferred to the resulting metal complex. Binding of the ligand to the ruthenium acetate may offer a different uptake and release mechanism of the ligand in the cells and allow the ligand to undergo ligand exchange reactions in the cells. This can leave the ruthenium complex to interact with DNA through traditional DNA-cisplatin adduct type of complex formation. Axial coordination of solvents to the diruthenium acetate can help retain properties brought about by ruthenium metal such as transferrin binding, and this can further improve the uptake of the complex through interaction with transferrin receptors. Availability of a vacant site for coordination after release of the ligand also allows for interaction with biologically active components such as glutathione (GSH) and other reducing agents, which can further promote the reduction of the metal from Ru(III). Ru(III) is biologically inactive unless it is converted by biologically reducing agents like GSH to Ru(II) which is the active form. Complexation of the ligand can help improve its solubility, which avoids the use of solubilising agents and need for conversion to salt forms to improve the solubility.

Although counterions are sometimes considered spectators in the biological activity of meta-based complexes,[10] the presence of different counterions can affect the anticancer activity of the different complexes as this affects solibility.[11] The effect of transition metal complexes containing different counterions on the anticancer activity of A549 human lung cancer cells was investigated by Zhang and co-workers.[12] This study showed that having bulky counterion groups like $BPh_4^-$ resulted in weak interaction of the $BPh_4^-$ with the complexes due to the presence of weak π-π interactions of the phenyl groups with the ligands on the complex and this decreased the anticancer activity. The counterions also form charge assisted ion pairs with the ligands which increases the half-lives for hydrolysis of the complexes, thus lowering the anticancer activity. The strength of interaction of a counterion is affected by its position relative to the ligands, with shielding of the hydrogen bond donor/ acceptors decreasing the number of interactions observed.

## 3.2 Single dose pre-screening of ligands and complexes against MCF-7 breast cancer cell lines

Towards the development of ruthenium-based metallodrugs with potential anticancer activity, ligands **L1** – **L5** and their corresponding complexes **C5** – **C13** were pre-screened for *in vitro* cytotoxicity on MCF-7 breast cancer cells at 100 μM concentration using the cell viability 3-(4,5-dimethylthiazol-2-yl)-2,5-diphenyltetrazolium bromide (MTT) assay. This assay is a colorimetric assay capable of assessing cell viability or compound activity by quantifying the % viable cells upon exposure to complexes (% cell viability). This is carried out via the use of Nbf4ADH or NADPH as co-substrates in the reduction of the MTT to formazan crystals by the mitochondrial dehydrogenase enzymes. Cell proliferation is measured by evaluating the growth rate of cells as a linear relationship between the healthy cell activity and absorbance. This process is summarised in **Figure 3. 1**. Viable cells can be quantified colorimetrically by measuring the absorbance at 600 nm.

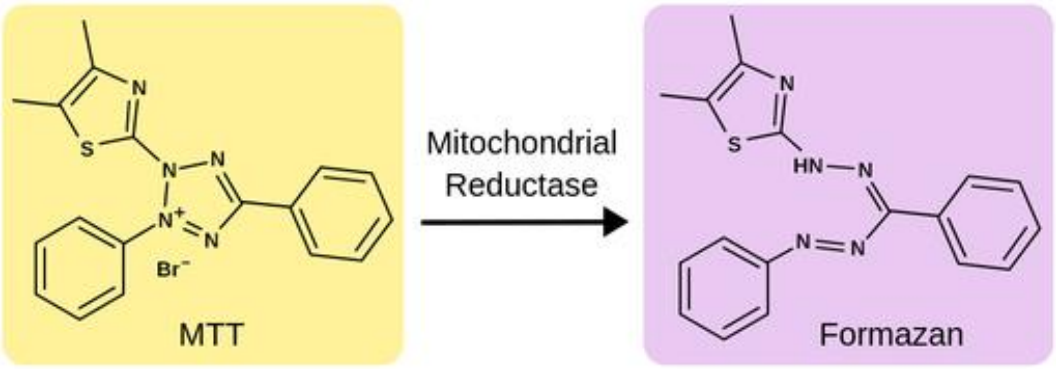


**Figure 3. 1**. The reduction of MTT by mitochondrial Reductase, and conversion to formazan.[13]

In functional tumorigenic cells, mitochondrial reductase enzymes convert the MTT dye from yellow to blue product formazan. The amount of formazan is thus indicative of the number of viable cells present. In the presence of complexes with anticancer activity, cells are killed and can no longer produce reductase enzymes, as a result the solution remains yellow.

Free uncoordinated ligands did not display as much promising cytotoxic activity as compared to their corresponding complexes. The data obtained for the *in vitro* pre-screening of the ligands **L1** – **L5** against MCF-7 breast cancer cell line at 100 μM is summarized in **Figure 3.2**. Comparing the activity of the ligands, the propyl substituted ligand **L5** displays the greatest activity against the MCF-7 cell line. Nevertheless, due to low product yields of the ligand resulting from strenuous reaction work-up, insufficient ligand was available for complexation with diruthenium acetate precursors.

The phenyl substituted ligand **L2** displays better activity in comparison to the two tautomeric forms of the phenyl ligand **L1** (A and B) which can interconvert in solution. The two tautomers of the ligand **L1** have moderate but comparable activity, with **L1B** being slightly more active. In general, the ferrocenyl ligands **L3** and **L4** display lower activity in comparison to the phenyl ligand **L2**, with the ferrocenyl ligand **L4** displaying the least activity. This difference in the activity between the ligands indicates that their anticancer activity against the MCF-7 breast cancer cells is greatly influenced by the type of substituent on the second position of the imidazopyridine ligand. Nitrogen position on the pyridine ring of the ligand also influences the activity of the ligands, with **L3** causing a 10% reduction in cell viability to the ferrocenyl ligand **L4**, and **L2** causing a 10% reduction in cell viability relative to **L1B**. The presence of the propyl chain in the ligand confers greater activity than the phenyl and ferrocene moiety, with the latter conferring the least activity. This result confirmed that the activity of the ligands is influenced by a combination of the type of imidazopyridine moiety present, and the substituent on the second position of the imidazopyridine ligand.

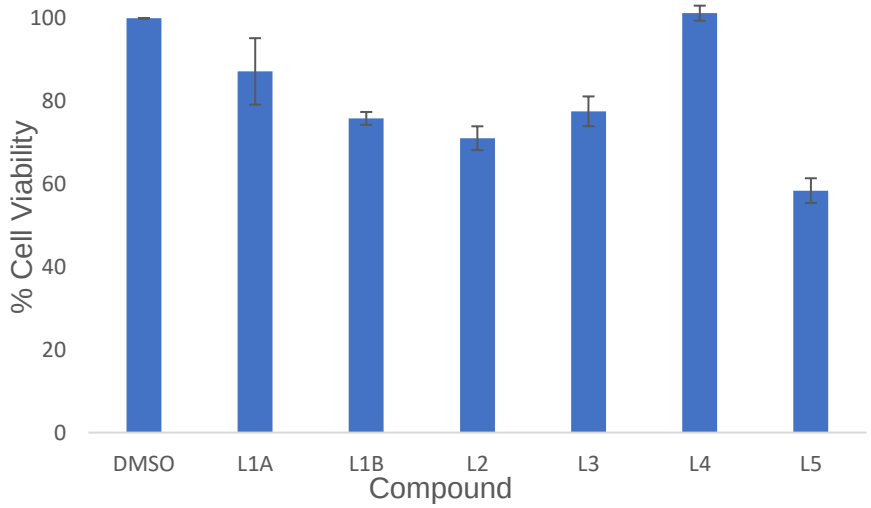


**Figure 3.2.** In vitro pre-screening of result, evaluating the viability of MCF-7 cells upon exposure to selected imidazopyridine ligands **L1** – **L5**. The results were recorded at 600 nm wavelength after 72 hours of ligand exposure. Four trials were conducted in triplicate.

Results for the pre-screening of proposed complexes (refer to **Figure 3.*3***) at 100 µM were compared with their respective ligands (**L1** – **L4**) as shown in **Figure 3.4**. The synthesised complexes are more cytotoxic relative to their respective imidazopyridine ligands which confirms that coordination of the ligand to the diruthenium tetraacetate metal core enhances the biological activity against the proliferation of cancer cells. The ferrocenyl ligand **L4** was the least active ligand with a 100% cell viability. Upon complexation of **L4** with the diruthenium tetraacetate to form **C12**, the cell viability decreased to 62%, indicating an increased

anticancer activity by ca. 40%. This likely resulted from a synergistic effect between the diruthenium tetraacetate complex and the coordinated ligand which improves the biological activity against MCF-7 breast cancer cells, perhaps through ROS generation by the ligand. Although no partition coefficients were obtained for the complexes, no visible precipitation was observed in 0.1% DMSO solvent, and the variation observed in the biological activities of the complexes was explained in terms of structural differences. The cell viability in **L1A** was 87% when tested at 100 μM, and this decreases by ca. 47% upon coordination to form the complex **C5**, indicating a synergistic effect between the ligand **L1A** and the diruthenium acetate complex **C2** which increases the anticancer activity. A similar trend is observed upon coordination of **L2** and **L3** to form their corresponding complexes

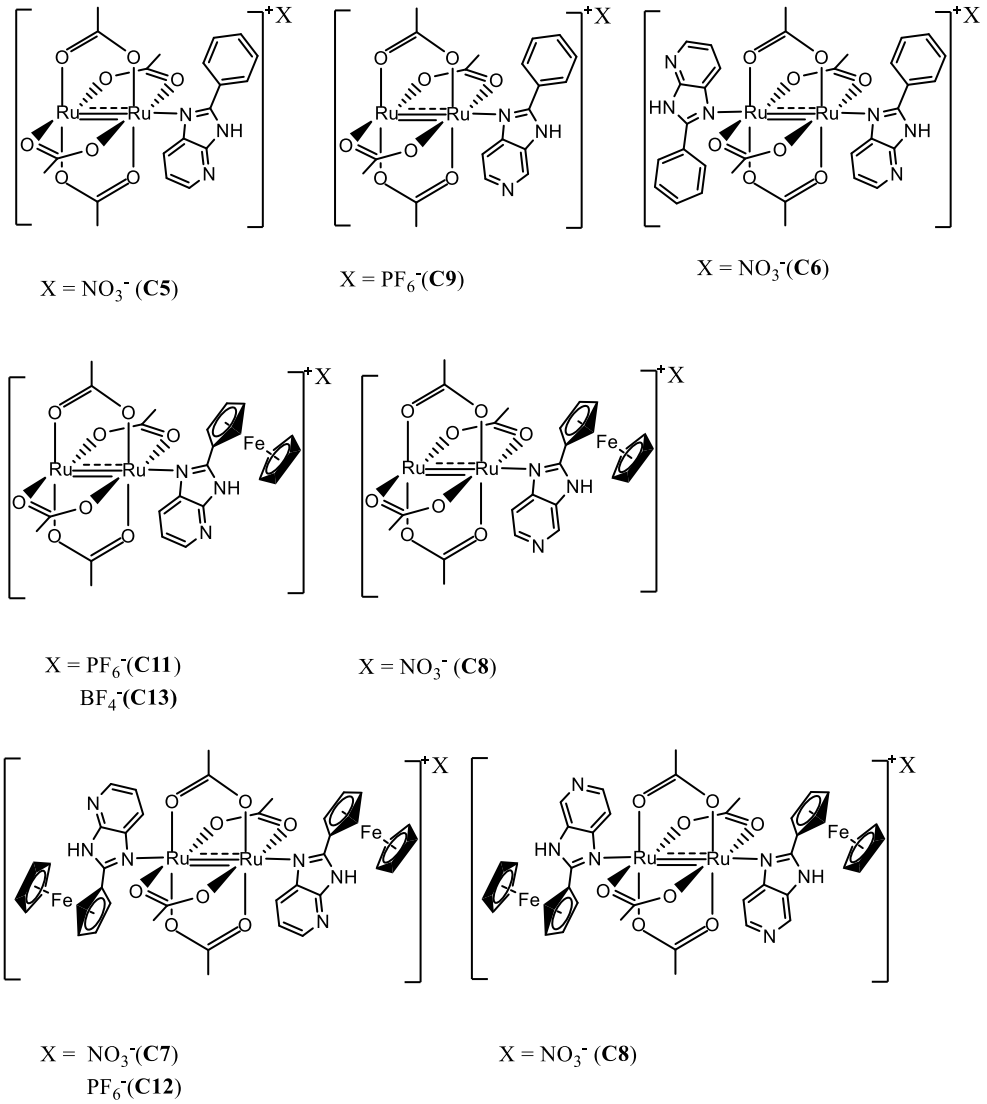


**Figure 3.3:** Proposed structures of imidazopyridine diruthenium acetate complexes (**C5** - **C13**) synthesised

The results obtained from the *in vitro* screening of the imidazopyridine diruthenium tetraacetate complexes **C5** – **C13** shows that at the chosen maximum concentration of 100 µM, all the tested compounds have good activity and significantly decreased cell viability relative to the DMSO control. It was observed that the complexes **C5** and **C7** containing an $NO_3^-$ counterion as well as **C13** containing a $BF_4^-$ counterion had the lowest cell viability which indicated the greatest anticancer activity against the MCF-7 breast cancer cell line. Overall, pre-screening of the complexes indicates that the activity was affected by the type of ligand coordinated to the metal centre as well as the type of counterion present on the complex.

At 100 µM, the complex **C5** containing the phenyl ligand **L1** and an $NO_3^-$ counterion shows a cell viability of 40%, which is slightly lower than that of its $PF_6^-$ counterpart, **C9** and this is indicative of a greater anticancer activity. The observed greater anticancer activity of complexes **C5** and **C7** bearing the $NO_3^-$ counterion relative to their $PF_6^-$ counterparts **C9** and **C11** was attributed to better solubility of the complexes relative to the generally less soluble $PF_6^-$ complexes. Furthermore, elevated amounts of nitric oxide (NO) in cells has been shown to contribute to tumour angiogenesis *via* the production of peroxynitrite ($NO_3^-$) which can induce the oxidation and nitration of DNA and this is likely responsible for the greater cytotoxic activity of the $NO_3^-$ complexes **C5** and **C7**.[14,15] The presence of a nitrate can also affect the solubility, which in turn can affect the activity of the complexes The complexes **C7**, **C11** and **C13** contained the ferrocenyl ligand **L3** with the counterions $NO_3^-$, $PF_6^-$ and $BF_4^-$, respectively. Complex **C13** displays the lowest cell viability of 38% of these complexes, which is indicative of the greatest anticancer activity being conferred by the presence of a $BF_4^-$ counterion. It was postulated that the $BF_4^-$ counterion enhances the anticancer activity due to its decreased size relative to the complexes **C7** and **C11**, which allows for better uptake of the complex in the cells and decreased ability to form ion pairings with the protons of the ligand as compared to the previous observations on the larger $BPh_4^-$ counterion.[11]

The significance of the position of the nitrogen (**L1** vs. **L2**) is more pronounced when comparing complexes **C5** (approx. 40% cell viability) and **C6** (approx. 76% cell viability) with $NO_3^-$ counterions and containing ligands **L1** and **L2**, respectively. The free ligand **L1** has cell viability of 87% and upon complexation to form **C5**, the cell viability decreased by 47%, indicating an increased anticancer activity. Similarly, the cell viability in the ferrocenyl ligand **L3** decreases from 77% to 41% and 38% in the $NO_3^-$ derivative **C7** and the $BF_4^-$ derivative **C13**, respectively. It can be speculated that the biological activities of **C5** and **C7** are enhanced due to the possible bis-coordination of the phenyl ligands **L1** and ferrocenyl ligands **L3** (pyridine nitrogen at position 7). Formation of a bis-ligated complex was previously indicated by mass spectrometry and elemental analysis, and this mode of coordination was observed

to enhance the biological activity against MCF-7 cells. The low anticancer activity observed for complexes bearing ligands **L2** or **L4** shows that the nitrogen atom on the pyridine ring of the ligand **L2** and **L4** might be at an unfavourable position for enhancing biological activity against MCF-7 breast cancer cells.

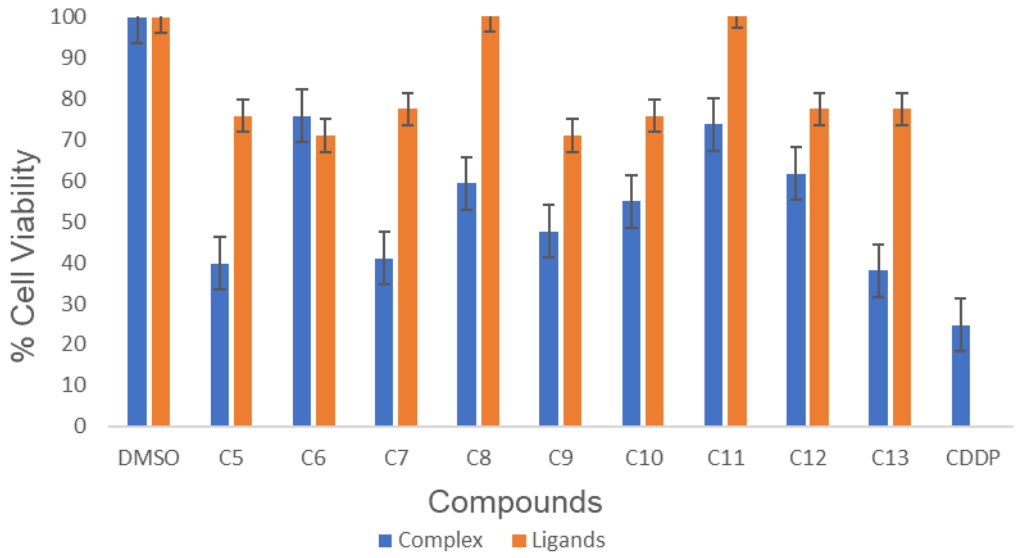


**Figure 3.4.** Screen test evaluating the viability of MCF-7 cells on exposure to selected complexes of diruthenium tetraacetate bearing imidazopyridine ligands (**C5** - **C13**) the corresponding ligands **L1** – **L4**. The results were recorded at 600 nm wavelength after 72 hours of drug exposure. Four trials were conducted in triplicate.

Comparing complexes with phenyl and ferrocenyl ligands, cell viability of the phenyl complex **C9** was 47% and this was 26% lower than that of its ferrocenyl counterpart, **C11** indicating a greater anticancer activity of the phenyl-based complexes. The same result can be seen for the complex **C10** and **C12**, where **C10** containing the phenyl ligand inducing lower cell viability than its ferrocenyl counterpart, complex **C12**. The lower cell viability of the complexes with phenyl ligands could be due to the ability of the phenyl complexes to intercalate into the DNA of the cells and interfere with the cell cycle, thus killing the cancer cells.[16]

### 3.3 Multidose screening of complexes against MCF-7 and the non-tumorigenic cell line MCF-12A cells

Complexes **C5**, **C7** and **C13** with the lowest cell viability were selected for multidose screening against MCF-7 breast cancer cell line, at concentrations ranging from 20 µM to 100 µM. Cells were suspended in 100 % media and dissolved in 0.1% DMSO and exposed to varying concentrations of the complexes. Cell viability results obtained were compared relative to those of the anticancer drug cisplatin as shown in **Figure 3.5**. At the lowest tested concentration of 20 µM, all three complexes display moderate anticancer activity which is

comparable to that of the anticancer drug cisplatin. Complex **C7** is the most active at this concentration, with cell viability of 77% and this is 5 % lower than that of cisplatin. Increasing the concentration from 20 μM to 40 μM resulted in an increased anticancer activity of complexes **C7** and **C13** with a reduction in viability of 18% and 10%, respectively. No significant change in activity was observed for the complex **C5** upon doubling the concentration from 20 μM to 40 μM.

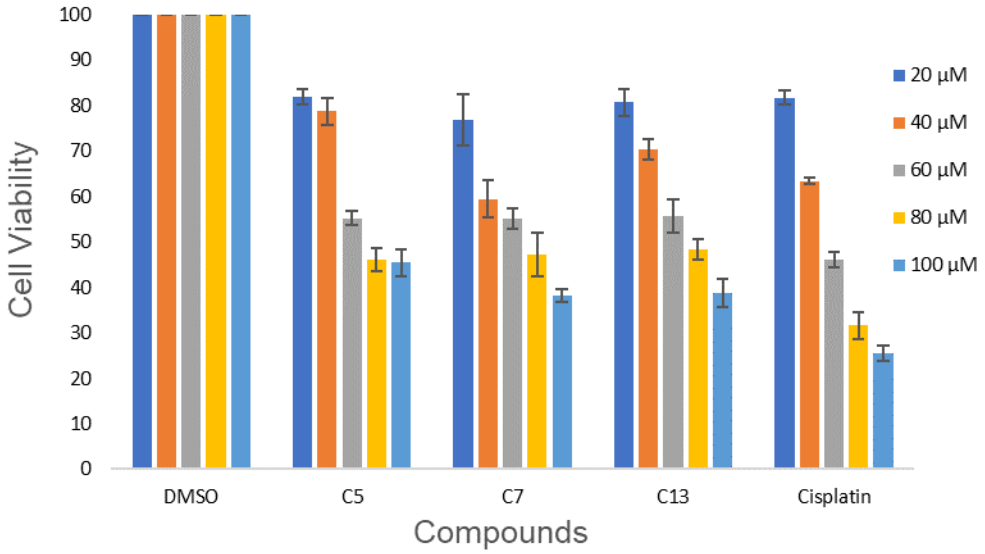


**Figure 3.5.** Single dose screen test evaluating the viability of MCF-7 breast cancer cells when exposed to increasing concentration of selected complexes of imidazopyridine diruthenium tetraacetate and the complex cisplatin. The cells were exposed to 0.1% DMSO as a control and the results were recorded at 600 nm wavelength after 72 hours of drug exposure. Four trials were conducted with each experiment performed in triplicate.

In order to assess the selectivity of the complexes for MCF-7 cancer cell line over the non-tumorigenic MCF-12A cell line, complexes **C5**, **C7** and **C13** were selected for multidose screening against the MCF-12A cell line, at concentrations ranging from 20 μM to 100 μM as shown in **Figure 3.6**. At 100 μM the complex **C5** reduced cell viability of the MCF-12A non-tumorigenic cell line by more than 90%, showing that **C5** was greatly cytotoxic to the MCF-12A cells and not selective to the MCF-7 cells.

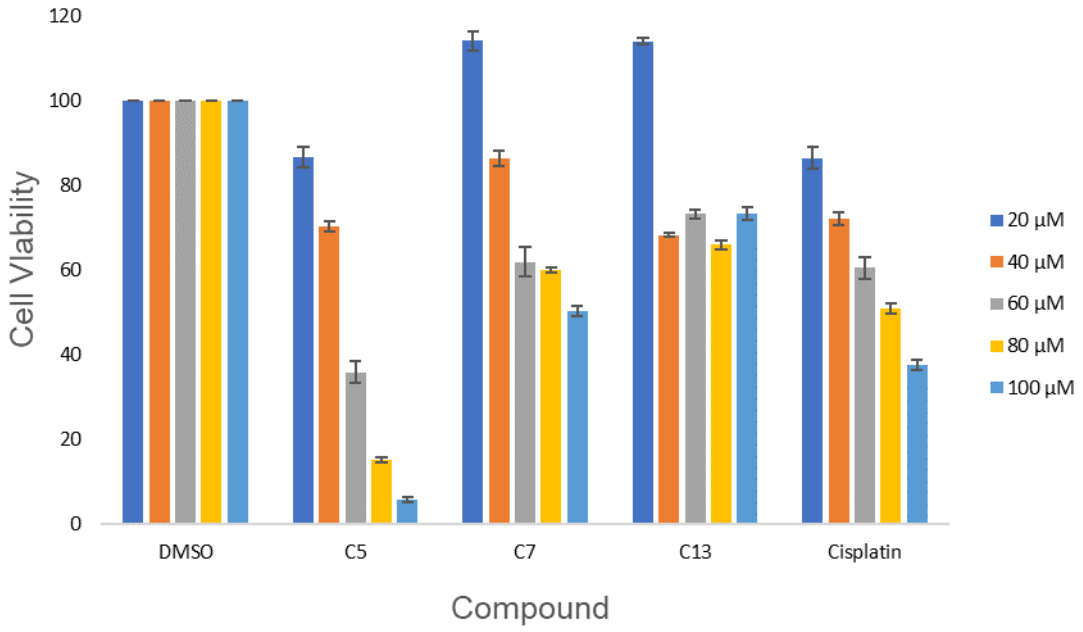


**Figure 3.6.** Multidose screen test evaluating the cell viability of MCF-12A cells when exposed to selected complexes of imidazopyridine diruthenium tetraacetate. The results were recorded at 600 nm wavelength after 72 hours of drug exposure. Four trials were conducted, with each experiment performed in triplicate.

At 20 µM, the cell viability in the complexes **C7** and **C13** is greatly increased relative to the DMSO vehicle control showing that the complexes do not kill the non-tumorigenic cells at this concentration and were selective for the MCF-7 cancer cells. The reduced cytotoxicity of **C7** and **C13** towards the MCF12A non-tumorigenic cell line relative to cisplatin is shown by the higher selectivity indices values as summarised in **Table 3.1**. The selectivity indices are ratios which compare the cytotoxicity of complexes in anticancer cells relative to normal healthy cells. Complex **C5** has a low S.I. value, which agrees with the cytotoxicity results observed for the complex.

**Table 3.1.** Table showing the $IC_{50}$ and selectivity indices values of the complexes **C5**, **C7** and **C13** in MCF-12A and MCF-7 breast cancer cells, compared with those of cisplatin. The $IC_{50}$ values were determined and extrapolated from their respective sigmoidal curves using the GraphPad Prism V6.

| Compound | $IC_{50}$ (µM) ± SE MCF-12A | $IC_{50}$ (µM) ± SE MCF-7 | S.I |
|---|---|---|---|
| **C5** | 49.78 ± 3 | 79.58 ± 5.8 | 0.626 |
| **C7** | 92.98 ± 5 | 66.47 ± 9,8 | 1.399 |
| **C13** | 165.5 ± 6 | 73.70 ± 4,7 | 2.246 |
| **CDDP** | 76.66 ± 2,9 | 57.28 ± 1,7 | 1.338 |

## 3.4 Conclusion

The anticancer activity and cytotoxicity of ligands (**L1** – **L5**) and their corresponding complexes (**C5** – **C13**) was successfully determined *in vitro* against MCF-7 breast cancer cell line. The complexes displayed significantly improved anticancer activity relative to the free uncoordinated ligands. The complex **C5** bearing the phenyl ligand **L1**, $NO_3^-$ derivative complex **C7** and $BF_4^-$ derivative complex **C13** bearing the ferrocenyl ligand **L3** displayed the greatest anticancer activities. The $IC_{50}$ values of **C5**, **C7** and **C13** against breast cancer cell line were 79.58 µM, 66.47 µM and 73.70 µM, respectively. $IC_{50}$ values were slightly greater but comparable to those of cisplatin. Complexes **C5**, **C7** and **C13** were further analysed for selectivity by evaluating the anticancer activity against the MCF-12A non-tumorigenic cell line. Complex **C5** was highly cytotoxic to the non-tumorigenic cell line at all tested concentrations and reduced cell viability of MCF-12A cell line by more than 90% at the maximum tested concentration. Complexes **C7** and **C13** displayed moderate cytotoxicity towards the healthy cell line relative to cisplatin, with **C13** being more selective to breast cancer cell line (S.I value = 2.246 vs. cisplatin S.I = 1.339). It was concluded that changing the position of the nitrogen on the ligands significantly affects the anticancer activity of the ligands and corresponding complexes. Complexation of the ligands (**L1** – **L4**) to the diruthenium acetate precursors significantly enhances the anticancer activity of the poorly soluble ruthenium acetate and imidazopyridine ligands against MCF-7 breast cancer cells.

### 3.5 References


1. Nguyen Van Long, F.; Lardy-Cleaud, A.; Bray, S.; Chabaud, S.; Dubois, T.; Diot, A.; Thompson, A. M.; Bourdon, J.-C.; Perol, D.; Bouvet, P.; Diaz, J.-J.; Marcel, V., Druggable Nucleolin Identifies Breast Tumours Associated with Poor Prognosis That Exhibit Different Biological Processes. *Cancers* **2018,** *10* (10), 390.
2. Barresi, E.; Tolbatov, I.; Marzo, T.; Zappelli, E.; Marrone, A.; Re, N.; Pratesi, A.; Martini, C.; Taliani, S.; Da Settimo, F.; La Mendola, D., Two mixed valence diruthenium(ii,iii) isomeric complexes show different anticancer properties. *Dalton Trans.* **2021,** *50* (27), 9643-9647.
3. Ribeiro, G.; Benadiba, M.; Colquhoun, A.; Silva, D., Diruthenium(II, III) complexes of ibuprofen, aspirin, naproxen and indomethacin non-steroidal anti-inflammatory drugs: Synthesis, characterization and their effects on tumor-cell proliferation. *Polyhedron* **2008,** *27*, 1131-1137.
4. Lee, S. Y.; Kim, C. Y.; Nam, T. G., Ruthenium Complexes as Anticancer Agents: A Brief History and Perspectives. *Drug. Des. Devel Ther.* **2020,** *14*, 5375-5392.
5. Alves Rico, S. R.; Abbasi, A. Z.; Ribeiro, G.; Ahmed, T.; Wu, X. Y.; de Oliveira Silva, D., Diruthenium(II,III) metallodrugs of ibuprofen and naproxen encapsulated in intravenously injectable polymer-lipid nanoparticles exhibit enhanced activity against breast and prostate cancer cells. *Nanoscale* **2017,** *9* (30), 10701-10714.
6. Osterloh, W. R.; Galindo, G.; Yates, M. J.; Van Caemelbecke, E.; Kadish, K. M., Synthesis, Structural and Physicochemical Properties of Water-Soluble Mixed-Ligand Diruthenium Complexes Containing Anilinopyridinate Bridging Ligands. *Inorg. Chem.* **2020**, *59* (1), 584-594.
7. Medupe T.T, M. K., Prince S Monoanionic substituted anilinopyridinate (ap) tricarboxylate diruthenium (II, III) paddlewheel complexes are evaluated for antiproliferative activity against human breast MCF7 carcinoma cells: Synthesis, characterization, and in vitro cytotoxic preliminary screen. *unpublished data,* **2021**.
8. He, L.-J.; Yang, D.-L.; Chen, H.-Y.; Huang, J.-H.; Zhang, Y.-J.; Qin, H.-X.; Wang, J.-L.; Tang, D.-Y.; Chen, Z.-Z., A Novel Imidazopyridine Derivative Exhibits Anticancer Activity in Breast Cancer by Inhibiting Wnt/β-catenin Signaling. *OncoTargets and ther.* **2020,** *13*, 10111-10121.
9. Wang, J.; Wu, H.; Song, G.; Yang, D.; Huang, J.; Yao, X.; Qin, H.; Chen, Z.; Xu, Z.; Xu, C., A Novel Imidazopyridine Derivative Exerts Anticancer Activity by Inducing Mitochondrial Pathway-Mediated Apoptosis. *Biomed. Res. Int.* **2020,** *2020*,1 - 8.
10. Martínez-Alonso, M.; Sanz, P.; Ortega, P.; Espino, G.; Jalón, F.; Martín, M.; Rodríguez, A.; López, J.; Tejel, C.; Manzano, B., Analysis of Ion Pairing in Solid State and Solution in p-Cymene Ruthenium Complexes. *Inorg. chem.* **2020,** *59,* A - H

11. Loughrey, B.; Healy, P.; Parsons, P.; Williams, M., Selective cytotoxic Ru(II) arene Cp* complex salts [R-PhRuCp*]+X- for X = BF4-, PF6-, and BPh4. *Inorganic chemistry* **2008,** *47*, 8589-8591.
12. Zhang, H.; Guo, L.; Tian, Z.; Tian, M.; Zhang, S.; Xu, Z.; Gong, P.; Zheng, X.; Zhao, J.; Liu, Z., Significant effects of counteranions on the anticancer activity of iridium(iii) complexes. *Chem. commun.* **2018,** *54* (35), 4421-4424.
13. Ghasemi, M.; Turnbull, T.; Sebastian, S.; Kempson, I., The MTT Assay: Utility, Limitations, Pitfalls, and Interpretation in Bulk and Single-Cell Analysis. *Int J Mol Sci* **2021,** *22*, 12827.
14. Khan, F. H.; Dervan, E.; Bhattacharyya, D. D.; McAuliffe, J. D.; Miranda, K. M.; Glynn, S. A., The Role of Nitric Oxide in Cancer: Master Regulator or NOt? *Int. J. Mol. Sci.* **2020,** *21* (24), 9393.
15. Xu, W.; Liu, L.; Loizidou, M.; Ahmed, M.; Charles, I., The role of nitric oxide in cancer. *Cell Res.* **2003,** *12*, 311-20.
16. Atwell, G. J; Bros, C. D.; Baguley, B. C.; Denny, W. A, Potential antitumor agents. 56. Minimal DNA-intercalating ligands as antitumor drugs: phenylquinoline-8-carboxamides. *J. Med. Chem*. **1988**, 31(5), 1048-1052.

# Chapter 4: Future Work

## 4.1 Future Studies

Future studies should involve the use of molecular docking studies to determine if the position of the pyridine nitrogen atom on the ligands **L1** – **L5** and their corresponding complexes **C5** – **C13** affects the biological interaction with proteins and bioactive components in the cells. It will also be interesting to evaluate if the substitution of one or more equatorial acetate groups on our synthesised complexes with other ligands such as diphenyl formamidines which have previously been shown to display anticancer activity,[1] can improve the biological activity of our synthesised complexes against breast or prostate cancer cells. It has previously been shown by our group that the removal of acetate groups and replacing them with N,N donor ligands such as anilinopyridines stabilises and improves the solubility of the diruthenium acetate complexes. The complexes can also be purified using column chromatography, since the removal of the equatorial bridging acetate (O,O) groups by formamidine ligands reduces the extent of interaction of the polar acetate groups with the polar silica gel, allowing for movement on the column. Therefore, in future work, complexes of diruthenium tetraacetate bridged on the equatorial position by one or more symmetrical or unsymmetrical formamidine ligands, with the benzimidazole ligands attached on the axial positions will be synthesised as shown in **Figure 4.1**.

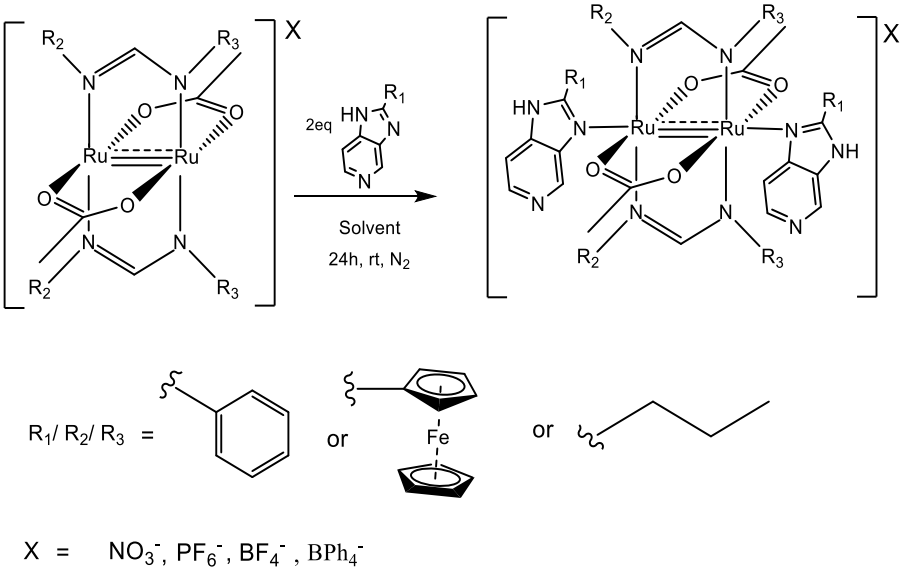


**Figure 4.1.** Proposed synthesis procedure for the mixed ligand complexes of diruthenium acetate bridged by imidazopyridine and formamidine derivatives.

Future work will also employ the use of Single crystal X-ray diffraction to confirm differences in the number of ligands coordinating to the metal centre, in the presence of $NO_3^-$, $PF_6^-$ and $BF_4^-$ counterions and to confirm the mode of coordination to metal centres. The solubility of

these complexes will be evaluated in suitable solvents like DMSO and methanol by determining the partition coefficient. The purity of the complexes will be evaluated using techniques like high pressure liquid chromatography (HPLC) in addition to mass spectrometry and elemental analysis. The anticancer activity and mechanism of action of the most active and less cytotoxic complexes (**C7** and **C12**) in tumorigenic MCF-7 breast cancer cell line will be evaluated by determining the interaction of the complexes with DNA, through DNA binding studies and UV-Vis titration studies in the presence of GSH.

## 4.2 References

1. Soliman, A.; Alajrawy, O. I.; Attaby, F.; Shaaban, M.; Linert, W., New formamidine ligands and their mixed ligand palladium(II) oxalate complexes: Synthesis, characterization, DFT calculations and in vitro cytotoxicity. *Spectrochim. Acta A Mol. Biomol. Spectrosc.* **2015,** *152*.358-369

# Chapter 5: Experimental

## 5.1 Materials and Physical techniques

All reagents and solvents used were purchased from commercial sources (Sigma Aldrich, Kimix or Merck) and used without further purification. Infrared spectra results were recorded using the Perkin-Elmer 100 FT-IR spectrometer using Attenuated Total Reflectance (ATR), with frequency scanned from 4000 – 400 $cm^{-1}$. Nuclear Magnetic Resonance (NMR) spectra were recorded on the Varian Mercury XR300 MHz ($^{1}H$ NMR at 300 MHz), a Bruker 400 Biospin GmbH ($^{1}H$: at 400.22 MHz, $^{13}C$ at 150.60 MHz) or a Bruker 600 FT spectrometer (1H: at 600.10 MHz, $^{13}C$ at 150.60 MHz) spectrometer at ambient temperature. Chemical shifts and coupling constants were obtained using 1D NMR analysis and the signals assigned were confirmed by 2D NMR analysis. Magnetic susceptibility measurements were determined using the Evan's method[3] at room temperature in solution.

Mass spectrometry results were obtained using Electrospray Ionisation (ESI) on a Waters API Quattro Micro triple quadrupole mass spectrometer with data recorded using the positive ion modes. The mass spectrometer scanned from m/z 0 to 1120. ESI – TOF MS spectra were collected with 4.8 ml h−1 acetonitrile as the mobile phase. The samples were dissolved in acetonitrile and a 30 ml solution was injected into the electron spray ion source. The extraction cone voltage was 10 V. Electrochemical experiments were carried out in a one-compartment cell with a glassy carbon as the working electrode. $Ag/AgNO_3$ was used as the reference electrode and a Pt wire was used as an auxiliary electrode. The electrochemical experiments were carried out in degassed methanol solutions containing 0.10 M $TBANO_3$, $TBAPF_6$, and $TBABF_4$ supporting electrolytes. The solvent was saturated with $N_2$ gas prior to taking measurements, which were carried out at 0.1 V/s unless stated otherwise. Melting point data were determined using a Büchi Melting Point Apparatus B-540. Ruthenium trichloride hydrate was purchased from Sigma-Aldrich and used without further purification. Diruthenium tetraacetate precursor complexes were synthesised using literature methods.[1] Stability studies of the complexes were carried out by UV-Vis spectroscopy in the 200–1000 nm range. A $1 \times 10^{-4}$ M solution of each complex was prepared by dissolving the complexes in DMSO. The electronic absorption spectra of the solutions were measured over a period of 72 h.

## 5.2 Biological evaluation

### 5.2.1 Cell culture conditions

Breast adenocarcinoma MCF-7 (oestrogen receptor positive) and the non-tumorigenic MCF-12A were grown according to the recommendations provided by the manufacturer and maintained in Roswell Park Memorial Institute Medium (RPMI)-1640 (Sigma Aldrich, USA),

Dulbecco's Modified Eagle's Medium (DMEM) (Sigma Aldrich) and Dulbecco's Modified Eagle's Medium (DMEM/F12), respectively. All media were supplemented with Foetal Bovine Serum (FBS, 10%) and Penstrep (P/S, 5%), with the exception of DMEM/F12 medium supplemented with FBS (5%), P/S (1%), epidermal growth factor (EGF, 10µl), hydrocortisone (16.6µl), choleratoxin (8.3µl) and insulin (125µl). Cell lines were grown and maintained in 10cm Petri dishes and T75cm flasks at 37°C in 5% $CO_2$ and 95% air humidified incubator. Cells were passaged as required at 80 – 90% confluence. Medium was replaced after 2 to 3 days and cell lines were continuously tested for mycoplasma infection. Only cells that were mycoplasma infection free were utilized in experiments.

### 5.2.2 Cellular metallodrug treatments (MTT Assay).

After seeding cells in 96-well plates, cells were preincubated in drug-free medium at 310K for 48 hours before additions of complexes at various concentrations for multidose testing. $[Ru_2(OAc)_4(L)Cl]$ complexes were prepared in DMSO to give a master mix concentration of 10mM. The master mix solutions were diluted down with the working cell culture medium to give a stock concentration of 100µM, with the DMSO concentration reduced to 1%, and further diluted to various concentrations of 3, 6, 9, 12 and 15 µM as working drugs for treatment in respective medium and the concentration of DMSO now reduced further down to 0.1%. Complexes were prepared to their appropriate concentrations on the day of treatment to avoid possible coordination of the solvent on vacant axial sites/positions of the $Ru_2$ metal cores. After 48 hours of incubation, cells were treated with complexes (20 –100µM) or vehicle for 72 hours. The negative vehicle control (DMSO) was prepared at the highest concentration of the drug compounds under investigation (100µM) and as well as the clinically prepared cisplatin drug which was used as a positive vehicle control and prepared at the same concentrations as the working drugs.

Cells were seeded at a density of 4500 and 5000 for MCF7 and MCF12A cell lines to obtain a confluency between 60-70% on the day of treatment in 96 well plates. For MCF12A, cells were starved for 48 hours before they were seeded on 96 well plates and they were maintained with media consisting of Foetal Bovine Serum (FBS, 5%) and PenStrep (P/S, 1%). Cells were preincubated in a drug free medium for 48 hours, followed by treatment with diruthenium compounds at various concentrations ranging from (20-100µM) for a 72-hour time period. Cell viability was measured using the 3-(4,5-dimethylthiazol-2-yl)-2,5-diphenyl-trazolium bromide (MTT) assay (11465007001; Sigma Aldrich) according to the manufacturer's instructions. Subsequently, 10µL of MTT (5mg/ml) solution was added and cells were re-incubated for 4 hours. After this period, the solubilizing solution was added, and the cells returned to the incubator for 24 hours. The results were recorded using a microplate reader (Promega Glomax

Explorer Multimode Microplate Reader) at an absorbance reading of 600 nm. Each well was quadrupled, and three independent experiments were performed on for all cell lines. Mean cell viability was calculated as a percentage of the mean vehicle control ± Standard deviation of the means.

### 5.2.3 Statistical analysis

Statistical analysis was conducted with the acquisition of the data represented as mean values and the calculated standard error of the means (SEM) of the three independent experiments. Data were analyzed using GraphPad Prism version 6.0 (GraphPad Software). A parametric unpaired t-test (a student's statistical hypothesis test) was performed. Significance of values *p<0.05, **P<0.005 and ***p<0.0005 were accepted and considered to be significant.

## 5.3 Synthesis of imidazopyridine ligands (L1 – L5)

### 5.3.1 Synthesis and characterisation of 2-aryl-1H-Imidazo(4,5-b)pyridine (L1)

2,3-diaminopyridine (0.423 g, 3.87 mmol) was dissolved in 10 mL nitrobenzene, followed by benzaldehyde (0.411 g, 3.87 mmol) and TFA (0.100 mL, 1.30 mmol). The solution was stirred at room temperature for 48 h. The green solution was extracted with sodium bicarbonate (40 mL), water (3 x 50 mL), sodium chloride (50 mL) and dried over magnesium sulphate. Column chromatography was used to separate the products. Elution with ethyl acetate/ hexane (1:1) separated two new spots. A green-orange solid (**L1a**) and a crystalline colourless solid (**L1b**) were isolated by vacuum filtration, washed with hexane or diethyl ether, and dried under vacuum. Yield (**L1a**): 21% (0.0888 g) Rf (Ethyl Acetate/ Petroleum ether, 30:70): 0.32. **M.P.** 287 – 288 °C. Yield (**L1b**): 3% (0.0123 g). Rf (Ethyl Acetate/ Petroleum ether, 30:70): 0.30. **M.P.** 292 – 293 °C. **$^1$H NMR (400 MHz, DMSO)**: δ 8.35 (d, *J* = 4.7 Hz, 1H, *d*), 8.23 (d, *J* = 4.7 Hz, 1H, *a*), 8.03 (d, *J* = 7.9 Hz, 1H, *f*), 7.56 (m, 3H, (*b* & *c*)), 7.27 (dd, *J* = 8.0, 4.8 Hz, 1H, *e*). **LCMS** Purity > 99% ($t_R$ = 0.554)

### 5.3.2 Synthesis and characterisation of complexes with 2-aryl-1H-Imidazo(4,5-c)pyridine (L2)

3,4-DAP (1.00 g, 9.16 mmol) was dissolved in 40 mL ethanol, followed by benzaldehyde (0.800 g, 7.54 mmol), TFA (0.100 mL, 1.30 mmol) and magnesium sulphate (3.00 g, 0.025 mmol) were added. The reaction solution was stirred at room temperature for 48 h. Ethanol was removed under vacuum and the product was re-dissolved in 40 mL ethyl acetate. The final yellow-orange solution was extracted with sodium bicarbonate (40 mL), water (3 x 50 mL), sodium chloride (50 mL) and dried over magnesium sulphate, which was then removed by filtration under gravity. Column chromatography was used to separate the product from the

unreacted starting material. Elution with ethyl acetate/ petroleum ether (3:7) separated two orange bands. Solvent removal followed by a DCM/hexane co-precipitation resulted in an orange solid (**L2a**) and a green solid (**L2b**). Yield (**L2a**): 43% (0.430 g) Rf (Ethyl Acetate/ Petroleum ether, 50:50): 0.32. Yield (**L2b**): 5% (0.05 g) yield. Rf (Ethyl Acetate/ Petroleum ether): 0.30. **M.p.** 256 – 258 °C. **$^{1}$H NMR (300 MHz, MeOD)**: δ 8.91 (s, 1H), 8.34 (d, *J* = 5.7 Hz, 1H), 8.16 (s, 2H), 7.68 (d, *J* = 5.7 Hz, 1H), 7.60 (s, 3H). **LCMS** Purity = 94.5% [$t_R$ = 0.285]

### 5.3.3 Synthesis and characterisation of 2-ferrocenyl-1H-Imidazo(4,5-b)pyridine (L3)

2,3-DAP (0.668 g, 6.12 mmol) was dissolved in a 1:2 ethanol: water (40 mL) in a round bottom flask. Ferrocenecarboxaldehyde (0.600 g, 2.80 mmol) and Trifluoroacetic Acid (0.0900 mL, 1.18 mmol) were added to the flask, followed by magnesium sulphate (2.00 g, 0.0166 mmol). The black solution was refluxed at 60 °C for 72 h. The product was extracted with ethyl acetate and water, washed with sodium bicarbonate (50 mL), water (3 x 100 mL) and sodium chloride/ brine (50 mL) and then dried over magnesium sulphate. The resulting solution was collected and separated using silica column chromatography. Eluting with Ethyl Acetate/ Hexane (1:1) separated two orange bands. Solvent removal and layering with hexane afforded an orange solid (**L3a)** and a dark brown solid (**L3b**). Yield (**L3a**): 17% (0.114 g), Rf (1:1 Ethyl Acetate/hexane): 0.53. Yield (**L3b**): 14% (0.0935), Rf (1:1 Ethyl Acetate/hexane): 0.30. **M.P.** Decomposes with onset at 336 °C. **$^{1}$H NMR (400 MHz, DMSO-d$_6$)**: δ 12.98 (s, 1H, *g*), 12.56 (s, 1H, *g'*), 8.25 (s, 1H, *d*), 7.83 (s, 1H, *f*), 7.12 (s, 1H, *e*), 5.07 (s, 2H, *a*), 4.46 (s, 2H, *b*), 4.07 (s, 4H, *c*), 1.15 (s, 4H). **$^{13}$C NMR (151 MHz, DMSO)**: δ 157.17 (s), 156.40 (s), 155.40 (s), 149.78 (s), 143.64 (s), 142.81 (s), 136.20 (s), 133.77 (s), 132.56 (s), 125.3 (s), 118.35 (s), 117.80 (s), 117.43 (s), 73.94 (s).

### 5.3.4 Synthesis and characterisation of 2-ferrocenyl-1H-Imidazo(4,5-c)pyridine (L4)

3,4-DAP (0.500 g, 4.58 mmol) was dissolved in 20 mL of ethanol in a round bottom flask and Ferrocenecarboxaldehyde (0.450 g, 2.10 mmol) and Trifluoroacetic Acid (0.0900 mL, 1.18 mmol) were added to the flask, followed by magnesium sulphate (2.00 g, 0.0166 mmol). The product was extracted with ethyl acetate and water, washed with sodium bicarbonate (50 mL), water (3 x 100 mL) and sodium chloride/ brine (50 mL) and then dried over magnesium sulphate. The resulting solution was collected and separated using silica column chromatography. Eluting with Ethyl Acetate/ Hexane (1:1) separated an orange band. Solvent removal and layering with hexane afforded an orange solid (**L4)**. Yield (**L4**): 37% (0.185 g). **M.P.** Decomposes with onset at 283 °C. **$^{1}$H NMR (300 MHz, DMSO-d$_6$)**: δ 8.27 (d, *J* = 17.8 Hz, 1H), 7.91 (q, *J* = 18.4 Hz, 1H), 7.28 – 7.06 (m, 1H), 5.11 (s, 2H), 4.55 (d, *J* = 19.4 Hz, 2H), 4.30 – 4.00 (m, 5H). **$^{13}$C NMR (151 MHz, DMSO)**: δ 155.33 (s), 149.71 (s), 143.46 (s), 142.80

(s), 136.28 (s), 133.77 (s), 132.62 (s), 127.42 (s), 125.29 (s), 118.45 (s), 117.98 (s), 117.43 (s), 73.94 (s), 70.67 (s).

### 5.3.5 Synthesis and characterisation of 2-propyl-1H-Imidazo(4,5-b)pyridine (L5)

2,3-DAP (1.00 g, 9.17 mmol) was dissolved in 20 mL of ethanol in a round bottom flask and butyraldehyde (0.331 g, 9.17 mmol) and TFA (0.0900 mL, 1.18 mmol) were added to the flask, followed by magnesium sulphate (2.00 g, 0.0166 mmol). Yield (**L5**): 37% (0.373 g). Rf (Ethyl Acetate): 0.19. **M.P.** Oily. **$^1$H NMR** (300 MHz, DMSO) $\delta$ 8.28 (dd, *J* = 22.2, 13.4 Hz, 1H), 7.92 (ddd, *J* = 32.7, 22.2, 7.1 Hz, 1H), 7.33 – 6.97 (m, 1H), 2.80 (s, 2H), 1.81 (s, 2H), 0.94 (t, 3H).

## 5.4 Synthesis of tetraacetate diruthenium precursor complexes

### 5.4.1 Synthesis of $[Ru_2(OAc)_4]Cl$ (C1)

Synthesised from modified literature protocols. $RuCl_3{\cdot}xH_2O$ (1.00 g, 4,82 mmol) and LiCl (0.994 g, 2.35 mmol) were placed in a 250 mL round bottom flask equipped with a magnetic stirrer. Acetic anhydride (24 mL) and acetic acid (45 mL) were added to the flask and the solution stirred under an open-air atmosphere for 24 hours at 130 °C. The solution was left to cool at room temperature and the brown solid precipitate was collected by filtration under vacuum. The filtrate was washed with cold diethyl ether and then dried *in vacuo*. Yield: 65% (0.646 g). UV-Vis spectrum in methanol: $\lambda_{max}$, nm ($\varepsilon$ x $10^{-4}$, $M^{-1}$ $cm^{-1}$): 431 (0.05).

### 5.4.2 Synthesis of $[Ru_2(OAc)_4]NO_3$ (C2)

A methanolic solution of $Ru_2(OAc)_4Cl$ (0.103 g, 0.217 mmol) was reacted with an equimolar solution of $AgNO_3$ (0.0369 g, 0.217 mmol) in a 100 mL round bottom flask at room temperature, under nitrogen. Silver chloride formed as a white precipitate and was filtered under gravity. The solvent in the filtrate was removed under reduced pressure to give a reddish-brown solid which was re-dissolved in tetrahydrofuran/ petroleum ether (1:10) to reveal a dark-brown solid. The product was collected by filtration under vacuum and then dried *in vacuo*. Yield: 91% (0.0937 g). **UV-Vis** (in methanol): $\lambda_{max}$, nm ($\varepsilon$ x $10^{-4}$, $M^{-1}$ $cm^{-1}$) at 431. **FTIR ($cm^{-1}$)**: 2933 w (C-H), 1435 s $\nu_a(OCO^-)$, 1393 s $\nu_s(OCO^-)$,1268 s $\nu$(N – O), 687 s $\nu$(C-$CH_3$). **EA**. (found: C= 19.4%, H= 2.04%, N= 2.81%; calculated for $[Ru_2(OAc)_4(C_{12}H_9N_3)]NO_3$: C = 19.6%, H = 2.40%, N = 2.86%).

### 5.4.3 Synthesis of $[Ru_2(OAc)_4]PF_6$ (C3)

Synthesised using the same procedure followed for the synthesis of **C2**. A solution of $Ru_2(OAc)_4Cl$ in methanol (0.250 g, 0.528 mmol) was reacted with an equimolar amount of silver hexafluorophosphate (0.133 g, 0.528 mmol) using a 100 mL round bottom flask. A white

precipitate (AgCl) was formed within ten minutes of reaction onset. The solution was left to stir at room temperature overnight. The precipitate was removed by filtering under gravity and the solvent in the filtrate was removed under reduced pressure to reveal a brown solid. Hexane was added to yield a light brown solid which was obtained by filtering under vacuum. Yield: 91.4% (0.229 g). **M.P.** Decomposes with onset at 347 °C. **UV–Vis** (in methanol): $\lambda_{max}$, nm (ε x $10^{-4}$, $M^{-1}$ $cm^{-1}$) at 431. **FTIR ($cm^{-1}$)**: 2884 w (C-H), 1440 s $\nu_a(OCO^-)$, 1399 s $\nu_s(OCO^-)$,830 s $\nu(PF_6)$, 1048 m, 690 s $\nu$(C-$CH_3$). **ES-MS:** Calculated 438.376; m/z 438.843 [M–$PF_6$].

### 5.4.4 Synthesis of $[Ru_2(OAc)_4]BF_4$ (C4)

$[Ru_2(OAc)_4(THF)_2]BF_4$ was synthesised following literature procedures reported by Barral et al.,[2] The reaction was performed under dry and non-reactive nitrogen conditions. $Ru_2(OAc)_4Cl$ (0.100 g, 0.211 mmol) was weighed into a 100 mL Schlenk flask. Nitrogen was connected and $AgBF_4$ (0.041 g, 0.211 mmol) was weighed and quickly transferred to the Schlenk flask. THF (20 mL) was added to the flask and the solution stirred for 24 hr at room temperature in the dark. The light brown solution was observed to become dark brown, and AgCl precipitate that formed was removed by filtering under gravity. The filtrate solution was concentrated to a minimum (ca. 2 mL) and layered with petroleum ether (40 – 60 °C). A crystalline reddish-brown precipitate was collected by filtration under vacuum. Yield: 44% (0.044 g). **M.P.** Decomposes with onset at 318 °C. **UV–Vis** (in methanol): $\lambda_{max}$, nm (ε x $10^{-4}$, $M^{-1}$ $cm^{-1}$) at 431 (0,064). **FTIR ($cm^{-1}$)**: 3373 m $\nu$(C-O, THF), 2884 w (C-H), 1437 s $\nu_a(OCO^-)$, 1394 s $\nu_s(OCO^-)$,1007 s $\nu(BF_4)$, 686 s $\nu$(C-$CH_3$). **ES-MS:** Calculated 438.376; m/z 438.844 ($[M–Cl]^+$). **Ea**. (found: C= 17.33%, H= 2.65%) calculated for $[Ru_2(OAc)_4(C_{12}H_9N_3)]BF_4$: C = 18.28%, H = 2.30%).

## 5.5 Synthesis of $[Ru_2(OAc)_4(L)]X$ where ($X = NO_3^-, PF_6^-, BF_4^-$)

### 5.5.1 Synthesis and characterisation $[Ru_2(OAc)_4(L1)]NO_3$ (C5)

To a stirring solution of $[Ru_2(OAc)_4]NO_3$ (0.0231 g, 0.0461 mmol) in 5.00 mL isopropanol was added 2-aryl-1H-imidazo(4,5-c)pyridine/ **L1** (0.0180 g, 0.0923 mmol) in isopropanol dropwise. The solution was stirred at room temperature for 24 hours and a colour change from orange solution to dark brown was observed. The solvent was reduced to a minimum (ca. 1 mL) and the solution was layered with petroleum ether and THF (10:1) to give a milky-brown solid which was dried under vacuum. Yield: 69% (0.0159 g). **M.P**. Decomposes with onset at 266 °C. Electronic absorptions at $\lambda_{max}$ (nm) in methanol: 300 nm and 421 nm. FTIR ($cm^{-1}$): 1857 w, 1541 m $\nu(C=N)_{imd}$, 1421 s, 1410 s $\nu_s(OCO^-)$, 1284 s ($NO_3$), 1167 m, 1039 m, 939 w, 882 m, 689 s (C-$CH_3$). **MS** (ESI-TOF, Acetonitrile + 1%TFA): *m/z,* 634.9459 [M-**L1**]$^+$. 438.8636 [M-2**L1**]$^+$. **Ea**. (found: C= 27.62%, H= 3.52%, N= 4.62%; calculated for $[Ru_2(OAc)_4(C_{12}H_9N_3)]NO_3$: C = 34.54%, H = 3.04%, N = 8.06%).

### 5.5.2 Synthesis and characterisation of $[Ru_2(OAc)_4(L2)_2]NO_3$ (C6)

$Ru_2(OAc)_4Cl$ (48.7 mg, 0.0975 mmol) and 2-Aryl-Imidazo(4,5-b)pyridine/**L2** (0.0380 g, 0.195 mmol) were dissolved in 10 mL of isopropanol. The solution was stirred at room temperature for 10 minutes and $AgNO_3$ (0.0216 g, 0.127 mmol) was added to the reaction mixture. The solution was stirred at room temperature for 24 hours and a colour change from dark brown to light brown was observed. The white silver chloride precipitate was removed by filtering under gravity. The filtrate was concentrated and layered with hexane to form a brown precipitate. Yield: 68% (0.00331 g). **M.P**. Decomposes with onset at 354 °C. Electronic absorption at $\lambda_{max}$ (nm) in methanol: 310, 348 – 335 (shoulder). FTIR ($cm^{-1}$): 2939 m, 1629 w $\nu$(C=N), 1437 s $\nu_s(OCO^-)$, 1397 s $\nu_s(OCO^-)$, 1264 s, 1110 w, 1026 m, 946 w, 768 m, 669 s $\nu$(C-$CH_3$). **EA**. (found: C = 41.14%, H= 4.07%, N= 11.42%; calculated for $[Ru_2(OAc)_4(C_{12}H_9N_3)_2]NO_3$: C = 43.04%, H = 3.63%, N = 10.99%).

### 5.5.3 Synthesis and characterisation of $[Ru_2(OAc)_4(L3)_2]NO_3$ (C7)

$[Ru_2(OAc)_4]NO_3$ (0.0224 g, 0.0466 mmol) and 2-ferrocenyl-1H-Imidazo(4,5-c)pyridine/**L3** (0.0284 g, 0.0932 mmol) were added to a 50 mL round bottom flask in 10 mL of isopropanol. The solution was stirred at room temperature for 24 hours. Yield: 72% (0.0161 g). **M.P.** Decomposes with onset at 347 °C. Electronic absorptions at $\lambda_{max}$ (nm) in methanol: 3092 w, 2935 w. FTIR ($cm^{-1}$): 1628 m, 1561 m $\nu(C=N)_{pyr}$, 1439 s $\nu_a(OCO^-)$, 1412 m $\nu_s(OCO^-)$, 1285 s $\nu(NO_3^-)$, 1169 w, 1106 w, 1030 w, 820 m, $\nu$(C-$CH_3$) 683 s. **MS** (ESI-TOF, Acetonitrile + 1%TFA): *m/z* 1045.9642 $[M\text{-}NO_3]^+$, 742.9104 – 745.9066 [M-**L3**-$NO_3$]$^+$, 438.8645 [M-2**L3**-$NO_3$]$^+$, 304.0540 [**L3**]+. **EA**. (found: C= 39.19%, H= 3.49%, N= 8.59%; calculated for $[Ru_2(OAc)_4(C_{16}H_{12}N_3Fe)_2]NO_3$: C= 43.24 H= 3.42%, N= 8.83%).

### 5.5.4 Synthesis and characterisation of $[Ru_2(OAc)_4(L4)_2]NO_3$ (C8)

$[Ru_2(OAc)_4]NO_3$ (0.0210 g, 0.0420 mmol) and 2-ferrocenyl-1H-Imidazo(4,5-b)pyridine/**L4** (0.0256 g, 0.0839 mmol) were dissolved in 10 mL of isopropanol. The solution was stirred at room temperature overnight. A brown solid was obtained by concentrating the solution and layering with THF/ petroleum ether (1:10). Yield: 48% (0.0100 g). **M.P.** Decomposes with onset at 351 °C. Electronic absorptions at $\lambda_{max}$ (nm) in methanol: 321 and 465. FTIR ($cm^{-1}$): 3089 w ($\nu(CH)_{aromatic}$), 2928 w ($\nu(CH)_{aliphatic}$), 1560–1531 s $\nu$(C=N), 1433 s $\nu_a(OCO^-)$, 1413 s $\nu_s(OCO^-)$,1257 s ($NO_3^-$), 1202 w, 1027 w, 1229 w, 1000 w, 820 m, 796 m $\nu$(C-$CH_3$), 696 s $\nu(OCO^-)$ **MS** (ESI-TOF, Acetonitrile + 1%TFA): *m/z* 1047.9559 $[M\text{-}NO_3]^+$, 741.1271 – 744.1252 [M-**L4**-$NO_3$]$^+$, 438.8644 [M-2**L4**-$NO_3$]$^+$, 304.0537 [**L4**]$^+$. **EA**. (found: C= 40.41%, H= 3.30%, N= 8.29%; calculated for $[Ru_2(OAc)_4(C_{16}H_{12}N_3Fe)_2]NO_3$: C = 43.24%, H = 3.42%, N = 8.83%).

### 5.5.5 Synthesis and characterisation of $[Ru_2(OAc)_4(L1)]PF_6$ (C9)

To a stirring solution of $[Ru_2(OAc)_4]PF_6$ (0.0224 g, 0.0385 mmol) in 5.00 mL isopropanol, 2-aryl-1H-imidazo(4,5-c)pyridine/**L1** (0.0150 g, 0.0769 mmol) in 5.0 mL isopropanol was added dropwise. The solution was stirred at room temperature for 24 hours and a colour change from light brown to milky brown was observed. The solvent was reduced to a minimum (ca. 1 mL) and the solution layered with THF/ hexane (1:10) to give a brown solid. Yield: 69% (0.0154 g). **M.P.** Decomposes with onset at 359 °C. Electronic absorptions at $\lambda_{max}$ (nm) in methanol: 290, 330 (shoulder) and 429. FTIR ($cm^{-1}$): 1616 w, 1440 s $\nu_a(OCO^-)$, 1398 s $\nu_s(OCO^-)$,1356 w, 1285 s, 1146 m, 1028 w, 884 m, 853 s, 683 s $\nu$(C-$CH_3$). **MS** (ESI-TOF, Acetonitrile + 1%TFA): 634.9434 $[M\text{-}PF_6]^+$, 438.8648 [M-**L1**-$PF_6]^+$, 196.0876 $[L1]^+$. **EA**. (found: C= 34.56%, H= 2.95%, N= 7.11%; calculated for $[Ru_2(OAc)_4(C_{12}H_9N_3)]PF_6$: C= 33.90%, H = 2.67%, N= 8.79%).

### 5.5.6 Synthesis and characterisation of $[Ru_2(OAc)_4(L2)]PF_6$ (C10)

To a stirring solution of $[Ru_2(OAc)_4]PF_6$ (0.0411 g, 0.0705 mmol) in 5.00 mL isopropanol, 2-aryl-1H-imidazo(4,5-c)pyridine/**L2** (0.0275 g, 0.141 mmol) in 5.0 mL isopropanol was added dropwise. The solution was stirred at room temperature for 24 hours and a colour change from light brown to milky brown was observed. The solvent was reduced to a minimum (ca. 1 mL) and the solution was layered with THF/ hexane (1:10) to give a brown solid which was dried under vacuum. Yield: 66% (0.0271 g). **M.P.** Decomposes with onset at 355 °C. Electronic absorption at $\lambda_{max}$ (nm) in methanol: 310, 348 – 335 (shoulder). Yield: 69. FTIR ($cm^{-1}$): 3631 vw, 3374 vw, 2951 vw, 1618 w $\nu(C{=}N_{lmd})$, 1529 w $\nu(C{=}N_{pyr})$, 1436 s $\nu_a(OCO^-)$, 1398 s $\nu_s(OCO^-)$, 1280 s, 1258 s, 1146 m, 883 m, 842 $\nu(PF_6)$, 767 (m), 679 s $\nu$(C-$CH_3$). **MS** (ESI-TOF, Acetonitrile + 1%TFA): 634.9454 $[M\text{-}PF_6]^+$,438.8645 [M-**L1**-$PF_6]^+$, 196.0882 [**L2**]$^+$. **EA**. (found: C= 30.11%, H=2.98%, N= 5.65%; calculated for $[Ru_2(OAc)_4(C_{12}H_9N_3)]PF_6$: C = 31.08%, H = 3.11%, N = 5.18%).

### 5.5.7 Synthesis and characterisation of $[Ru_2(OAc)_4(L3)]PF_6$ (C11)

To a stirring solution of $[Ru_2(OAc)_4]PF_6$ (0.020 g, 0.0343 mmol) in 5.00 mL isopropanol, 2-ferrocenyl-1H-Imidazo(4,5-b)pyridine/**L3** (0.0211 g, 0.0686 mmol) in 5.00 mL isopropanol was added. The solution was stirred at room temperature for 3 hours. A colour change from orange solution to dark brown was observed. A reddish-brown solid was observed upon solvent removal, layering with petroleum ether. Yield: 33% (0.00696 g). **M.P.** Decomposes with onset at 350 °C. Electronic absorptions at $\lambda_{max}$ (nm) in methanol: 319 and 462. FTIR ($cm^{-1}$): 3083 w ($\nu$(CH)$_{aromatic}$), 2950 w ($\nu$(CH)$_{aliphatic}$), 1733 w, 1563 m $\nu(C{=}N_{Imidazole})$, 1440 ($\nu_a$ ($COO^-$)) s,1398 ($\nu_s$ ($COO^-$)) s, 1147 m $\nu$(Ru-Ru), 1042 m, 883 m, 824 s $\nu(PF_6^-)$, 689 s $\nu$(C-$CH_3$). **MS** (ESI-TOF,

MeOH + 1%TFA): *m/z* 741.1271 $[M\text{-}PF_6]^+$, 438.8642 [M-**L3**-$PF_6]^+$, 304.0539 [**L3**]+. **EA**. (found: C=29.15%, H= 2.75%, N= 4.05%; calculated for $[Ru_2(OAc)_4(C_{16}H_{12}N_3Fe)]PF_6$: C = 32.40%, H = 2.82%, N = 4.73%).

### 5.5.8 Synthesis and characterisation of $[Ru_2(OAc)_4(L4)_2]PF_6$ (C12)

$[Ru_2(OAc)_4]PF_6$ (0.0191 g, 0.0328 mmol) and 2-ferrocenyl-1H-Imidazo(4,5-c)pyridine/**L4** (0.0200 g, 0.0656 mmol) were dissolved in 15 mL of isopropanol. The brown solution was stirred at 40 °C for 24 hours and a brown-black solid was obtained by layering with petroleum ether and washing with THF/ Hexane. Yield: 27%. **M.P.** Decomposes with onset at 350 °C. Electronic absorptions at $\lambda_{max}$ (nm) in methanol: 301, 453. FTIR ($cm^{-1}$): 3087 vw $\nu$(CH)$_{aromatic}$, 1626 m $\nu$(C=N)$_{Imd}$, 1560 m $\nu$(C=N)$_{pyr}$, 1440 s $\nu_a(OCO^-)$,1406 s $\nu_s(OCO^-)$,1351 w, 1286 s, 1169 m, 1025, 694 s $\nu(C\text{-}CH_3)$. **MS** (ESI-TOF, Acetonitrile + 1%TFA):1045.9395 $[M\text{-}PF_6]^+$, 741.9117 [M-**L4**-$PF_6]^+$, 439.8635 [M-2**L4**-$PF_6]^+$. **EA**. (found: C=39.93%, H= 3.56%, N= 6.88%; calculated for $[Ru_2(OAc)_4(C_{16}H_{12}N_3Fe)_2]PF_6$: C = 40.39%, H = 3.22%, N = 7.06%).

### 5.5.9 Synthesis and characterisation of $[Ru_2(OAc)_4(L4)]BF_4$ (C13)

$[Ru_2(OAc)_4(THF)_2]BF_4$ (0.00342 g, 0.0393 mmol) and 2-Aryl-1H-Imidazo(4,5-b)pyridine (0.012 g, 0.0393 mmol) were dissolved in 15 mL of isopropanol and the solution was stirred at room temperature for three days to obtain a brown solid. Yield: 83% (0.00129 g). **M.P.** Decomposes with onset at 306 °C. Electronic absorptions at $\lambda_{max}$ (nm) in methanol: 321 and 465. FTIR ($cm^{-1}$): 2922 w ($\nu$(CH)$_{aromatic}$), 1559 s $\nu$(C=N), 1409 s $\nu_a(OCO^-)$, 1398 s $\nu_s(OCO^-)$,1024 s $\nu(BF_4)$, 797 m $\nu(C\text{-}CH_3)$, 689 s $\nu(OCO^-)$. **MS** (ESI-TOF, MeOH + 1%TFA): *m/z* 741.9091 $[M]^+$, 438.8642 [M-**L1**]$^+$, 304.0540 [**L4**]$^+$. **EA**. (found: C=33.96%, H= 3.42%, N= 5.79%; calculated for $[Ru_2(OAc)_4(C_{16}H_{12}N_3)Fe][BF_4]$: C = 34.77%, H = 3.04%, N = 5.07%).

## 5.6 References


1. Castro, M. A.; Roitberg, A. E.; Cukiernik, F. D., Theoretical and Experimental Studies of Diruthenium Tetracarboxylates Structure, Spectroscopy, and Electrochemistry. *J. Org. Chem.* **2008,** *47* (11), 4682-4690.
2. Urbanos, F. A.; Barral, M. C.; Jiménez-Aparicio, R., Synthesis and properties of some diruthenium acetate compounds. *Polyhedron* **1988,** *7* (24), 2597-2600.
3. Evans, D. F.; The determination of the paramagnetic susceptibility of substances in solution by nuclear magnetic resonance. *J. Chem. Soc. (Resumed)* **1959,** (0), 2003-2005.

# Appendix Section

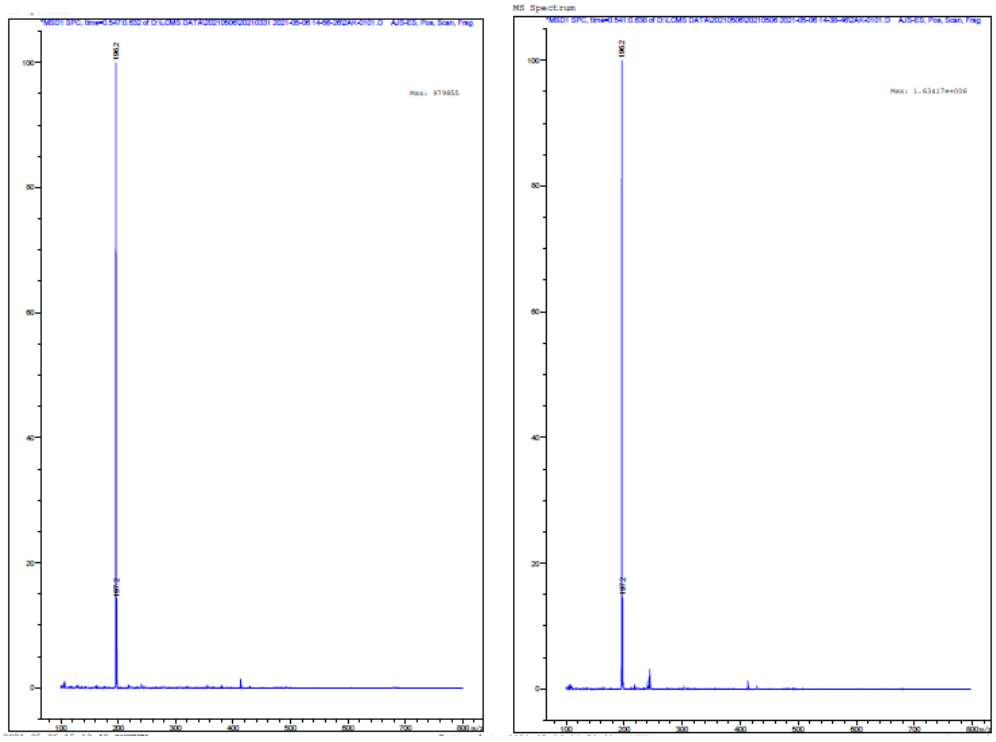

**Figure S1.** LCMS spectra of the ligand **L1a** and its tautomeric form **L1b**.

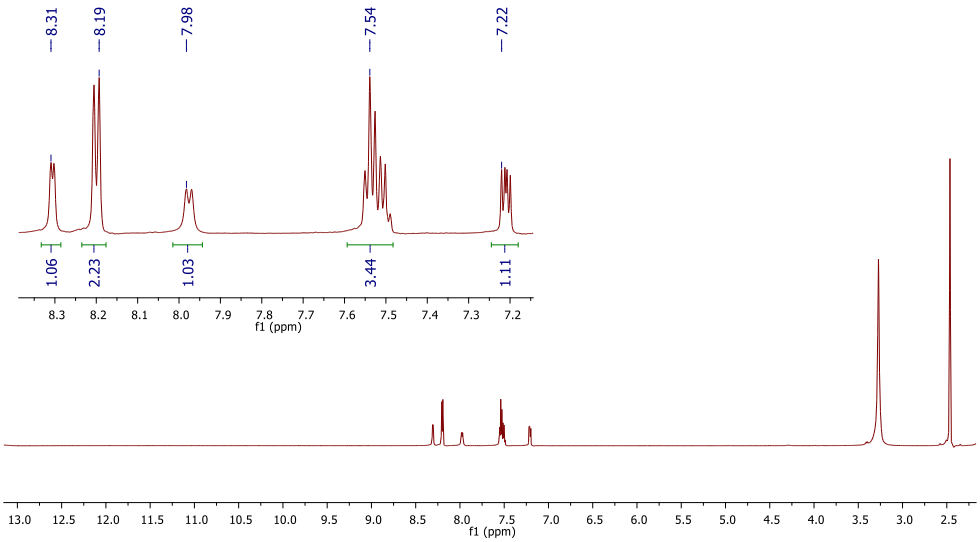


**Figure S2.** $^{1}$H NMR of ligand **L1b** obtained in DMSO.

2D NMR was not performed to distinguish the two tautomers L1a and L1b due to only trace levels of isomer L1a isolated, leading to insufficient sample available.

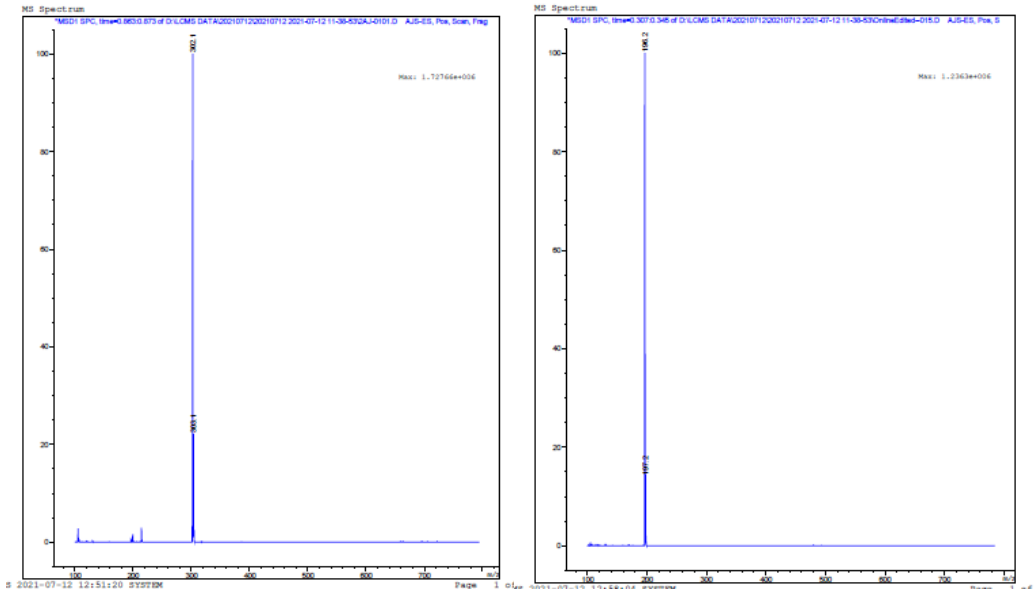

**Figure S3.** LCMS spectra of the Schiff base by-product (left) and the ligand **L2** (right).

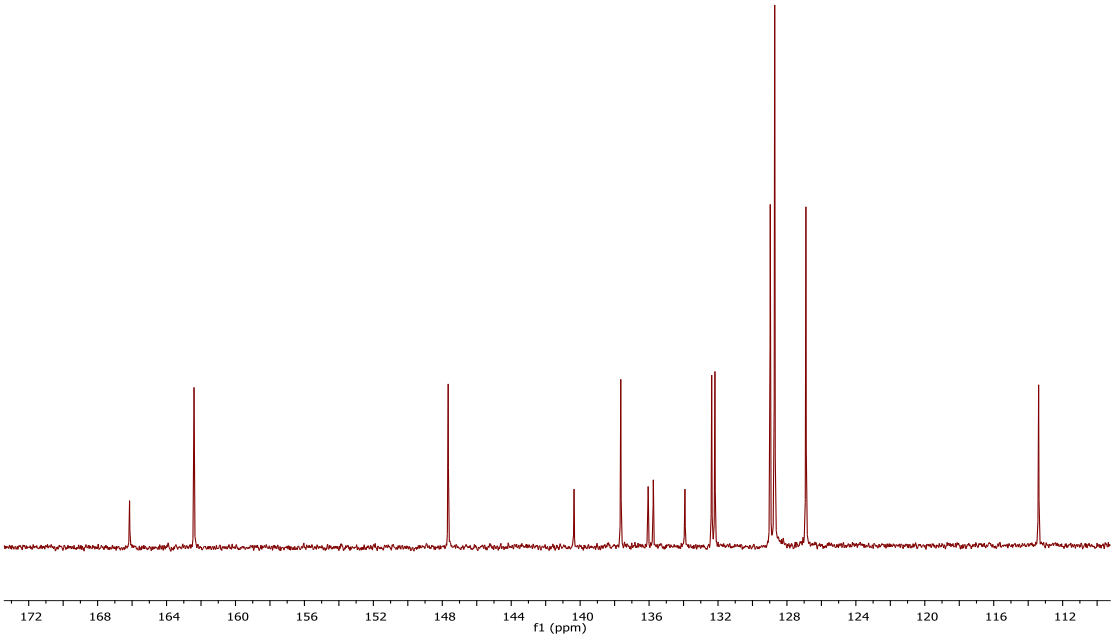


**Figure S4.** $^{13}C$ NMR spectrum a by-product obtained from the reaction between benzaldehyde and 3,4-DAP.

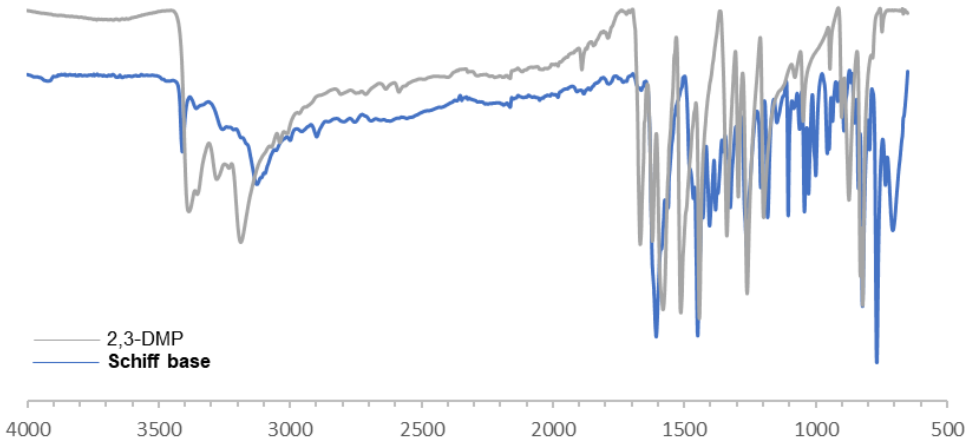


**Figure S5**. Infrared spectrum of the 2-ferrocenyl substituted intermediate Schiff base product.

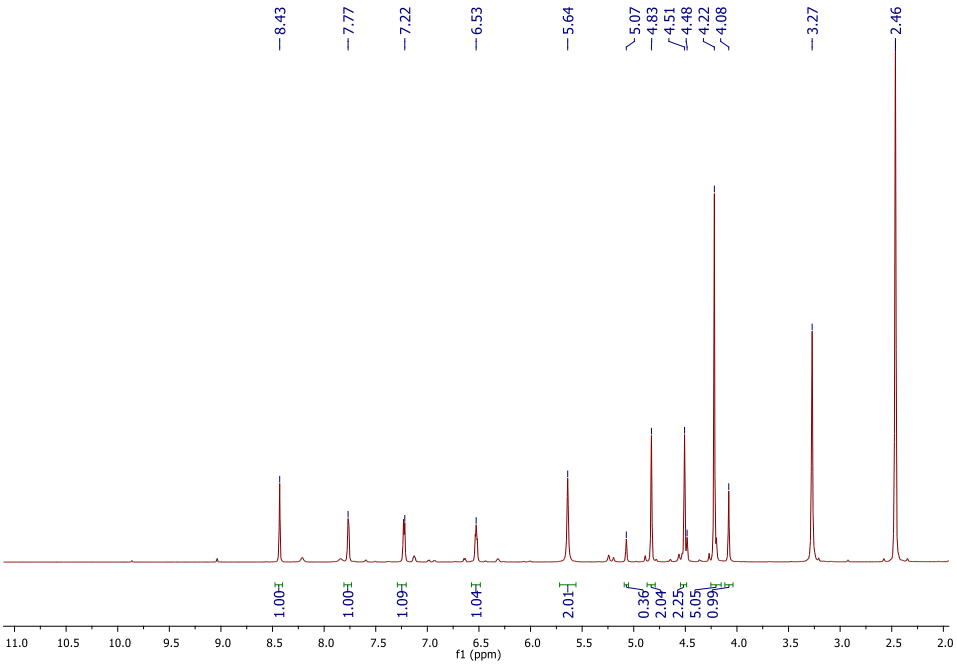


**Figure S6.** $^{1}$H NMR spectrum of the intermediate Schiff base product of the ligand **L3**.

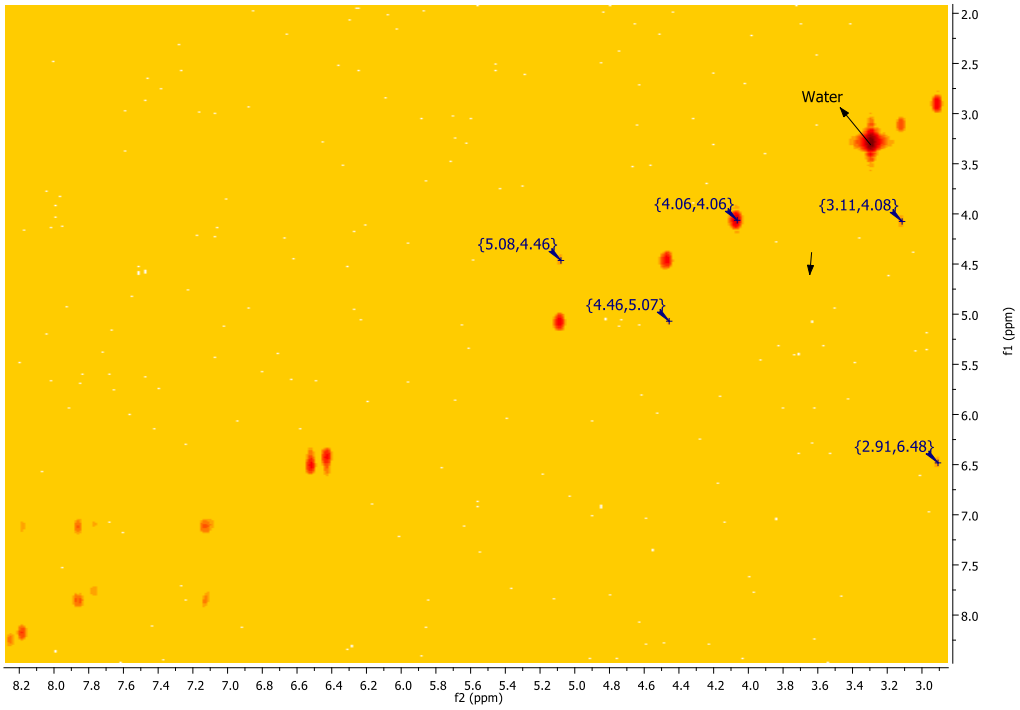


**Figure S7**. COSY NMR spectrum of the ligand **L3a** showing the absence of coupling between the ferrocene and imidazopyridine signals.

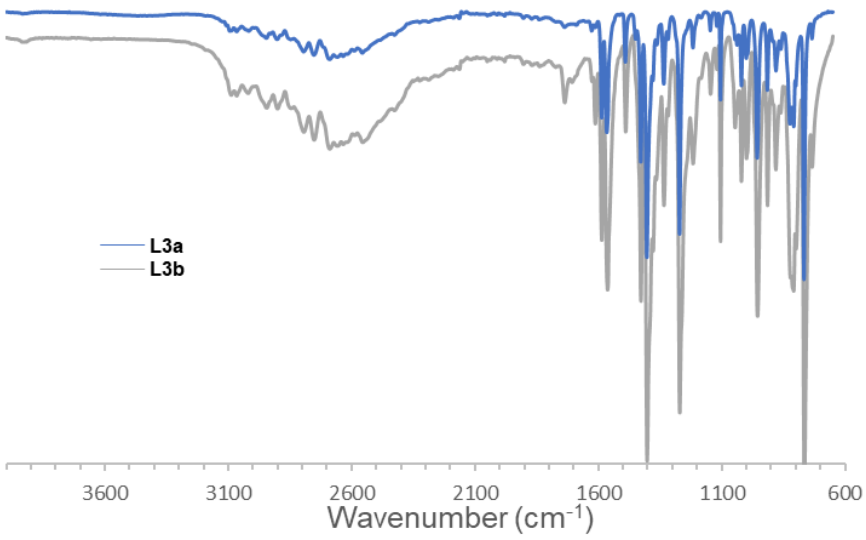


**Figure S8.** Stacked Infrared spectra of the ligands 2-ferrocenyl-1H-Imidazo(4,5-b)pyridine products (**L3a** and **L3b**).

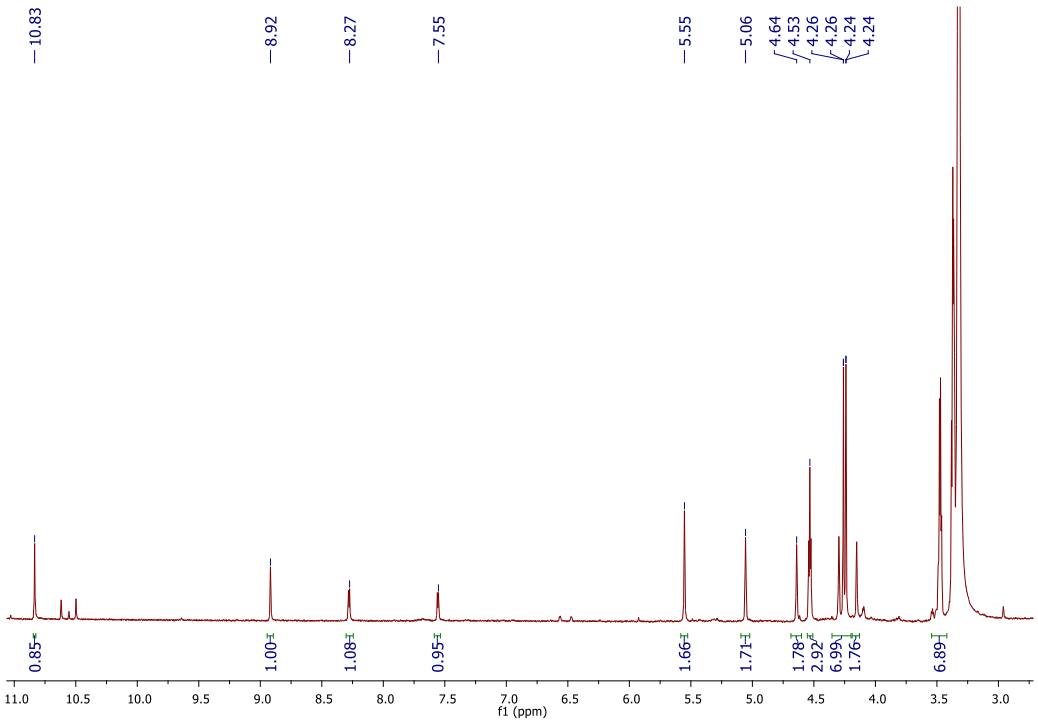


**Figure S9.** $^{1}$H NMR spectrum of N-methylferrocenyl-2-ferrocenyl-1H-Imidazo(4,5-c)pyridine showing presence of unreacted ferrocene carboxaldehyde peaks.

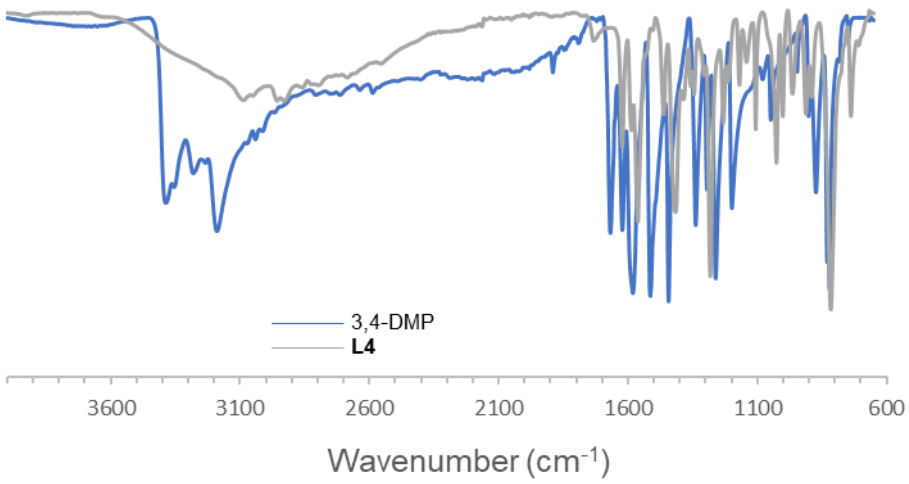


**Figure S10.** Stacked Infrared spectra of the ligands 2-ferrocenyl-1H-Imidazo(4,5-c)pyridine product (**L4**) and 3,4-DAP.

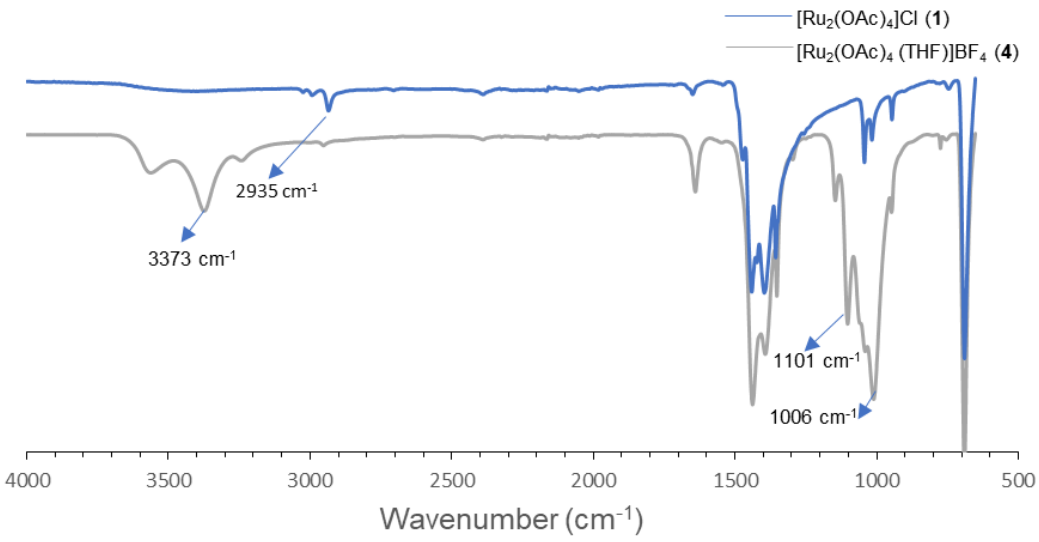


**Figure S11**. Overlaid infrared spectra of precursor complexes **1** and **4**.

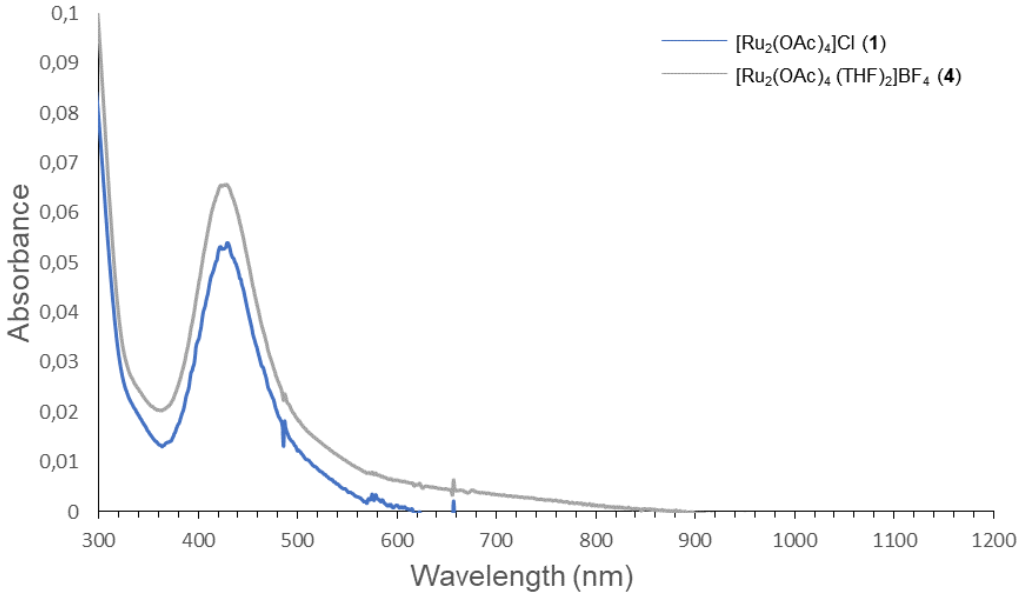


**Figure S12**. Stacked UV-Vis spectra of the complexes **1** and **4**.

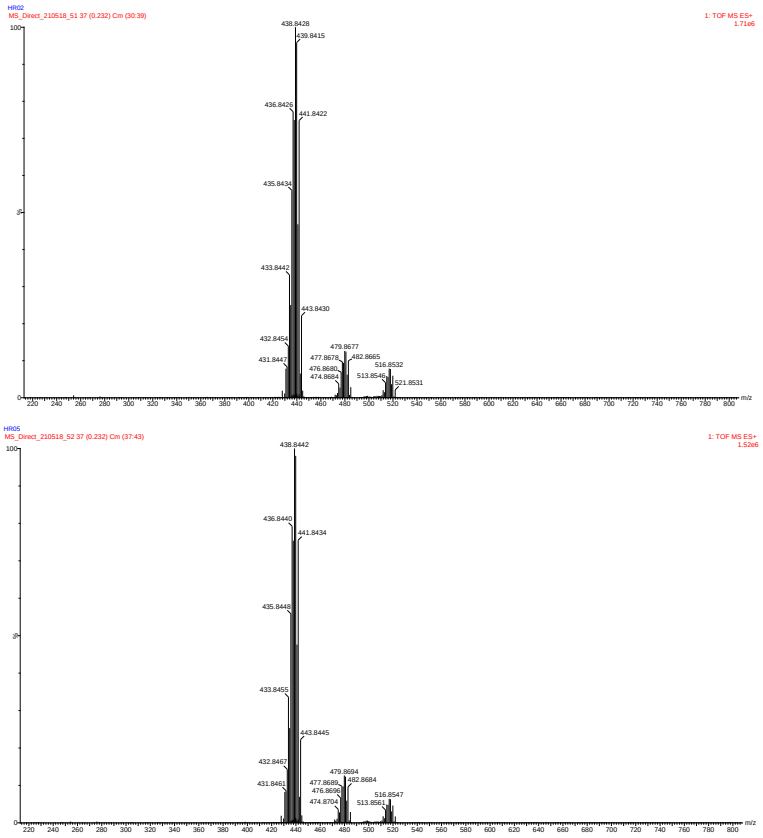


**Figure S13.** ESI mass spectrum of complexes **3** (top) and **4**(bottom).

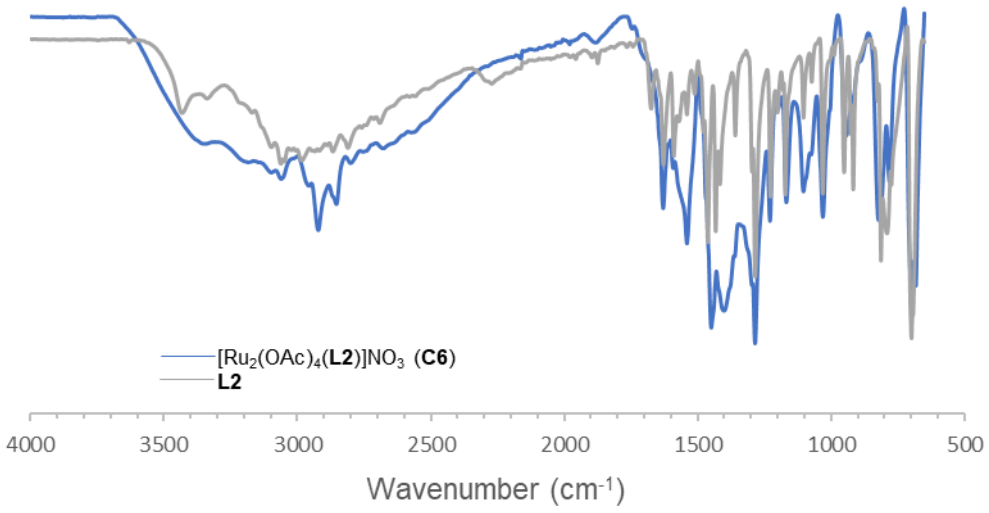


**Figure S14.** Stacked infrared spectra of the complex **C6** and the ligand **L2**.

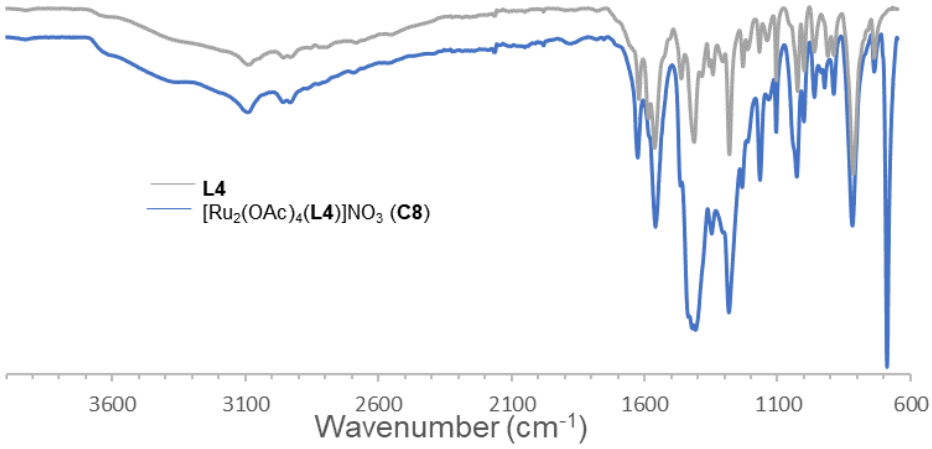


**Figure S15.** Stacked infrared spectra of the complexes **C8** as well as the ligand **L4**.

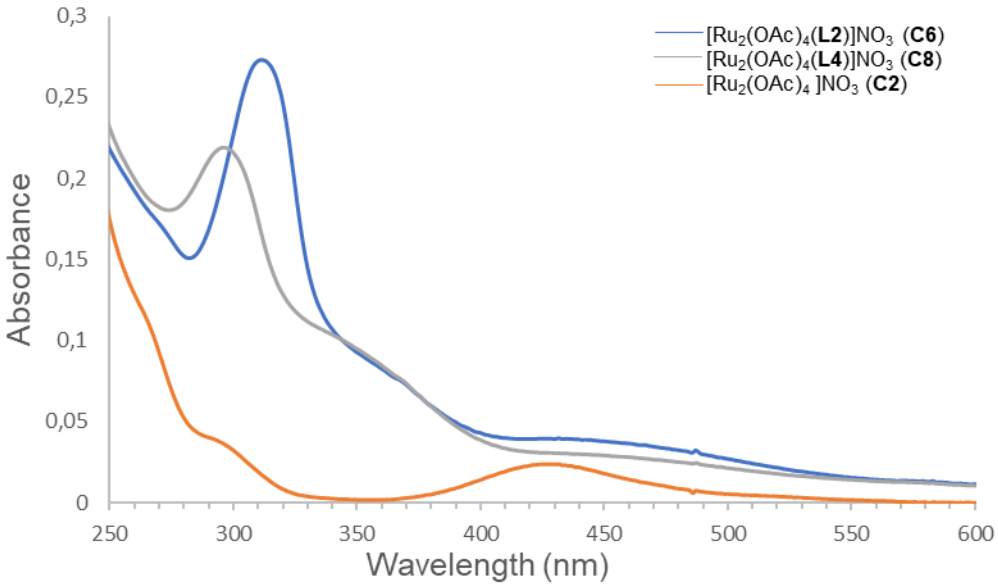


**Figure S16.** Stacked UV-Vis spectra (in methanol) of the complexes **C6** and **C8** obtained in methanol compared with the spectrum of the precursor complex $[Ru_2(OAc)_4]NO_3$(**C2**).

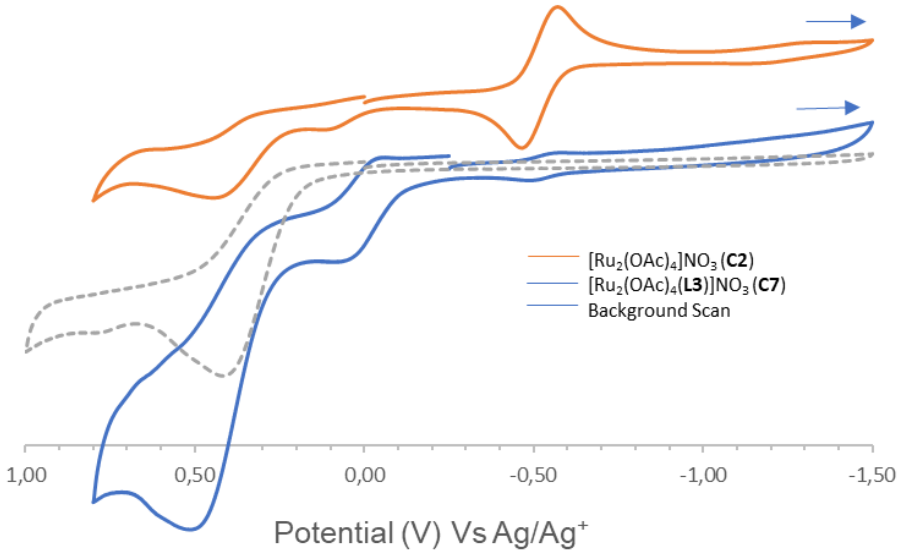


**Figure S17.** Cyclic voltammograms showing the electrochemical processes of the precursor complex **C2**, and **C7** obtained in a methanol solution containing 0.10 M $TBANO_3$ at a scan rate of 100 mV/s.

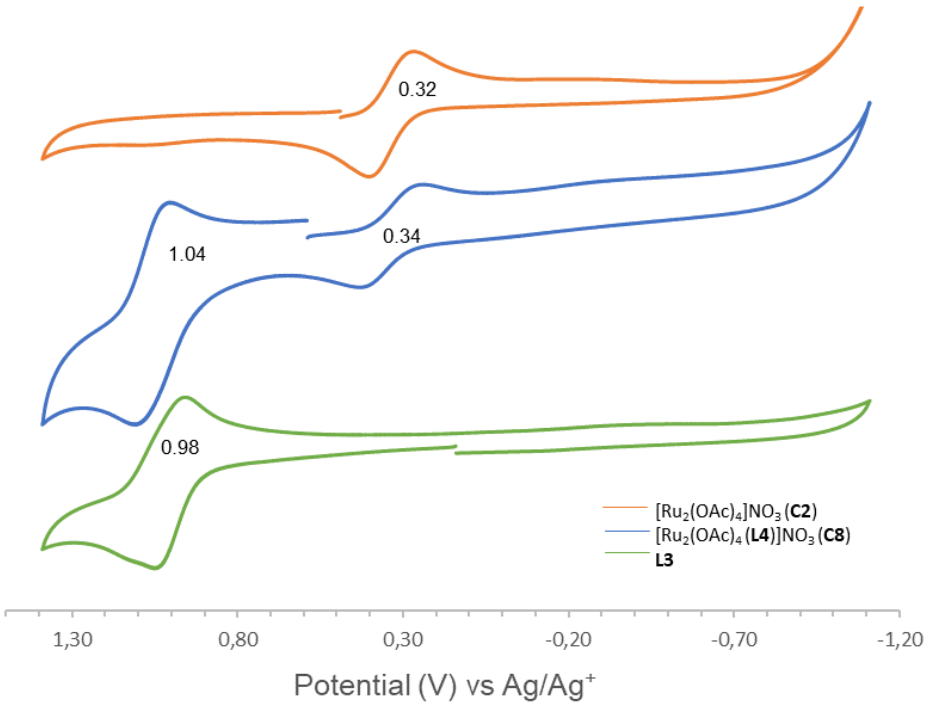


**Figure S18.** Cyclic voltammograms showing the electrochemical processes of the complexes **C2**, **C8** overlaid with that of the ligand **L4**. Obtained in a methanol solution containing 0.10 M TBACl at a scan rate of 100 mV/s.

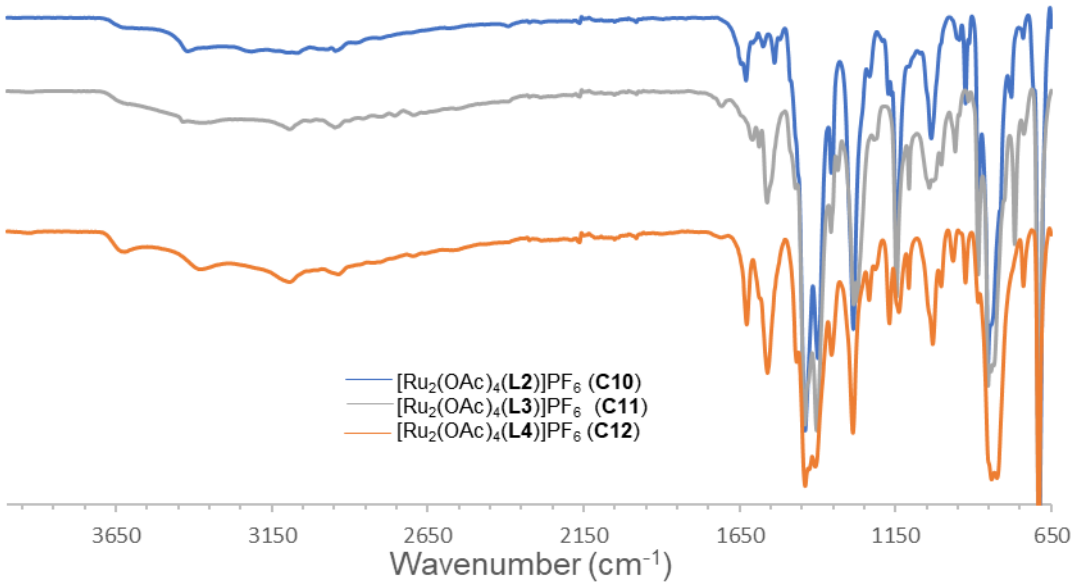


**Figure S19.** Stacked Infrared spectra of the complexes **C10**, **C11** and **C12**.

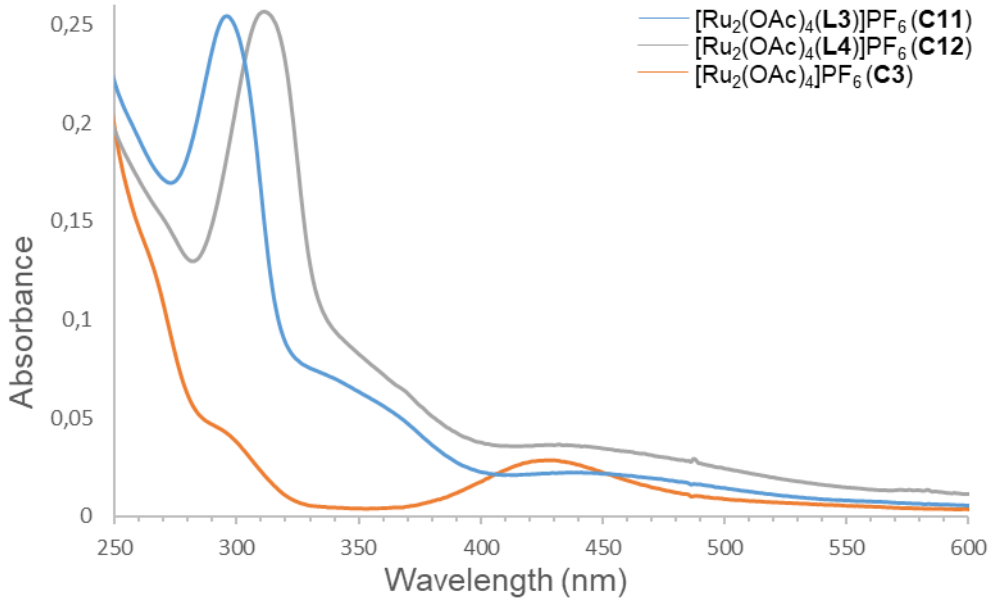


**Figure S20.** Overlaid UV-Vis spectra (in methanol) of the complexes **C11**, **C12** and the precursor complex **C3**.

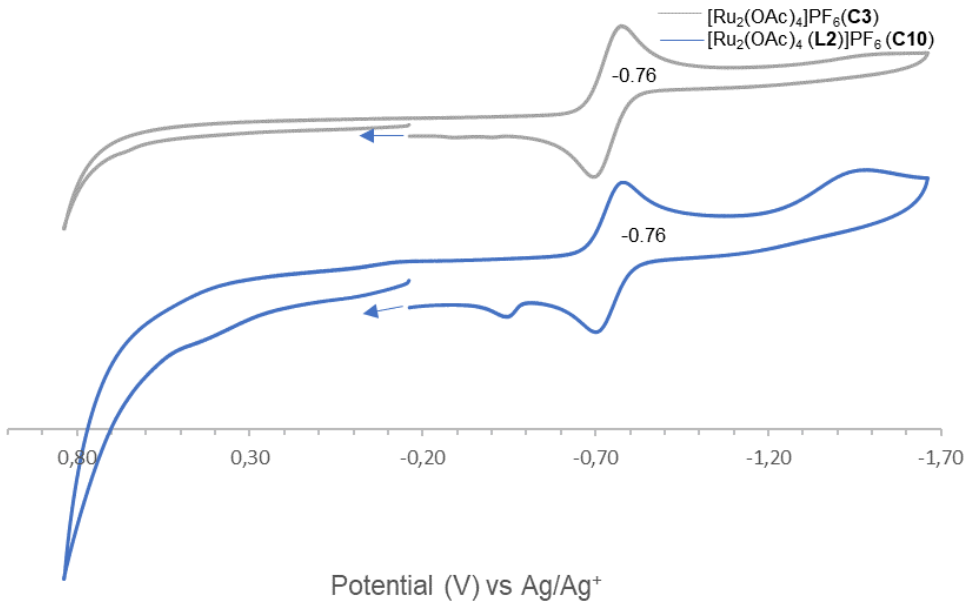


**Figure S21.** Cyclic voltammograms of precursor complexes $[Ru_2(OAc)_4]PF_6$ **C3** and complex **C10**, obtained in a methanol solution containing 0.10 M $TBAPF_6$. The scan rate is 100 mV/s.

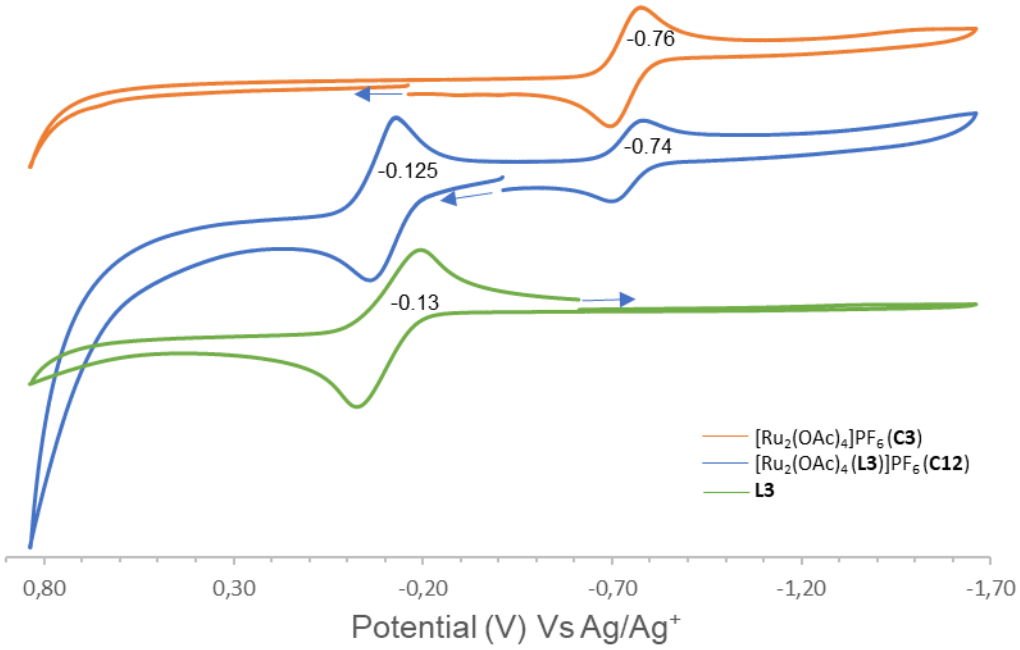


**Figure S22.** Cyclic voltammograms showing the electrochemical processes of the complexes $[Ru_2(OAc)_4]PF_6$ **C3**, $[Ru_2(OAc)_4$(**L3**)$]PF_6$ **C12** and (c) the Ligand **L4,** obtained in a methanol solution containing 0.10 M $TBAPF_6$. The scan rate is 100 mV/s.

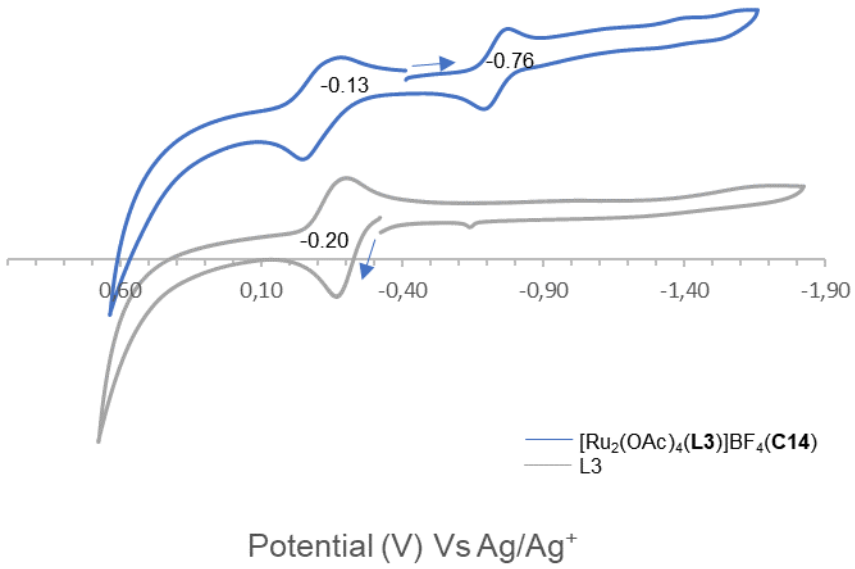


**Figure S23.** Cyclic voltammograms showing the electrochemical process of the complex $[Ru_2(OAc)_4(\mathbf{L3})]BF_4$ (**C14**) overlapped with that of Ligand **L3,** obtained in a methanol solution containing 0.10 M $TBABF_4$. The scan rate is 100 mV/s.

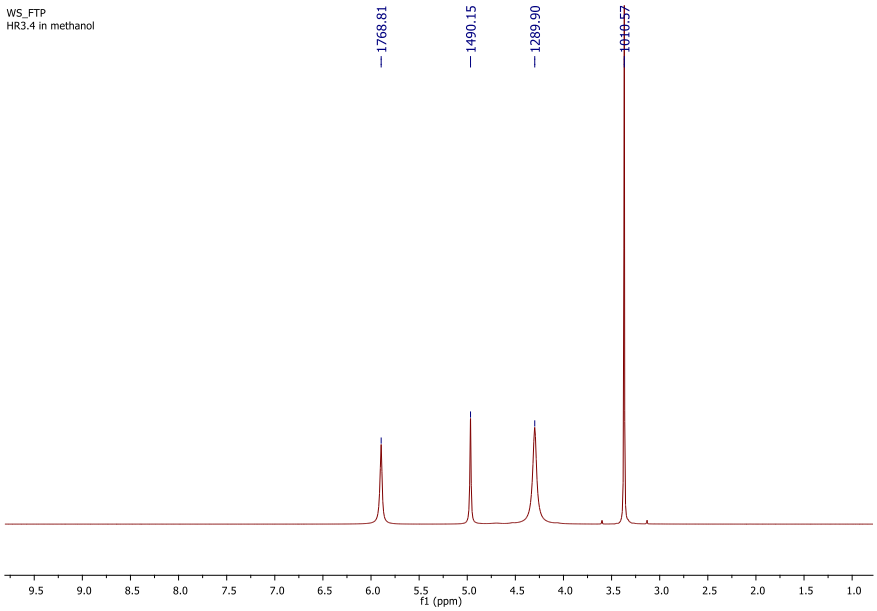


**Figure S24**. Representative $^1H$ NMR spectrum of the precursor complexes **C2** obtained in a 50:1 mixture of MeOD: Proteo MeOH using the Evan's method.

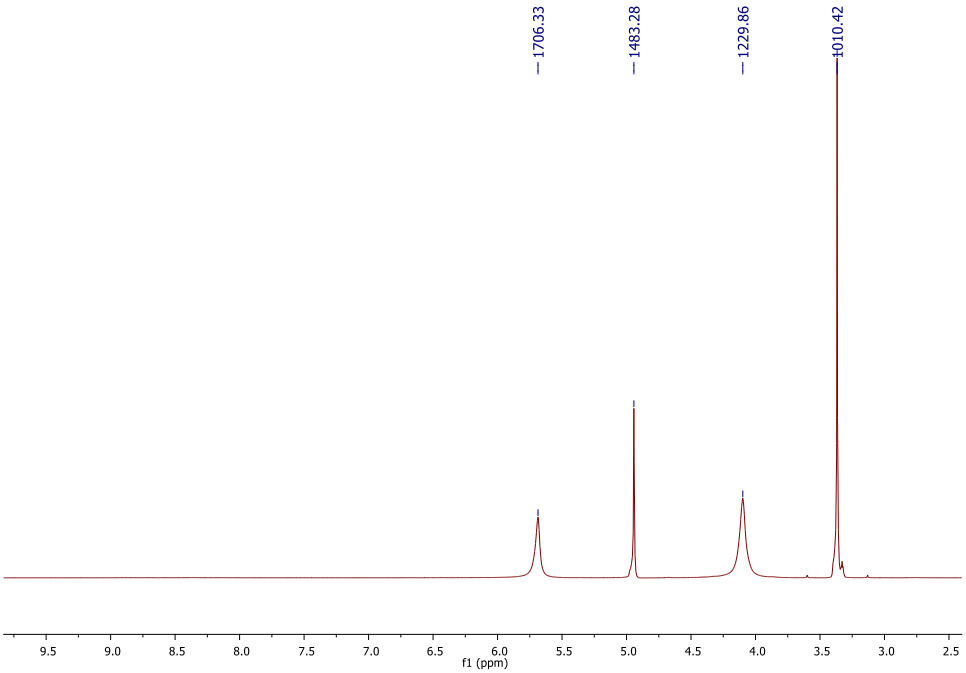


**Figure S25.** $^{1}$H NMR spectrum of complex **C9** obtained in a 50:1 mixture of MeOD: MeOH using the Evan's method.

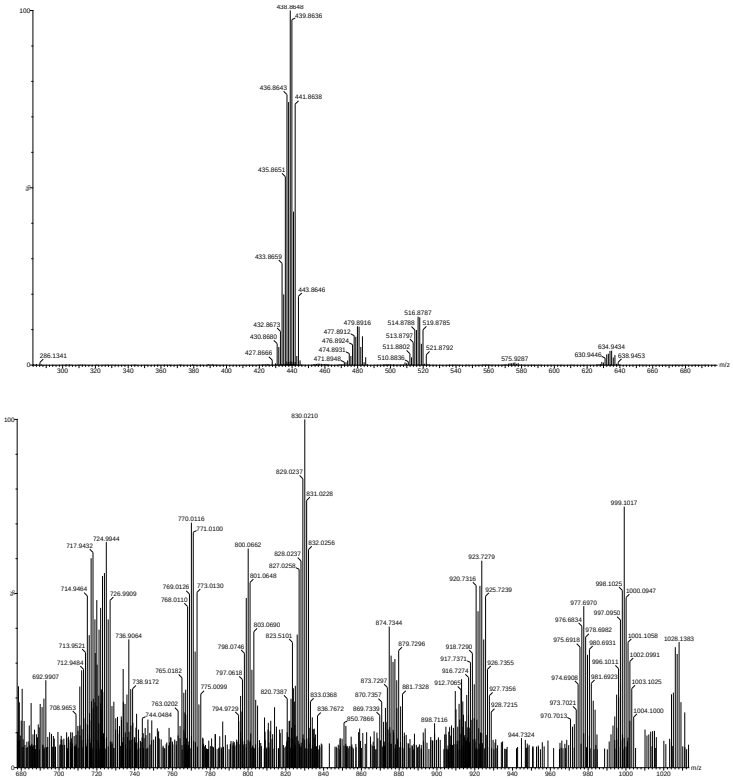

**Figure S26.** High resolution ESI mass spectra of complex **C5**.

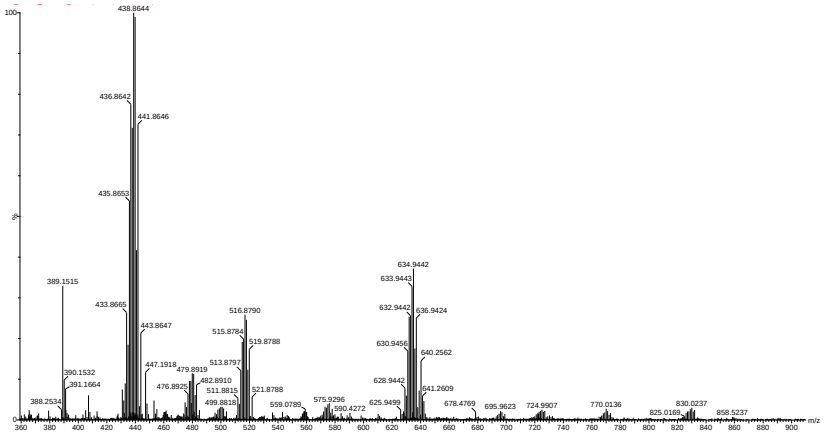


**Figure S27.** ESI-TOF mass spectrum of the complex **C6**.

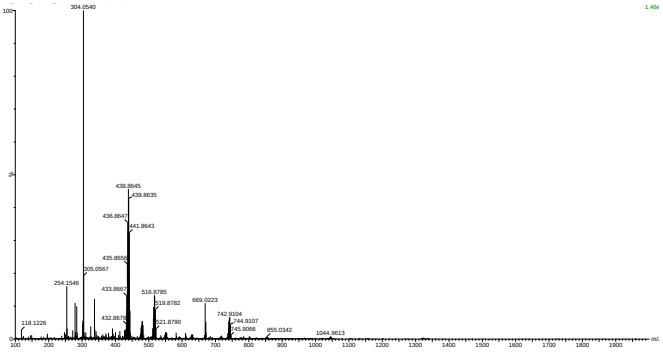


**Figure S28.** High resolution ESI mass spectrum of complex **C7** showing the $[M\text{-}\mathbf{L}]^+$ (top) and $[M]^+$ (bottom) fragmentation peaks.

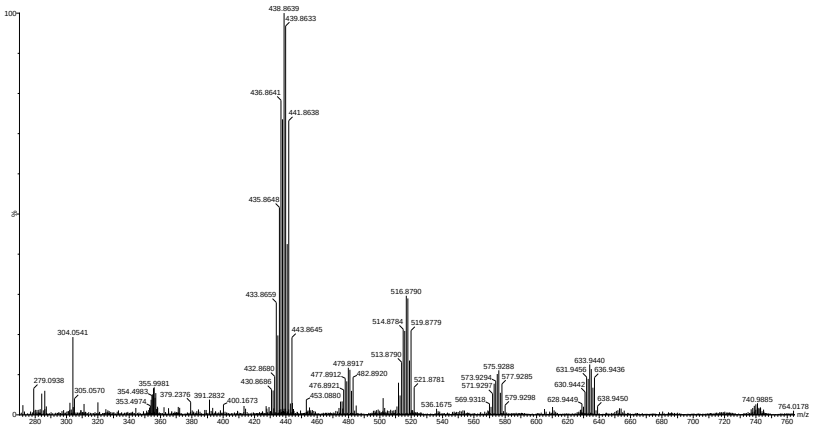


**Figure S29.** ESI mass spectrum of complex **C9**.

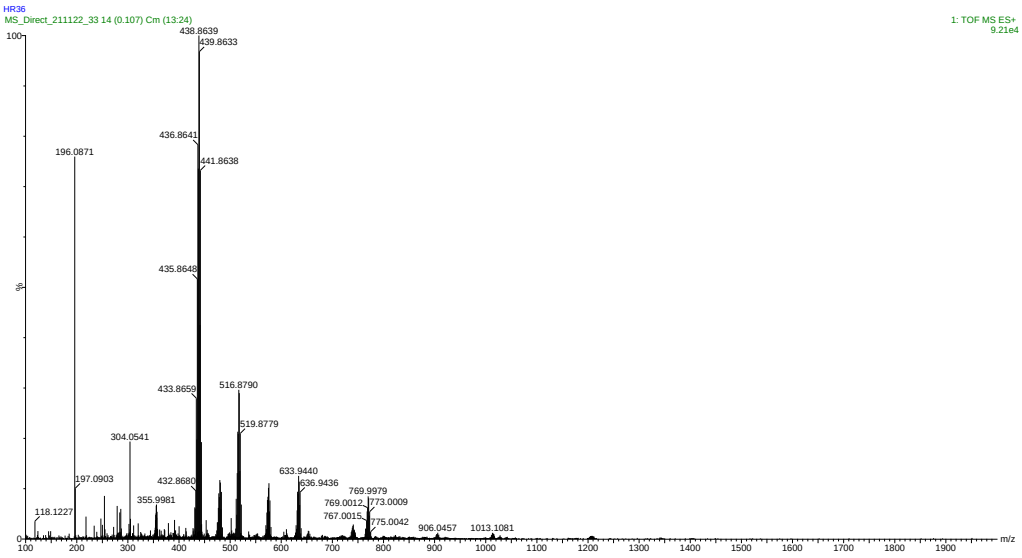


**Figure S30.** High resolution ESI mass spectrum the complex (**C10**).

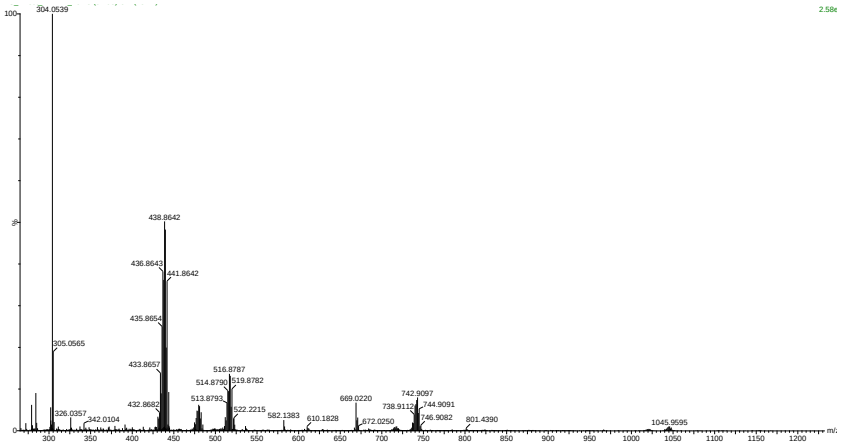


**Figure S31.** ESI mass spectrum of complex **C11**.

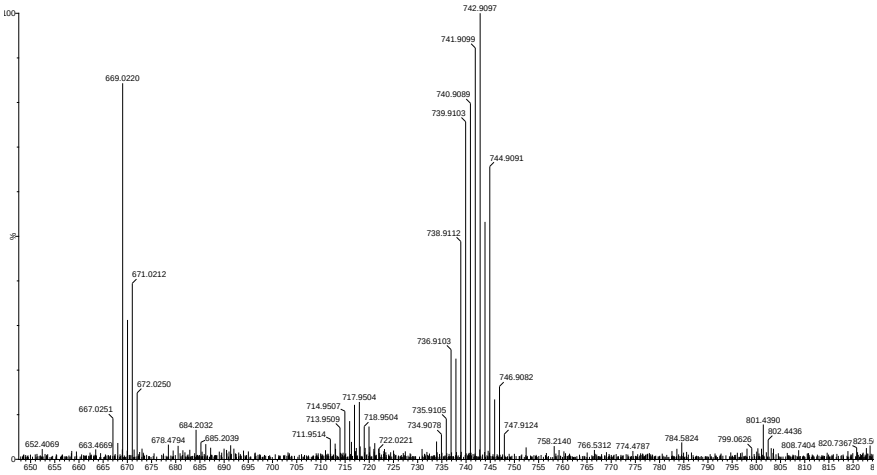


**Figure S32.** High resolution ESI mass spectra of complex **C12** showing the $[M\text{-}\mathbf{L}]^+$ fragmentation peak.

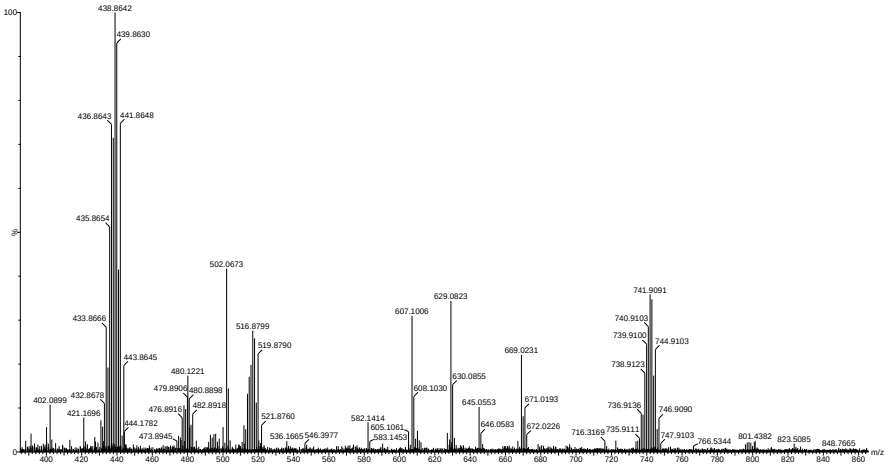


**Figure S33.** High resolution ESI mass spectra of complex **C13** showing the [M-**L4**]$^{+}$ peak.

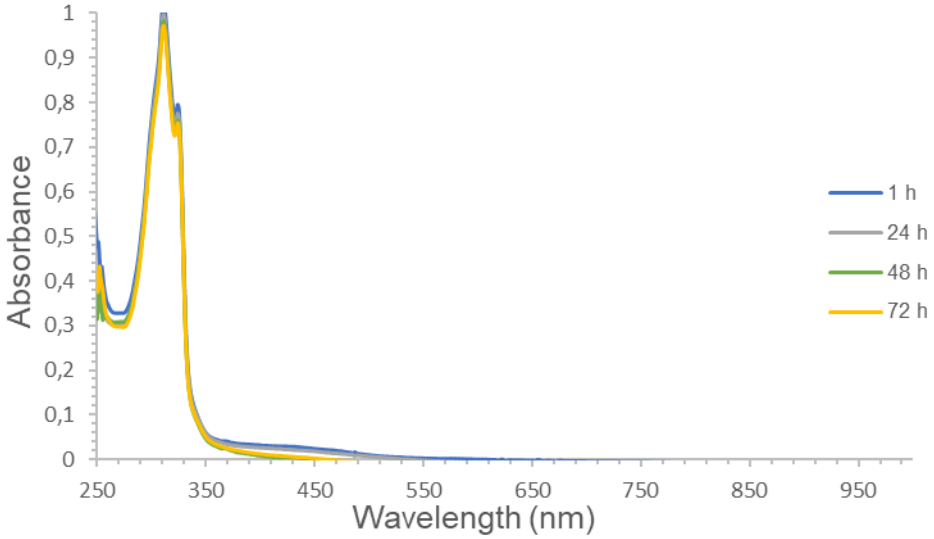


**Figure S34.** UV-Vis spectra (in methanol) of the complex $[Ru_2(OAc)_4(\mathbf{L2})]NO_3$(**C6)** obtained in DMSO over 72 h.

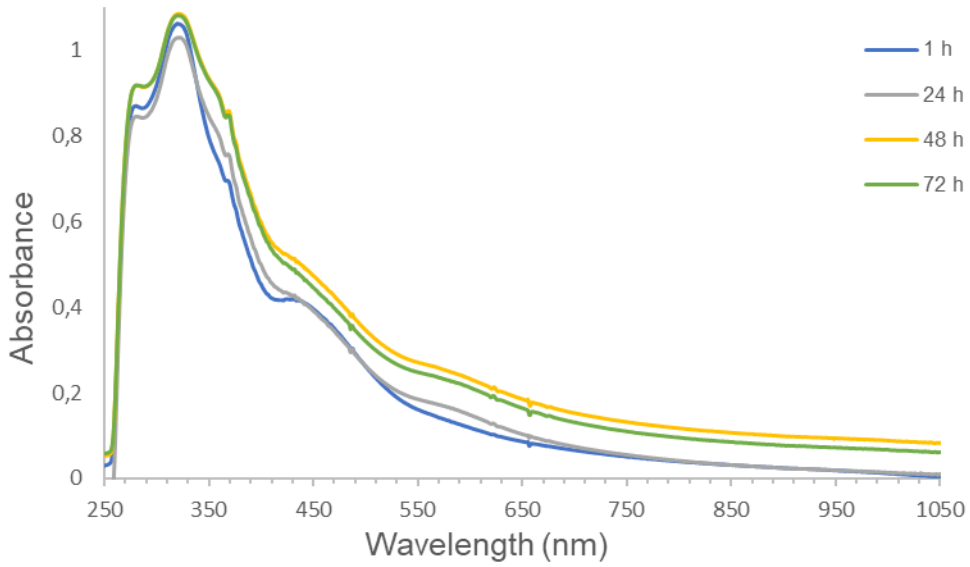


**Figure S35.** UV-Vis spectra of $[Ru_2(OAc)_4(\mathbf{L3})]NO_3$(**C7**) (1 x $10^4$ M) obtained in DMSO, over a period of 72 h.

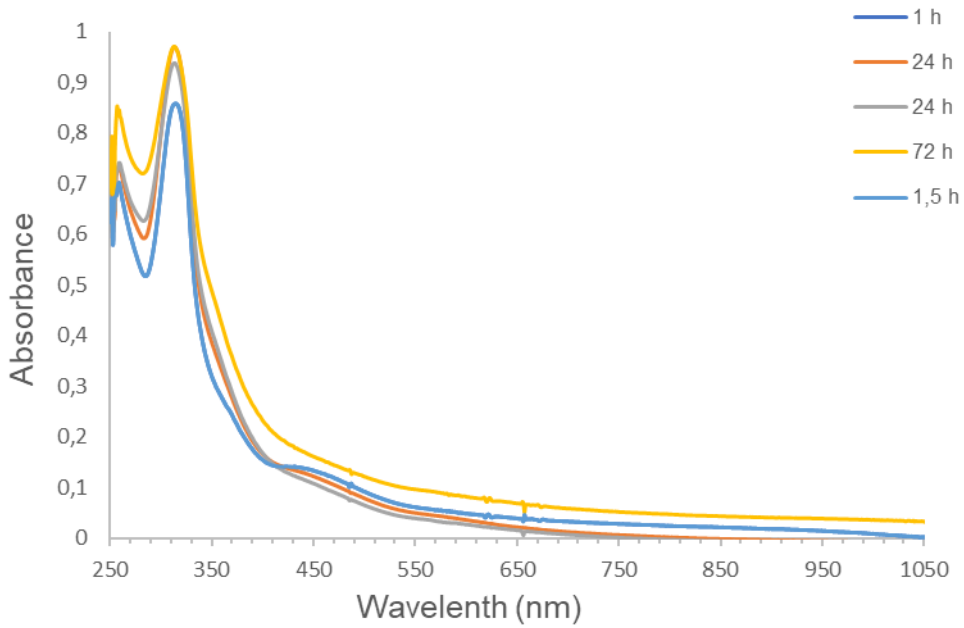


**Figure S36.** UV-Vis spectra of complex $[Ru_2(OAc)_4(\mathbf{L4})]NO_3$(**C8**) (1 x $10^4$ M) obtained in DMSO.

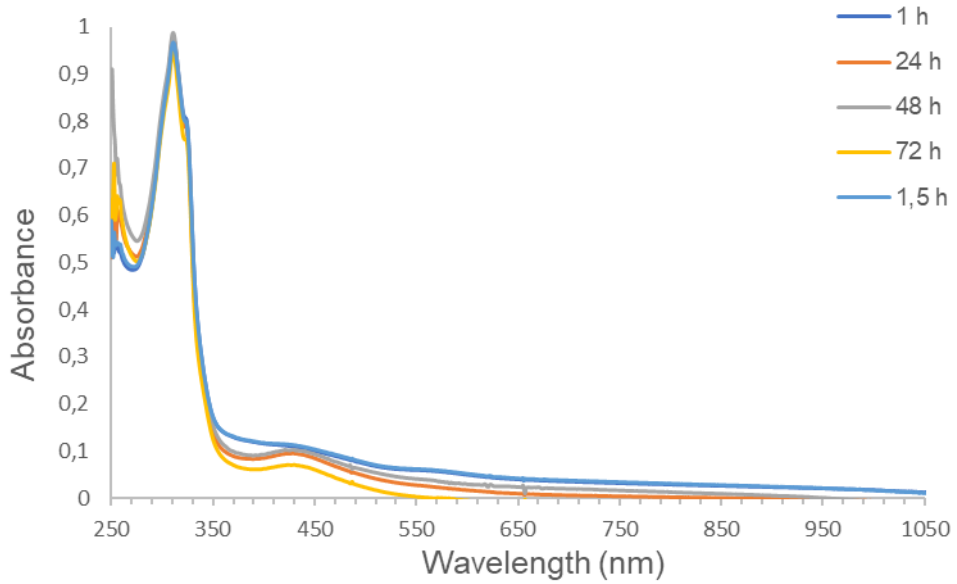


**Figure S37.** UV-Vis spectra (in DMSO) of the complex $[Ru_2(OAc)_4(\mathbf{L1})]PF_6$ (**C9**).

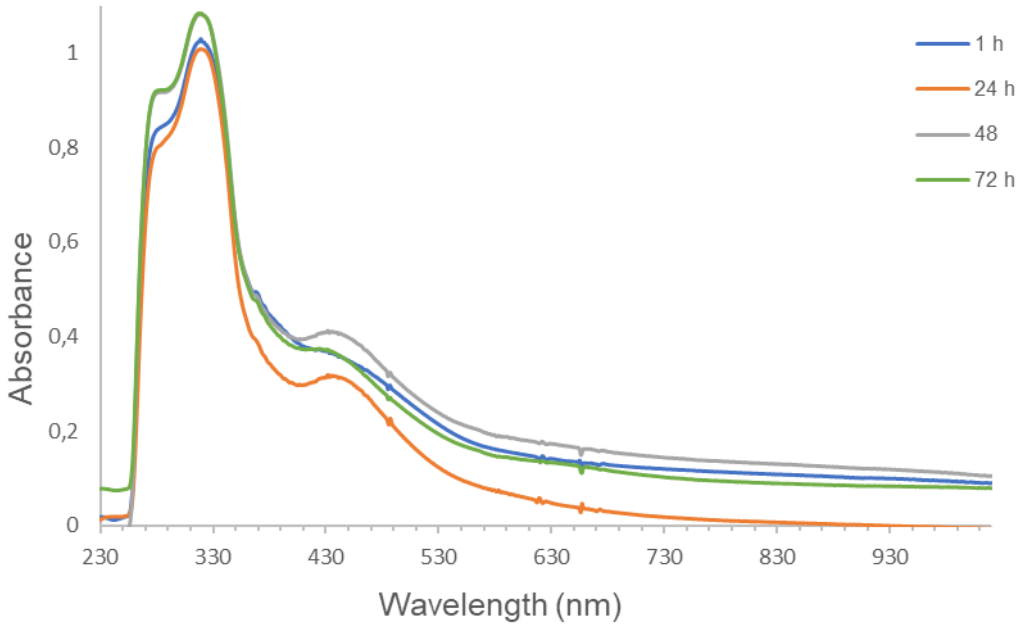


**Figure S38.** UV-Vis spectrum of $[Ru_2(OAc)_4(\mathbf{L2})]PF_6$ (**C10**) (1 x $10^4$ M) in DMSO.

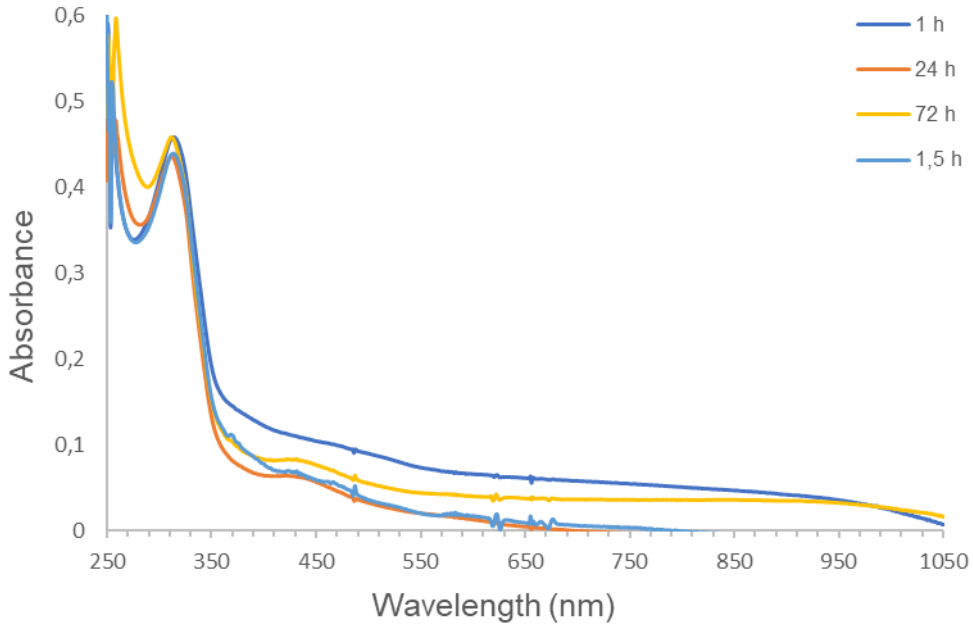


**Figure S39.** UV-Vis spectra (in DMSO) of the complex $[Ru_2(OAc)_4(\mathbf{L4})]BF_4$ **(C14)** (1 x $10^4$ M).

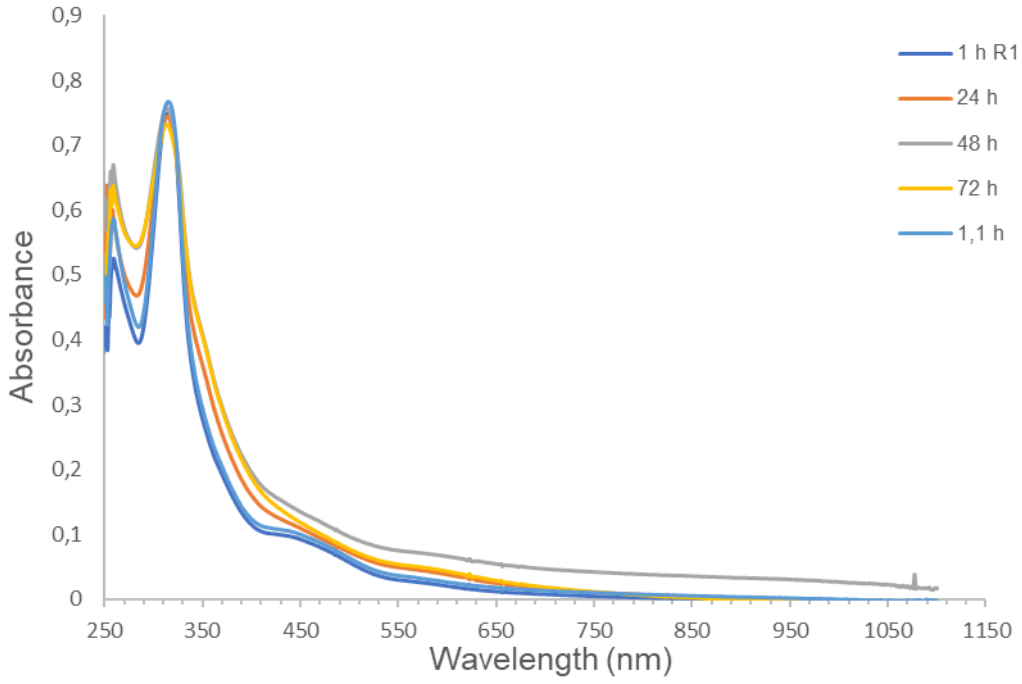


**Figure S40.** UV-Vis spectra (in DMSO) of the complex $[Ru_2(OAc)_4(\mathbf{L4})]BF_4$ **(C15)** (1 x $10^4$ M).

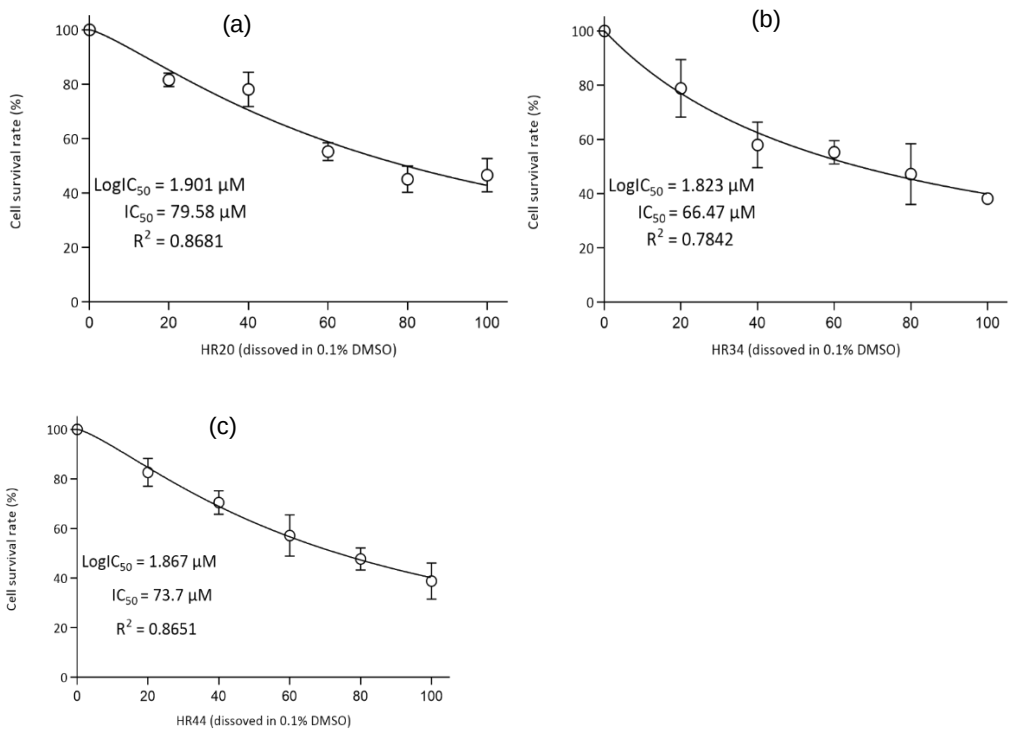


**Figure S41.** $IC_{50}$ graphs for complexes **C5**, **C7** and **C13** after 72 hours of drug exposure